**Zeitschrift:** IABSE publications = Mémoires AIPC = IVBH Abhandlungen
**Band:** 36 (1976)

**Teilband:** IABSE Publications = Mémoires AIPC = IVBH Abhandlungen

**Nutzungsbedingungen**
Die ETH-Bibliothek ist die Anbieterin der digitalisierten Zeitschriften auf E-Periodica. Sie besitzt keine Urheberrechte an den Zeitschriften und ist nicht verantwortlich für deren Inhalte. Die Rechte liegen in der Regel bei den Herausgebern beziehungsweise den externen Rechteinhabern. Das Veröffentlichen von Bildern in Print- und Online-Publikationen sowie auf Social Media-Kanälen oder Webseiten ist nur mit vorheriger Genehmigung der Rechteinhaber erlaubt. Mehr erfahren

**Conditions d'utilisation**
L'ETH Library est le fournisseur des revues numérisées. Elle ne détient aucun droit d'auteur sur les revues et n'est pas responsable de leur contenu. En règle générale, les droits sont détenus par les éditeurs ou les détenteurs de droits externes. La reproduction d'images dans des publications imprimées ou en ligne ainsi que sur des canaux de médias sociaux ou des sites web n'est autorisée qu'avec l'accord préalable des détenteurs des droits. En savoir plus

**Terms of use**
The ETH Library is the provider of the digitised journals. It does not own any copyrights to the journals and is not responsible for their content. The rights usually lie with the publishers or the external rights holders. Publishing images in print and online publications, as well as on social media channels or websites, is only permitted with the prior consent of the rights holders. Find out more

**Download PDF:** 02.04.2026

**ETH-Bibliothek Zürich, E-Periodica, https://www.e-periodica.ch**

ASSOCIATION INTERNATIONALE DES PONTS ET CHARPENTES
INTERNATIONALE VEREINIGUNG FÜR BRÜCKENBAU UND HOCHBAU
INTERNATIONAL ASSOCIATION FOR BRIDGE AND STRUCTURAL ENGINEERING

# MÉMOIRES
# ABHANDLUNGEN

## 36-II

## 1976

PUBLIÉS PAR LE SECRÉTARIAT GÉNÉRAL À ZURICH
HERAUSGEGEBEN VOM GENERALSEKRETARIAT IN ZÜRICH
PUBLISHED BY THE GENERAL SECRETARIAT IN ZURICH

*Editeur - Verleger - Publisher*

*Association Internationale des Ponts et Charpentes*
*Ecole Polytechnique Fédérale de Zurich*

*Internationale Vereinigung für Brückenbau und Hochbau*
*Eidgenössische Technische Hochschule Zürich*

*International Association for Bridge and Structural Engineering*
*Swiss Federal Institute of Technology, Zurich*

ETH – Hönggerberg
CH – 8093 Zürich

*Printed in Switzerland*
ISBN 3 85748 012 2

# Préface

Le présent volume des «Mémoires» est le quarante-cinquième et le dernier de la série inaugurée en 1932. Cette constatation résulte des décisions prises par notre Association qui prévoit dès 1977 une conception différente de nos publications. Si l'on jette un regard en arrière, nous pouvons constater que les 700 articles publiés, tous originaux et de haut niveau, ont joué un rôle incontestable, quoique difficile à mesurer, dans l'amélioration de la conception et du calcul des structures. Pour l'avenir, nous voulons intensifier encore notre action, cherchant à satisfaire aussi bien les chercheurs que les praticiens et les entrepreneurs. En effet, nous sommes convaincus qu'une liaison toujours plus étroite entre tous les acteurs de la construction est indispensable pour la réussite économique, esthétique et fonctionnelle. C'est ainsi que nous continuerons à ouvrir nos colonnes dans nos nouvelles publications à tous ceux qui sont intéressés au développement des ponts et charpentes, en souhaitant une intervention accrue des constructeurs et des spécialistes du management de la construction.

Je remercie les auteurs des 11 contributions de ce volume. Par leur qualité et leur actualité, ces exposés illustrent parfaitement la valeur de nos publications et l'intérêt de leur diffusion internationale.

Zurich, août 1976.

Le Président de l'AIPC:

Prof. MAURICE COSANDEY

## Vorwort

Der vorliegende Band der «Abhandlungen» ist der 45. und zugleich letzte der im Jahre 1932 eingeführten Reihe. Diese Tatsache beruht auf Beschlüssen unserer Vereinigung, welche ab 1977 ein neues Konzept für unsere Veröffentlichungen vorsehen. Rückblickend können wir feststellen, dass die 700 veröffentlichten Artikel von hohem Wert sind und unzweifelhaft einen wesentlichen, wenn auch schwer messbaren Einfluss auf die Verbesserungen von Konzept und Berechnung von Bauwerken hatten. In der Zukunft wollen wir unsere Anstrengungen noch verstärken, um Wissenschafter wie Praktiker und Unternehmer zufriedenzustellen. Wir sind überzeugt, dass eine immer engere Verbindung zwischen allen am Bauwesen Beteiligten unerlässlich ist, um einen wirtschaftlichen, ästhetischen sowie funktionellen Erfolg zu gewährleisten. Im Hinblick auf dieses Ziel werden wir weiterhin die Spalten in unseren Publikationen offenhalten für alle diejenigen, die an der Entwicklung des Brückenbaus und Hochbaus interessiert sind. Wir hoffen auf eine vermehrte Beteiligung von Seiten der Konstrukteure und der Spezialisten des Baumanagements.

Ich danke den Verfassern der 11 Beiträge dieses Bandes. Die Qualität und Aktualität dieser Beiträge begründen den Wert und rechtfertigen das unseren Veröffentlichungen entgegengebrachte Interesse und deren internationale Verbreitung.

Zürich, August 1976.

Der Präsident der IVBH:

Prof. MAURICE COSANDEY

## Foreword

This edition of the "Memoires" is the 45th to be published since the first issue was produced in 1932. It is also the last in the present series. The Association has now decided that, as from 1977, there will be a re-organization in the production of our publications. A survey of the previous 700 articles shows that they are of a very high quality and originality of thought. Although it is difficult to assess their exact degree of influence it is evident that they have played an indisputable part in the improvement of planning and design in structural engineering. Our aim in the future is to intensify our activities in order to satisfy the needs of those engaged in research, design and construction. We are convinced that a closer collaboration between all those engaged in every aspect of construction is absolutely necessary in order to achieve more economical, aesthetic and functional results. With this purpose in mind we shall continue to reserve space in our new publications for all those who are interested in bridge and structural engineering development. We hope for an increased participation by engineers and specialists in construction management.

I should like here to offer my thanks to all authors of the eleven contributions to this volume. The quality and topicality of the papers which they have submitted illustrate perfectly not only the excellent value of our publications; it also indicates the wider scope of international interest which they now cover.

Zurich, August 1976.

The President of the IABSE:

Prof. MAURICE COSANDEY

Leere Seite
Blank page
Page vide

# Table des matières - Inhaltsverzeichnis - Table of Contents


Etude et essais sur modèle d'un caisson de réacteur en béton précontraint, à cavités multiples
Studien und Modellversuche an einem mit Hohlräumen durchsetzten Reaktordruckgefäss aus vorgespanntem Beton
Studies and Tests on Model of a Prestressed Concrete Nuclear Vessel with Multiple Cavities

I R. Lafitte, F. Vuilleumier, J.-D. Marchand ..... Français 1
Projet du caisson et du modèle

II M. Paquet, B. Rebora, Th. Zimmermann ..... Français 12
Analyse numérique non linéaire du modèle du caisson

III R. Favre, M. Koprna, J.-P. Jaccoud ..... Français 16
Essai sur modèle d'un caisson en béton précontraint à cavités multiples

IV R. Lafitte, B. Saugy, F. Vuilleumier ..... Français 26
Synthèse des calculs et des essais sur modèle

F. Cheong-Siat-Moy, Le-Wu Lu ..... English 31

Stiffness and Strength Design of Multistory Frames
Critères de rigidité et de résistance pour les cadres étagés
Steifigkeits- und Festigkeitskriterien beim Entwurf von Stockwerkrahmen

J.M. Davies, F. Thompson ..... English 49

Light Gauge Steel Folded Plate Construction
Toits plissés formés d'éléments minces en acier
Faltwerke aus Stahlleichtprofilen

M.-H. Derron, J. Jirousek ..... Français 65

Eléments spatiaux de barres courbes
Räumlich gekrümmte Balkenelemente
Space-Curved Rod Elements

R. Favre, P. Kropf ..... Deutsch 89

Reibungsmessungen an Gleitlagern
Friction Tests on Sliding Bearings
Mesures du frottement d'appuis glissants

JOSEF GROB, BRUNO THÜRLIMANN ..... English 105

Ultimate Strength and Design of Reinforced Concrete Beams under Bending and Shear
Résistance et dimensionnement des poutres en béton armé soumises à la flexion et à l'effort tranchant
Bruchwiderstand und Bemessung von Stahlbetonbalken unter Biegung und Schub

KUANG HAN CHU, MARVIN JONES ..... English 121

Theory of Dynamic Analysis of Box Girder Bridges
Théorie d'une analyse dynamique de ponts à poutres en caisson
Theorie einer dynamischen Berechnung von Kastenträgerbrücken

MARVIN JONES, KUANG HAN CHU ..... English 133

Dynamic Analysis of a Box Girder Bridge
Analyse dynamique d'un pont à poutres en caisson
Dynamische Berechnung einer Kastenträgerbrücke

P. MÜLLER ..... English 147

Failure Mechanisms for Reinforced Concrete Beams in Torsion and Bending
Mécanismes de ruine pour des poutres en béton armé soumises à la torsion et à la flexion
Bruchmechanismen für Stahlbetonbalken unter Torsion und Biegung

K.S. VIRDI, P.J. DOWLING ..... English 165

A Unified Design Method for Composite Columns
Une méthode unifiée de calcul des colonnes mixtes acier-béton
Eine vereinheitlichte Methode für den Entwurf von Verbundstützen

U. WALDER, E. ANDERHEGGEN ..... Deutsch 185

Das Computerprogramm FLASH
The Computer Program FLASH
Le programme FLASH

# Etude et essais sur modèle d'un caisson de réacteur en béton précontraint, à cavités multiples

*Studien und Modellversuche an einem mit Hohlräumen durchsetzten Reaktordruckgefäss aus vorgespanntem Beton*

*Studies and Tests on Model of a Prestressed Concrete Nuclear Vessel with Multiple Cavities*

PARTIE I

## Projet du caisson et du modèle

R. LAFITTE, sous-directeur, F. VUILLEUMIER, ingénieur principal, J.D. MARCHAND, ingénieur, chez Bonnard & Gardel, Ingénieurs-conseils S.A.

### 1. Introduction

Dans le cadre d'un accord germano-suisse, des études de développement d'une centrale nucléaire, équipée d'un réacteur à haute température et de turbines à hélium, ont été entreprises.

Un élément important de cette centrale est constitué par un caisson en béton précontraint qui englobe non seulement le réacteur, les échangeurs et récupérateurs de chaleur, mais encore trois turbines à gaz de 500 MW chacune. Le caisson se présente (fig. 1) sous la forme d'un cylindre de 48 mètres de diamètre et de 39 mètres de hauteur, comportant 28 cavités. Celles-ci sont remplies d'hélium atteignant dans la majeure partie des zones une pression de 65 kg/cm$^2$ et une température de 850° C.

Le caractère particulier de ce caisson, d'une forme encore jamais exécutée notamment si l'on considère la forte épaisseur des parois percées de nombreuses cavités, a nécessité que l'on fasse clairement la démonstration de sa faisabilité et que l'on assure à l'ouvrage une sécurité suffisante tout en obtenant une conception économique de la structure. Ainsi, sans attendre le stade du projet définitif, a-t-il été jugé nécessaire d'entreprendre des essais statiques sur modèle réduit. Il est aussi apparu important, parallèlement aux essais, de recourir à l'utilisation d'un programme de calcul puissant à l'ordinateur, permettant de simuler et par conséquent de prévoir le comportement du modèle statique dans le domaine non linéaire et jusqu'à la rupture. La comparaison des essais et du calcul valorise en outre l'outil mathématique dans son utilisation pour le projet du caisson en vraie grandeur.

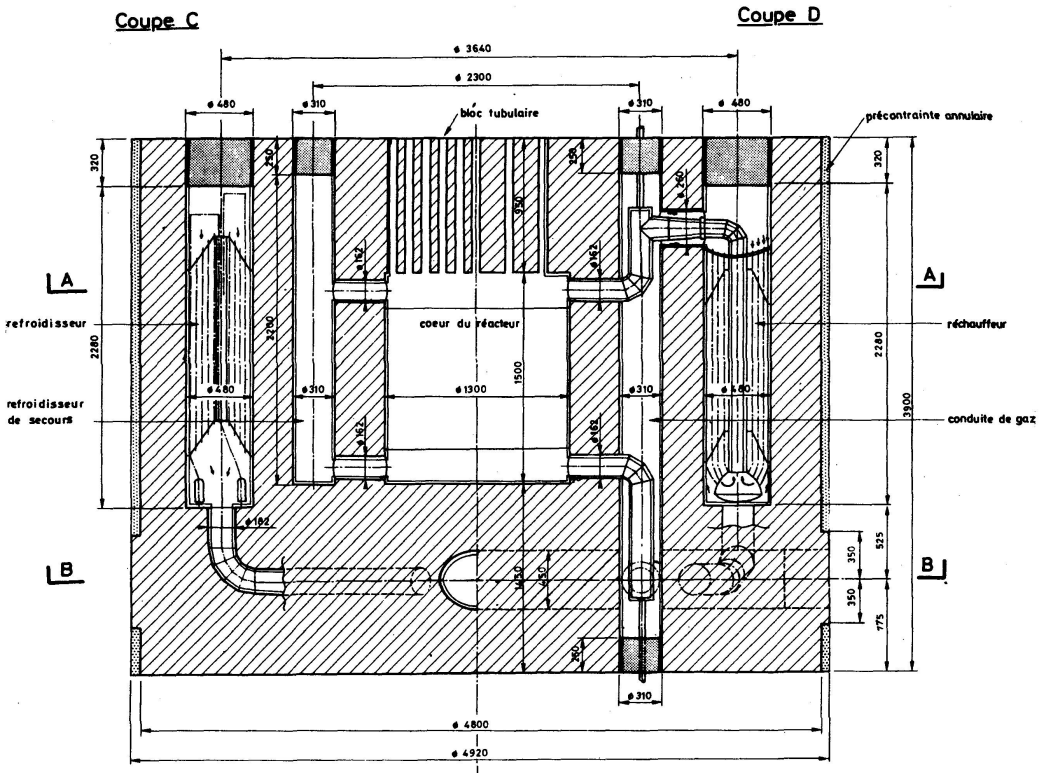


Fig. 1a.

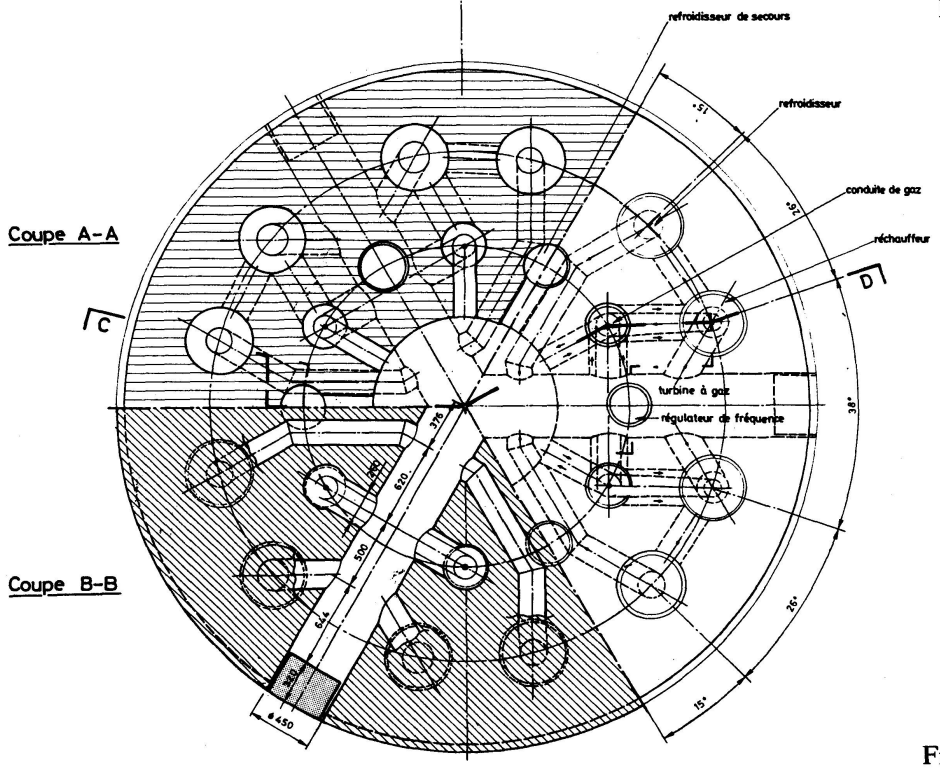


Fig. 1b.

Fig. 1. Caisson de référence.

## 2. Conception du caisson

### *2.1. Généralités*

Comme dans tout caisson de réacteur, la précontrainte du béton a pour but de créer des contraintes de compression qui s'opposent aux contraintes de traction créées par la pression dans les cavités et dans une certaine mesure à celles qui résultent d'un gradient thermique dans les parois. L'étanchéité des cavités est assurée par une peau en acier ductile de 20 à 40 mm d'épaisseur ancrée dans le béton. Une isolation thermique disposée contre la peau d'étanchéité, côté intérieur des cavités, limite les pertes de chaleur et, conjointement à un système de refroidissement de la peau, maintient la température du béton et des câbles de précontrainte au-dessous d'une valeur admissible (65° C environ en fonctionnement normal). Les cavités, qui doivent être accessibles pour permettre le démontage de l'équipement, sont obturées par des bouchons: structures importantes en acier et en béton transmettant les efforts qui les sollicitent aux câbles de précontrainte. L'exposé qui suit est essentiellement consacré à la conception du béton précontraint du caisson [1].

### *2.2 Cas de charge*

Les charges permanentes sont constituées par le poids propre du caisson et celui des équipements qu'il contient.

Différentes pressions agissent dans les cavités à l'état de service. En schématisant, on admet qu'elles sont de:

— 65 kg/cm$^2$ dans la cavité centrale et la première ligne de cavités périphériques;
— 46 kg/cm$^2$ dans les cavités des turbines;
— 25 kg/cm$^2$ dans la ligne extérieure des cavités périphériques.

On prévoit en outre de contrôler le comportement du caisson en le sollicitant par une pression dite de «test» uniforme fixée à 75 kg/cm$^2$.

Pour ce qui est des effets thermiques, dans une première phase de l'étude, seul un régime permanent est considéré. La température du béton sur les parois est maintenue à une valeur de 65° C; la face extérieure du caisson est à la température de 35° C. Etant donné la répartition des cavités, on admet qu'il règne une température uniforme de 65° C dans la masse du béton depuis la cavité centrale jusqu'à un cercle qui circonscrit les cavités périphériques. Depuis là, la température décroît linéairement pour atteindre 35° C sur la face extérieure du caisson.

Les cas de charge considérés doivent permettre de déterminer les contraintes maximales dans les différents états du caisson:

*a*) poids propre + précontrainte initiale (lors de la mise en tension des câbles);
*b*) poids propre + effet thermique + précontrainte finale (toutes pertes effectuées);

[1] Notons que l'isolation thermique, dont nous ne parlerons pas ici, constitue un élément déterminant dans le projet de l'ouvrage. Réalisée en matériaux céramiques pour des températures de 850° C et des variations de pression de 100 kg/cm$^2$/s, l'isolation doit donner lieu à des études de développement très importantes tendant à mettre au point une solution fiable et encore économique.

[2] Pression maximale du circuit 65 kg/cm$^2$ multipliée par un coefficient tenant compte des fluctuations de pression (1.05) et d'un coefficient de sécurité sur l'ouverture des soupapes (1.1).

*c*) poids propre + pression de test + précontrainte finale;
*d*) poids propre + pression de test + effet thermique + précontrainte finale.

### *2.3. Matériaux*

Le béton prévu pour cet ouvrage a les caractéristiques suivantes:

— résistance sur cube à 28 jours $\beta w_{28} = 450$ kg/cm$^2$
— module d'élasticité $E_{28} = 300000$ kg/cm$^2$
— module d'élasticité thermique $E_{th} = 200000$ kg/cm$^2$
— coefficient de dilatation d $= 10^{-5}/°C$

Trois types de câbles assurent la précontrainte du caisson: annulaires réalisés par frettage du fût, traversants horizontaux dans la zone des turbines et traversants verticaux dans les parois du cylindre. Les câbles utilisés ont une tension à la rupture élevée (170 à 180,5 kg/mm$^2$); leur stabilisation permet de garantir des pertes par relaxation inférieures à 7,5%. Le frettage annulaire est réalisé au moyen de torons de ⅜ de pouce disposés en couches superposées dans des canaux de 48 cm de hauteur et sur une épaisseur de 25 cm de profondeur environ. Les câbles traversants horizontaux ou verticaux, d'une force unitaire de rupture de 1180 t, sont constitués de 180 fils de 7 mm de diamètre. Les câbles restent libres dans leurs gaines, celles-ci étant injectées d'une graisse anticorrosion.

Des armatures de couture sont prévues dans la masse du béton afin de répartir la fissuration pouvant résulter de concentrations de contraintes ou d'effets thermiques. Ces armatures seront notamment disposées au voisinage de la peau d'étanchéité, sous les têtes d'ancrage des câbles, dans la zone périphérique du caisson soumise à un gradient thermique important. La densité d'armature pourra atteindre dans cette zone 120 kg/m$^3$.

### *2.4. Dimensionnement*

La disposition des cavités dans le caisson, qui impose notamment sa forme cylindrique, résulte de considérations concernant la conception optimale du circuit d'hélium. La distance entre les cavités est cependant définie par le projeteur du caisson. Elle doit être suffisante pour permettre la mise en place de câbles verticaux autour des bouchons, pour que ces câbles puissent traverser la zone des turbines encombrée de câbles horizontaux, et enfin pour éviter des concentrations de contraintes dans le béton entre cavités. Les formes de béton étant ainsi déterminées par des raisons constructives, il convient de définir le câblage de précontrainte qui satisfasse les critères de dimensionnement. Ceux-ci sont de deux ordres:

— les contraintes dans l'ouvrage, pour les cas de charge, doivent être inférieures aux contraintes admissibles;
— la sécurité à la rupture du caisson doit être admissible.

On notera qu'il n'existe pas de norme applicable sans autre à un tel caisson et il appartient au projeteur de l'ouvrage de poser les conditions qu'il juge admissibles. Il se basera pour cela sur une connaissance de la technique des caissons, le plus souvent moins complexes, réalisés depuis vingt ans et sur une adaptation

au cas présent des normes existantes. Référence sera notamment faite à la dernière norme américaine: ASME Boiler and pressure vessel code, section III, division 2, édition du 1er janvier 1975.

a) *Contraintes admissibles*

Dans la définition de contraintes admissibles, il convient de distinguer les effets thermiques dits secondaires (au même titre que le retrait et le fluage du béton) des sollicitations primaires telles que pression, précontrainte, poids propre. Les contraintes thermiques n'ont pas le même degré d'importance par leur caractère d'autocontraintes qui conduit à leur diminution ou même à leur disparition en cas de fissuration ou de fluage.

Le caisson considéré ayant une épaisseur de paroi considérable, on constate que les contraintes thermiques de traction qui se développent à la périphérie atteignent des valeurs très importantes, de l'ordre de 70 kg/cm$^2$. Une augmentation de la précontrainte dans le but de compenser ces tractions créerait des contraintes de compression inadmissibles autour de la cavité centrale. En outre, la quantité d'acier de précontrainte deviendrait largement surabondante en regard de la sécurité à la rupture de l'ouvrage. Il serait par ailleurs illusoire de vouloir diminuer ces tractions thermiques en agissant sur le gradient par une augmentation de l'épaisseur des parois [1]. Par contre, on pourrait envisager de modifier le gradient dans l'épaisseur des parois au moyen d'un système de refroidissement plus puissant ou encore en calorifugeant la face extérieure du caisson. A ce stade du projet, il a été jugé préférable de tolérer un état de précontrainte partielle sur la face extérieure du caisson, c'est-à-dire d'admettre que la zone périphérique peut se fissurer mais reste en mesure de transmettre les forces de précontrainte sur la partie comprimée du caisson. La condition posée est cependant que la peau d'étanchéité sur les parois des cavités se trouve toujours dans une zone comprimée.

La zone fissurée doit bien entendu être fortement couturée d'armature passive. Cette façon de concevoir le caisson n'empêche pas de chercher à améliorer son comportement en agissant sur le gradient thermique comme indiqué précédemment par refroidissement ou calorifugeage.

Dans ces conditions, les contraintes admissibles dans le béton, tenant compte de son comportement sous étreinte triaxiale (qui a fait l'objet de nombreuses études récentes), se déduiront des contraintes admissibles uniaxiales suivantes, déterminées à partir de la résistance sur cube à 28 jours $\beta w_{28}$.

| Contraintes admissibles | primaires | primaires + secondaires |
|---|---|---|
| Compression moyenne | $0{,}25\ \beta w$ | $0{,}3\ \beta w$ |
| Compression d'arête ou ponctuelle | $0{,}4\ \beta w$ | $0{,}5\ \beta w$ |
| Traction moyenne | 0 | $0{,}7\sqrt{\beta w}$ |
| Traction d'arête ou ponctuelle | $0{,}6\sqrt{\beta w}$ | $2\ \sqrt{\beta w}$ |

[1] La logique voudrait au contraire que l'on diminue la rigidité des parois en diminuant leur épaisseur mais cela est impossible en raison de la présence des nombreuses cavités.

b) *Sécurité à la rupture*

Le coefficient de sécurité à la rupture est défini dans le cas présent comme le rapport entre la pression entraînant la ruine du caisson (rupture de câbles de précontrainte et perte d'étanchéité) et la pression maximale possible pendant la vie du caisson, pression supposée égale dans toutes les cavités. Il s'agit ici de la pression de test (75 kg/cm$^2$). Le coefficient de sécurité admis ne devrait pas être inférieur à 2,5.

Pour des caissons à parois plus minces (de l'ordre de 5 m d'épaisseur par exemple) une condition de sécurité face à une rupture fragile est définie. On admet que suite à une forte déformation des parois dans un stade ultime de ruine, la peau peut perdre son étanchéité et le gaz s'infiltrer dans les fissures pour créer un gradient de pression dans l'épaisseur des parois. On considère alors que les aciers de précontrainte doivent être en mesure de résister avec une sécurité de l'ordre de 1,5 à ce cas de charge.

Pour un caisson à parois très épaisses, un coefficient de sécurité aussi élevé ne paraît pas devoir se justifier. Il est peu probable qu'un schéma de ruine apparaisse qui conduise à une infiltration de gaz généralisée dans une section complète horizontale ou verticale du caisson. Nous admettrons donc un coefficient de sécurité de l'ordre de 1,0 pour ce schéma de rupture en prévoyant en outre la mise en place d'un système de drainage au contact des parois des cavités ou dans la masse du béton afin de couper toute sous-pression éventuelle. Le câblage de précontrainte et les aciers passifs qui en résultent ne prennent pas ainsi une importance démesurée.

c) *Calculs*

Différents calculs ont été effectués, que nous citons brièvement:

— détermination globale de la précontrainte à l'aide de schémas de ruine simplifiés;
— analyse bidimensionnelle de l'état de contrainte dans le fût du caisson;
— détermination de la précontrainte dans les dalles à partir de considérations sur les déformations relatives dalle-fût;
— contrôle de la sécurité à la rupture par l'analyse de mécanismes de ruine plus complexes;
— calcul tridimensionnel par éléments finis dans le domaine linéaire pour les différents cas de charge cités au paragraphe 2.2.

Les mécanismes de ruine les plus défavorables sont indiqués sur la fig. 2. On note les valeurs de pression de rupture et les coefficients de sécurité par rapport à la pression de test suivants:

| | Pression de rupture kg/cm$^2$ | Coefficient de sécurité |
|---|---|---|
| Rupture par cisaillement du fût | 275 à 400 | 3,7 à 5,3 |
| Rupture par cisaillement de la dalle inférieure | 280 à 330 | 3,7 à 4,4 |
| Rupture par cisaillement de la dalle supérieure | 260 à 300 | 3,5 à 4 |
| Rupture par éjection de blocs de béton de la zone périphérique | 190 à 250 | 2,5 à 3,3 |

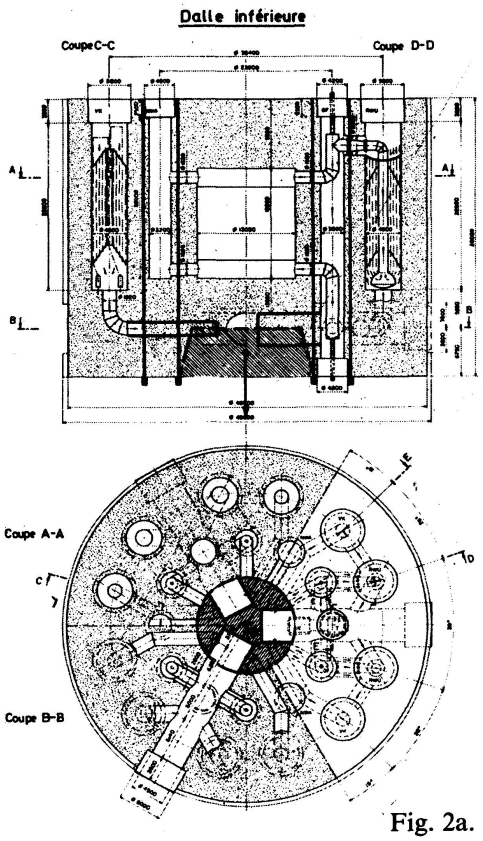


Fig. 2a.

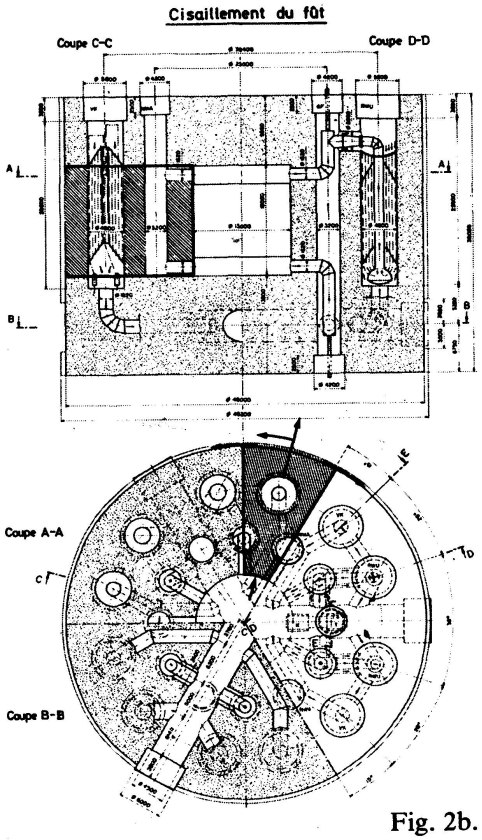


Fig. 2b.

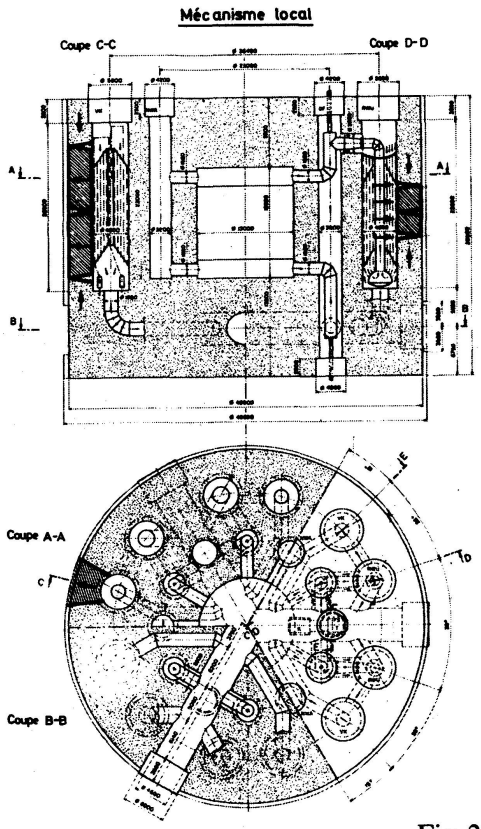


Fig. 2c.

Fig. 2. Mécanismes de ruine défavorables.

d) *Câblage de précontrainte*

La précontrainte retenue en définitive est conçue comme suit:

*Précontrainte verticale*

Elle est disposée de façon à garantir le maintien des bouchons avec une sécurité de 3 par rapport à la pression de test. Cela impose pour les grandes cavités périphériques 35 câbles répartis sur deux couronnes. Les bouchons des petites cavités comportent chacun 15 câbles. Les autres câbles sont disposés autour de la cavité centrale. La pression moyenne exercée par les 903 câbles de précontrainte verticale est plus forte dans la zone centrale (valeur lors de la mise en tension 80 kg/cm$^2$) qu'à la périphérie (42 kg/cm$^2$).

*Précontrainte annulaire*

La pression exercée par le frettage est 30% plus élevée dans les zones des dalles que dans le fût. Celle-ci crée une pression de 54 kg/cm$^2$.

*Pression horizontale traversante*

Le nombre de câbles est limité au niveau des turbines par l'encombrement dû aux cavités verticales. Les têtes d'ancrage sont concentrées autour des bouchons des turbines. Pour le passage de la zone centrale, les câbles se croisent en 12 nappes de 6 câbles.

## 3. Essais sur modèle

### *3.1. But des essais*

Un programme d'essais sur modèle a été établi dans le but essentiel de déterminer *le schéma de ruine* et *le coefficient de sécurité à la rupture* du caisson. Les essais devaient aussi permettre de connaître la limite du comportement élastique du caisson. Le comportement de l'ouvrage a donc été analysé sous charges de pression intérieure croissante jusqu'à la rupture. Il a été admis, à ce stade du projet, que les effets thermiques n'avaient pas une influence importante sur la rupture.

### *3.2. Description du modèle*

Le choix s'est porté sur un modèle en microbéton précontraint à l'échelle 1/20. Cette échelle permet de réaliser une maquette d'un coût raisonnable et qui satisfasse encore aux critères de similitude. Le choix du microbéton plutôt que la résine synthétique est dicté par le fait qu'il s'agit principalement d'un essai de rupture, ce qui nécessite d'avoir un matériau dont le comportement à la rupture est aussi proche que possible de celui du matériau réel.

a) *Formes de béton*

Le dessin du modèle est représenté sur la fig. 3. Ses dimensions sont de 1,95 m de hauteur et de 2,40 m de diamètre. La géométrie est conforme au caisson réel,

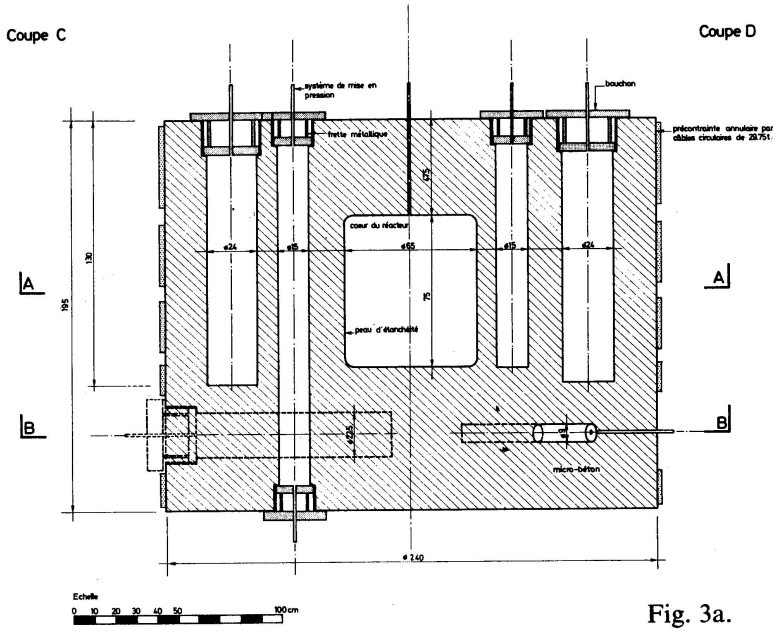


Fig. 3a.

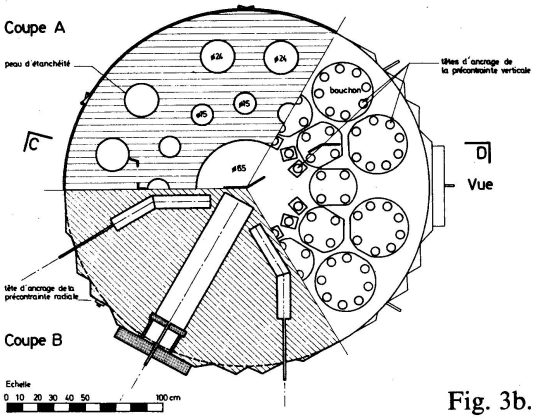


Fig. 3b.

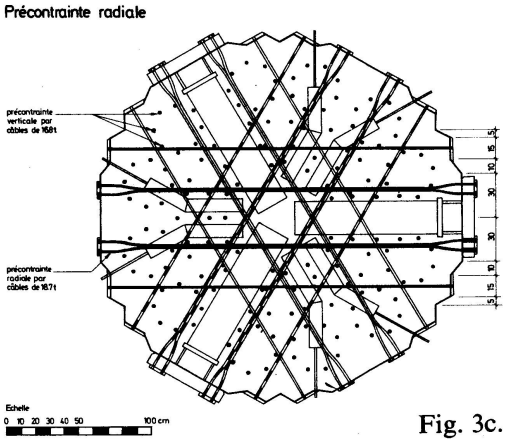


Fig. 3c.

Fig. 3. Modèle de caisson.

en ce qui concerne les cavités principales. Les cavités des turbines ne sont pas jointives afin de simplifier les soudures de la peau et ainsi de mieux garantir son étanchéité. Pour ce qui est des conduites horizontales, seules ont été simulées, dans l'ensemble du caisson, les conduites reliant les turbines aux cavités périphériques extérieures. Les autres conduites de moindre importance ont été introduites dans un secteur de 120° afin d'améliorer la similitude dans cette zone où seront concentrés des points de mesure. La dalle supérieure du modèle est réalisée en béton plein, sans la multitude de pénétrations de petit diamètre que l'on trouve dans le caisson réel pour le passage des éléments de combustible et des barres de contrôle.

b) *Précontrainte*

La précontrainte verticale est composée de 159 câbles de 16,8 t à la rupture. Sur la face supérieure, la majorité des câbles est ancrée sur les bouchons des

cavités. La précontrainte annulaire est réalisée non par enroulement, mais par 59 câbles circulaires de 29,75 t à la rupture. La précontrainte horizontale traversante est assurée par 36 câbles de 18,7 t à la rupture. Les deux tiers de ces câbles sont ancrés sur les bouchons des turbines.

c) *Bouchons*

Il a été retenu un dispositif simple offrant une grande sécurité lors des essais. Il s'agit de pièces métalliques composées de deux plaques circulaires et d'un élément de transition tubulaire. La tôle de fermeture de la peau d'étanchéité s'applique sur la plaque inférieure du bouchon qui est lui-même directement tenu par les câbles de précontrainte.

d) *Peau d'étanchéité*

La peau d'étanchéité de la cavité centrale est constituée par une tôle en acier ductile de 4 mm d'épaisseur. Les autres cavités comportent une peau en acier ductile de 2 mm et sont fermées à leurs extrémités par des plaques de 4 mm.

e) *Armatures passives*

Elles n'ont pas été simulées. Seuls des renforcements tubulaires en acier ont été disposés autour des bouchons afin d'assurer le frettage du béton sous les plaques d'ancrage des câbles de précontrainte.

### *3.3. Similitude*

Une analyse systématique de la similitude du modèle a permis de s'assurer que sa représentativité était satisfaisante compte tenu du but fixé.

Les caractéristiques mécaniques du microbéton (dont les agrégats ne sont pas mis à l'échelle du modèle) sont très voisines de celles du béton réel. La principale différence porte sur la résistance du béton en compression et en traction (voir partie III). L'influence de l'écart de résistance à la traction sur la fissuration peut être déterminée simplement. Le microbéton est légèrement moins déformable que le béton réel.

L'écart de similitude introduit dans la dalle supérieure, réalisée sans le réseau des pénétrations de petit diamètre, conduit à augmenter sa rigidité et sa résistance de l'ordre de 10%. La disposition adoptée paraît cependant préférable à celle d'une modélisation qui serait réalisée par un nombre limité de pénétrations, créant alors un risque de fissuration prématurée de la dalle. La dalle inférieure du modèle est par contre un peu moins résistante que la dalle réelle. Si aucune pression n'agit au centre de la dalle, les trois cavités des turbines n'étant pas jointives, la surface d'application de la pression au centre de la dalle est réduite. Par contre, le poids propre n'est pas simulé et la peau d'étanchéité, dans le modèle, est plus faible que celle du caisson réel qui a été augmenté en cours d'étude. De ces deux effets, qui vont en sens contraire, le deuxième est plus important. La résistance de la dalle inférieure du modèle est donc plus faible que celle du caisson.

Pour des raisons constructives (place à disposition pour les têtes d'ancrage et pour le bétonnage), le nombre de câbles traversants est diminué d'un facteur 6, la pression moyenne exercée par la précontrainte étant par ailleurs identique à celle du caisson réel. Les pointes de contrainte exercées par les têtes d'ancrage apparaissent négligeables dans le phénomène d'ensemble du caisson massif; en outre, les câbles n'étant pas injectés au coulis de ciment, les effets d'adhérence n'entrent pas en considération. Pour ce qui est de la précontrainte, des dispositions ont été prises quant à la répartition des têtes d'ancrage et au mode de mise en tension afin que les câbles circulaires créent une répartition uniforme de la pression autour du caisson, ainsi que le ferait un enroulement.

Le système d'ancrage des bouchons est très simplifié par rapport à celui du caisson réel. Cependant, la façon dont les forces de pression sont transmises aux câbles de précontrainte est globalement représentative de la réalité.

La nécessité de garantir l'étanchéité de la peau pour des pressions pouvant atteindre 250 kg/cm$^2$ a imposé des épaisseurs minimales de 2 et 4 mm. L'échelle n'est donc pas respectée. La comparaison de la quantité d'acier de la peau du modèle à celle du caisson réel, auquel sont ajoutés, pour ce dernier, les aciers passifs, montre que tant que le comportement reste globalement élastique la similitude est respectée, l'amorce de la fissuration se produisant cependant plus tôt sur le modèle. Au moment de la rupture, l'effet du manque d'aciers passifs dans le modèle est assez exactement compensé par la surépaisseur de la peau.

Pour ce qui est du comportement global de l'ouvrage dans le domaine élastique, on peut dire que les dispositions constructives retenues conduisent à un modèle plus rigide que le caisson réel. Ceci est accentué par le fait que ce dernier est microfissuré par des phénomènes de retrait et thermiques. Par contre, la non-simulation des armatures passives, l'absence de pattes d'ancrage sur la peau d'étanchéité ont des effets de sens opposé. On peut en définitive estimer que l'écart de similitude sur les déformations et les contraintes dans le caisson, qui résulte de la modélisation, ne devrait pas dépasser 10% environ. Pour ce qui est de la rupture, les calculs ont montré que l'ordre d'apparition des différents mécanismes de ruine (cités au paragraphe 2.4.c, ci-dessus) était le même pour le caisson réel et le modèle, permettant de conclure que le résultat de l'essai de rupture du modèle était significatif.

# PARTIE II

## Analyse numérique non linéaire du modèle du caisson

M. PAQUET, B. REBORA, TH. ZIMMERMANN,
Ingénieurs à l'Institut de production d'énergie et travaux hydrauliques
de l'Ecole Polytechnique Fédérale de Lausanne.

### 1. But et méthode du calcul

L'analyse numérique a deux buts. Tout d'abord, de définir le comportement du modèle physique en stade linéaire puis non linéaire jusqu'à la ruine. Ensuite, d'effectuer l'ajustement du modèle mathématique pour son application ultérieure au calcul des caissons en vraie grandeur, et éventuellement d'éviter des essais coûteux.

L'analyse en stade non linéaire doit permettre par ailleurs d'étudier les développements de la fissuration dans le caisson et d'en localiser les éventuelles faiblesses. Le schéma de fissuration ultime en résulte ainsi que la charge de ruine.

La méthode des éléments finis que l'on applique ici est combinée pour la solution du problème non linéaire avec une technique itérative du type «contraintes initiales» [1]. La méthode a déjà été appliquée avec succès au calcul d'une dalle et d'un caisson de réacteur [2], [3], ainsi qu'à différents problèmes de fondations [4]. La formulation non linéaire des lois des matériaux et la méthode d'analyse ont été décrites antérieurement [5], [6], [7].

### 2. Modélisation: géométrie, charges et matériaux

Le modèle est une réduction à l'échelle 1:20 du caisson projeté, après suppression des cavités horizontales secondaires sauf cinq. Il comprend trois plans de symétrie, son comportement est donc correctement représenté par un sixième de la structure. Malgré cela, la complexité géométrique reste telle que de nouvelles simplifications doivent être introduites. Le modèle est soumis à une pression uniforme dans toutes les cavités dont l'étanchéité est garantie par une peau en acier. Il est posé sur trois appuis.

#### *2.1. Géométrie et charges*

La modélisation adoptée simule un douzième du caisson. On la compare sur la fig. 1 à la géométrie réelle. Le réseau d'éléments défini comprend 110 éléments et 2475 degrés de liberté (3 déplacements par nœud). L'élément type isoparamétrique est également représenté sur la fig. 1.

Le choix de ce réseau résulte de la comparaison de 4 mailles calculées en stade linéaire élastique. On remarquera qu'on introduit ainsi 3 turbines supplémentaires. La peau d'étanchéité n'est pas simulée, sa participation, non négligeable dans l'essai, est prise en considération par une réduction de la pression interne calculée à partir des déformations des cavités.

La précontrainte annulaire et verticale est simulée comme la pression par une charge répartie (voir fig. 1). On tient compte dans la phase finale du calcul d'une augmentation de précontrainte résultant de la dilatation du caisson.

Ces hypothèses ne permettent toutefois pas de simuler le comportement jusqu'à la ruine complète de l'ouvrage.

### *2.2. Caractéristiques des matériaux*

Le béton, tel que l'on en tient compte dans le calcul, a les caractéristiques suivantes:

| | |
|---|---|
| — résistance à la compression simple (sur prisme) | $\beta_p = -460$ kg/cm$^2$ |
| — résistance à la traction | $\beta_z = 46$ kg/cm$^2$ |
| — résistance à la compression biaxiale | $\beta_b = -598$ kg/cm$^2$ |
| — module d'élasticité «instantané» | $E = 300\ 10^3$ kg/cm$^2$ |
| — coefficient de Poisson | $\nu = 0.2$ |

Le calcul ayant précédé l'essai, ces valeurs diffèrent de la réalité au jour de l'essai ($\beta_z \cong 75$ kg/cm$^2$).

Les caractéristiques de la peau d'étanchéité et des câbles de précontrainte sont définies au paragraphe 3.2, première partie.

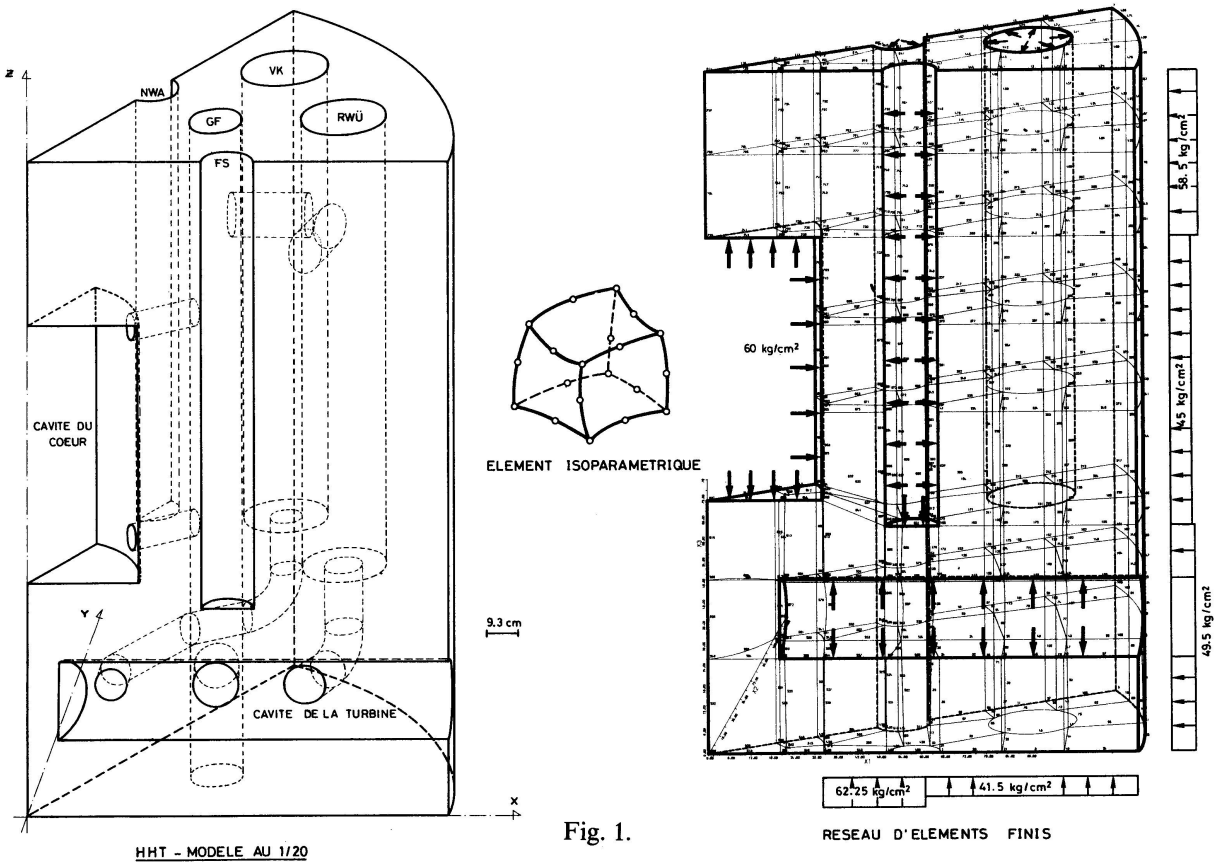


Fig. 1.

## 3. Analyse non linéaire

Jusqu'à 75 kg/cm$^2$ (pression d'essai), le comportement est élastique. Les premières fissures apparaissent à 85 kg/cm$^2$ dans la zone de convergence des turbines. A cette pression, on remarque l'apparition de fortes tractions entre les cavités externes et aux angles du cœur, zones fissurées dès 103 kg/cm$^2$. A 117 kg/cm$^2$, la contrainte de traction entre les cavités internes est proche de la rupture; la fissuration au niveau des turbines continue à se propager. De 129 à 133 kg/cm$^2$, on observe entre les cavités internes un début de fissuration qui se propage et tend finalement à désolidariser la dalle supérieure du reste de la structure. A l'extérieur, la fissuration a presque achevé d'isoler une zone de la paroi dont l'équilibre

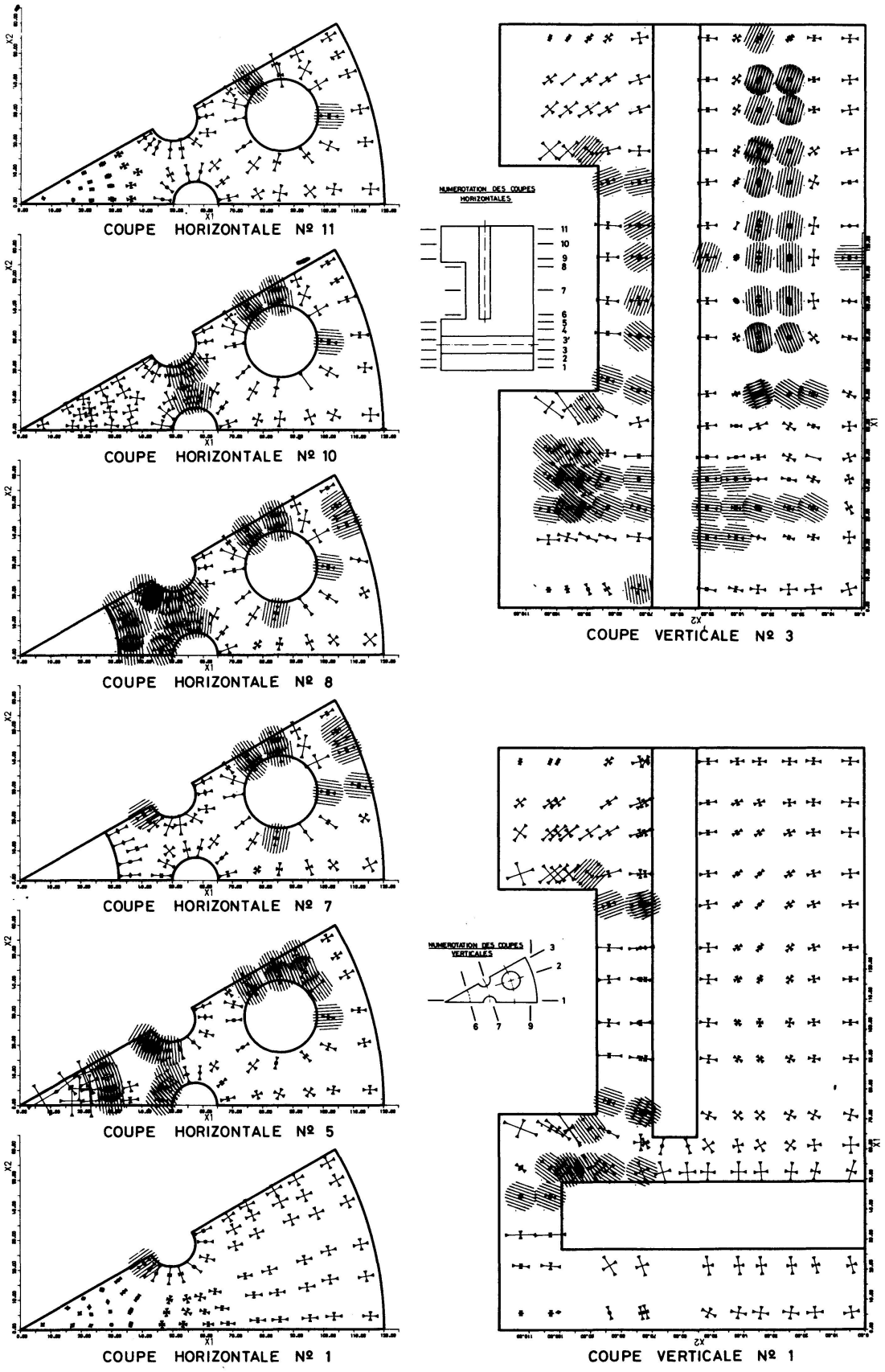
COUPE HORIZONTALE Nº 11
COUPE HORIZONTALE Nº 10
COUPE HORIZONTALE Nº 8
COUPE HORIZONTALE Nº 7
COUPE HORIZONTALE Nº 5
COUPE HORIZONTALE Nº 1
NUMEROTATION DES COUPES HORIZONTALES
11
10
9
8
7
6
5
4
3'
3
2
1
COUPE VERTICALE Nº 3
NUMEROTATION DES COUPES VERTICALES
3
2
1
6
7
9
COUPE VERTICALE Nº 1

Fig. 2.

n'est désormais plus assuré que par les câbles annulaires. La fissuration horizontale dans la dalle inférieure continue à se propager (fig. 2).

L'analyse des résultats met en évidence les trois mécanismes suivants (fig. 3):

a) *Séparation de la dalle inférieure* au niveau des axes des turbines. Cette rupture semble principalement due à la concentration de charge dans la zone de convergence des cavités horizontales. On notera toutefois que la modélisation utilisée altère le comportement réel de cette zone (en augmentant le nombre de turbines, on augmente la charge).

b) *Rupture entre les cavités externes et la paroi externe.*
A 133 kg/cm$^2$, il se forme un prisme vertical qui tend à se désolidariser de la structure. Les câbles de précontrainte continuent à résister seuls à la pression interne.

c) *Rupture entre les cavités internes* puis *séparation de la dalle supérieure.*
L'action des câbles verticaux ne s'oppose que partiellement à la désolidarisation de cette zone.

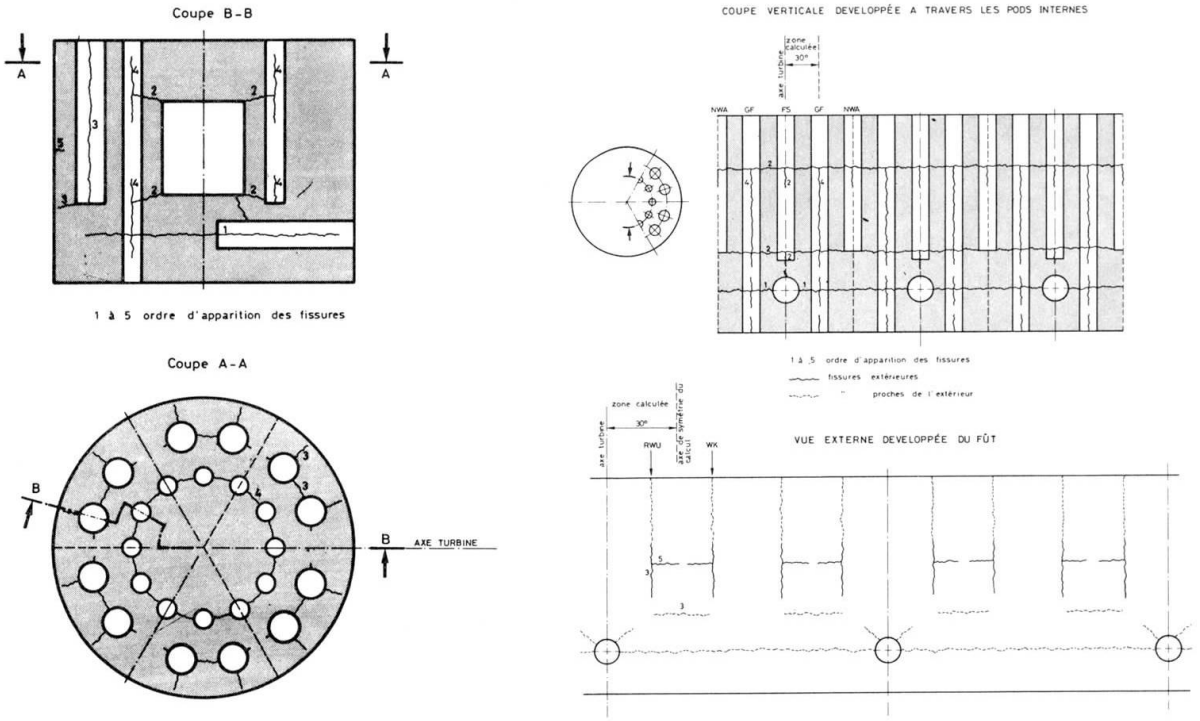


Fig. 3.

## 4. Discussion des résultats

Remarquons tout d'abord qu'aucune non-linéarité en compression n'apparaît, ni sous précontrainte seule, ni dans l'analyse jusqu'à la ruine. Au moment où la divergence du calcul signale la rupture, la fissuration est également avancée dans les trois mécanismes détectés. L'affaiblissement de la zone des turbines par une modélisation imparfaite n'a donc pas d'influence significative.

L'apparition du schéma de ruine dépend par contre fortement de la résistance à la traction et on peut prévoir qu'il aurait été retardé notablement avec la résistance effective au jour de l'essai. La valeur de la charge de ruine dépend, elle, surtout des câbles de précontrainte.

# PARTIE III

## Essai sur modèle d'un caisson en béton précontraint à cavités multiples

R. FAVRE, professeur, M. KOPRNA, adj. scient., J.-P. JACCOUD, ingénieur
Centre d'étude du béton armé et précontraint de l'Ecole polytechnique fédérale de Lausanne, Suisse.

### 1. Introduction

Le but du présent article est de présenter l'essai sur modèle d'un caisson de centrale nucléaire en béton précontraint à cavités multiples, essai qui fut réalisé au Centre d'étude du béton armé et précontraint (CEBAP) de l'EPF-Lausanne. Le mandat confié au CEBAP comprenait la construction du modèle de caisson à l'échelle 1/20 (fig. 1) et la réalisation de différents programmes de mesures sous charge de pression intérieure uniforme dans toutes les cavités en vue de:

*a*) déterminer la pression et les mécanismes de rupture, afin de pouvoir en déduire la sécurité globale;
*b*) déterminer la limite du comportement élastique du modèle;
*c*) observer le comportement du modèle sous la pression de service, sans toutefois tenir compte des effets thermiques ou des effets de fluage et retrait du béton.

Le délai total, y compris la planification de l'essai, la construction du modèle, les tests et mesures ainsi que la livraison du rapport final, n'a pas dépassé une année.

### 2. Construction du modèle

Le modèle fut réalisé en microbéton dont le diamètre des agrégats ne dépassait pas 6 mm; il consistait en un bloc cylindrique massif de 2,40 m de diamètre et de 1,95 m de hauteur (fig. 1). Pour un volume brut d'environ 8,8 $m^3$, le modèle comprenait 40 évidements d'un volume total égal à 1,4 $m^3$ et répartis comme suit:

*a*) 28 cavités principales (fig. 2 et 3), simulant les cavités du réacteur (au centre), des turbines (horizontales sous le réacteur) et des refroidisseurs, récupérateurs, etc. (verticales autour du réacteur);
*b*) 12 cavités plus petites, simulant certaines galeries de liaison entre les cavités principales; elles n'ont été totalement représentées que dans un tiers du modèle, appelé «zone de faiblesse».

Le modèle est précontraint tridimensionnellement au moyen d'un triple système de câbles verticaux, annulaires et radiaux, ces derniers au niveau des turbines uniquement (fig. 2 et 3). Les câbles, au nombre de 254, sont des monotorons non injectés. A l'extrémité libre des cavités, les poussées dues à la pression intérieure sont transmises aux câbles par l'intermédiaire de bouchons métalliques.

Vu ses dimensions et son poids importants (environ 20 tonnes), le modèle fut construit et bétonné en place dans la halle d'essais du CEBAP (fig. 1). La multiplicité des tâches à réaliser dans un délai relativement court nécessita la mise en œuvre de moyens considérables. Outre la participation du personnel du CEBAP, on doit mentionner l'aide de nombreux instituts ou laboratoires de l'EPF-Lausanne ainsi que la participation de l'industrie suisse, notamment en ce qui concerne la réalisation des cavités en tôle d'acier inox, de la précontrainte et des bouchons.

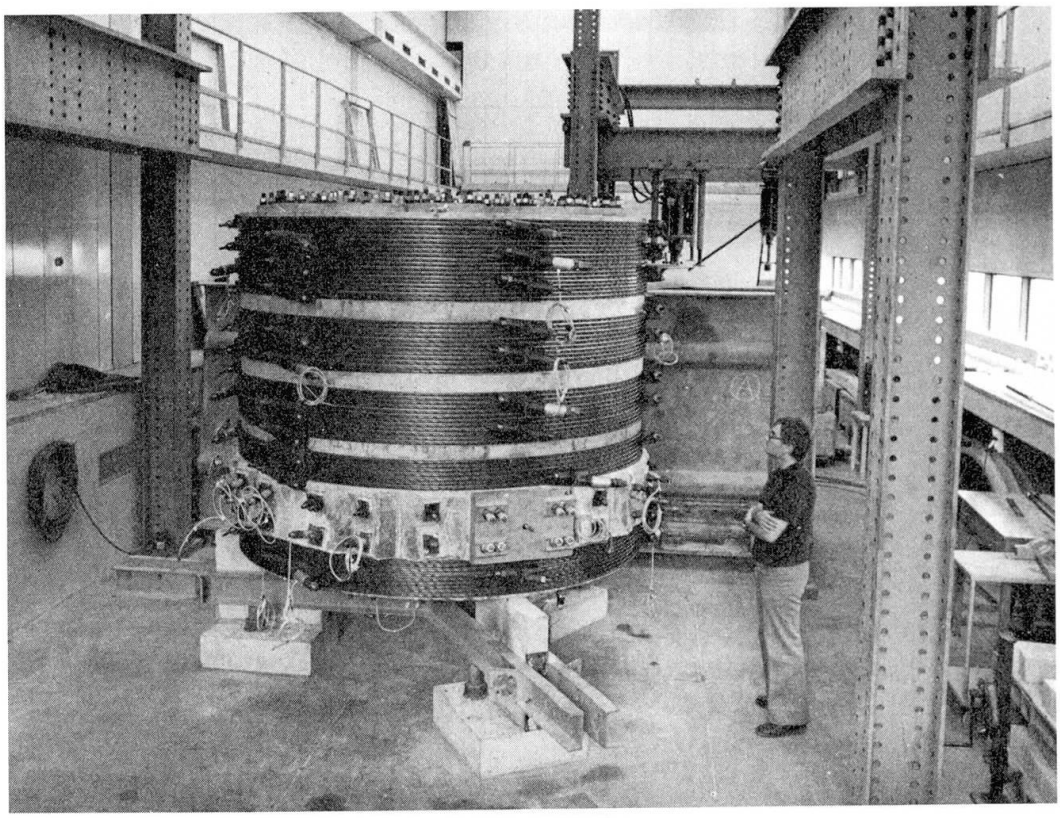

Fig. 1. Vue du modèle dans la halle du CEBAP.

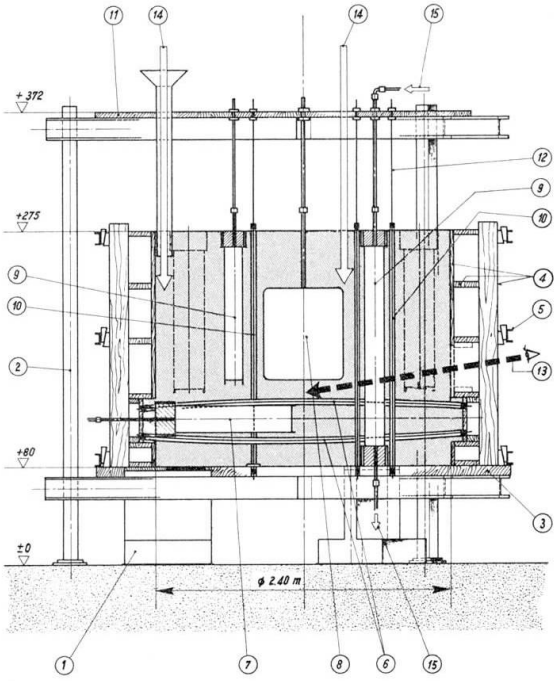


Fig. 2. Coupe schématique du modèle lors de sa construction.

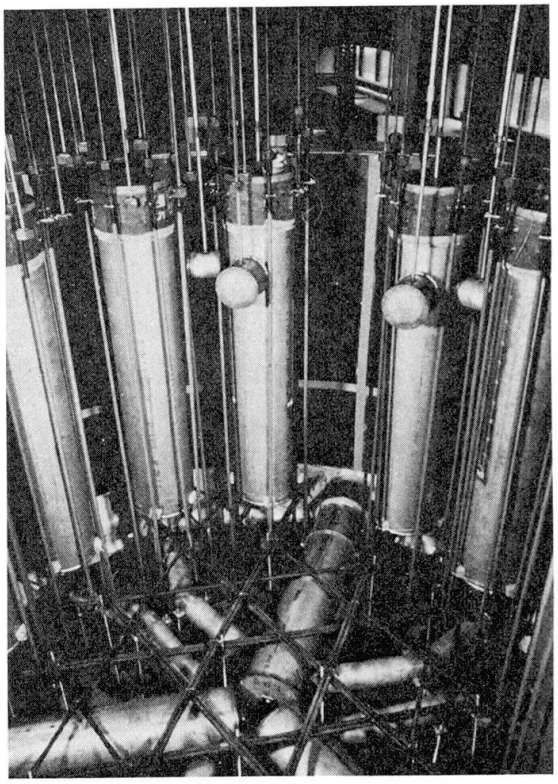

Fig. 3. Vue de l'intérieur du modèle lors de la pose des cavités et câbles de précontrainte.

Les cavités et les câbles de précontrainte radiaux et verticaux furent mis en place dans un coffrage en bois supporté par un étayage métallique (fig. 2 et 3). Pour leur positionnement et afin d'assurer leur stabilité vis-à-vis des pressions du béton frais au moment du bétonnage, les cavités et câbles verticaux furent fixés et mis légèrement sous tension entre le fond du coffrage et une plate-forme supérieure (fig. 2).

Le bétonnage du modèle s'effectua en une seule étape d'un jour; environ 8 $m^3$ de microbéton furent mis en œuvre par le haut du modèle au moyen de goulottes (fig. 2).

La mise en place des câbles de précontrainte annulaire et la mise en tension de tous les câbles s'effectua par étapes, environ un mois après le bétonnage.

## 3. Caractéristiques des matériaux

### *3.1. Le microbéton*

La composition et les caractéristiques du microbéton furent définies lors d'essais préliminaires effectués par les soins du Laboratoire d'essais des matériaux pierreux (LMP) de l'EPF-Lausanne. Cette composition fut la suivante:

435 kg/$m^3$ de ciment CPA HTS Lafarge;
222 kg/$m^3$ d'eau;
1693 kg/$m^3$ d'agrégats roulés répartis en 3 classes (0/1, 1/3 et 3/6 mm).

Lors des essais proprement dits, soit environ cinq mois après le bétonnage, les valeurs moyennes mesurées sur éprouvettes prismatiques $12 \times 12 \times 36$ cm étaient les suivantes:

| | |
|---|---|
| résistance à la compression sur cube: | $\beta_w = 653$ kg/cm$^2$ |
| résistance à la traction par flexion: | $\beta_{bz} = 109$ kg/cm$^2$ |
| module d'élasticité instantané: | $E_{bo} = 380000$ kg/cm$^2$ |
| retrait spécifique: | $\varepsilon_s = -470 \cdot 10^{-6}$ |
| effet de la précontrainte verticale ($\sigma_b = -49$ kg/cm$^2$) | |
| raccourcissement élastique: | $\varepsilon_{él} = -109 \cdot 10^{-6}$ |
| raccourcissement dû au fluage: | $\varepsilon_k = -160 \cdot 10^{-6}$ |

### *3.2. La peau d'étanchéité*

La peau d'étanchéité des 40 évidements (fig. 2 et 3) fut réalisée en tôle d'acier inox X5CrNi18 9 d'épaisseur 4 mm pour la cavité centrale et 2 mm pour toutes les autres cavités. Les propriétés mécaniques mesurées de cette tôle étaient les suivantes:

| | |
|---|---|
| limite apparente d'élasticité: | $\sigma_{02} \cong 28$ kg/mm$^2$ |
| contrainte de rupture: | $\beta_z = 67 \div 70$ kg/mm$^2$ |
| allongement de rupture: | $\lambda_5 = 55 \div 60\%$ |
| module d'élasticité: | $E \cong 16000$ kg/mm$^2$ |

Les rôles que devait assumer cette peau d'étanchéité étaient multiples:

*a*) elle servait de coffrage des évidements, au moment du bétonnage;

*b*) elle devait assurer une parfaite étanchéité des cavités à l'eau, ceci afin de permettre leur mise en pression jusqu'à la pression maximale de rupture du caisson; elle devait notamment être apte à continuer d'assumer son rôle en cas de fissurations et déformations importantes du caisson.

Les essais ont montré que la peau d'étanchéité a parfaitement rempli son rôle jusqu'à la rupture du modèle.

### *3.3 Les câbles de précontrainte*

Le modèle fut précontraint au moyen d'un triple système de câbles (fig. 1) dont les caractéristiques sont les suivantes:

— 159 torons VSL 0.5″ (section du câble: 93 mm$^2$) pour la précontrainte verticale.
— 59 torons VSL 0.6″ Dyform (section 163 mm$^2$) pour la précontrainte annulaire.
— 36 torons VSL 0.5″ Supa (section 99 mm$^2$) pour la précontrainte radiale.

Les têtes d'ancrage avec douille sertie sur le toron furent construites spécialement pour cet essai. Des essais préliminaires effectués à l'Institut des métaux et des machines (IMM) de l'EPF-Lausanne démontrèrent le comportement satisfaisant de ces ancrages; ces essais ont d'autre part mis en évidence le glissement du fil central dans les ancrages de ce type dès que les contraintes atteignent 0.7 $\beta_z$.

Pour diverses raisons techniques, la précontrainte annulaire du modèle fut réalisée au moyen de câbles indépendants, contrairement au caisson réel où elle sera vraisemblablement réalisée au moyen de fils continus. Ce choix n'était cependant pas sans inconvénient, notamment en ce qui concerne les pertes par frottement. Grâce à de nombreux essais préliminaires, on put déterminer très exactement ces pertes et, d'autre part, les diminuer et les égaliser de manière optimale par des dispositions techniques et constructives appropriées. Les câbles annulaires, graissés avec du Spec. Moly. Grease, furent placés sur une tôle d'acier d'épaisseur 1 mm; ils furent mis en tension en tirant simultanément leurs 2 extrémités. On détermina ainsi un coefficient de frottement $\mu$ égal à 0.09. La précision atteinte dans les forces de précontrainte ne fut nulle part inférieure à $\pm$ 2,5%.

La mise en précontrainte du modèle s'effectua en deux étapes et débuta un mois après le bétonnage; chaque câble fut mis en tension en une seule étape à une valeur moyenne correspondant à 0.67 $\beta_z$.

## 4. Dispositifs d'essais

Les essais de charge du modèle eurent lieu dans la halle d'essai climatisée du CEBAP. La variation de la température étant négligeable on a pu utiliser un cadre de référence (pour fixation des capteurs de déplacement) indépendant, fixé directement sur la dalle d'essai (fig. 4); ceci facilita énormément le dépouillement des résultats de mesure.

Les mesures enregistrées furent effectuées au moyen de différentes sortes de capteurs électriques, répartis sur le modèle en 168 points et groupés essentiellement dans la «zone de faiblesse».

On été employés:

— des jauges de déformation (déformation relative $> 20^0/_{00}$) collées d'une part sur la peau d'étanchéité, d'autre part sur la surface du béton. Quelques difficultés, posées surtout par la protection des jauges intérieures et leurs câblages (danger d'une amorce de fissuration) et par la pression intérieure anormalement élevée, furent surmontées d'une manière satisfaisante grâce à de nombreux essais préliminaires;

— des capteurs inductifs de déplacement (course de $\pm 5$ mm à $\pm 50$ mm) fixés sur un cadre de référence indépendant (voir fig. 4); cette solution simple s'est avérée satisfaisante;

— des capteurs de force (système à jauges de déformation – portée nominale de 20 t et 30 t) pour mesurer la variation de la précontrainte, montés sur les câbles lors de leur mise en place (voir fig. 4);

— des capteurs de pression (système à jauges – portée nominale de 200 kg/cm$^2$ et 500 kg/cm$^2$) pour des mesures précises de la pression introduite;

— des thermorésistances, destinées à mesurer les éventuelles variations de température.

A part les capteurs susmentionnés, certaines cavités sélectionnées furent équipées de manomètres mécaniques afin de pouvoir d'une part contrôler la pression interne visuellement, d'autre part détecter, le cas échéant, la cavité dont la peau d'étanchéité aurait cédé.

A titre d'essai, un capteur de bruit (signal amplifié enregistré sur un oscilloscope à mémoire) fut utilisé dans le but d'essayer de capter le bruit dû à la fissuration (l'expérience était assez concluante).

L'acquisition des valeurs mesurées s'effectuait par l'intermédiaire d'une chaîne de mesures automatique, la sortie étant imprimée et simultanément enregistrée sur une bande perforée (fig. 6). Cette bande était ensuite traitée sur l'ordinateur à partir d'une console de télétype, ce qui a permis de livrer les résultats traités presque immédiatement.

Le système de mise en pression comprenait en principe un agrégat de pompes avec mainteneur de charge (pression maximale de 380 bars), complété par un vérin (changeur de pression et de milieu) et un réseau de distribution équipé de vannes permettant, le cas échéant, de court-circuiter les cavités ayant des pertes de pression dues à une rupture locale prématurée de la peau d'étanchéité. La mise en pression du modèle s'effectua au moyen d'une émulsion d'eau avec 2% d'huile soluble.

Lors de cycles de rupture, le comportement du modèle (surtout la fissuration) dans la zone de faiblesse fut observé à distance au moyen de 3 caméras de télévision et enregistré simultanément sur 3 magnétoscopes (fig. 6).

## 5. Programme d'essais

Les essais préliminaires avaient pour but de contrôler (sous une faible pression ne dépassant pas 20 kg/cm$^2$) les parties principales du modèle, les capteurs, la chaîne de mesure et la chaîne de mise en charge.

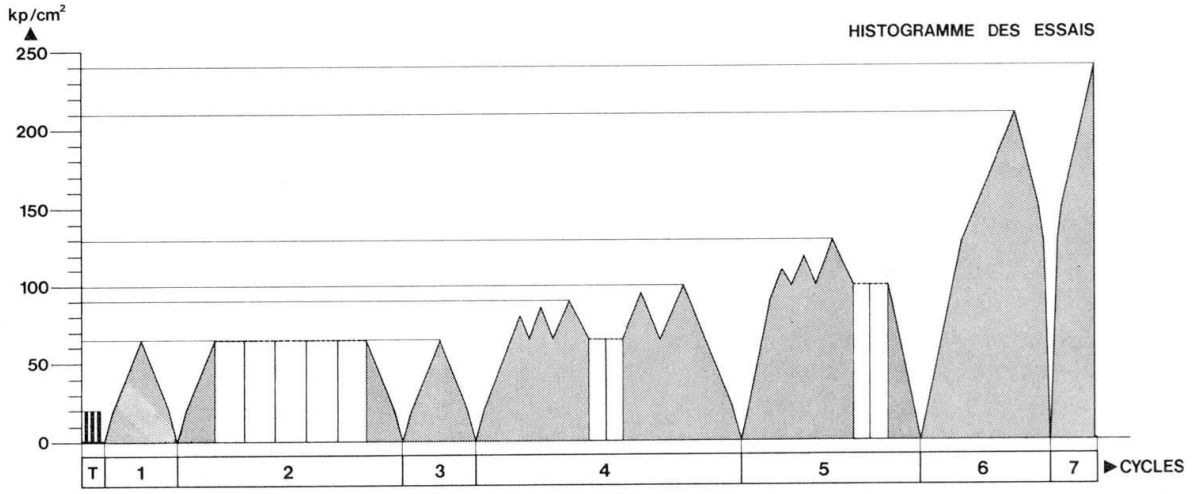


Fig. 5. Histogramme des essais.

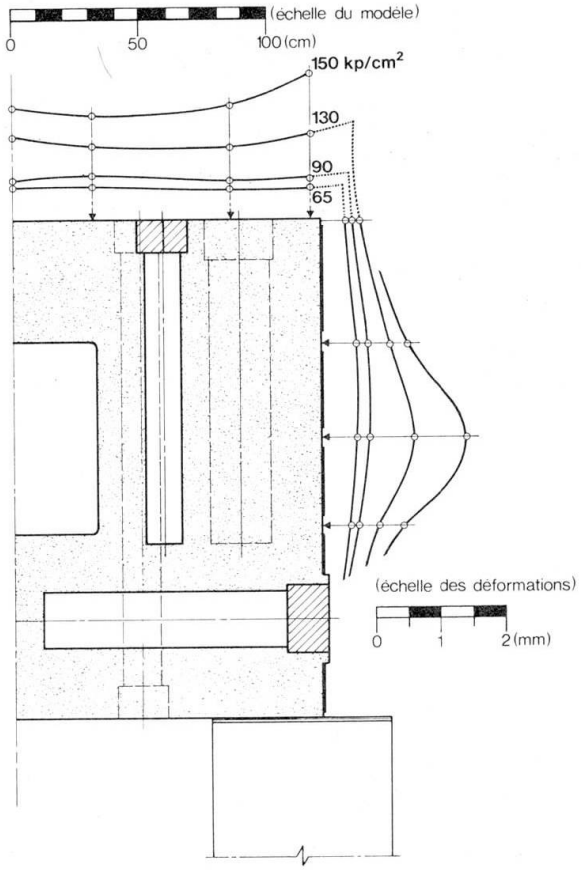


Fig. 11. Déformée du modèle.

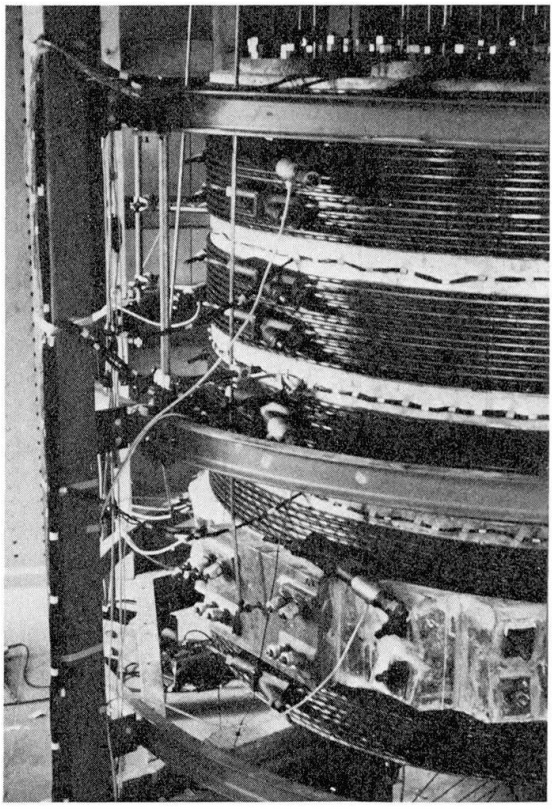

Fig. 4. Vue des dispositifs de mesure et du cadre de référence.

Les essais proprement dits comportaient 7 cycles de charge. On y distingue 3 phases essentielles (fig. 5):

*a*) cycles 1, 2, 3: observation du comportement du modèle sous la pression de service;

*b*) cycles 4, 5: observation du comportement du modèle dans l'état limite d'utilisation et au-delà (pour déterminer le début de la fissuration et de la plastification);

*c*) cycles 6, 7: essai de rupture.

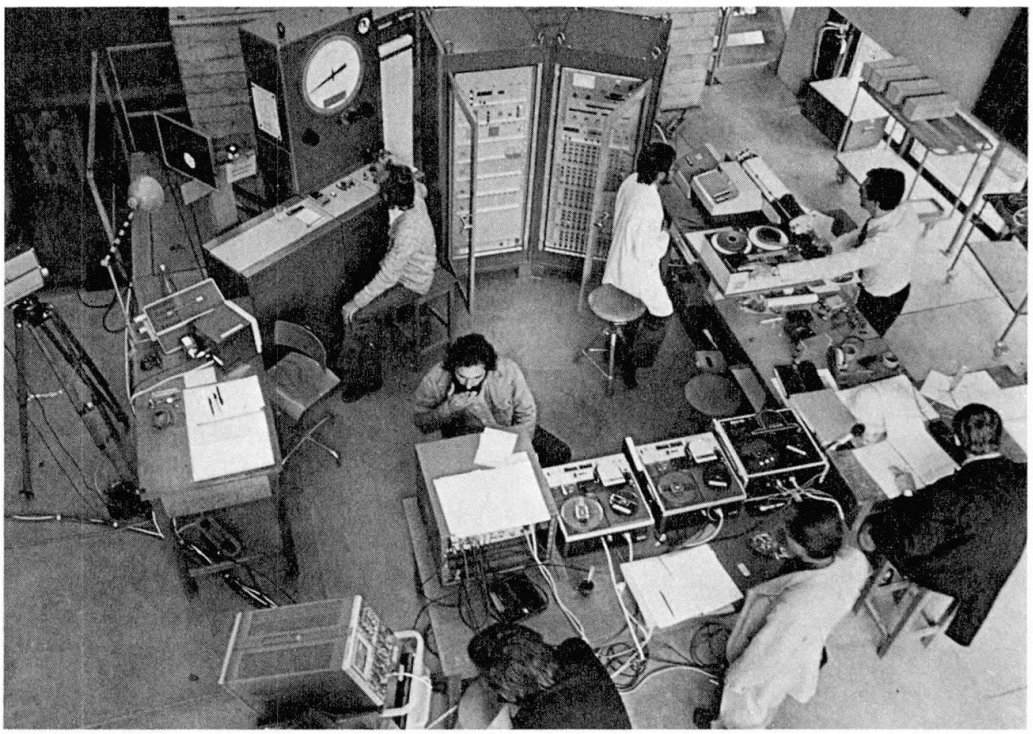

Fig. 6. Vue de l'ensemble des chaînes de sollicitation et de mesures lors des essais.

Pendant les cycles 2, 4 et 5, on a procédé aux essais de longue durée, pour examiner le comportement du modèle sous une pression constante.

Les paliers de charge étaient de 5 kg/cm$^2$ pendant les cycles et de 10 kg/cm$^2$ au début et à la fin de ceux-ci, à l'exception des cycles de rupture où l'on a choisi également des paliers de valeurs plus élevées. La durée d'un palier était de quinze minutes.

Les essais ont duré deux mois et il a été accompli au total 250 lectures sur 168 points de mesure, non comprises celles faites lors des phases de test.

## 6. Résultats et commentaires des essais

Lors des essais, les résultats numériques des mesures furent livrés immédiatement après chaque cycle. Ces résultats furent ensuite complétés par des représentations graphiques (fig. 7 à 10): les courbes montrent les variations de déformations spécifiques, de déplacements ou de forces dans les câbles de précontrainte

en fonction de la pression. Sur chacun de ces graphiques, la courbe en trait plein représente les valeurs mesurées en fonction des pressions atteintes pour la première fois, l'autre, en traitillé, représente le dernier cycle de charge au complet.

Les résultats ont montré que le comportement global du modèle était linéaire jusqu'à une pression intérieure de l'ordre de 120 à 130 kg/cm$^2$. Lors des essais de longue durée, aucun phénomène particulier n'a en outre été observé.

Une image de la déformation globale du modèle est donnée à la figure 11. Les mesures n'ont montré aucune déformation significative de la dalle inférieure. Les déformations maximales mesurées à la rupture furent de 12 à 19 mm à mi-hauteur de la face verticale et de 5 à 6 mm pour la dalle supérieure.

Les premières fissures détectables sont apparues sur la face latérale à mi-hauteur du modèle dès que la pression dépassa 120 kg/cm$^2$. Elles devinrent nettement visibles à partir de 150 kg/cm$^2$; tout d'abord, la fissure horizontale à mi-hauteur puis des fissures verticales, une au droit de chaque cavité verticale périphérique (fig. 12). Sous la pression de rupture, l'ouverture maximale de la fissure horizontale à mi-hauteur était de 10 à 15 mm.

La pression maximale atteinte à la rupture fut égale à 240 kg/cm$^2$. La rupture se manifesta extérieurement par de grandes déformations et des fissures largement ouvertes, par la rupture d'un câble annulaire et par des fuites importantes dues à une rupture de la peau d'étanchéité de deux cavités verticales périphériques (rupture provoquée par la fissuration et les mouvements importants du béton; cf. fig. 14).

Des coupes du modèle (fig. 13 à 15), effectuées par sciage au fil, montrent de manière éloquente la fissuration à l'intérieur de celui-ci. Elles montrent notamment le mécanisme d'éjection qui se développa à la périphérie des faces verticales du modèle (fig. 14), la fissuration des dalles supérieure et surtout inférieure (fig. 13 et 14), quoique aucune fissure de celles-ci ne fût visible au cours des essais. On remarquera également le réseau de fissures verticales reliant les différentes cavités (fig. 15) et la manière remarquable dont travailla et se déforma la peau d'étanchéité en tôle d'acier inox.

En conclusion, il faut relever le fait que l'essai a permis de vérifier, outre la grande réserve par rapport à la ruine, un comportement relativement ductile du modèle. Bien qu'il fût dépourvu d'armatures intimement liées au béton (câbles non injectés et absence d'armature passive), la fissuration et la déformation ont évolué de manière très progressive, ce qui est de grande importance pour la qualité de service du caisson.

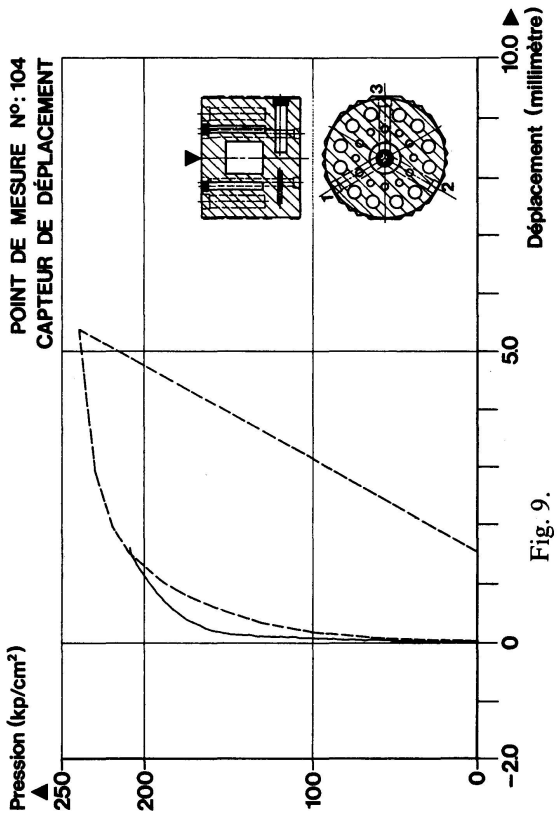


Fig. 9.

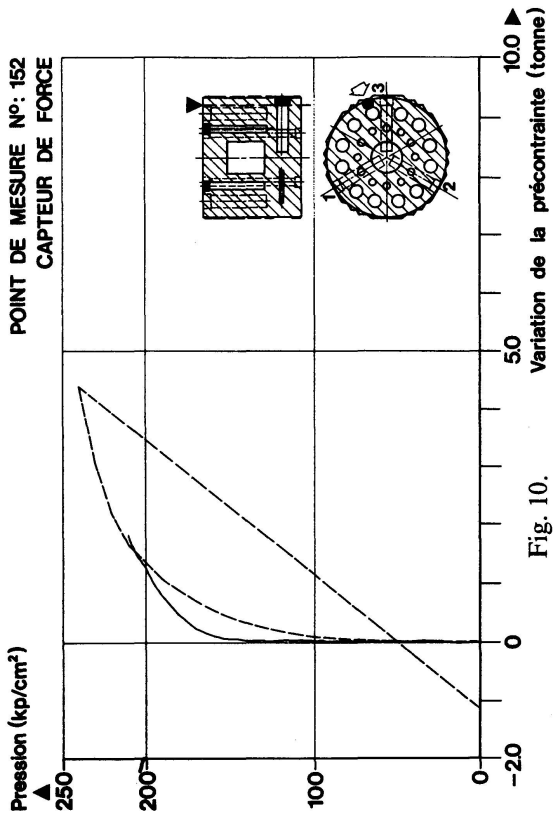


Fig. 10.

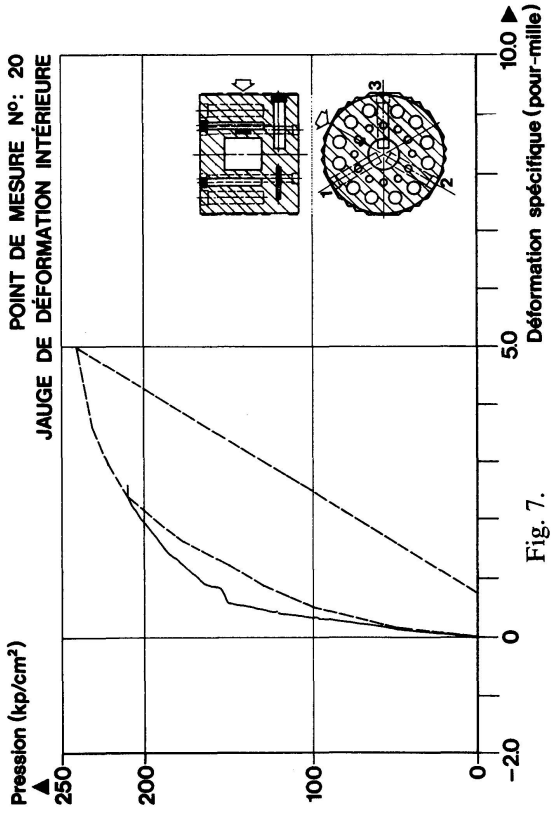


Fig. 7.

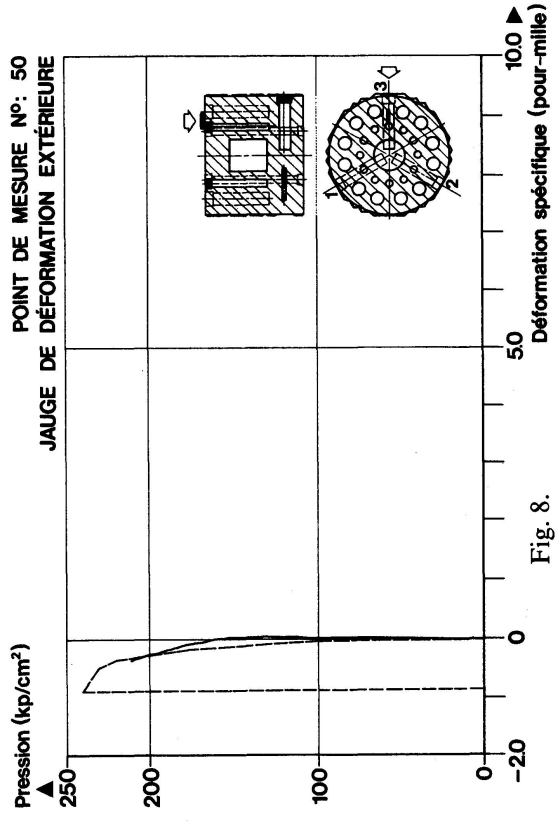


Fig. 8.

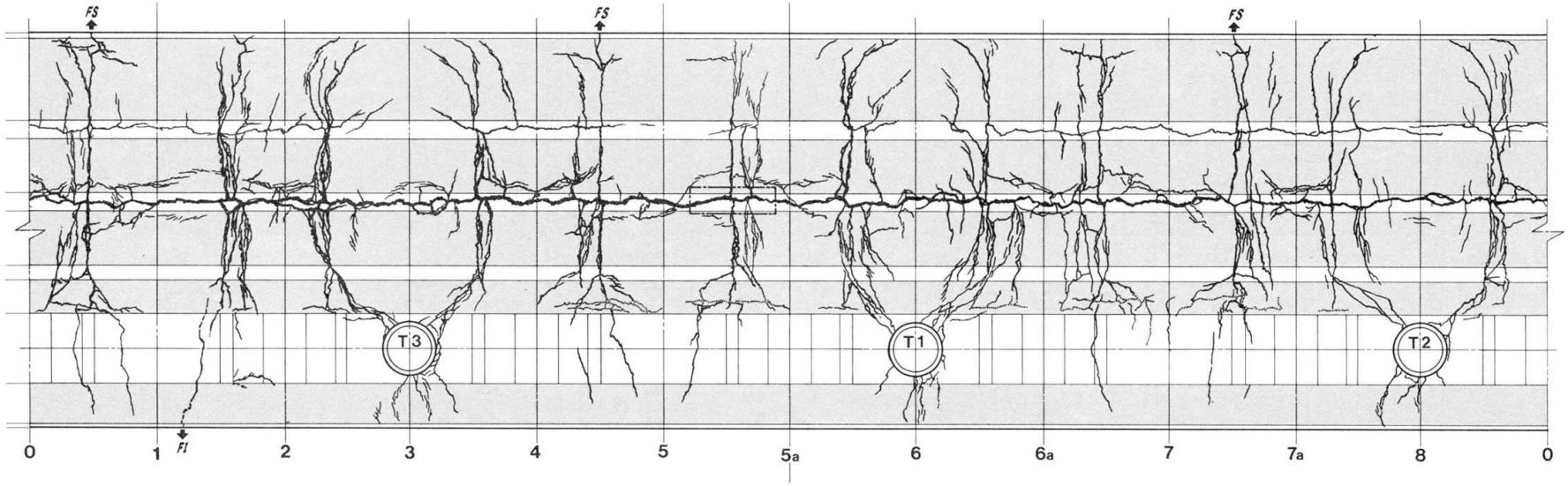


Fig. 12. Relevé des fissures sur la face verticale développée (T1, T2 et T3 sont les trois turbines).

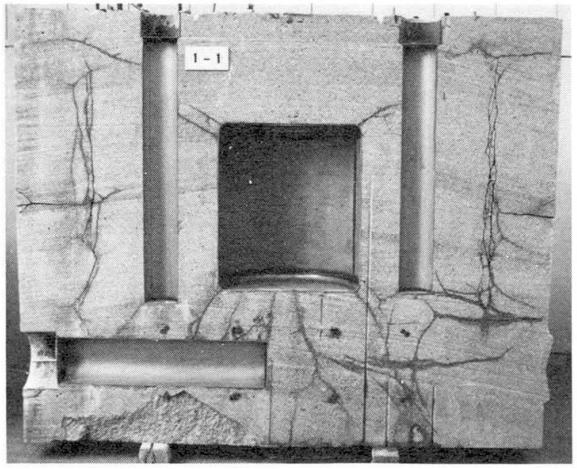


Fig. 13. Vue de la coupe verticale du modèle dans l'axe d'une turbine (T3).

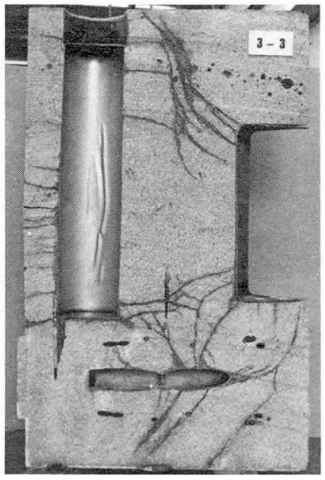


Fig. 14. Vue d'une demi-coupe verticale dans l'axe d'une cavité verticale périphérique (V22).

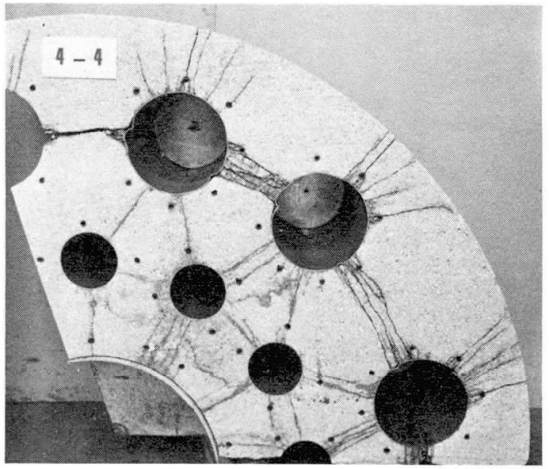


Fig. 15. Vue d'une coupe horizontale au niveau de la cavité centrale du réacteur.

# PARTIE IV

## Synthèse des calculs et des essais sur modèle

R. LAFITTE, sous-directeur, B. SAUGY, ingénieur, F. VUILLEUMIER, ingénieur principal
chez Bonnard & Gardel Ingénieurs-conseils S.A.

### 1. Introduction

Il convient de comparer les résultats obtenus par le calcul non linéaire du comportement du modèle du caisson, à l'aide d'un modèle mathématique, et les essais sur modèle physique à l'échelle 1/20, et d'en tirer des conclusions quant au caisson réel. Pour cela, les trois phases successives du comportement du modèle sont examinées:

— comportement globalement élastique; la limite de ce comportement est atteinte lorsque les déplacements deviennent non linéaires et irréversibles;
— phase de fissuration: elle est considérée comme achevée lorsque le réseau des fissures dans le béton est formé et qu'apparaissent les mécanismes entraînant la ruine du caisson;
— phase de ruine.

### 2. Comportement globalement élastique

Pour le modèle mathématique, la limite du comportement élastique se situe aux environs de 85 kg/cm$^2$ de pression intérieure, au moment où les premières fissures apparaissent dans la zone de convergence des turbines.

Pour le modèle physique, la limite du comportement globalement élastique apparaît à partir de 120 kg/cm$^2$. Les câbles de précontrainte n'ont pratiquement pas subi d'augmentation de tension. La valeur maximale de la tension des câbles les plus sollicités est estimée à 0,63 $\beta_z$ ($\beta z$ étant la contrainte de rupture de l'acier). La peau d'étanchéité qui suit la déformation du béton est encore peu sollicitée.

La part de pression, de 120 kg/cm$^2$, reprise par la peau, varie comme suit:

— cavité centrale: 7%;
— turbines: 11%;
— cavités périphériques: 12%;
— cavités périphériques extérieures: 16%.

En raison de la modélisation imparfaite dans la zone des turbines, l'analyse numérique surestime de 10% environ les forces qui agissent sur la dalle inférieure. Les caractéristiques du béton, prises en compte dans le calcul, sont plus faibles que celles réalisées sur le modèle physique (46 kg/cm$^2$ de résistance à la traction, au lieu de 65 kg/cm$^2$ au moment de l'essai). Si l'on introduit dans le modèle mathématique des caractéristiques de matériaux identiques à celles du modèle physique, la limite du comportement élastique est atteinte pour une pression de 115 kg/cm$^2$, donc très proche de celle résultant de l'essai.

### 3. Phase de fissuration

Pendant cette phase, le réseau des fissures se développe. La participation du béton à la reprise des efforts de traction diminue jusqu'à s'annuler, les charges étant progressivement reprises par les aciers de peau d'étanchéité et de précontrainte.

*L'analyse numérique* prend fin pour une pression de 133 kg/cm$^2$, par l'impossibilité de reprendre les efforts une fois le béton fissuré dans de larges zones. Cette valeur marque donc bien la limite de la participation du béton à la résistance.

Pour le *modèle physique*, la phase de fissuration, qui a débuté à 120 kg/cm$^2$, prend fin dès 165 kg/cm$^2$. A ce stade, le réseau principal des fissures apparaît clairement: fissure horizontale au milieu du fût et fissures verticales au droit des cavités périphériques. On commence à noter une augmentation de tension dans les câbles, notamment annulaires, qui atteint en moyenne 0,65 $\beta z$.

Il est malaisé de connaître de façon précise la pression reprise par la peau d'étanchéité; des plastifications locales peuvent fausser l'interprétation des valeurs fournies par les jauges de contraintes qui sont en nombre limité. On peut cependant estimer comme suit la part de pression reprise par la peau:

— cavité centrale: 7%;
— turbines: 13%;
— cavités périphériques: 20%;
— cavités périphériques extérieures: 21%.

L'écart entre les résultats des modèles mathématique et numérique provient, d'une part, de la différence des valeurs de rupture en traction du béton (la résistance du béton du modèle physique étant plus élevée que prévu), et, d'autre part, du fait que le réseau de calcul retenu ne prend pas en considération l'influence de la peau d'étanchéité lorsque la fissuration devient importante. Mais, si l'on ajuste la valeur fournie par le modèle mathématique en introduisant la valeur réelle de la résistance à la traction du béton, et la participation de la peau, la limite de fissuration atteint la valeur de 160 kg/cm$^2$.

### 4. Phase de ruine

Ainsi que nous l'avons vu précédemment pour le *modèle mathématique*, le calcul ne peut être poursuivi qu'en introduisant la rigidité des aciers, ou manuellement, sur la base du schéma de ruine qui est parfaitement déterminé. On constate que la rupture des câbles de précontrainte annulaires et des peaux d'étanchéité intervient pour une pression de l'ordre du 200 kg/cm$^2$.

A partir de 165 kg/cm$^2$, on constate que le *modèle physique* se déforme rapidement et que la peau d'étanchéité est fortement sollicitée. Elle se plastifie dans les cavités des turbines et les cavités périphériques extérieures, aux environs de 180 kg/cm$^2$. La tension dans les câbles annulaires du fût augmente rapidement. A partir de 210 kg/cm$^2$, les efforts engendrés par l'augmentation de pression sont intégralement repris par les aciers. Dès lors, et jusqu'à la rupture, le modèle se comporte latéralement comme une structure, composée d'un assemblage de blocs de béton dissociés, frettée par des éléments métalliques (câbles et peau). La ruine survient par la rupture d'un câble annulaire à 238 kg/cm$^2$, suivie de la rupture de la peau d'étanchéité des deux cavités périphériques extérieures à 240 kg/cm$^2$.

Dans la comparaison des deux moyens d'analyse, mathématique et physique, on peut noter la remarquable correspondance des réseaux de fissures obtenus par le calcul (fig. 3 de la 2e partie de l'exposé concernant le calcul non linéaire), et par l'essai sur modèle (photographies Nos 13, 14 et 15 de la 3e partie concernant les essais). C'est cette identité qui permet d'effectuer le calcul manuel des mécanismes de ruine, et de juger de l'influence des composantes de la structure sur la pression ultime.

## 5. Transposition des résultats au caisson réel

La limite du comportement élastique du caisson réel va se situer au-dessous de celle relevée sur le modèle physique, en raison de la résistance à la traction plus faible du béton. Cependant, la résistance plus grande de la dalle inférieure et la présence d'armatures passives permettent de réduire l'écart. On peut estimer que la limite du comportement élastique du caisson réel est voisine d'une pression intérieure de 110 kg/cm$^2$. Rapportée à la pression de test de 75 kg/cm$^2$, cette valeur correspond à un coefficient de sécurité de 1,5.

Dans la *phase de fissuration,* l'influence de différences sur la résistance à la traction du béton tend à diminuer; la limite de la phase de fissuration dépend, par contre, de la présence plus ou moins grande d'armatures passives. Nous avons vu dans l'examen du problème de similitude que, dans les sections les plus sollicitées, la quantité d'acier était pratiquement identique dans le modèle physique et dans le caisson réel. On doit cependant remarquer que, dans ce dernier, l'acier est mieux réparti dans la masse du béton, en raison de la présence des armatures passives, ce qui répartit la fissuration et retarde le développement des mécanismes de ruine. La limite de la phase de fissuration du caisson réel se situe donc au-dessus de celle déterminée par le modèle. On estime à 175 kg/cm$^2$ la pression correspondante, soit un coefficient de sécurité de 2,3 par rapport à la pression de test.

Dans la *phase de ruine,* le caisson réel est une structure entièrement fissurée, dans laquelle le réseau des fissures est fortement ramifié, du fait de la présence des armatures passives et de l'ancrage de la peau d'étanchéité. Les mécanismes de ruine n'apparaissent pas avec autant de clarté que dans les modèles. Le caisson se comporte comme une structure plus plastique dont les déformations croissent plus rapidement. On estime que la ruine du caisson par rupture des câbles ou de la peau d'étanchéité, moins résistante dans le caisson réel, devrait survenir pour une pression un peu inférieure à celle enregistrée lors de l'essai sur modèle. Elle serait de l'ordre de 220 kg/cm$^2$, ce qui représente un coefficient de sécurité de 2,9 par rapport à la pression de test.

## 6. Conclusions générales

6.1. Les études et essais sur modèle ont confirmé que la structure en béton précontraint d'un caisson à cavités multiples, particulièrement complexe, était réalisable avec la sécurité voulue.

6.2. La sécurité à la rupture admissible, rapport de la pression entraînant la ruine du caisson (rupture de câbles de précontrainte et perte d'étanchéité)

à la pression de test (pression maximale dans le circuit d'hélium majorée de 15%), était fixée à 2,5. Les calculs et essais ont montré que le caisson projeté avait une sécurité de 2,9.

6.3. Trois phases dans le comportement du caisson réel ont pu être distinguées:

— comportement globalement élastique, jusqu'à une pression intérieure de 110 kg/cm$^2$, égale à 1,5 fois la pression de test (75 kg/cm$^2$);
— phase de fissuration jusqu'à une pression de 175 kg/cm$^2$, égale à 2,3 fois la pression de test;
— phase de ruine se terminant par la rupture du caisson pour une pression de 220 kg/cm$^2$, égale à 2,9 fois la pression de test.

6.4 La limite du comportement globalement élastique du caisson est fonction, principalement, de la résistance à la traction du béton.

On constate que l'on peut agir sur la fin de la phase de fissuration en modifiant la quantité d'armatures passives.

Enfin, on dispose d'une certaine liberté d'action sur le coefficient de sécurité à la rupture en modifiant la quantité de précontrainte annulaire. Cette marge, à l'intérieur de laquelle les résultats de la présente étude sont garantis, est estimée à $\pm 10\%$.

6.5 La rupture du modèle s'est produite dans le fût du caisson par éjection des éléments du béton entre cavités extérieures, éléments qui se trouvaient dans un milieu tendu dans toutes les directions. Cette rupture est intervenue dans la zone du caisson dont le comportement est le mieux connu, ce qui est satisfaisant pour la conception du projet final.

6.6 Les calculs manuels des mécanismes de ruine effectués sur le caisson de référence ont conduit à un résultat qui s'est trouvé globalement confirmé par les modèles. On notera surtout la remarquable correspondance entre le réseau de fissures calculé à l'aide du modèle mathématique et celui obtenu sur le modèle physique. Ce résultat valorise fortement le modèle mathématique comme moyen de démonstration de la sécurité d'un caisson.

## Références

1. Zienkiewicz, O.C.: The Finite Element Method. Mc.-Graw-Hill, 1971.
2. Hussain, M., Saugy, B., et Zimmermann, Th.: Analyse tridimensionnelle du Comportement non linéaire d'un Caisson de Réacteur nucléaire en Béton précontraint. 1st Conference on Structural Mechanics in Reactor Technology, Berlin, 1971.
3. Saugy, B., Zimmermann, Th., et Hussain, M.: Three-Dimensional Rupture Analysis of a Prestressed Concrete Pressure Vessel Including Creep Effect. 2nd Conference on Structural Mechanics in Reactor Technology, Berlin, 1973.
4. Saugy, B., et Zimmermann, Th.: Analyse non linéaire des Structures massives. Annales ITBTP, avril 1972.
5. Saugy, B.: Contribution à l'Etude théorique du Comportement non linéaire des Structures massives en Béton armé sous Charges rapides. Bulletin technique de la Suisse romande, N° 22, 1969.
6. Saugy, B., et Zimmermann, Th.: The Finite Element Method Applied to Massive Heterogeneous Structures. Int-Rep 71, presented at Conference on Computational Aspect of the Finite Element Method at ISD, 1971.
7. Rebora, B., Zimmermann, Th., et Wolf, J.-P.: Dynamic Rupture Analysis of Reinforced Concrete Shells. ELCALAP-Seminar, Berlin, 1975.

## Résumé

Afin de démontrer que la structure en béton précontraint d'un caisson à cavités multiples d'une centrale nucléaire est réalisable avec une sécurité suffisante, par rapport à la pression de test p, une étude comportant un essai sur modèle à l'échelle 1/20 et une analyse numérique non linéaire par éléments finis tridimensionnels a été réalisée.

Le comportement du caisson est globalement élastique jusqu'à une pression intérieure de 110 kg/cm$^2$ (1,5 p) et il se rompt à une pression de 220 kg/cm$^2$ (2,9 p).

Les schémas de ruine obtenus par le calcul et par le modèle sont remarquablement semblables; ce résultat confirme la validité du modèle mathématique comme moyen de démonstration de la sécurité du caisson.

Cette étude montre l'intérêt d'une collaboration étroite entre le projeteur, le laboratoire d'essais et les analystes.



## Zusammenfassung

Zum Beweis, dass ein von zahlreichen Hohlräumen durchsetztes Reaktordruckgefäss aus vorgespanntem Beton für ein Kernkraftwerk, bezogen auf den Versuchsdruck p mit genügender Sicherheit ausführbar ist, wurde eine Studie an einem Modell im Masstab 1:20 und eine nichtlineare numerische Berechnung mittels dreidimensionaler finiter Elemente durchgeführt.

Es zeigte sich, dass das Druckgefäss bis zu einem Innendruck von 110 kg/cm$^2$ (1,5 p) elastisch ist und bei einem Druck von 220 kg/cm$^2$ (2,9 p) zu Bruch geht.

Die durch Rechnung und am Modell erhaltenen Versagensdiagramme zeigen sehr gute Übereinstimmung; dieses Resultat bestätigt die Gültigkeit des mathematischen Modells für den Sicherheitsnachweis des Druckgefässes.

Die vorliegende Untersuchung zeigt die Bedeutung einer engen Zusammenarbeit zwischen Projektersteller, Versuchslaboratorium und Berechner.



## Summary

To prove that the prestressed concrete structure of a pressure vessel with multiple cavities of a nuclear plant is feasible with a sufficient safety in relation with the test pressure p, a study including a model test at a scale 1:20 and a non-linear numerical analysis with tridimensional finite elements has been achieved.

The behaviour of the vessel is mainly elastic up to an inside pressure of 110 kg/cm$^2$ (1.5 p) and rupture happens for a pressure of 220 kg/cm$^2$ (2.9 p).

The rupture patterns computed and obtained by the model are remarkably similar; this result confirms the validity of the mathematical model as a mean to demonstrate the safety of the pressure vessel.

This study shows the interest of a close collaboration between the designer, the tests laboratory and the analysts.

# Stiffness and Strength Design of Multistory Frames

*Critères de rigidité et de résistance pour les cadres étagés*

*Steifigkeits- und Festigkeitskriterien beim Entwurf von Stockwerkrahmen*

F. CHEONG-SIAT-MOY
Post-doctoral Research Associate,
Lehigh University

LE-WU LU
Professor of Civil Engineering,
Lehigh University

## Special Chapter

Subassemblage methods of analyzing unbraced multistory steel frames, although approximate in nature, have been proved to be simple and economical alternatives to conventional second-order elastic-plastic methods. One of the limitations of existing subassumblage techniques, however, is their inability to readily analyse the lowest story in a frame where the column bases are fixed. They also do not consider proportional loading cases.

The proposed treatment, which is based upon the subassemblage stiffness concept, develops simple algebraic expressions for representing the stiffnesses of both the intermediate and the lowest stories. By considering strength as a function of deteriorating stiffnesses, the entire elastic-plastic load-deformation characteristics of a story under proportional and nonproportional loadings can be generated. It is thus possible to determine the stiffness and strength of a story by the one approach.

As a design tool, the present technique eliminates the need for assuming sways and collapse mechanisms at failure, a feature generally present in existing subassemblage methods of design. Instead, it predicts the sway at collapse and chooses the mode of failure of a story. It, therefore, does not involve any iterations before the final design is reached.

The one important feature of the design method is that, from a preliminary design, it modifies the beams to satisfy strength. After selecting the beam sizes, the moments and axial loads on the columns are known. Consequently, these can be selected so as to force the story stiffness to become either negative or zero when hinges appear in them. In this way, it is possible to ensure that all stories fail at approximately the same pre-selected load factor, resulting in a frame which is not over-designed. Further, the stories have the same general load-deformation characteristics.

Following the proportioning for strength, the frame may be modified to satisfy stiffness constraints, again using the same basic stiffness equations. A typical design example is given to illustrate the principles involved. It is noted that, in agreement with previously observed trend, frames which are designed to meet stiffness constraints fail at load factors higher than those proportioned for strength only.

## Introduction

Recognition of the fact that unbraced multistory steel frames are complex and highly redundant structures has led to the development of relatively simple plastic methods of analysis and design based upon the subassemblage concept. In these methods, a story unit is the basic substructure which is analyzed or designed without giving regard to the stress states of the other stories in the frame. Consequently, they are only approximate in nature.

Subassemblage techniques can be arbitrarily classified into 2 categories namely one which consists essentially of analytical methods and one which deals mainly with design. Obviously, analytical methods can be adapted to design. Those in the first group range from a pure manual method [5] to sophisticated computer systems [13]. The manual method [5] has since been simplified [3, 5], automated [7] and associated with optimization routines [14, 16]. The methods proposed by WRIGHT [15] and by POWELL and HAFEZ [3] also belong to the first class.

The second category of subassemblage techniques include those by HAFEZ and POWELL [8] and by EMKIN and LITLE [9, 10]. Failure mechanisms and sways are generally assumed in the design process, and several iterations may be necessary before calculations converge to the sway consistent with the idealized mechanism.

## Purpose

This paper presents an alternative approximate method for analyzing and designing unbraced multistory steel frames. Its versatility is brought about by the use of algebraic expressions for describing elastic and inelastic behavior. As an analytical technique, it removes some of the shortcomings existing in current subassemblage methods such as their inability to investigate readily the strength of the lowest story in a frame.

In contrast to existing plastic design methods [5, 7, 8, 9, 10], the proposed treatment does not follow the usual procedure of assuming sway values and failure mechanisms. This obstacle is overcome by considering story stiffness as the prime variable. Once the stiffnesses have been evaluated, other dependent variables such as sways and moments can be readily found.

Apart from omitting the need for estimating sways and for idealizing failure mechanisms, it eliminates the use of auxiliary techniques to satisfy both stiffness and strength requirements, since strength is considered as a function of deteriorating stiffness. Besides, the story to be designed can be controlled to fail at pre-selected load-factors. Consequently, a balanced frame with no over-designed or under-designed stories results.

A two-stage development is presented. After introducing the story stiffness concept, the power of the method as an analytical tool is demonstrated. Comparison with a conventional, second-order, elastic-plastic method is carried out to indicate the degree of accuracy to be expected. Principles developed in the analysis part are subsequently employed in the design phase.

## Assumptions

The following major assumptions are made herein. Only the in-plane behavior of rigidly-jointed frames with regular geometry is considered. All members are perfectly elastic-plastic and are initially straight. Bending is about their major axes. No story eccentricities exist. Panel zone deformations are neglected. Although applied loads can increase non-proportionally, only the proportional case is considered. Note that such a loading case has not been considered in any sub-assemblage techniques developed so far.

## Basic Concepts

A typical load-deformation relationship for a story under proportional loads is shown in Figure 1 in which $\lambda$ = load factor by which all loads are multiplied and $\Delta$ = sway. Also shown is the load-stiffness curve; the story stiffness $S_T = \frac{d\lambda}{d\Delta}$. Instead of studying story behavior from the $\lambda - \Delta$ relationship, it is convenient to study the $\lambda - S_T$ characteristic. The critical load-factor $\lambda_C$ corresponds to the highest point on the $\lambda - S_T$ curve. After failure, a lower load factor, such as $\lambda_B$, is necessary for maintaining equilibrium. Note that at a load factor greater than $\lambda_C$, equilibrium cannot be satisfied and the computed story stiffness will be negative.

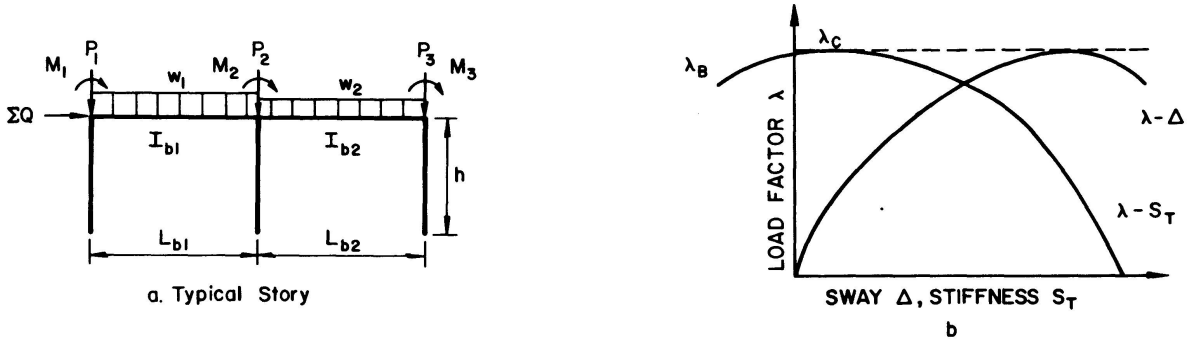


Fig. 1. Story Load-stiffness Characteristic.

The moments which are induced in a story can be approximated by two componnts, one caused by pure gravity loads and one by sway, $P - \Delta$ effect, Figure 2 (a). Gravity moments at the beams' ends are conservatively taken as the fixed-end moments, FEM = $wL^2/12$, which are shared equally by the columns at the top and at the bottom. Moments generated by sway are calculated once the story stiffness has been evaluated.

The story stiffness $S_T$ is the sum of the stiffnesses, s, of the subassemblages whose number equals that of the columns in the story. Figure 2 (b) shows some typical subassemblages in an intermediate story. Each consists of one column and of one or two restraining beams. Points of inflection are assumed to develop at the centres of the members under sway conditions so that each subassemblage can be represented by the restrained column in Figure 2(c) – case (a). Cases (b) and (c) which are also depicted in Figure 2(c) refer to the columns of the lowest story in which points of inflection do not occur at mid-heights.

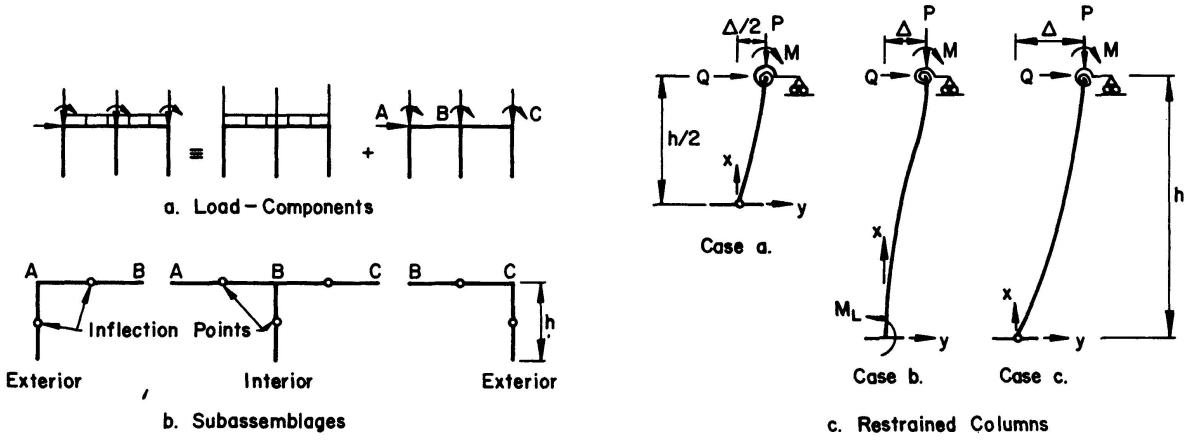


Fig. 2. Idealized Story Behavior.

## Story Stiffness

The load-deformation relationships of these subassemblages can be derived algebraically as described in detail in Refs. 3 and 4. Briefly, these expressions are obtained in the following manner. Simple integration shows that the moment $M_x$ in the columns is

$$M_x = A \sin(Kx) + B \cos(Kx) \tag{1}$$

in which A and B = constants of integration, $K^2 = \frac{P}{EI_c}$, P = column axial load, E = Young's Modulus, and $I_c$ = column inertia. Denoting the rotational stiffnesses of the restraining beams in a subassemblage by $C = \Sigma\ (6EI_b/L_b)$ and satisfying compatibility of slope at the column's upper end, $\theta = \frac{dy}{dx}$, the stiffenesses of the restrained columns are obtained:

$$\text{Cases (a) and (c): } s = \frac{Q}{\Delta} = \frac{P}{h}\frac{G}{1-G} \tag{2}$$

$$\text{in which } G = \frac{Kh}{2}\cot\frac{(Kh)}{2} - \frac{UPh}{2C} \tag{3}$$

$$\text{Case (b): } s = \frac{Q}{\Delta} = P\left[\frac{\sin(Kh)}{K} - h + A_o - A_o\cos(Kh)\right]^{-1} \tag{4}$$

$$A_o = \left[1 - \cos(Kh) + \frac{UP}{KC}\sin(Kh)\right]\left[K\sin(Kh) + \frac{UP}{C}\cos(Kh)\right]^{-1} \tag{5}$$

One other quantity needed for case (b) is the moment $M_L$ at the base,

$$M_L = A_o Q \tag{6}$$

In the above equations, the quantity U is the ratio of moments generated in the restraining beams to the column upper end moment. Based upon some simplifying assumptions, the following results have been obtained [3, 4]. For case (a), U = 2; for case (b), U is given by Eq. 7; and for case (c) U = 3/2,

$$U = \frac{4 - 4\cos(Kh)}{2 - 2\cos(Kh) - P(KC)^{-1}\sin(Kh)} > 2 \tag{7}$$

By using the first two terms in the expansion series of the trigonometric functions, the stiffness equations can be considerably simplified with only a minor loss of accuracy [3, 4].

$$\text{Case (a) – simplified: } s = \frac{Q}{\Delta} = \frac{12EI_c}{h^3(1+2\Psi)} - \frac{P}{h} \tag{8}$$

$$\text{Case (b) – simplified: } s = \frac{Q}{\Delta} = \frac{12EI_c}{h^3}\frac{3+\Psi}{3+4\Psi} - \frac{P}{h} \tag{9}$$

$$\text{Case (c) – simplified: } s = \frac{Q}{\Delta} = \frac{12EI_c}{h^3(4+1.5\Psi)} - \frac{P}{h} \tag{10}$$

The relationship between the load factor $\lambda$ and the sway $\Delta$ is obtained by multiplying all Q's and P's by $\lambda$. For example, for case (a),

$$\lambda Q = \left[\frac{12EI_c}{h^3(1+2\Psi)} - \frac{\lambda P}{h}\right]\Delta \tag{11}$$

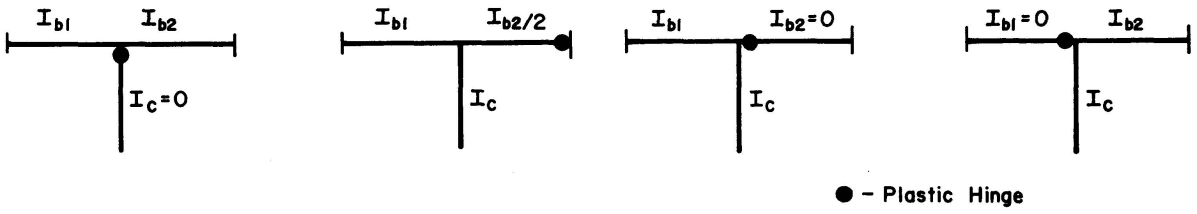


Fig. 3. Reduction in Member Stiffness.

It is convenient in this study to consider the story stiffness $S_T$ as $\lambda\Sigma Q/\Delta$ where $\Sigma Q$ = total wind loads on the story.

The quantity $\Psi$ in Eqs. 8-11 is a measure of the ratio of column stiffness to restraining beam stiffnesses,

$$\Psi = \frac{I_c}{h\left[\frac{I_{b1}}{L_{b1}} + \frac{I_{b2}}{L_{b2}}\right]} \tag{12}$$

in which $I_{b1}$ and $I_{b2}$ are the beam inertias, and $L_{b1}$ and $L_{b2}$ are their respective lengths. In an exterior subassemblage, either $I_{b1}$ or $I_{b2} = 0$. At the formation of plastic hinges, column inertias and beam inertias will change. Figure 3 illustrates the rules employed to evaluate these quantities for a given subassemblage.

## Elastic Analysis

### *Deflections*

The analytical aspect of the present treatment will be demonstrated on Frame A shown in Figure 4 and described in Table 1. For elastic deflections taking into account $P - \Delta$ effects, two sets of calculations are performed. First, the relative

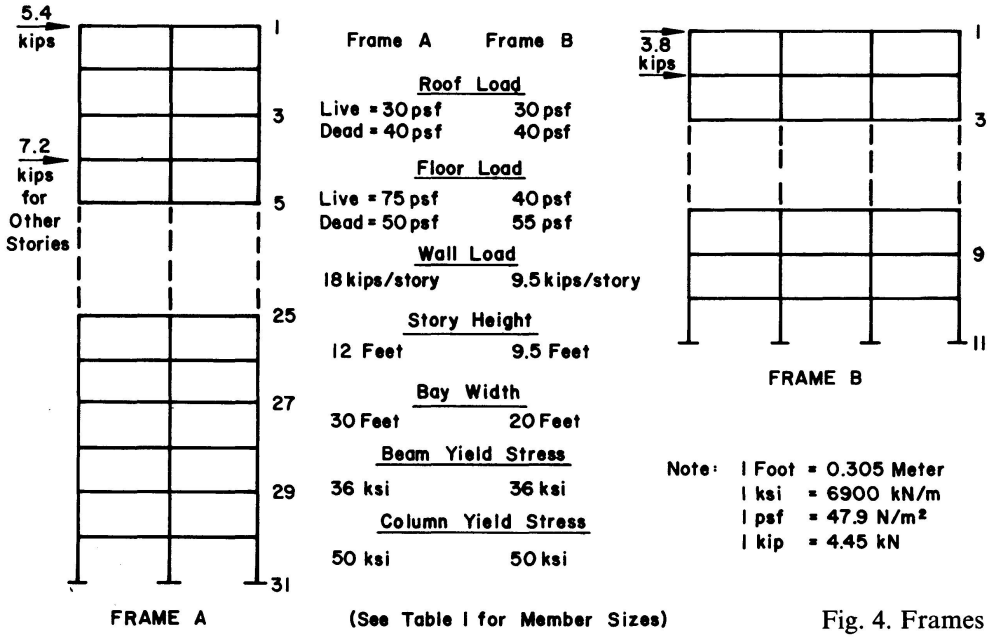


Fig. 4. Frames Studied.

*Table 1: Members for frames in figure 4.*

FRAME A

| Level | Beam | Level | Columns Ext: | Columns Int: |
|---|---|---|---|---|
| 1 | W21 x 44 | 1 - 3 | W10 x 54 | W10 x 33 |
| 2 - 4 | W21 x 55 | 3 - 5 | W14 x 68 | W14 x 68 |
| 5 | W24 x 61 | 5 - 7 | W14 x 95 | W14 x 95 |
| 6 - 7 | W24 x 68 | 7 - 9 | W14 x 119 | W14 x 127 |
| 8 - 10 | W24 x 76 | 9 - 11 | W14 x 142 | W14 x 158 |
| 11 - 12 | W24 x 84 | 11 - 13 | W14 x 167 | W14 x 193 |
| 13 - 14 | W27 x 84 | 13 - 15 | W14 x 193 | W14 x 219 |
| 15 - 17 | W27 x 94 | 15 - 17 | W14 x 219 | W14 x 246 |
| 18 - 21 | W30 x 99 | 17 - 19 | W14 x 246 | W14 x 287 |
| 22 - 24 | W30 x 108 | 19 - 21 | W14 x 287 | W14 x 314 |
| 25 - 30 | W30 x 116 | 21 - 23 | W14 x 314 | W14 x 342 |
| | | 23 - 25 | W14 x 342 | W14 x 398 |
| | | 25 - 27 | W14 x 370 | W14 x 426 |
| | | 27 - 29 | W14 x 398 | W14 x 455 |
| | | 29 - 31 | W14 x 500 | W14 x 550 |

FRAME B

| Level | Beam | Level | Columns Ext: | Columns Int: |
|---|---|---|---|---|
| 1 - 2 | W12 x 22 | 1 - 3 | W8 x 13 | W8 x 13 |
| 3 - 4 | W14 x 22 | 3 - 5 | W8 x 20 | W8 x 20 |
| 5 - 8 | W14 x 26 | 5 - 7 | W8 x 28 | W8 x 28 |
| 9 - 10 | W16 x 26 | 7 - 9 | W8 x 35 | W8 x 35 |
| | | 9 - 11 | W8 x 40 | W8 x 40 |

story sways are calculated using Eq. 8 and Eq. 9. These deflections are then used to calculate the moments and shears at the beams' ends. Additional sways [1] caused by axial deformations are subsequently evaluated.

Some results are plotted in Figure 5 together with those obtained from a conventional second-order, elastic-plastic method [12]. Good agreement is observed between the two methods.

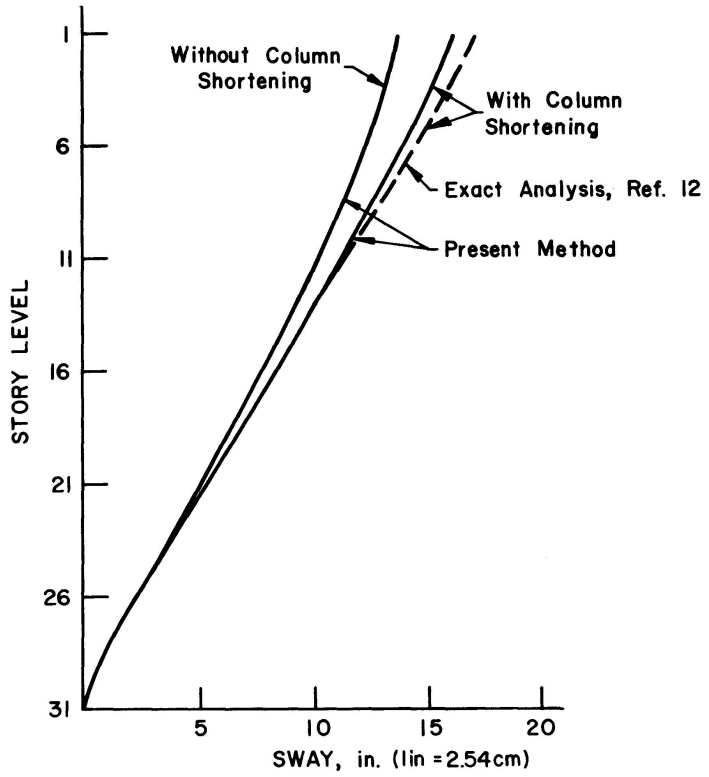


Fig. 5. Load-deformation Relationship of Frame a at $\lambda = 1.0$.

### *Increase In Member Sizes*

The story stiffness concept was used in Refs. 3 and 4 to provide simple guidelines for improving frame stiffnesses. It was explained why increases in beam sizes has a more significant effect than column sizes in reducing lateral sway in conventional multistory frames in which $\Psi > 0.5$. However, column axial shortening was not considered. To fill the gap, some further examples are given.

The relative sway index, including the effects of column deformations, of the story below Level 26 of Frame A (Fig. 4 and Table 1) is 0.0041 at $\lambda = 1.0$. When all the columns are changed to W14X500, the sway index becomes 0.0039. Thus, a 50% increase in column inertias causes only a 5% decrease in sway. On the other hand, when the beams are changed to W33X130, the deflection index improves to 0.0029, i.e., an increase in beam inertias of about 35% causes a sway decrease of about 30%. Note that when $\Psi$ is not much larger than 0.5, increasing both column and beam sizes may be more desirable [3, 4].

In the upper stories where column shortening has a more pronounced influence, similar results are obtained. For example, when the columns in the story below level 4 of Frame A are changed to W14X68, $I_C$ increases by 35% and the sway decreases by 10%. Note that an increase in column area will ensure a reduction in chord drift, but this is only a minor component in the sway of unbraced frames.

### *Bending Moments*

Other quantities which are of interest to the designer are the bending moments which occur at working loads. In an intermediate story, the moment $M_C$ which acts at the top of a column is the sum of moments caused by the sway and beam gravity loads,

$$M_c = \frac{P\Delta}{2} + \frac{Qh}{2} \pm \frac{(FEM)_c}{2} \tag{14}$$

Since $Q = s\Delta$, Eq. 14 can be simplified to

$$M_c = \frac{6EI_c\Delta}{h^2(1+2\Psi)} \pm \frac{(FEM)_c}{2} \tag{15}$$

in which $(FEM)_c$ = resultant beam fixed-end moments on the joint. Similarly, the moments $M_b$ which occur at the beam's ends are

$$M_b = R\,\frac{12EI_c\Delta}{h^2(1+2\Psi)} \pm FEM \tag{16}$$

in which R = ratio of stiffness $I_{b2}/L_{b2}$ of the leeward beam to the total beam stiffnesses $\frac{I_{b1}}{L_{b1}} + \frac{I_{b2}}{L_{b2}}$. In an exterior subassemblage, R = 1. When calculating the above quantities, $\Delta$ to be used is the relative sway excluding column shortening influence. Moreover, in an interior subassemblage, beam moments are calculated for the leeward beam only.

Table 2 shows typical results obtained for Frame A. Comparison of bending moments with the second-order, elastic-plastic method [12] shows good agreement. The discrepancy in the upper levels arises partly because gravity beam moments are over-estimated and partly because the columns do not bend in exact double curvature.

*Table 2: Comparison between present and exact methods at working loads.*

| | Beam Leeward-end Moments kip-in | | | | Column Maximum Moments kip-in | | | | | |
|---|---|---|---|---|---|---|---|---|---|---|
| | A - B | | B - C | | A | | B | | C | |
| Level | Present | Ref.12 | Present | Ref.12 | Present | Ref.12 | Present | Ref.12 | Present | Ref.12 |
| 4 | 3740 | 3341 | 3657 | 3313 | 726 | 492 | -923 | -940 | -1870 | -1700 |
| 15 | 6992 | 6393 | 7034 | 7056 | -900 | -731 | -3936 | -4387 | -3496 | -3612 |
| 26 | 10198 | 9610 | 10546 | 10051 | -2503 | -2542 | -6915 | -7337 | -5099 | -5115 |

Note: 1 kip-in = 113N-M

### *Axial Loads*

Provided the bending moments at the beams' ends are known with sufficient accuracy, column axial forces can be predicted with a reasonable degree of precision. However, since bending moments change as the load factor increases, prediction of column forces appears complicated. To simplify design, idealizations are necessary.

Some column forces for Frame A are shown in Figure 6. They vary almost linearly with $\lambda$ even in the inelastic range. Note that at $\lambda = 1.35$ there are 24 hinges present and that at $\lambda = 1.40$, 48 hinges have developed. Similar studies made on the frames of Ref. 11 show that the deviation from linearity is small especially when plastic hinges appear less in the columns. At collapse, however, there is a sudden unloading in the windward columns and a corresponding loading in the leeward columns. For design purposes, the nonlinearity may be neglected.

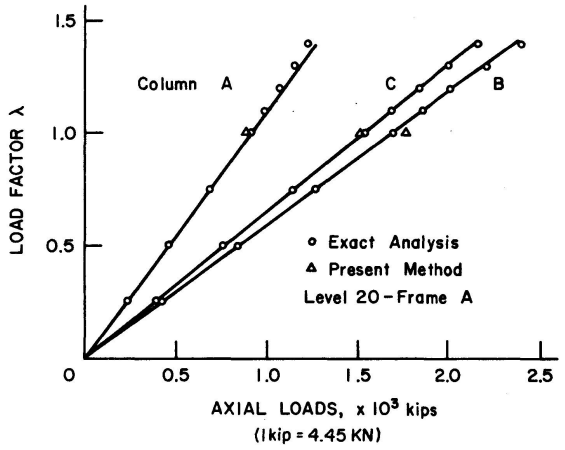


Fig. 6. Prediction of Column Loads.

With this idealization, the following relationship may be postulated,

$$P_\lambda = \lambda P_W \tag{17}$$

in which $P_\lambda =$ column load at a load factor $\lambda$, and $P_W =$ column load at $\lambda = 1.0$. Shown in Figure 6 are some values of $P_W$ obtained using the present technique and the $P - \lambda$ distribution of Frame A given by the "exact" analysis [12]. The good agreement reached suggests that it is sufficiently accurate to employ Eq. 17 provided $P_W$ is known. This procedure finds an important use in design where axial forces have to be predicted quickly and with sufficient accuracy.

## Inelastic Behavior

### *Intermediate Stories*

Prediction of the formation of a hinge at the leeward end of a beam in an intermediate story is carried out using the following expressions:

$$S_T = \frac{12E}{h^3}\sum_1^m \left[\frac{I_c}{1+2\Psi}\right] - (\lambda_p + \delta\lambda)\frac{\Sigma P}{h} \tag{18}$$

$$\delta\Delta = \frac{\delta\lambda \cdot \Sigma Q}{S_T} \tag{19}$$

$$(M_b)_p + R\,\frac{12EI_c}{h^2(1+2\Psi)}\delta\Delta + \delta\lambda\ \mathrm{FEM} = M_p \tag{20}$$

$$\lambda_n = \lambda_p + \delta\lambda \tag{21}$$

in which $\delta\Delta$ = sway increment caused by a load factor increment $\delta\lambda$, $\lambda_p$ = load factor in previous cycle = zero in the first cycle, $\lambda_n$ = load factor in present cycle, $(M_b)_p$ = total moment on the beam in previous cycle = zero in first cycle, and R = beam stiffness ratio which changes according to the hinge formation, Figure 3.

The procedure works in the following manner. Assume that there are no hinges present in the story. Set $(M_b)_p = \lambda_p = 0$ for all beams. Substitute Eqs. 18 and 19 into Eq. 20 and calculate $\delta\lambda$ as the load factor increment required for a hinge to form in each beam. The smallest $\delta\lambda$ corresponds to the first hinge in the story. Calculate $\delta\Delta$ from Eq. 19. The increment in the leeward moment in each beam $\delta M_b$ caused by $\delta\Delta$ is calculated,

$$\delta M_b = R\,\frac{12EI_c}{h^2(1+2\Psi)}\delta\Delta + \delta\lambda\ \mathrm{FEM} \tag{22}$$

Add $\delta M_b$ to $(M_b)_p$ of the previous cycle to give the actual total moment of the beam. Recalculate beam stiffnesses and repeat above process.

Hinges forming in the windward ends of the beams are predicted in a similar way except that FEM has to be re-determined when a leeward hinge exists and a negative sign must be associated with it. Furthermore, the right hand term in Eq. 20 is the lesser value of $M_p$ or $M_{pw}$,

$$M_{pw} = \lambda\,\frac{wL^2}{2}\left[\left(\frac{16M_p}{\lambda wL^2}\right)^{1/2} - 1\right] - M_p \tag{23}$$

Collapse occurs when $S_T \leq 0$.

Formation of hinges in the columns is calculated in a similar way, but with Eq. 20 replaced by Eq. 24 and Eq. 22 by Eq. 25,

$$(M_c)_p + \frac{6EI_c}{h^2(1+2\Psi)}\delta\Delta + \frac{\delta\lambda}{2}(\mathrm{FEM})_c = 1.18\,(M_p)_c\left[1 - (\lambda_p + \delta\lambda)\frac{P_w}{P_y}\right] \tag{24}$$

$$\delta M_c = \frac{6EI_c\,\delta\Delta}{h^2(1+2\Psi)} + \frac{\delta\lambda}{2}(\mathrm{FEM})_c \tag{25}$$

in which $(M_c)_p$ = total moment applied to column in previous cycle = zero in first cycle, $(M_p)_c$ = full plastic moment of column, $P_y$ = column yield load and $\delta M_c$ = increment in column moment caused by $\delta\lambda$. A test is always made in the calculations to determine whether hinges form in the beams or in the columns and subassemblage stiffnesses are changed accordingly.

Frame A was analyzed by the method of Ref. 12 and the weakest story was found to be the one below level 26. This story was then analyzed by the present technique. Comparison of results in Figure 7(a) shows good agreement. In order to investigate the effect of omitting column shortening in the present treatment, the story below level 26 was deliberately strengthened using W14X500 columns, and the story below level 4 weakened using W10X66 columns and W21X44 beams. Results of analyses are shown in Figure 7(b). If is observed that column shortening effects may be neglected when computing ultimate strength. A similar observation was made by PARIKH [12].

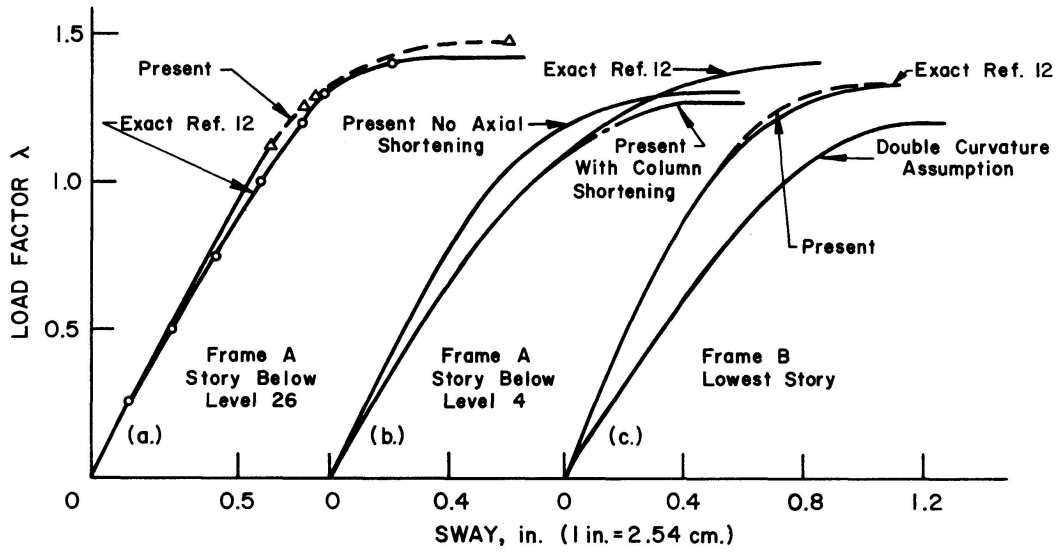


Fig. 7. Comparison of Methods.

### *Lowest Story*

Expressions similar to Eqs. 18-24 can be derived for the lowest story. However, a computer program was written to remove the tediousness associated with keeping track of hinge formations and changing member stiffnesses. Note that a hinge will form at the fixed base of a column before appearing at the top since $M_L > M_C$, and that when the hinge has formed, the subassemblage stiffness is no longer given by Eq. 9, but by Eq. 10. The lowest story of Frame B which is described in Table 1 and Figure 4 was analyzed and the results are plotted in Figure 7(c). The conservativeness which follows from assuming exact double curvature bending in the lower columns is also demonstrated in Figure 7(c).

It must be remarked that when the number of bays is few and when $\Psi > 1.0$, Eq. 9 tends to be unconservative in the elastic range, but sufficiently accurate in predicting ultimate strengths.

## Design

It has been demonstrated how relevant quantities such as bending moments, sway and axial forces can be evaluated up to the collapse load factor once story stiffnesses have been computed. It has also been shown that changes in column sizes

do not affect story stiffnesses to any significant extent provided the ratio of column stiffness to beam stiffnesses $\Psi > 0.5$. In fact, they do not affect story strengths to any appreciable degree if the columns stay elastic.

This information can be fully exploited in design by forcing the columns to remain elastic until the point of collapse and by modifying the beams to satisfy story strength requirements. A simple design procedure is now proposed. However, the following fixed quantities must be given: frame dimensions, applied gravity and wind loads, required failure load factor under pure gravity loads $\lambda_g$, and required failure load factor under combined lateral and vertical forces $\lambda_F$.

A typical set of design steps would be:

STEP 1 – Obtain a preliminary design using $\lambda_g$ and simple plastic theory, neglecting secondary effects [5].

STEP 2 – Calculate story stiffness $S_T$ and sway $\Delta$ at $\lambda = 1.0$. Calculate required plastic moment of beams using Eq. 16 by replacing $M_b$ by $M_p$. This step ensures that no hinges form in the beams at working load level.

STEP 3 – Analyse the story assuming that the columns remain perfectly elastic. The load factors at which the leeward beam hinges form will be greater than 1.0, but may be less or greater than $\lambda_F$. Ensure that the windward hinges develop at $\lambda > \lambda_F$ by using Eqs. 20 and 23. Increase beam sizes if necessary.

STEP 4 – From step 4, all column axial forces and bending moments are known for load factors up to values slightly larger than $\lambda_F$. Choose sections sizes so that the columns fail at a load factor slightly larger than $\lambda_F$.

STEP 5 – If stiffness constraints are imposed, calculate required story stiffness. Use Eq. 8 directly to compute required size of new girders. [See also Refs. 3 and 4.]

## Comments

The above-listed routine actually recommends the design to follow curve AB in Figure 8. All plastic hinges are initially compelled to develop in the beams which are selected so that $\lambda_c \geq \lambda_F$, where $\lambda_c$ = critical load factor based upon the premises that the columns do not yield. Usually, the columns selected in the preliminary design will have yielded before $\lambda_F$ is reached. By a judicious choice of larger column sections, hinges are forced to form in the columns at a load factor not less than $\lambda_F$. As soon as the hinges appear in the columns, a drastic decrease in story stiffness occurs and the design follows path CD. Considering curve ACD, it is appreciated that $\lambda_F$ has now become the failure load factor of the story designed.

Frame B shown in Figure 4 was designed for $\lambda_g = 1.7$ and $\lambda_F = 1.3$, with no stiffness constraints imposed at $\lambda = 1.0$. The member sizes are those given in Table 1. This frame was analyzed by the method of Ref. 12 which considers it in its entirety. Some results are plotted in Figure 9. It can be observed that all the lower stories have almost the same ultimate strengths. They fail at a load factor slightly above 1.3, thereby indicating a well balanced frame. Note that the frame and its stories have the same load-deflection characteristics.

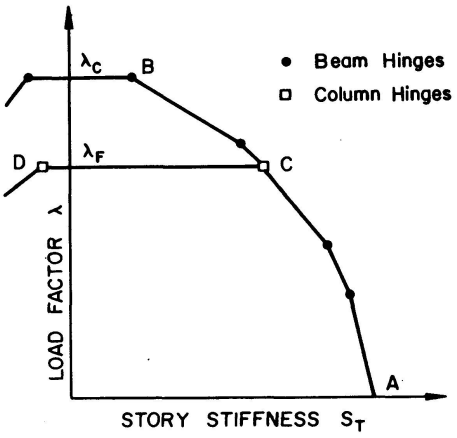


Fig. 8. Load-stiffness Path of Typical Design.

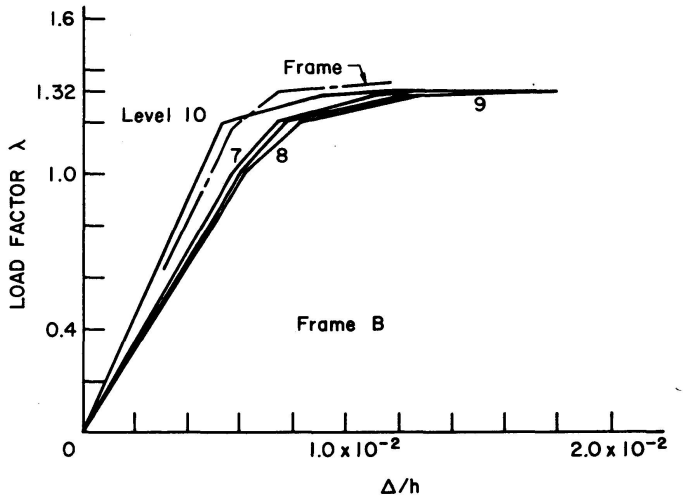


Fig. 9. Load-Deformation Curves of Frame B Stories.

For further illustration of the application of the present method, Frame B is proportioned to meet a second-order deflection constraint of 0.003h per story. Rapid calculations of the ratio of column stiffness to beam stiffnesses, Eq. 12, shows that the quantity $\Psi$ is of the order of 0.5 for the interior subassemblages. As explained in Refs. 3 and 4, changing beam sizes, in this particular case, is not the most effective way of reducing sway since the design will result in very large girders and relatively small columns.

One procedure that may be adopted is to increase all member sizes in the same proportion. The final frame dimensions are given in Figure 10. Obviously, this frame has an ultimate load factor greater than 1.3 since it has larger member sizes than Frame B given in Table 1.

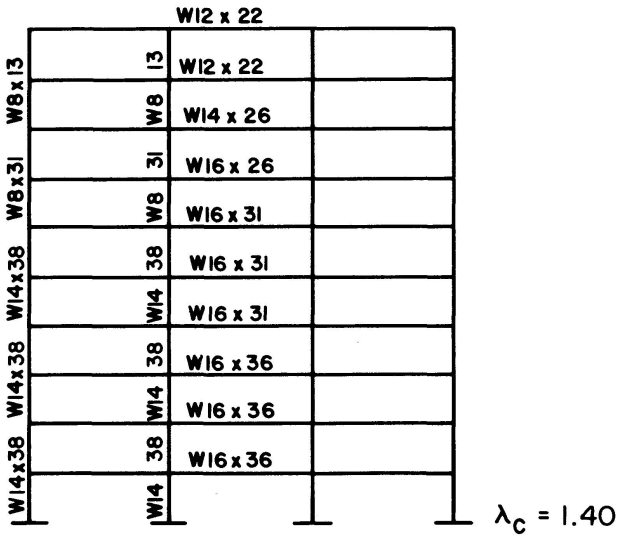


Fig. 10. Frame B Designed for Stiffness ($\Delta/h = 0.003$).

It may be pointed out that, generally, in most unbraced multistory steel frames $\Psi > 0.5$ so that only beam sizes need be increased to satisfy stiffness limits. A typical example can be found in Refs. 3, 14 and 16.

Note further that the above-designed frames illustrate the advantages of using subassemblage techniques as design tools. Consider, for instance, the conventional allowable stress method [2]. Neither does it aim at satisfying strength nor does it steer the design to neet deflection constraints, except through the use of additional auxiliary techniques. In the present treatment, however, the sway and strength of each story can be controlled individually.

## Safety and Economy

The use of plastic theory in the design of unbraced multistory steel frames has been advocated because of the economic advantages it offers over allowable stress concepts. The penalty for employing plastic theory, however, is the difficulty in accounting for the secondary moments which have a pronounced influence on the failure modes and the computed collapse loads. Existing plastic design methods attempt to overcome this problem by assuming failure mechanisms and sway values at collapse. This procedure generally requires several iterations in analysis before agreement is obtained between assumed sways and actual ones.

The present technique eliminates the need for the iterations by choosing stiffness as the main variable instead of sway. After all, sway and ultimate strengths are merely functions of story stiffness. Furthermore, the one concept presented is amply satisfactory for both strength and stiffness design, requiring no additional sub-routines. This is a feature not available in existing design techniques.

Rapidity in analysis and design is realized because of the simple nature of the working algebraic equations. In the advent of the unavailability of a computer, the method is very suitable for hand calculations.

The weight of the structure designed for strength tends to be close to optimum because the member sizes are so selected as to just satisfy strength. Moreover, all stories are forced to fail at the same pre-selected load factor. Consequently, the stories are of almost equal strength and the frame is a well balanced one.

The accuracy of the method has been well substantiated by comparison with a conventional second-order elastic-plastic method which considers the frame in its entirety. The present treatment has a tendency to err slightly on the conservative side. As a consequence, it produces safe designs.

## Conclusion

The power of using story stiffness as the basic independent variable in the analysis and design of unbraced multistory steel frames has been demonstrated. Unlike previously proposed techniques, the present treatment can analyze without difficulty the lowest story in a frame and can predict with sufficient accuracy frame behavior in the elastic and inelastic range under proportional loading conditions. As a design tool, it eliminates the need to assume failure mechanisms and sways at ultimate strength. Neither does it require auxiliary sub-programs to satisfy strength and stiffness requirements, nor does it nêcessitate the use of iterations to reach the final design. Moreover, while it ensures that all stories remain elastic at the working load level, it also proportions them to fail at about the

same load factor, at a value somewhat higher than a pre-selected one. Consequently, the resulting design is well balanced. The accuracy of the method has been confirmed by comparison with a conventional second-order, elastic-plastic method.

## Notations

| | |
|---|---|
| A, B | constants of integration. |
| E | Young's Modulus. |
| FEM | beam fixed-end moments. |
| $(FEM)_c$ | resultant FEM at a joint. |
| $I_{b1}$, $I_{b2}$ | inertias of beams in a subassemblage. |
| $I_c$ | column inertia. |
| $K^2$ | $P/EI_c$. |
| $L_{b1}$, $L_{b2}$ | lengths of beams in a subassemblage. |
| $M_b$ | leeward-end beam moment. |
| $M_c$ | upper-end column moment. |
| $M_L$ | moment at lower end of column with fixed base. |
| $M_P$ | full plastic moment of beam. |
| $M_{pw}$ | applied moment causing hinge formation at windward end of beam. |
| $M_x$ | moment at any point x in column. |
| $(M_b)_p$ | beam moment in previous cycle of calculation. |
| $(M_c)_p$ | column moment in previous cycle of calculation. |
| $(M_p)_c$ | column full plastic moment. |
| P | column axial load. |
| $P_w$ | column force at working loads. |
| $P_\lambda$ | column force at load factor $\lambda$. |
| $\Sigma P$ | total gravity loads on a story. |
| Q | column shear force. |
| $\Sigma Q$ | total shear on a story. |
| R | ratio of leeward beam stiffness to windward beam stiffness. |
| $S_T$ | story stiffness. |
| U | ratio of restraining beam moments to column moment. |
| h | story height. |
| s | subassemblage stiffness. |
| w | distributed floor load. |
| $\Delta$ | story sway. |
| $\delta M_b$ | increment in beam leeward moment due to $\delta\Delta$. |
| $\delta M_c$ | increment in column moment due to $\delta\Delta$. |
| $\delta\Delta$ | increment in story sway caused by $\delta\lambda$. |
| $\delta\lambda$ | increment in load factor. |
| $\lambda$ | load factor. |
| $\lambda_B$ | load factor less than $\lambda_c$. |
| $\lambda_c$ | maximum load factor. |
| $\lambda_g$ | required failure load factor under pure gravity forces. |
| $\lambda_F$ | required failure load factor under combined loads. |
| $\lambda_n$ | load factor in present cycle of calculations. |
| $\lambda_p$ | load factor in previous cycle of calculations. |
| $\Psi$ | ratio of column stiffness to restraining beam stiffnesses. |

## Acknowledgements

This investigation originally started at the University of Sydney under the guidance of H.B. Harrison and the general supervision of J.W. Roderick who is the head of the Department of Civil Engineering. It was subsequently completed at Fritz Engineering Laboratory, Department of Civil Engineering, Lehigh University, where L.S. Beedle is director and D.A. Van Horn is chairman. Resources made available by these two institutions are gratefully acknowledged.

## References

1. AISI Committee: Plastic Design of Braced Multistory Steel Frames. AISI, New York, 1968.
2. AISC: Manual of Steel Construction. American Institute of Steel Construction, 1970.
3. Cheong-Siat-Moy, F.: Automatic Plastic Analysis and Design of High Rise Steel Structures. Ph.D. Thesis, Department of Civil Engineering, Sydney University, Australia, March 1974.
4. Cheong-Siat-Moy, F.: Control of Deflections in Unbraced Steel Frames. Proceedings, Part 2, Paper No. 7718, Institution of Civil Engineers, England, December 1974, pp. 619-634.

5. DANIELS, J.H., and LU, L.W.: Plastic Subassemblage Analysis for Unbraced Frames. Journal of the Structural Division, ASCE, Vol. 98, No. ST8, Proc. Paper 9148, August 1972, pp. 1769-1788.
6. DE BUEN, O.: A Modification to the Subassemblage Method of Designing Unbraced Multistory Frames. AISC Engineering Journal, October 1969, pp. 138-146.
7. DRISCOLL, G.C., Jr., ARMACOST, J.O., and HANSELL, W.C.: Plastic Design of Multistory Frames by Computer. Journal of the Structural Division, ASCE, Vol. 96, No. ST1, Proc. Paper 6995, January 1970, pp. 17-33.
8. EL HAFEZ, M.B., and POWELL, G.H.: Preliminary Plastic Design of Tall Steel Frames. Journal of the Structural Division, ASCE, Vol. 100, No. ST 9, Proc. Paper 10796, Sept. 1974, pp. 1837-1850.
9. EMKIN, L.Z., and LITLE, W.A.: Plastic Design of Multistory Steel Frames by Computer. Journal of the Structural Division, ASCE, Vol. 96, No. ST 11, Proc. Paper 7689, Nov. 1970, pp. 2373-2388.
10. EMKIN, L.Z., and LITLE, W.A.: Storywise Plastic Design for Multistory Steel Frames. Journal of the Structural Division, ASCE, Vol. 98, No. ST 1, Proc. Paper 8675, January 1972, pp. 327-345.
11. LU, L.W., OZER, E., et al.: Effective Column Length and Frame Stability. Fritz Engineering Laboratory Report No. 375.2, Lehigh University, July 1975.
12. PARIKH, B.P.: Elastic-Plastic Analysis and Design of Unbraced Multistory Steel Frames. Fritz Engineering Laboratory Report No. 273.44, Lehigh University, May 1966.
13. POWELL, G.H., and EL HAFEZ, M.B.: Subassemblage Concept for Tall Frame Analysis. Journal of the Structural Division, ASCE, Vol. 100, No. ST 8, Proc. Paper 10739, August 1974, pp. 1611-1625.
14. TOAKLEY, A.R. et al.: Design Studies of Steel Buildings Proportioned by Plastic Theory. Institution of Engineers Conference on Metal Structures Research and Its Applications, Sydney, Australia, Nov. 1972.
15. WRIGHT, E.W.: Unbraced Multistory Steel Frames With Wind Loads. Journal of the Structural Division, ASCE, Vol. 98, No. ST 1, Proc. Paper 8633, January 1972, pp. 185-202.
16. YOSHIDA, H., and DANIELS, J.H.: Minimum Weight Design of Frames Using Sway Subassemblage Theory. Fritz Engineering Laboratory Report, No. 273.65, Lehigh University, January 1969.

## Summary

The use of subassemblage stiffness as the main variable can facilitate the satisfaction of both strength and stiffness constraints in the design of unbraced multistorey steel frames. Strength is merely considered as a function of detoriorating stiffness. As a design tool, the present treatment overcomes the limitations associated with the assumption of sways and collapse mechanism at failure, a feature generally present in conventional plastic design technics. It can control the individual stories to fail at pre-selected load factors resulting in a frame which is neither over-designed nor under-designed.

## Résumé

Le choix de la rigidité de sous-ensembles comme variable principale dans le calcul des ossatures métalliques en cadres non contreventés peut permettre de remplir plus facilement les conditions de résistance et de rigidité. La résistance y est considérée uniquement comme fonction de la diminution de rigidité. Comme outil de calcul, la méthode proposée permet d'éviter les limites associées à l'adoption de mécanismes de déplacements et de ruine, c'est-à-dire une caractéristique générale du calcul plastique conventionnel. On peut ainsi contrôler à la ruine chaque étage en admettant des facteurs de pondération choisis au préalable de façon à obtenir une ossature qui ne soit ni sur- ni sous-dimensionnée.

## Zusammenfassung

Die Wahl der Steifigkeit von Rahmeneinheiten als Hauptvariable beim Entwurf von seitlich verschieblichen stählernen Stockwerkrahmen kann die Erfüllung sowohl der Festigkeits- als auch der Steifigkeitsbedingungen vereinfachen. Die Festigkeit wird dabei lediglich als Funktion einer Steifigkeitsverminderung betrachtet. Als Entwurfsgrundlage vermeidet die vorliegende Behandlung die Begrenzungen, die mit der Annahme von Verschiebungs- und Versagensmechanismen gekoppelt sind, eine im normalen Traglastverfahren meistens vorkommende Erscheinung. Die einzelnen Stockwerke werden für im voraus gewählte Lastfaktoren auf Versagen so bemessen, dass der Rahmen weder über- noch unterbemessen ist.

Leere Seite
Blank page
Page vide

# Light Gauge Steel Folded Plate Construction

*Toits plissés formés d'éléments minces en acier*

*Faltwerke aus Stahlleichtprofilen*

J.M. DAVIES
BSc, PhD, MICE, MIStructE, CEng,
Reader in Civil Engineering,
University of Salford, England

F. THOMPSON
ARTCS, MSc, MIStructE, CEng,
Lecturer in Civil Engineering,
Bolton Institute of Technology, England

## Abstract

The alternative types of light gauge steel folded plate structures are briefly described and the current state of the art reviewed. Previous work in this subject, including a considerable number of actual structures, has been almost exclusively in the USA and has utilised welded construction. The fabrication of such structures using a single skin of corrugated sheeting and conventional sheeting fasteners such as self-tapping screws clearly presents an attractive possibility and the investigation described in this paper is directed towards demonstrating the viability of this approach.

The analysis and design of light gauge steel folded plates is dependent on the readily justifiable assumption that plate and slab action may be separated and revolves critically around the prediction of the behaviour of individual plate elements. An extensive test series, based on the full scale testing of a range of plate elements of 17.6 m span and 2.54 m depth is described and results for both strength and stiffness are compared with available theories. It is concluded that this form of design is readily and economically possible for spans up to and possibly exceeding 20-25 m. The limiting factors are shear buckling of the sheeting which is largely independent of the mode of fastening and deflection which is greatly influenced by the distribution of fasteners.

Various practical considerations are discussed including erection of folded plate roofs and the possibility of particularly favourable sheeting arrangements purpose-made for folded plate construction.

## Introduction

A typical light gauge steel folded plate roof is shown conceptually in Figure 1. Apart from gable framing the roof structure has only two primary elements, namely longitudinal fold line members and sheeting spanning between them. NILSON [1, 2]

showed some years ago that the design of such a structure could be attractively simple and as a result of his work a variety of folded plate structures have been built in the USA [3, 4, 5, 6].

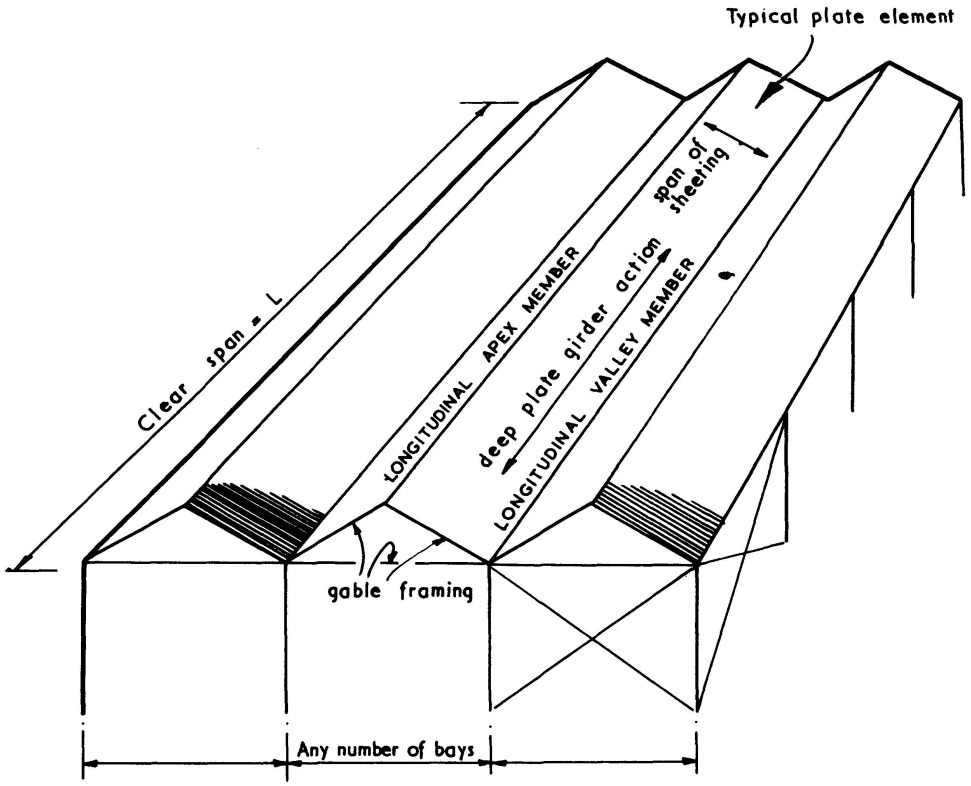


Fig. 1. Concept of Light Gauge Folded Plate Roof.

Little of fundamental importance has been added since Nilson's early investigations although FALKENBURG [7] has proposed some interesting alternative shapes and given detailed consideration to the connection between corrugated steel sheeting and the fold line members and SCHOELLER et al. [8] have utilised finite elements for light gauge steel folded plate analysis.

Nilson demonstrated a number of basic principles applicable to the design of light gauge steel folded plates, namely:

(1) Panels of corrugated steel sheeting span between fold line members so that uniformly distributed loads on the roof appear as line loads at the fold lines as far as overall behaviour is concerned. The almost complete lack of bending rigidity transverse to the corrugations means that the sheets span one way only; there is no redistribution of load along the panel.

(2) Line loads on the fold lines resolve themselves into in-plane loads on the two plate elements which meet at a given fold line. Out-of-plane bending stiffness of complete plate elements can be neglected when compared with the considerable in-plane stiffness so that it is merely necessary to resolve the line load into two components in the planes of the plates. A necessary consequence of the lack of out of plane stiffness is that both edges of each individual plate element

must be stiffened either by another plate element meeting at an appreciable angle or by some other means such as an edge beam or vertical cladding.

(3) It follows that the force system acting on an individual plate element is statically determinate and consists solely of an in-plane distributed load. Thus the basic design problem is as shown in Figure 2 and it is necessary to predict the strength and stiffness of such typical plate elements.

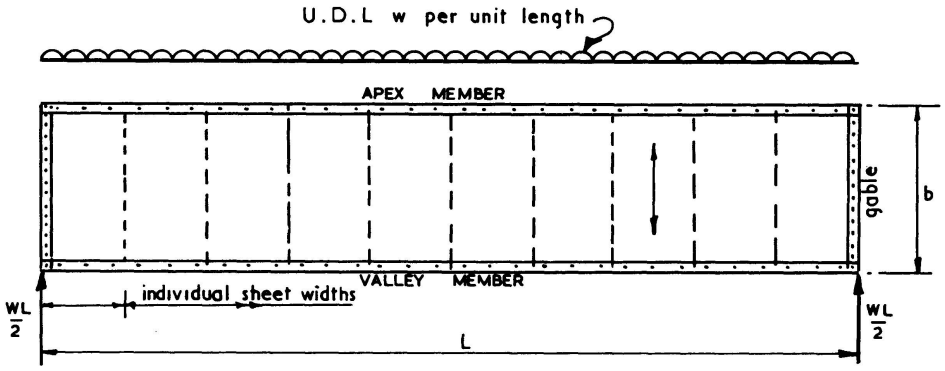


Fig. 2. Typical Plate Element.

(4) These in-plane forces give rise to bending moments and shear forces in the individual plate elements. The bending moments give rise to axial forces in the fold line members, the shear forces are carried entirely in the sheeting and the two effects may be considered independently.

Thus the complete roof acts as a series of interconnected deep plate girders spanning between gable framing which must be capable of carrying the roof loads to the foundations.

(5) Provided that the deflection of the individual plate elements can be estimated the deflection of the complete roof can be derived by considering simple displacement diagrams at the fold lines.

It may also be mentioned that a wide range of alternative structural arrangements are possible. For instance, although the simple saw-tooth arrangement is the most efficient other cross-sections are feasible such as those shown in Figure 3 and plate elements may be tapered giving rise to more interesting shapes such as the pleated dome shown in Figure 4.

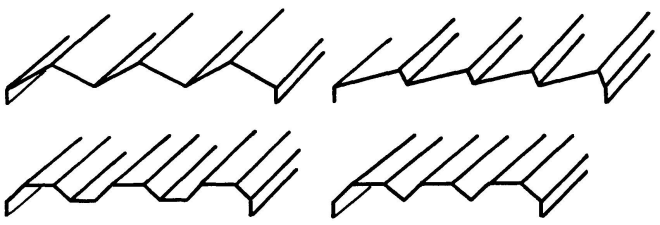

Fig. 3. Some Alternative Cross-sections for Folded Plate Structures.

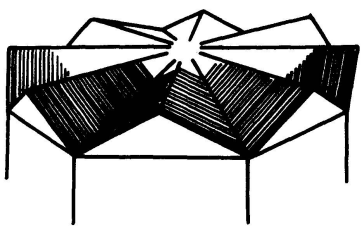

Fig. 4. Pleated Dome Structure.

Because many such structures exist, the principles underlying the use of light gauge steel sheeting as the shear-carrying component of a folded plate roof must be considered to be sound. However, previous practice has typically utilised welded construction with a double skin of sheeting resulting in an extremely stiff and strong structure in which neither distortions or deflections are usually significant.

No attempt has previously been made to form the plate elements more economically by applying the constructional practice which is more conventional in Britain, namely using a single skin of corrugated steel sheeting with discrete fasteners such as fired pins or self-tapping screws. The investigation reported in this paper is part of a program of research which is being carried out in order to establish the feasibility of this latter form of construction and to demonstrate that both the strength and the stiffness of such folded plate roofs may be predicted from simple expressions. As the crucial factor is the in-plane behaviour of individual plate elements, the investigation has concentrated to date on this aspect which is more readily amenable to full-scale laboratory investigation.

Expressions for the flexibility and strength of individual plate elements subjected to uniformly distributed load have been derived and justified by finite element analysis [9]. They have also been compared [9] with the results of tests on plate elements of very thin sheeting (0.46 mm thickness and 19 mm depth). Very good correlation of experimental and theoretical deflections was obtained but it was only possible to obtain very limited information regarding failure loads as a result of the very low buckling capacity of the sheeting used.

This paper describes how the test series was continued using a stronger sheeting which is typical of the lightest sheeting likely to be used in practice. The test arrangement, which simulated the uniformly distributed load by a series of point loads, is first described. The appropriate forms of the design expressions for this form of loading are then given, thus enabling a comparison of experimental and theoretical results to be made.

Finally some of the practical issues involved in the design and construction of complete folded plate structures are considered. It is concluded that such structures are a most attractive possibility both aesthetically and economically and that spans in excess of 20 metres are readily possible using conventional sheeting and fasteners.

## Tests on Full Scale Panels

In order to initiate this test series, a specific situation was considered and a plate element chosen as a typical element of a complete folded plate roof as shown in Figure 1. In order to suit the fixing points in the laboratory floor, the dimensions shown in Figure 5 were adopted. It was assumed that the roof slope was 36.9° (3-4-5 triangle) and that the total vertical loading on the roof was 0.7 kN/m$^2$. For this loading, British Steel Corporation "Longrib 700" sheeting was adequate to span simply supported between the fold line members and was adopted for the tests. The profile of this sheeting was as shown in Figure 6. The sheeting was galvanised and had a total thickness of 0.7 mm. The net thickness was taken to be 0.66 mm for the purpose of theoretical comparison. The sheeting was fixed with seams in the crests of the corrugations.

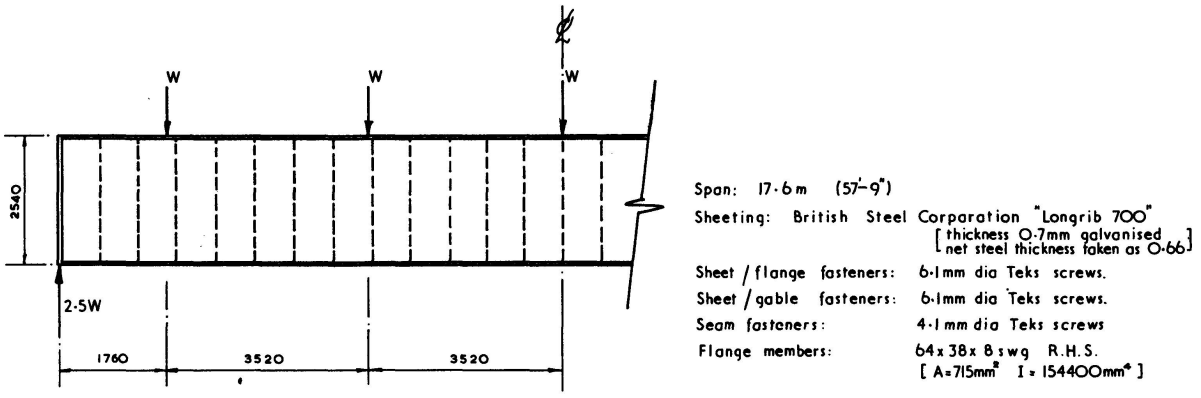


Fig. 5. General Arrangement of Test Panels.

In order to facilitate the loading of the test panel by five hydraulic jacks simulating the uniformly distributed load, the flange members were chosen from the available range of rectangular hollow sections. 64 mm × 38 mm × 8 SWG (2½" × 1½") RHS were found to be adequate to carry the flange forces and were adopted. With the benefit of hindsight it is evident that more useful information regarding failure loads would have been obtained if a section with greater resistance to local bending from the jack forces had been chosen. Even with spreader beams and flexible packing there was a tendency for extensive local distortion in the vicinity of the jacks to occur before the failure load of the panel could be attained. Thus although a total of nine different tests were carried out only two of these were carried through to failure the remainder being either confined to the working load range or terminated before failure due to excessive local distortion at the loading points.

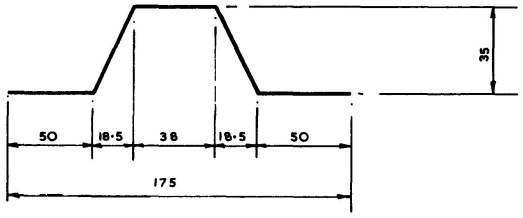


"LONGRIB 700" SHEETING PROFILE [dimensions in mm]

Fig. 6. "Longrib 700" Profile.

With the dimensions and details described above, the working load was 8.4 kN per jack. Tests were carried out using a variety of arrangements of fasteners giving (with the exception of test No. 8) theoretical factors of safety against fastener failure of the order of 2.0 and giving a reasonable range of panel flexibilities. The entire test series is described in table 1, the meaning of the symbols defining the fastener arrangements being shown in Figure 7 and Appendix A.

Figure 8 shows a typical test in progress. It may be observed that the compression flange was prevented from buckling laterally by suitable restraints incorporating needle bearings to eliminate friction. The only measurements taken during loading were deflection readings opposite the loading points.

*Table 1. Summary of fastener arrangements and experimental results*

| Test Number | Pitch of flange fasteners (mm) $p_1$ | $p_2$ | $p_3$ | Number of gable fasteners $n_{sc}$ | Number of seam fasteners $n_1$=2 $n_{s1}$ | $n_2$=5 $n_{s2}$ | $n_3$=5 $n_{s3}$ | Test Results: Central deflection (mm) | Ultimate Load (kN) | Theoretical Predictions: Initial Deflection (mm) | Reloading Deflection (mm) | Ultimate load (kN) and mode of failure |
|---|---|---|---|---|---|---|---|---|---|---|---|---|
| 1 | 175 | | | 18 | 24 | | 12 | 2.13 / 1.63 | | 1.94 | 1.76 | |
| 2 | 175 | | | 18 | 24 | | 6 | 1.64 | | 1.97 | 1.77 | |
| 3 | 175 | | | 18 | 24 | 16 | 6 | 1.73 / 1.84 | 16.1 | 2.01 | 1.78 | 18.1 (seam a-b) |
| 4 | 175 | | | 10 | 24 | 16 | 6 | 1.71 | | 2.02 | 1.78 | |
| 5 | 175 | | 350 | 10 | 24 | 16 | 6 | 2.31 | | 2.81 | 2.57 | |
| 6 | 175 | 350 | | 10 | 24 | 16 | 6 | 4.54 | | 5.22 | 4.94 | |
| 7 | 175 | 350 | 525 | 10 | 24 | 16 | 6 | 5.18 | | 6.27 | 5.97 | |
| 8 | 350 | | | 10 | 24 | 16 | 6 | 6.30 / 5.07 | | 7.22 | 6.91 | |
| 9 | 175 | | | 10 | 49 | 26 | 12 | 1.64 | 16.7 | 1.92 | 1.76 | 17.8 / 14.2 (tension flange fasteners) |

(Note: central deflections are per unit jack load, ultimate loads are load per jack)

In each test, load was applied in increments of 1 kN at each jack and deflection readings taken. The load deflection curves were linear up to the working load and from the slope of these curves the test results for central deflection given in table 1 were obtained.

Two tests were continued to failure. In test 3 a seam failure was obtained adjacent to the left hand support as shown in Figure 9. In test 9, the tension flange fasteners tore first followed immediately by buckling of the sheeting as shown in Figures 10 and 11. The excessive number of seam fasteners shown in Figure 11 served solely to ensure that a different mode of failure to that of test 3 was obtained.

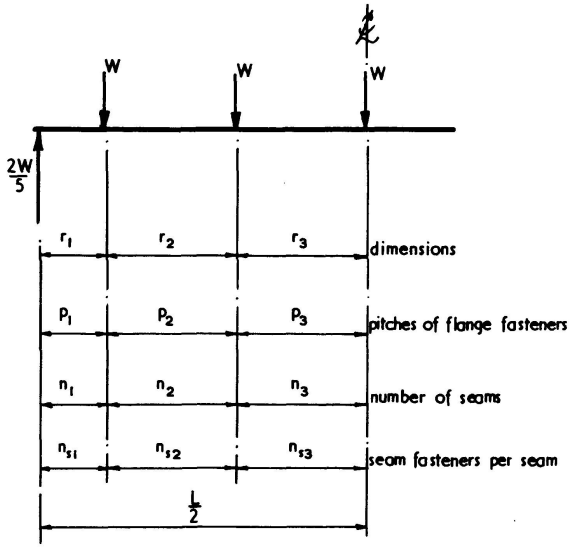


Fig. 7. General Arrangement of Fasteners for Theory.

*Table 2. Factors for distribution of flange fastener forces*

| $n_f$ | $g_1$ seam fasteners in crests | $g_1$ gable fasteners in troughs |
|---|---|---|
| 2 | 0.13 | 1.00 |
| 3 | 0.30 | 1.00 |
| 4 | 0.44 | 1.04 |
| 5 | 0.58 | 1.13 |
| 6 | 0.71 | 1.22 |

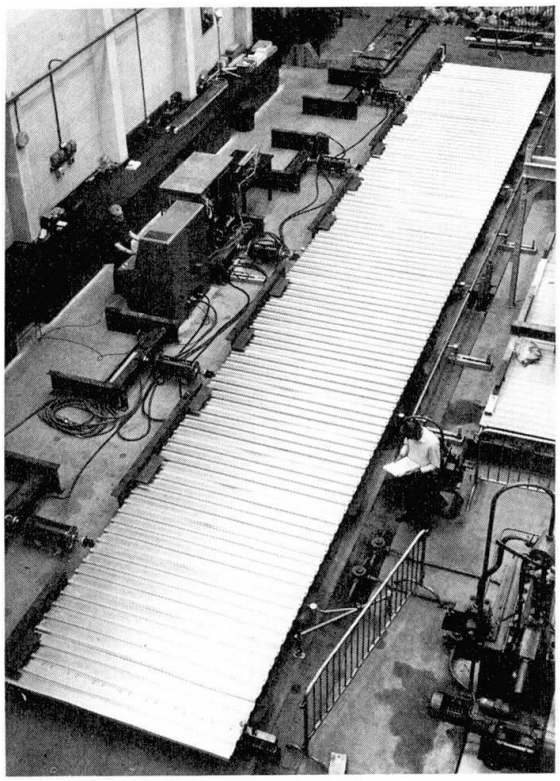

Fig. 8. Typical Test in Progress.

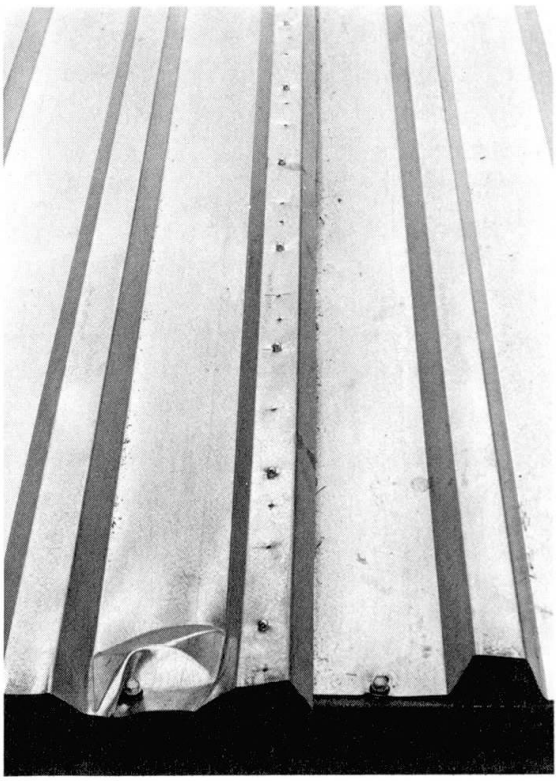

Fig. 9. Seam Failure – Test 3.

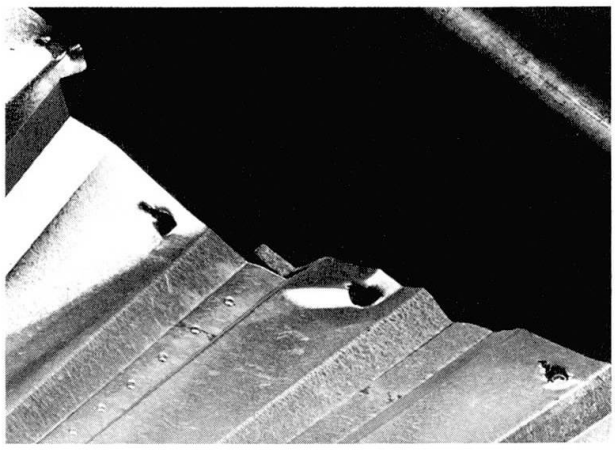

Fig. 10. Tearing of Flange Fasteners – Test 9.

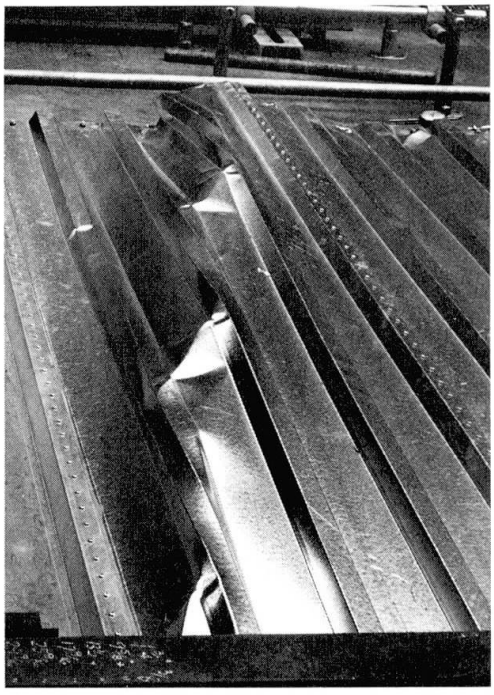

Fig. 11. Illustrating Overall Buckling Following Fastener Failure – Test 9.

It may be noted that in table 1, two values of deflection are given for tests 1, 3 and 8 each of which was repeated. It has been found that during the testing of both shear diaphragms and folded plate elements the initial loading is always more flexible than subsequent loadings as a consequence of fasteners "bedding in". This effect is very noticeable in reloading tests on individual fasteners. The higher of the two central deflection results shown for tests 2 and 8 were both obtained for panels that had been completely refastened before the test and therefore represent the only genuine results for initially unloaded panels. The remaining results all reflect some degree of prior loading. In order to accommodate this state of affairs, theoretical predictions based on both the initial and reloading flexibility of the fasteners are included in table 1. It can be seen that the difference is not marked as much of the theoretical flexibility is in the distortion of the corrugation profile and in axial strain in the flange members, fastener flexibility playing a comparatively minor role.

## Theoretical Expressions for Strength and Deflection

As the light gauge folded plate structure offers an efficient means of spanning considerable distances, one of the prime objectives of the design process must be the accurate prediction of deflections which often tend to be large when light loadings are carried over long spans. The expressions that follow are more readily derived from the work of BRYAN [10] on shear diaphragms as subsequently modified by the author [11] than from the expressions for plates subject to uniformly distributed loading [9]. They are derived by considering assumed internal force distributions which have been found to be very close to those found by comprehensive finite element analysis and have given very good results for shear diaphragms.

Expressions for failure load arise directly out of the assumed internal forces. Expressions for deflection arise by assuming that the total deflection to be the sum of the following components which may be considered separately:

$d_{1.1}$ distortion of the corrugation profile of the sheeting.
$d_{1.2}$ shear strain in the sheeting.
$d_{1.3}$ bending action causing axial strains in the flanges.
$d_{2.1}$ slip in the sheeting/flange fasteners.
$d_{2.2}$ slip in the seam fasteners.
$d_{2.3}$ slip in the sheeting/gable member fasteners.

The detailed derivations will not be given as in most cases the expressions can be written down directly, the only exception being $d_{1.3}$ which requires some elementary structural mechanics. The notation used is defined in Appendix A and appropriate numerical values for the test series are given there.

### *Expressions for Strength*

The expressions that follow arise from the consideration of various possible failure modes. The ultimate load of the structure is the lowest ultimate load obtained when all possible modes of failure are considered.

*Sheet/flange Fastener Failure*

$$W_{ult} = \frac{0.32\ bF_p}{p}$$

This expression incorporates an empirical reduction factor of 0.8 to allow for the influence of prying action at the fasteners as described in detail by FALKENBURG [7]. In the evaluation of the failure load for test 9, as shown in table 1, values with and without this factor are given for comparison purposes.

*Seam Failure*

$$W_{ult} = \frac{(n_s s + g_1 s_s) F_s}{2.5\ s}$$

In this expression, $g_1$ is a tabulated factor for the distribution of sheet/flange fastener forces and is given for the case of "sheeting" (seam fasteners at the crest of the corrugations) in Table 2. The full significance of this factor is described in reference 9.

*Gable Fastener Failure*

$$W_{ult} = \frac{(n_{sc} s + 2g_1 s_{sc})}{(n_{sc} s + 2s_{sc})} \frac{(n_{sc} F_{sc} + 2F_p)}{2.5}$$

In this expression, the appropriate value of $g_1$ is that for "decking" (fasteners in the troughs of the corrugations) and is again given in Table 2.

*Buckling Failure of Sheeting*

Hlavecek's theory [12] has been found easiest to use but has generally appeared to require an arbitrary reduction factor ($\geq 0.65$) when applied to discretely fastened folded plate elements. As it is not directly relevant to the interpretation of the test results the appropriate expressions will not be reproduced herein.

*Expressions for Deflection*

The central deflection is found by summing the components $d_{1.1}$ to $d_{2.3}$.

*Deflection due to Distortion of the Corrugation Profile of the Sheeting*

$$d_{1.1} = \frac{0.144\ d^4}{Et^3 b^3} (2.5\ K_1 r_1 + 1.5\ K_2 r_2 + 0.5\ K_3 r_3)\ W$$

In this expression, $r_1$, $r_2$, $r_3$ are the dimensions of the regions of constant shear between the loads as shown in Figure 7 and $K_1$, $K_2$, $K_3$ are the corresponding values of the sheeting constant K which depends critically on the pitch of the

sheet/flange fasteners. The appropriate values of K were obtained by finite element analysis over the correct sheet length and incorporating the influence of the supporting members [13]. The values used in the theoretical comparisons in table 1 were:

every corrugation fastened (p = 175) K = 0.54;
alternate corrugations fastened (p = 350) K = 3.77;
every third corrugation fastened (p = 525) K = 8.01.

*Deflection due to Shear Strain in the Sheeting*

$$d_{1.2} = \frac{2(1+\nu)(1+2h/d)}{Etb}(2.5\, r_1 + 1.5\, r_2 + 0.5\, r_3)\, W$$

*Deflection due to Axial Strain in the Flanges*

$$d_{1.3} = \frac{0.132\, L^3 W}{E\, A\, b^2}$$

*Deflection due to Slip in the Sheeting/flange Fasteners*

$$d_{2.1} = \frac{2s}{b^2}(2.5\, p_1 r_1 + 1.5\, p_2 r_2 + 0.5\, p_3 r_3)$$

*Note.* s represents the slip per unit load of the sheet/flange fasteners. Typical fastener slip characteristics for a series of simple lap joints in a similar thickness non-galvanised m.s. sheet are shown in Figure 12. The method of extracting s from these curves is [9] to take the average slip at half the average ultimate load leading to the nominal average slip of 0.076 mm/kN shown on the figure. Similar results for other thicknesses of sheet suggest that this may have been an unusually stiff value and a value of 0.15 mm/kN was used in the theoretical comparisons representing a reasonable upper limit of fastener flexibility. Based on a number of fastener reloading tests a lower limit of 0.01 mm/kN was also included in the theoretical comparisons.

*Deflection due to Slip in the Seam Fasteners*

$$d_{2.2} = s_s s \left(\frac{2.5\, n_1}{n_{s1} s + g_1 s_s} + \frac{1.5\, n_2}{n_{s2} s + g_1 s_s} + \frac{0.5\, n_3}{n_{s3} s + g_1 s_s}\right)$$

*Note.* Similar considerations apply to $s_s$, the slip per unit load at the seam fasteners, as were discussed for s above. Figure 13 shows typical characteristics for a similar non-galvanised sheet thickness. The values adopted for theoretical comparison were $s_s = 0.15$ mm/kN (initial loading) or 0.05 mm/kN (reloading).

*Deflection due to Slip in the Gable Fasteners*

$$d_{2.3} = \frac{2.5\, s_{sc} s}{n_{sc} s + 2 g_1 s_{sc}}$$

*Note.* Gable fasteners were identical to sheet/purlin fasteners so that: $s_{sc} = 0.15$ mm/kN (initial loading) or 0.01 mm/kN (reloading).

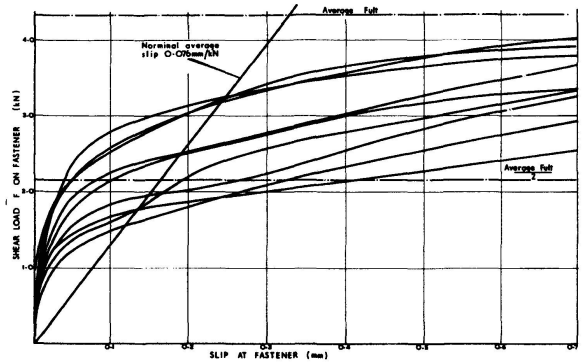


Fig. 12. Fastener Slip Characteristics for Barber Colman ¼-14 Tek Fasteners in 0.76 mm Thick Non-galvanised M.S. Sheet.

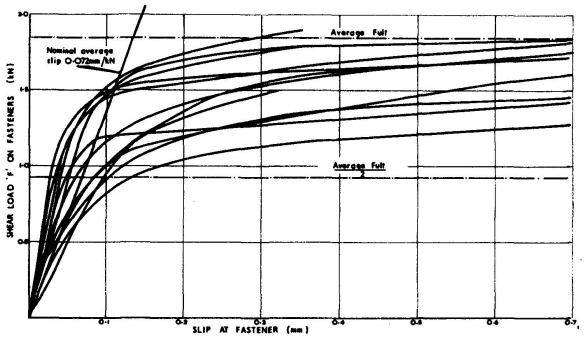


Fig. 13. Fastener Slip Characteristics for Barber Colman No. 8 Tek Fasteners in 0.76 mm Thick Non-galvanised M.S. Sheet.

*Fastener Ultimate Loads*

From a series of tests similar to those giving rise to Figures 12 and 13 the following values were adopted in calculating theoretical ultimate loads:

| | |
|---|---|
| for sheet/flange fasteners | $F_p = 3.83$ kN |
| for seam fasteners | $F_s = 1.85$ kN |
| for sheet/gable fasteners | $F_{sc} = 3.83$ kN |

## Comparison of Experimental and Theoretical Results

The complete comparison summarising both deflection and strength is shown in table 1.

In almost every test, the experimentally obtained flexibilities fall slightly below the theoretical values, even when the reloading value of fastener flexibility is used. The differences become proportionally greater as the panels become more flexible. As this additional flexibility is due almost entirely to the increase in sheet distortion when the ends of the sheeting are fastened in alternate or every third corrugation, it may be concluded that the theoretical flexibilities used for these cases are on the high side. The reason for this is not completely clear and is under investigation. As any discrepancy is on the safe side it may be concluded that it is readily possible to predict adequately the deflections of discretely fastened folded plate roofs.

Relatively limited information is available regarding failure loads. The seam failure (test 3) was about 11% low which may well represent a slight deficiency in self-drilling self-tapping screws, when used in thin-to-thin connections at the thinner end of the range of sheeting thicknesses [9]. The sheet/flange fastener failure (test 9) lay between the limits of no reduction in strength due to prying action and the 20% reduction advocated for normal sheeting profiles [9] and this must be regarded as a satisfactory test result. The predicted buckling load was a value greater than 18.1 kN per jack and the mode of failure for test 9 may suggest that buckling was about to take place at a load not greatly in excess of the maximum achieved of 16.7 kN.

There is room for more test results for failure loads but it is already clear that all failure modes can be predicted with reasonable accuracy for failure at the gable fasteners cannot have any independent significance.

## Erection of folded plate roofs

Up to date, the conventional method of erection has involved piecemeal erection on light internal scaffolding [4]. This is necessarily an expensive method and it may well be cheaper to build the roof either in its entirety or in sections on the ground and then to jack it into position using climbing jacks on the gable columns. A similar method was adopted for the hypars of the well known jumbo jet hangars [14] with great success. The lightness of construction would suggest that such an approach should prove ideal for more conventional folded plate structures and is to be adopted for prototype tests on a 21.6 m span folded plate roof at the University of Salford during 1976.

## Some Practical Considerations in the Design of Folded Plate Roofs

### *Alternative Sheeting Arrangements*

It must be recognised that conventional roof sheeting has a significant drawback when used in the context of light gauge steel folded plate construction. The cover width of commercially available sheets is generally less than one metre and as a result of considerable number of heavily loaded seams have to be fastened. This state of affairs suggests that there may be more satisfactory arrangements available, possibly with purpose made components. A number of alternative arrangements are recognised at this stage:

(a) *Wider sheets*

If the sheeting is formed in a press brake with the corrugations running across the width of the coil unlimited lengths of sheeting would become available. Coil widths currently available are rather restrictive and only relatively narrow plates could be made in this way at present. However it is possible that available coil widths may increase and with coil widths of 2 metres or more folded plate elements well within the practical range could be made far more efficiently.

(b) *Sheets formed in a dishing press*

Conventional corrugated steel sheeting has further disadvantages when applied to folded plate work which may be readily overcome using the purpose-made form of sheeting illustrated in Figure 14. In Figure 14 the corrugations do not continue to edge of the sheet but are pressed out of the flat sheet in a manner more familiar in radiator panels. The corrugations can here run along the length of the coil or, more advantageously as in (a) above, run transverse to the length.

This arrangement has the advantage of almost completely eliminating the significant component $d_{1.1}$ of the deflection due to profile distortion and also avoids the problem with sheet/flange fasteners mentioned in section 4.3. Furthermore, weatherproofing at the fold lines is greatly simplified if fluted edges are avoided in this way.

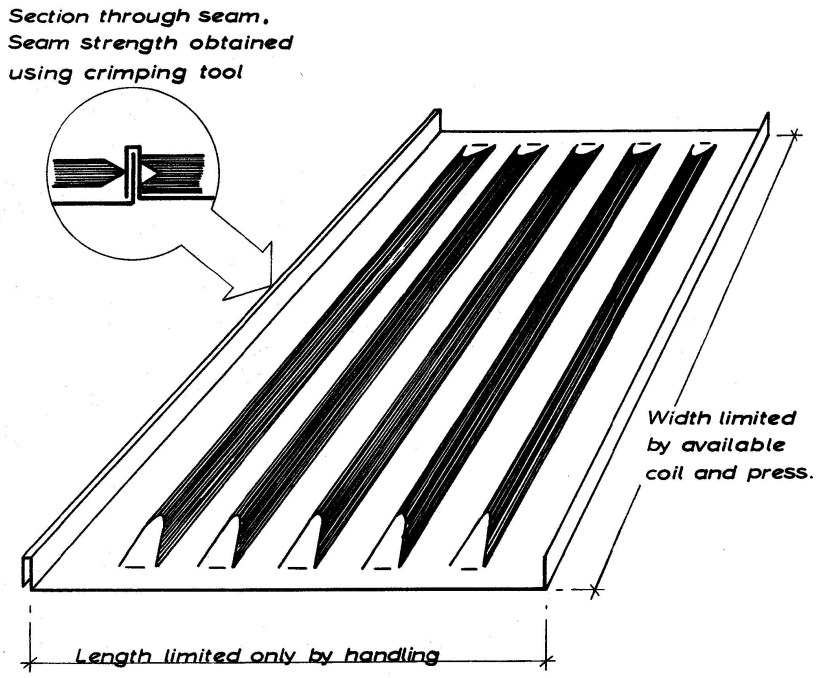


Fig. 14. Ideal Arrangement of Sheeting for Folded Plate Construction.

(c) *Alternative ways of forming seams*

The work reported in this paper has demonstrated that in the current state of the art fastening the seams between a large number of individual sheet widths may form a significant part of the fabrication process. Furthermore, self-tapping or self-drilling/self tapping screws have been found to be somewhat suspect in thin to thin connections where the individual sheet thicknesses are themselves at the thinner end of the practical range. This suggests that there may be better ways of making the seam connection than were used in the tests described previously particularly bearing in mind the necessity that the seams should be weather proof.

One possibility is also illustrated in Figure 14 where the seams are made weather-proof by forming a tight fold in one sheet covering an upstand in the adjacent sheet. Seam strength is obtained by crimping the three sheet thicknesses together using a specially designed tool. Other variations on this theme, which is being currently investigated at the University of Salford, are possible.

(d) *Sheeting running parallel to span*

The advantages of possibilities (a), (b) and (c) can be gained in an alternative way by providing light cross-members spanning between the fold lines and treating the sheeting as decking spanning over these cross-members. This requires a separate weatherproof membrane over the sheeting and it is a matter for the designer to decide whether the advantages outweigh the cost of the cross-members and weatherproofing. This possibility has been considered by THOMPSON [15] and will be discussed in more detail in a subsequent paper.

*Control of Deflections*

The deflections of folded plate roofs of span 15-20 metres or more are frequently significant. The dominant components of the total deflection are $d_{1.1}$ (distortion of the corrugation profile) and $d_{1.3}$ (axial deformation of flange members). Slip of fasteners is not usually of great significance. It follows that the most effective way to reduce deflection in an otherwise satisfactory design is to try to reduce $d_{1.1}$ either by fastening the ends of the sheets in every corrugation if this has not already been done or by using sheets formed in a dishing press as described in section 6(b). Alternatively the alternative arrangement mentioned in 6(d) may be considered.

Another effective way of reducing deflections is to increase the cross-sectional area of the fold-line members and this is often the main recourse when corrugation distortion has been minimised.

## Safety and Economy

In order to be able to ensure the safety of this relatively novel form of construction it is necessary to be able to predict all the likely failure modes and to associate with each an accurate ultimate load. It is to this end that the tests described in this paper and in references 9 and 15 were carried out and it is now clear that the behaviour of individual folded plate elements is well understood. This test programme will conclude, probably in 1976, with the full scale test to destruction of a complete roof structure measuring 21.6 metres span by 10.8 metres wide. This test is under preparation at the University of Salford and it is considered that its successful completion will open the way to the much more extensive use of light gauge steel folded plate roofs by British and European designers.

The economic advantages of light steel folded plate construction are intuitively obvious but have not yet been subject to a rigorous investigation. One reason for this is the significance of the erection procedure and it is considered desirable to demonstrate the successful erection of a prototype structure before evaluating its economic advantages. Nevertheless it is already clear that over a wide range of spans a considerable saving in material is possible using light gauge folded plate construction as compared with alternative methods of covering the same span. It is also clear that single skin construction with discrete fasteners is considerably cheaper than the alternative welded configurations while, at the same time, possessing adequate stiffness.

## Conclusions

Light gauge steel folded plate construction utilising a single skin of corrugated steel sheeting and discrete fasteners has been shown to be a viable method of construction for medium span roofs. The maximum spans possible will normally be limited by buckling and probably lie in the range 20-25 metres in the current state of the art.

There is scope for the development of alternatives to the utilisation of conventional roof sheeting and fasteners and some of these have been mentioned in the paper. It is clear that the efficiency of this form of construction will increase as further development takes place but it is considered that development has now reached the point where practical exploitation is possible and desirable.

## Notation

*Note.* This notation is chosen to accord with that adopted by Bryan for shear panels (10).

| | |
|---|---|
| A | cross-sectional area of flange member (715 $mm^2$). |
| b | depth of folded plate element (2540 mm). |
| d | pitch of corrugations (175 mm). |
| $d_{1.1}$, etc. | components of total deflection at centre of plate element (mm). |
| E | modulus of elasticity of steel (207 kN/$mm^2$). |
| $F_p$ | ultimate load of individual sheet/flange fastener (3.83 kN). |
| $F_s$ | ultimate load of individual seam faster (1.85 kN). |
| $F_{sc}$ | ultimate load of individual sheet/gable fastener (3.83 kN). |
| $g_1$ | factor to allow for number of sheet/flange member fasteners per sheet width (see table 2). |
| h | height of corrugations (35 mm). |
| K | constant for sheet distortion = 0.54 (p = 175 mm), 3.77 (p = 350 mm) or 8.01 (p = 525 mm). |
| L | span of folded plate element or roof (17600 mm). |
| n | number of seams in region of plate element between adjacent loads (see table 1). |
| $n_f$ | number of sheet flange fasteners per flange per sheet width. |
| $n_s$ | number of seam fasteners in each seam (see table 1). |
| $n_{sc}$ | number of gable fasteners at each gable (see table 1). |
| p | pitch of sheet/flange fasteners (mm – see table 1). |
| $r_1$, etc. | lengths of panel associated with different fastener pitches ($r_1$ = 1760 mm, $r_2$ = 3520 mm, $r_3$ = 3520 mm). |
| s | slip per sheet/flange fastener (0.01 – 0.15 mm/kN). |
| $s_s$ | slip per seam fastener (0.05 – 0.15 mm/kN). |
| $s_{sc}$ | slip per gable fastener (0.01 – 0.15 mm/kN). |
| t | net steel thickness (0.66 mm). |
| W | jack load (working value 8.4 kN per jack). |
| v | poisson's ratio (0.25). |

## References


1. NILSON, A.H.: Folded plate structures of Light Gauge Steel. Proc. ASCE, J. Struct. Div., Vol. 88, ST5, Oct. 1962.
2. NILSON, A.H.: Steel Shell Roof Structures. AISC Jnl., Vol. 3, No. 1, Jan. 1966.
3. Folded Plate Design (design manual). H.H. Robertson Company, Pittsburgh, 1967.
4. Folded Plate Metal Roof Tops New School. Building Construction, April 1965.
5. MARTINEZ, M.E.: Library on a Shoe String Budget. Modern Steel Construction, 3rd Quarter 1965.
6. Cost Control for Education Facilities. Building Construction, Sept. 1966.
7. FALKENBERG, J.C.: Shell and Folded Plate Roofs of Corrugated Sheet Steel Panels. Norwegian Building Research Institute, Oslo, 1972.
8. SCHOELLER, W.C., PIAN, R.H.J. and LUNDGREN, H.R.: Cold Formed Folded Plate Structures. Proc. 1st Speciality Conf. Cold-Formed Steel Structs, Rolla Missouri, Aug. 1971.
9. DAVIES, J.M.: Light Gauge Steel Folded Plate Roofs. University of Salford Report, Ref. No. 75/58, Jan. 1975.
10. BRYAN, E.R.: The Stressed Skin Design of Steel Buildings. Crosby Lockwood Staples, London, 1972.
11. DAVIES, J.M.: The Design of Shear Diaphragms of Corrugated Steel Sheeting. University of Salford Report, Ref. No. 74/50, Sept. 1974.

12. HLAVACEK, V.: Shear Instability of Orthotropic Panels. ACTA Technica CSAV, No. 1, 1968.
13. DAVIES, J.M. and LAWSON, R.M.: The Shear Flexibility of Corrugated Steel Sheeting. Proc. 3rd Speciality Conf. Cold-formed Steel Structs., Rolla Missouri, Nov. 1975.
14. THORNTON, C.H. and TOMASETTI, R.L.: Hangar Features Stressed Skin Hypars. Civil Engineering, ASCE, Nov. 1970.
15. THOMPSON, F.: The Design Development of Light Gauge Steel Folded Plate Structures. MSc Thesis University of Salford, 1974.

## Summary

This paper is concerned with the design of light gauge steel folded plate structures in which the plate elements comprise a single skin of corrugated steel shetting fastened together and to fold line members by discrete fasteners such as self tapping screws or blind rivets. An extensive test series on individual plate elements of 17.6 m span is described and the results compared with available theories. Various practical factors are also discussed.

## Résumé

La contribution est consacrée à l'étude des toits plissés en éléments métalliques minces. Les versants sont formés d'une seule tôle formée à froid, la fixation entre les tôles elles-mêmes d'une part et avec les barres d'arête d'autre part étant réalisée par des vis autotaraudeuses ou par des rivets aveugles. Les auteurs décrivent une importante série d'essais portant sur des éléments de versant de 17,6 m de portée; ils comparent les résultats aux théories existantes. On discute également divers facteurs d'importance pratique.

## Zusammenfassung

Die Autoren behandeln den Entwurf von Faltwerken aus Stahlleichtprofilen, bei denen die Scheibenelemente aus einer einzigen Lage profilierter Stahlbleche bestehen. Selbstschneidende Gewindeschrauben oder Blindniete dienen zur Befestigung sowohl der Bleche unter sich als auch der Bleche mit den Kantengliedern. Es wird eine ausgedehnte Versuchsreihe an einzelnen Scheibenelementen von 17,6 m Spannweite beschrieben, wobei die Ergebnisse mit vorhandenen Theorien verglichen werden. Ferner diskutieren die Autoren verschiedene Faktoren von praktischer Bedeutung.

# Eléments spatiaux de barres courbes

*Räumlich gekrümmte Balkenelemente*

*Space-curved Rod Elements*

M.-H. DERRON J. JIROUSEK, Dr es sc.
Professeurs à l'Ecole polytechnique fédérale de Lausanne, Suisse

## Introduction

Bien que la méthode des éléments finis soit aujourd'hui très élaborée dans le domaine des milieux continus (parois, dalles, coques, structures massives), il n'a été accordé jusqu'ici que relativement peu d'attention à l'étude de systèmes comprenant des éléments spatiaux de barres courbes. Le champ d'application des études antérieures (voir [7] par exemple) est le plus souvent limité par de sérieuses restrictions d'ordre géométrique. Dans notre étude, nous avons cherché à développer des éléments très généraux satisfaisant les conditions suivantes:

— La géométrie de l'élément doit permettre de réaliser avec une précision suffisante une courbe axiale aussi compliquée qu'on le désire et un taux quelconque de variation de la section le long de l'axe. Par ailleurs, il faut pouvoir tenir compte de l'excentricité éventuelle des nœuds par rapport à l'axe de l'élément.

— En vue de l'application au calcul des coques nervurées, le développement de la matrice de rigidité de l'élément doit être basé sur la méthode directe des rigidités plutôt que sur l'inversion de la relation déplacements-forces. Un choix convenable de fonctions paramétriques de déplacements généralisés permettra de satisfaire automatiquement les conditions de continuité aux interfaces des éléments.

— L'élément doit s'appliquer sans restrictions à tous les rapports entre la hauteur de la section et la longueur de la barre. En plus des déformations dues aux moments fléchissants et aux moments de torsion, il doit par conséquent tenir compte également des déformations dues aux efforts normaux et aux efforts tranchants.

Ci-après, nous proposerons deux familles d'éléments spatiaux courbes du type superparamétrique. La première est une famille d'éléments de section rectangulaire qui peut être représentée avec un minimum de données. La seconde est une famille d'éléments de section quelconque, pour autant que le centre de torsion de cette dernière se confond (au moins approximativement) avec le centre de gravité.

## 1. Considérations géométriques

### *1. Définition d'une famille d'éléments de section rectangulaire variable*

La figure 1 montre deux membres typiques de la famille d'éléments étudiée dans ce paragraphe. Chaque élément sera défini par une correspondance biunivoque entre les coordonnées globales x, y, z et les coordonnées curvilignes $\xi$, $\eta$, $\zeta$. En pratique, il est commode d'établir ces relations de telle façon que les coordonnées $\xi$, $\eta$, $\zeta$ varient entre $-1$ et $+1$ sur les diverses faces de l'élément (voir figures 1Ab et 1Bb, où l'on a choisi pour des raisons pratiques des échelles différentes pour la coordonnée $\xi$ et les coordonnées $\eta$ et $\zeta$).

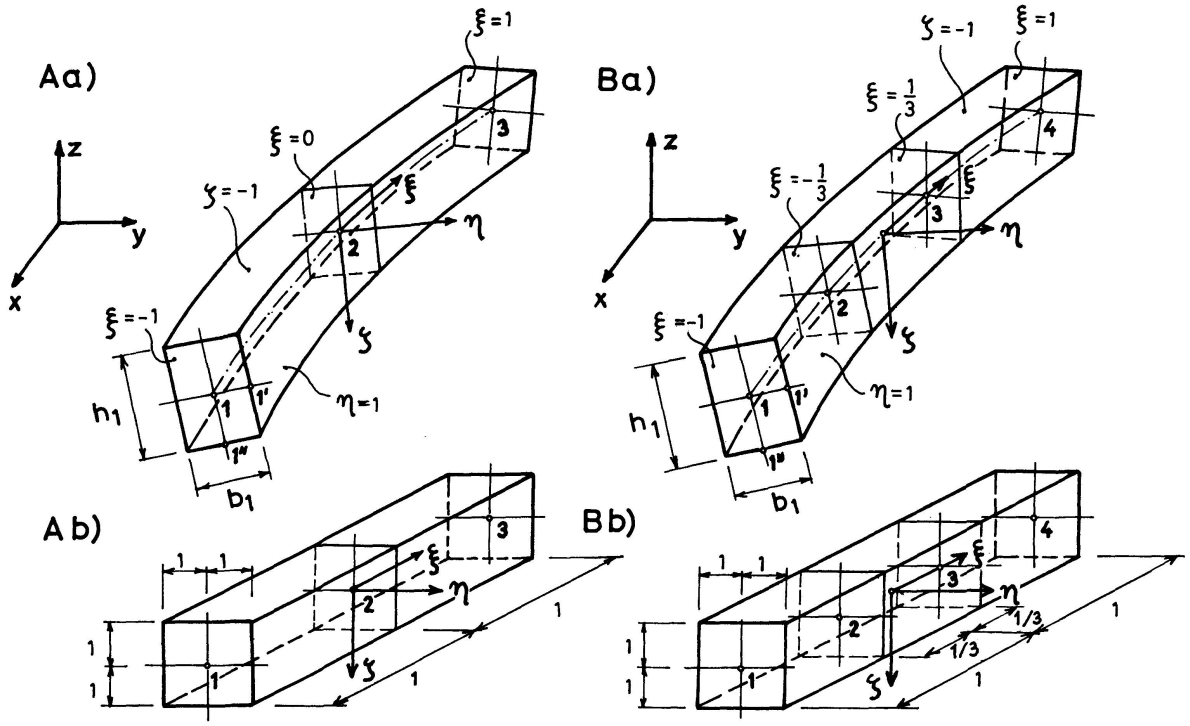


Fig. 1. Deux membres de la famille d'éléments spatiaux de barres courbes de section rectangulaire variable (a) obtenus par distorsion de leurs éléments de base (b): élément quadratique (A), élément cubique (B).

Pour définir l'axe de l'élément dans l'espace, on fixera sur cet axe un certain nombre de nœuds L = 1, 2 ... M, répartis plus ou moins régulièrement, et on fera passer par ces points une fonction d'interpolation. En désignant par $x_o$, $y_o$ et $z_o$ les coordonnées globales de l'axe, on peut par exemple écrire:

$$\begin{Bmatrix} x_o \\ y_o \\ z_o \end{Bmatrix} = \sum_{L=1}^{M} N_L(\xi) \begin{Bmatrix} x_L \\ y_L \\ z_L \end{Bmatrix}, \tag{1}$$

où les fonctions de base $N_L(\xi)$ sont représentées par des polynômes de Lagrange:

$$N_L(\xi) = \frac{(\xi-\xi_1)(\xi-\xi_2)\ldots(\xi-\xi_{L-1})(\xi-\xi_{L+1})\ldots(\xi-\xi_M)}{(\xi_L-\xi_1)(\xi_L-\xi_2)\ldots(\xi_L-\xi_{L-1})(\xi_L-\xi_{L+1})\ldots(\xi_L-\xi_M)}. \tag{1a}$$

Notons que les noms des éléments représentés dans la figure 1 («quadratique» pour M = 3, «cubique» pour M = 4), indiquent le degré des fonctions de base appliquées pour leur description. De même, pour M = 5, 6, etc., nous parlerons des éléments «quartique», «quintique», etc.

On remarquera que les triplets de points L, L′ et L″ (fig. 1), chacun affecté de ses coordonnées cartésiennes x, y, z connues, définissent les dimensions des sections nodales $\xi = \text{const.}$ et leur orientation dans l'espace. En partant de ces points, il devient possible de représenter la famille d'éléments considérée par la relation

$$\begin{Bmatrix} x \\ y \\ z \end{Bmatrix} = \sum_{L=1}^{M} N_L(\xi) \left( \begin{Bmatrix} x_L \\ y_L \\ z_L \end{Bmatrix} + \eta \begin{Bmatrix} x_{L'} - x_L \\ y_{L'} - y_L \\ z_{L'} - z_L \end{Bmatrix} + \zeta \begin{Bmatrix} x_{L''} - x_L \\ y_{L''} - y_L \\ z_{L''} - z_L \end{Bmatrix} \right). \tag{2a}$$

Cette relation s'écrit plus brièvement

$$\vec{r} = \sum_{L=1}^{M} N_L(\xi) (\vec{r}_L + \eta \vec{B}_L + \zeta \vec{C}_L) \tag{2b}$$

ou encore

$$\{r\} = ([G_0] + \eta [G_B] + \zeta [G_C]) \{N\}, \tag{2c}$$

où $\{N\}$ est la matrice-colonne des fonctions de base,

$$\{N\}^T = [N_1 \; N_2 \; \ldots \; N_M], \tag{3a}$$

et les matrices géométriques $[G_0]$, $[G_B]$ et $[G_c]$ ont pour expression:

$$[G_0] = \begin{bmatrix} x_1 & x_2 & \ldots & x_M \\ y_1 & y_2 & \ldots & y_M \\ z_1 & z_2 & \ldots & z_M \end{bmatrix}, [G_B] = \begin{bmatrix} (x_{1'} - x_1) & (x_{2'} - x_2) & \ldots & (x_{M'} - x_M) \\ (y_{1'} - y_1) & (y_{2'} - y_2) & \ldots & (y_{M'} - y_M) \\ (z_{1'} - z_1) & (z_{2'} - z_2) & \ldots & (z_{M'} - z_M) \end{bmatrix}, \tag{3b, c}$$

$$[G_C] = \begin{bmatrix} (x_{1''} - x_1) & (x_{2''} - x_2) & \ldots & (x_{M''} - x_M) \\ (y_{1''} - y_1) & (y_{2''} - y_2) & \ldots & (y_{M''} - y_M) \\ (z_{1''} - z_1) & (z_{2''} - z_2) & \ldots & (z_{M''} - z_M) \end{bmatrix} \tag{3d}$$

### 2. *Simplification des données géométriques*

Au moyen des relations (2), il s'agissait d'exprimer approximativement la forme d'un élément par une expression analytique unique et mieux adaptée aux besoins du calcul. Pour définir un élément de cette manière, que nous pouvons qualifier de passive, il est nécessaire de définir un nombre appréciable de données, soit 9M coordonnées des triplets de points L, L′, L″ qui définissent les sections nodales de la barre réelle.

Le nombre de données géométriques peut être considérablement réduit si l'on détermine la forme de l'élément de manière active: si l'on fixe convenablement dans l'espace un nombre approprié de points L, la relation (1) permet d'engendrer une forme aussi compliquée que l'on désire. On l'adopte alors comme axe réel de la barre. Puisque les sections nodales doivent être perpendiculaires à cet axe (cette condition n'est satisfaite qu'approximativement si l'on applique les relations

(2) de manière passive), chacune d'elle sera définie de manière univoque par trois paramètres seulement. En pratique, il suffit de spécifier par exemple les données suivantes (fig. 2):

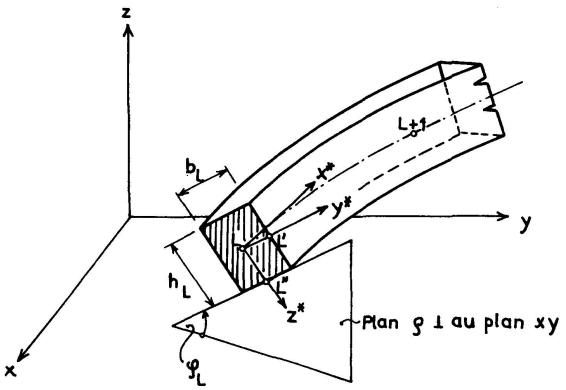


Fig. 2. Définition géométrique d'une section nodale. En partant des valeurs $x_L$, $y_L$, $z_L$ et $b_L$, $h_L$, $\varphi_L$ données, les nœuds auxiliaires L' et L'' seront déterminés à l'aide des relations résumées dans l'appendice.

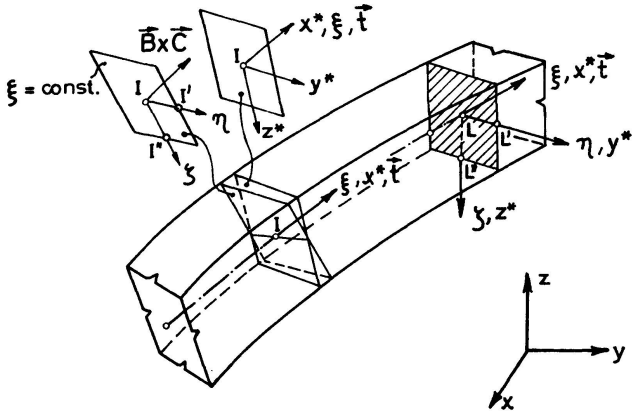


Fig. 3. Section ξ = const. et section perpendiculaire à l'axe en un point intermédiaire de l'élément.

*a*) les coordonnées $x_L$, $y_L$, $z_L$ des nœuds (L = 1, 2 ... M),
*b*) le «dévers» représenté par l'angle $\varphi_L$ entre le plan xy et l'axe principal $y_L^*$ des sections nodales (L = 1, 2 ... M),
*c*) les dimensions $b_L$ et $h_L$ des sections nodales (L = 1, 2 ... M).

Si le dévers et/ou les dimensions de la section sont constants, les données *b*) et/ou *c*) ne seront indiquées que pour une seule section de l'élément.

A partir des données *a*), *b*), *c*) et des bases du calcul vectoriel, on peut développer une routine permettant de déterminer les points L' et L'' et se ramener au cas fondamental du paragraphe 1. Les relations nécessaires sont données dans l'appendice en fin d'article.

### *3. Définition des axes locaux d'une section de l'élément*

*Généralités*

Afin de pouvoir tenir compte des hypothèses et des lois fondamentales de la théorie classique des barres, on considérera en tout point de l'axe de l'élément un système dit local d'axes orthogonaux, constitué par l'axe x* tangent à l'axe de l'élément et des axes y* et z* confondus avec les axes principaux de la section (voir par exemple la figure 3). La détermination de ce système local recèle quelques difficultés, propres à la méthode utilisée pour la définition géométrique de l'élément, définition qui, forcément, ne représente qu'imparfaitement la réalité. Il faut notamment remarquer qu'une section ξ = const. n'est en général qu'approximativement perpendiculaire à l'axe de l'élément (fig. 3). Nous nous en rendrons facilement compte en étudiant de plus près certaines propriétés de la définition (2).

On remarquera tout d'abord qu'en tout point I intermédiaire ($\xi = \xi_I \neq \xi_L$) de l'axe, les vecteurs

$$\vec{B} = \vec{r}_{I'} - \vec{r}_I = \sum_{L=1}^{M} N_L(\xi)\,\vec{B}_L \quad \text{et} \quad \vec{C} = \vec{r}_{I''} - \vec{r}_I = \sum_{L=1}^{M} N_L(\xi)\,\vec{C}_L \qquad (4a, b)$$

restent perpendiculaires l'un à l'autre, puisque les produits scalaires $\vec{B}_L \cdot \vec{C}_L$ des vecteurs nodaux sont par définition nuls. En revanche, la comparaison des expressions du vecteur $\vec{A}$ de la normale à une section $\xi = \text{const.}$,

$$\vec{A} = \sum_{L=1}^{M} N_L(\xi)\vec{B}_L \times \sum_{L=1}^{M} N_L(\xi)\vec{C}_L, \qquad (4c)$$

et du vecteur $\vec{t}$ de la tangente à l'axe de l'élément,

$$\vec{t} = \left(\frac{\partial \vec{r}}{\partial \xi}\right)_{\eta=\zeta=o} = \sum_{L=1}^{M} \frac{dN_L}{d\xi}\vec{r}_L = \sum_{L=1}^{M} N'_L(\xi)\,\vec{r}_L, \qquad (5)$$

montre que la définition géométrique (2) de l'élément n'implique pas que la normale de la section $\xi = \text{const.}$ est parallèle à la tangente de l'axe, si les sections nodales sont perpendiculaires à l'axe.

*Première méthode de définition*

Il découle de la discussion précédente que les sections $\xi = \text{const.}$ ne peuvent en général être perpendiculaires à l'axe qu'en un nombre limité de points particuliers (par exemple en tous les nœuds L, si l'on applique la définition active de la forme de l'élément selon le paragraphe 2). Dans ce cas, si le nombre M de nœuds est suffisant et si la distorsion de l'élément n'est pas excessive, on peut approximativement choisir les axes x*, y* et z* suivant les vecteurs $\vec{A}$, $\vec{B}$ et $\vec{C}$ (relations (4c, a, b)). Les vecteurs unités i*, j* et k* suivant ces axes s'expriment alors simplement par les relations

$$\vec{i}^* = \frac{\vec{B} \times \vec{C}}{|\vec{B} \times \vec{C}|}, \quad \vec{j}^* = \frac{\vec{B}}{|\vec{B}|}, \quad \vec{k}^* = \frac{\vec{C}}{|\vec{C}|}, \qquad (6a)$$

et les dimensions b et h de la section ont pour valeur

$$b = 2|\vec{B}| \quad \text{et} \quad h = 2|\vec{C}|. \qquad (6b)$$

*Deuxième méthode de définition*

Une méthode plus précise et plus générale de définition des axes locaux consiste à couper le solide défini par (2) par un plan perpendiculaire à l'axe (1). La section obtenue n'étant en général pas tout à fait rectangulaire, il s'agira de déterminer une section rectangulaire de remplacement. Ce problème n'est pas univoque et plusieurs formulations ont été tentées. Nous avons finalement retenu celle qui paraît la plus simple. Elle consiste à projeter sur le plan perpendiculaire à l'axe la section $\xi = \text{const.}$, soit la section rectangulaire ABCD de la figure 4a, et à ramener ensuite le parallélogramme (A) (B) (C) (D) ainsi obtenu à un rectangle A*B*C*D* (fig. 4b) par les rotations appropriées $\vartheta_1$ et $\vartheta_2$ de ses axes ($\eta$) et ($\zeta$). On admettra que les rotations $\vartheta_1$ et $\vartheta_2$ sont telles que les arcs circulaires (I')I*' et (I'')I*'' parcourus

pendant la rotation (fig. 4b) sont de longueur égale. La simplicité de cette hypothèse se justifie par le fait qu'en pratique, les corrections angulaires sont généralement faibles.

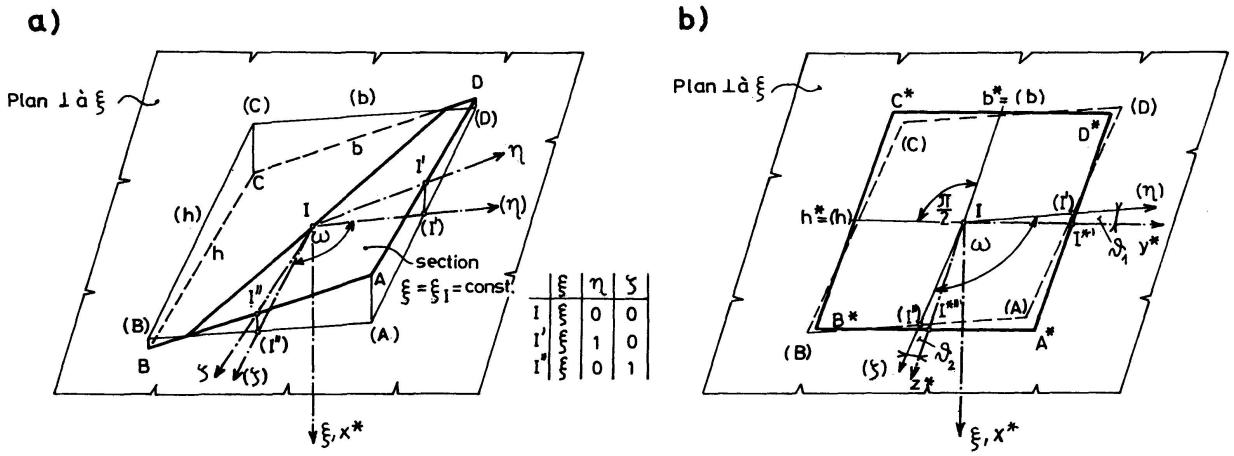


Fig. 4. Projection de la section $\xi = \xi_I$ sur le plan perdiculaire à l'axe et détermination des axes locaux x*, y* et z*.

Cette méthode conduit aux relations suivantes:

$$\vec{i}^* = \frac{\vec{t}}{|\vec{t}|}, \quad \vec{j}^* = \frac{\vec{B}^*}{|\vec{B}^*|}, \quad \vec{k}^* = \frac{\vec{C}^*}{|\vec{C}^*|}, \tag{7a}$$

$$b = 2|(\vec{B})|, \quad h = 2|(\vec{C})| \tag{7b}$$

où le vecteur $\vec{t}$ est défini par la relation (5) et les vecteurs $\vec{B}^*$ et $\vec{C}^*$ ont pour expression:

$$\left.\begin{aligned} \vec{B}^* &= (\vec{B}) + \tfrac{b}{h}[\sin\omega \cdot \operatorname{cotg}(\omega - \vartheta_1) - \cos\omega](\vec{C}), \\ \vec{C}^* &= (\vec{C}) + \tfrac{h}{b}[\sin\omega \cdot \operatorname{cotg}(\omega - \vartheta_2) - \cos\omega](\vec{B}), \end{aligned}\right\} \tag{7c}$$

$$\text{avec} \quad (\vec{B}) = \vec{r}_{I'} - \vec{r}_I - \frac{\vec{t}\cdot\vec{B}}{|\vec{t}|^2}\,\vec{t}, \quad (\vec{C}) = \vec{r}_{I''} - \vec{r}_I - \frac{\vec{t}\cdot\vec{C}}{|\vec{t}|^2}\,\vec{t}, \tag{7d}$$

$$\omega = \arccos\frac{4}{bh}(\vec{B})\cdot(\vec{C}), \tag{7e}$$

$$\vartheta_1 = \frac{h}{b+h}\left(\omega - \frac{\pi}{2}\right), \quad \vartheta_2 = \frac{b}{b+h}\left(\omega - \frac{\pi}{2}\right). \tag{7f}$$

*Expression matricielle des relations définissant les axes locaux*

Pour le calcul sur ordinateur, il convient de remplacer l'ensemble des relations définissant les vecteurs-unités $\vec{i}^*$, $\vec{j}^*$ et $\vec{k}^*$ par un ensemble équivalent de relations matricielles conduisant aux matrices-colonnes $\{i^*\}$, $\{j^*\}$ et $\{k^*\}$. On opérera les substitutions suivantes:

$$\vec{V} \Rightarrow \{V\}, \quad |\vec{V}| \Rightarrow V = \sqrt{\{V\}^T \{V\}}, \quad \vec{V}_1 \cdot \vec{V}_2 \Rightarrow \{V_1\}^T \{V_2\}, \tag{8a}$$

$$\vec{V}_1 \times \vec{V}_2 \Rightarrow \begin{Bmatrix} V_{1y} \cdot V_{2z} - V_{1z} \cdot V_{2y} \\ V_{1z} \cdot V_{2x} - V_{1x} \cdot V_{2z} \\ V_{1x} \cdot V_{2y} - V_{1y} \cdot V_{2x} \end{Bmatrix} \tag{8b}$$

où $\vec{V}$, $\vec{V}_1$ et $\vec{V}_2$ sont des vecteurs quelconques, et où l'indice supérieur T désigne la matrice transposée. Par ailleurs, en tenant compte de (2b), on aura:

$$\{B\} = [G_B]\{N\}, \quad \{C\} = [G_C]\{N\}, \tag{9a, b}$$

$$\{r_I\} = [G_0]\{N\}, \tag{9c}$$

$$\{r_{I'}\} = ([G_0] + [G_B])\{N\}, \quad \{r_{I''}\} = ([G_0] + [G_C])\{N\}, \tag{9d, e}$$

$$\{t\} = [G_0]\{N\}' \tag{9f}$$

où $\{N\}'$ est la matrice-colonne des premières dérivées des fonctions de base par rapport à $\xi$.

### 4. *Définition d'une famille généralisée d'éléments de section quelconque*

La figure 5 montre deux membres typiques de la famille généralisée d'éléments spatiaux de barre courbe. La section supposée varier lentement le long de l'axe peut être quelconque, pourvu que son centre de torsion se confonde (au moins approximativement) avec le centre de gravité. Outre les sections pleines, on peut admettre également des sections à parois minces de contour fermé, à condition que la torsion fléchie soit négligeable vis-à-vis de la tension de Saint-Venant.

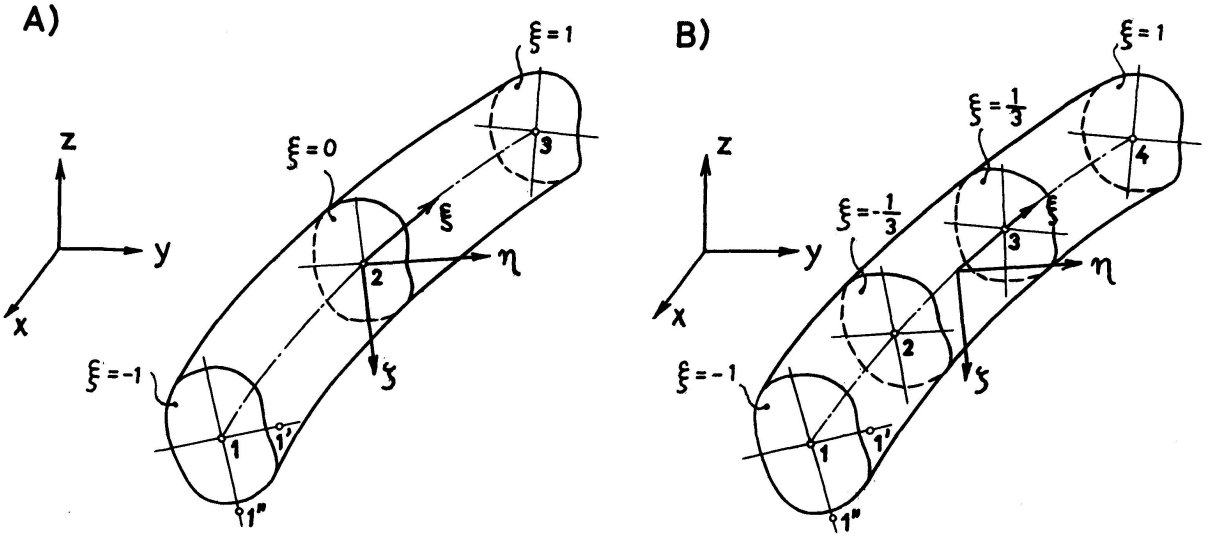


Fig. 5. Deux membres de la famille d'éléments spatiaux de barres courbes de section quelconque: élément quadratique (A), élément cubique (B).

Comme dans le cas de l'élément de section rectangulaire, l'axe de l'élément sera représenté par l'équation (1) et les axes principaux des sections nodales seront définis par les triplets de points L, L′ et L″. Pour définir les axes locaux x*, y*, z* d'une

section quelconque, on appliquera directement les relations développées au paragraphe 3. Les grandeurs b et h intervenant dans ces relations ne sont maintenant que de simples valeurs auxiliaires, ne permettant pas de déterminer la forme et les dimensions de la section correspondante; il faut donc définir de façon indépendante les constantes géométriques caractérisant la section dans les considérations statiques. Il s'agira des six grandeurs suivantes:

$F$ aire de la section;

$F_{y*}$, $F_{z*}$ aire réduite pour le calcul des déformations dues au cisaillement selon les axes principaux y* et z*;

$J$ moment de résistance à la torsion;

$I_{y*}$, $I_{z*}$ moments d'inertie par rapport aux axes principaux y* et z*.

La méthode la plus simple consiste à définir les valeurs nodales de ces grandeurs et à déterminer les valeurs intermédiaires par l'interpolation suivante:

$$\begin{Bmatrix} F \\ F_{y*} \\ F_{z*} \\ J \\ I_{y*} \\ I_{z*} \end{Bmatrix} = \sum_{L=1}^{M} N_L(\xi) \begin{Bmatrix} F_L \\ F_{y*L} \\ F_{z*L} \\ J_L \\ I_{y*L} \\ I_{z*L} \end{Bmatrix}. \tag{10}$$

Ajoutons encore que le principe de la définition active de la forme de l'élément énoncé au paragraphe 2 ainsi que les relations servant au calcul des points auxiliaires L′ et L″ données dans l'Appendice restent valables pour les éléments de section quelconque. Toutefois, le groupe c) de données (valeurs $b_L$ et $h_L$ qu'il est maintenant possible de remplacer par des valeurs fixes quelconques non nulles – par exemple unitaires – égales pour tous les L et pour tous les éléments) sera remplacé par:

c) $F_L, F_{y*L}, F_{z*L}, J_L, I_{y*L}, I_{z*L}$ $\quad (L = 1, 2 \ldots M)$.

## 2. Considérations statiques

### *1. Généralités*

Considérons l'élément courbe de la figure 6a repéré dans un système global de coordonnées cartésiennes x, y et z. En un nœud quelconque L de l'élément, on admettra six degrés de liberté:

les déplacements u, v, w selon les axes x, y, z,

les rotations $\alpha$, $\beta$, $\gamma$ autour des axes x, y, z.

Pour simplifier l'écriture, on désignera par $\delta_L$ le sous-vecteur des déplacements nodaux défini par la relation

$$\delta_L^T = [u_L, v_L, w_L, \alpha_L, \beta_L, \gamma_L], \tag{11}$$

et on attribuera le symbole $s_L$ au sous-vecteur des forces nodales équivalentes associé à $\delta_L$. Par ailleurs, on désignera respectivement par $\{\Delta\}$ et $\{S\}$ le vecteur

des déplacements nodaux et le vecteur des forces nodales constitués respectivement par tous les sous-vecteurs $\boldsymbol{\delta}_L$ et par tous les sous-vecteurs $\mathbf{s}_L$ de l'élément. Afin de pouvoir convenablement tenir compte des effets du poids propre, de la variation de température et des déformations initiales, la relation forces-déplacements de l'élément sera exprimée sous la forme

$$\{S\} = \{\bar{S}\} + [K]\{\Delta\}, \tag{12}$$

où $\{\bar{S}\}$ est le vecteur des forces nodales primaires équivalentes de l'élément. On remarquera que la matrice $[K]$ est d'ordre 6M, où M est le nombre de nœuds.

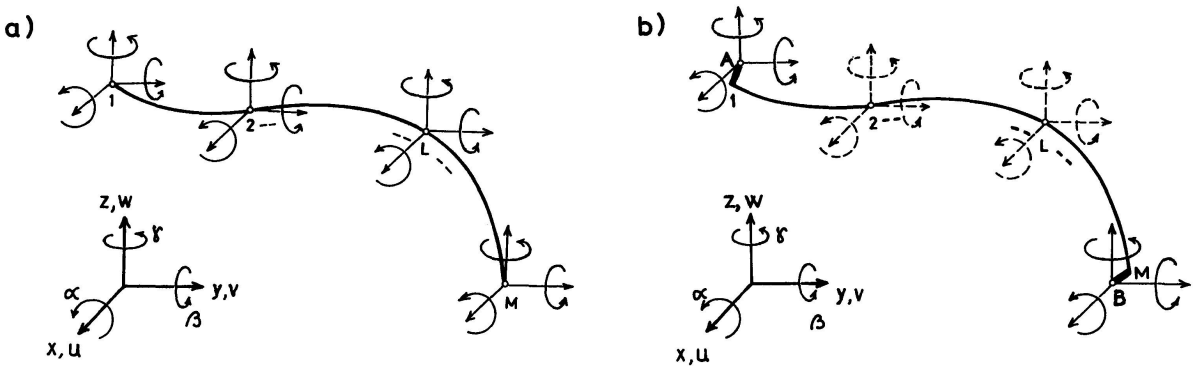


Fig. 6. Elément spatial de barre courbe et ses forces nodales.
*a*) Cas fondamental: tous les nœuds sont considérés comme nœuds de liaison et se situent sur l'axe de l'élément.
*b*) Exemple d'un cas dérivé du cas fondamental: les nœuds A et B sont seuls considérés comme nœuds de liaison. (Ils peuvent être excentrés par rapport à l'axe.) Les degrés de liberté des nœuds internes (en traitillé) sont éliminés de la relation forces-déplacements.

La situation représentée sur la figure 6a sera considérée comme cas fondamental. Lorsque le vecteur $\{\bar{S}\}$ et la matrice $[K]$ sont connus, d'autres cas peuvent en être dérivés par des transformations appropriées. Dans les applications concernant les structures constituées uniquement de barres, seuls les nœuds des extrémités interviendront dans le processus d'assemblage. Par ailleurs, si à la suite d'une forte différence entre les dimensions des sections, les axes des barres ne se coupent pas aux croisements des barres, on peut être amené à considérer des éléments possédant des nœuds de liaison excentrés par rapport à leur axe. L'élément type représenté sur la figure 6b satisfait à toutes ces exigences.

Les déplacements nodaux des nœuds intermédiaires peuvent être éliminés par le processus standard de condensation statique. En posant, pour simplifier:

$$\{\delta\} = \begin{Bmatrix} \boldsymbol{\delta}_1 \\ \boldsymbol{\delta}_M \end{Bmatrix} \quad \text{et} \quad \{s\} = \begin{Bmatrix} \mathbf{s}_1 \\ \mathbf{s}_M \end{Bmatrix}, \tag{13a}$$

on aboutit à la relation forces-déplacements suivante:

$$\{s\} = \{\bar{s}\} + [k]\{\delta\} \tag{13}$$

$$\text{avec} \quad \{\bar{s}\} = \bar{\mathbf{S}}_e + \mathbf{K}_{ee}\mathbf{K}_{ii}^{-1}(\mathbf{P}_i - \bar{\mathbf{S}}_i), \quad [k] = \mathbf{K}_{ee} - \mathbf{K}_{ei}\mathbf{K}_{ii}^{-1}\mathbf{K}_{ei}^{T} \tag{13b}$$

Dans ces relations, le vecteur $\mathbf{P}_i$ est formé de sous-vecteurs $\mathbf{p}_L$ des charges nodales données aux nœuds intermédiaires de l'élément

$$\mathbf{P}_i^T = [\mathbf{p}_2^T \ \cdots \ \mathbf{p}_{M-1}^T], \tag{13c}$$

tandis que la signification des autres termes découle de la partition suivante de la relation matricielle (12):

$$\{S\} = \begin{Bmatrix} s_1 \\ s_M \\ \hline s_2 \\ \vdots \\ s_{M-1} \end{Bmatrix} = \begin{Bmatrix} S_e \\ \hline S_i \end{Bmatrix} = \begin{Bmatrix} \bar{S}_e \\ \hline \bar{S}_i \end{Bmatrix} + \left[\begin{array}{c|c} K_{ee} & K_{ei} \\ \hline K_{ie} & K_{ii} \end{array}\right] \begin{Bmatrix} \Delta_e \\ \hline \Delta_i \end{Bmatrix}. \tag{13d}$$

Pour passer à l'élément avec nœuds de liaison excentrés, on admettra que ces nœuds sont liés aux extrémités de l'axe par des barres rigides (fig. 6b). Les déplacements $\delta_1$, $\delta_M$ et les déplacements $\delta_A$, $\delta_B$ seront alors liés par des relations linéaires du type

$$\delta_1 = T_1 \delta_A, \quad \delta_M = T_M \delta_B,$$

où les matrices de transformation $T_1$ et $T_M$ découlent de simples considérations géométriques. La matrice $T_1$, par exemple, a pour expression:

$$T_1 = \left[\begin{array}{ccc|ccc} 1 & 0 & 0 & 0 & \Delta z_1 & -\Delta y_1 \\ 0 & 1 & 0 & -\Delta z_1 & 0 & \Delta x_1 \\ 0 & 0 & 1 & \Delta y_1 & -\Delta x_1 & 0 \\ \hline 0 & 0 & 0 & 1 & 0 & 0 \\ 0 & 0 & 0 & 0 & 1 & 0 \\ 0 & 0 & 0 & 0 & 0 & 1 \end{array}\right], \tag{14a}$$

$$\text{avec} \quad \Delta x_1 = x_1 - x_A, \quad \Delta y_1 = y_1 - y_A, \quad \Delta z_1 = z_1 - z_A. \tag{14b}$$

Pour obtenir la matrice $T_M$, il suffit de remplacer les indices 1 et A par M et B. En définissant maintenant les vecteurs

$$\{\delta_{exc}\} = \begin{Bmatrix} \delta_A \\ \delta_B \end{Bmatrix}, \ \{s_{exc}\} = \begin{Bmatrix} s_A \\ s_B \end{Bmatrix}, \tag{14c}$$

on peut transformer la relation (13) en la relation forces-déplacements suivante:

$$\underline{\{s_{exc}\} = \{\bar{s}_{exc}\} + [k_{exc}]\{\delta_{exc}\},} \tag{14}$$

$$\text{avec} \quad \{\bar{s}_{exc}\} = [T]^T \{\bar{s}\}, \quad [k_{exc}] = [T]^T [k] [T] \tag{14d}$$

$$\text{et} \quad [T] = \begin{bmatrix} T_1 & 0 \\ 0 & T_M \end{bmatrix}. \tag{14e}$$

### 2. *Définition du champ des déplacements et du vecteur des efforts internes*

Le modèle de calcul permettant de tenir compte de l'effet du cisaillement consiste à admettre qu'une section plane avant déformation restera plane après déformation, mais que son plan ne sera plus nécessairement perpendiculaire à

l'axe déformé de la barre. Ceci signifie que les rotations des sections doivent être définies indépendamment de la déformée de l'axe. La déformation de l'élément sera alors donnée de manière univoque par trois composantes $u_o$, $v_o$, $w_o$ du déplacement du centre de gravité de la section selon les axes globaux x, y, z et par trois composantes $\alpha$, $\beta$, $\gamma$ de la rotation de la section autour de ces axes. On les définira de manière analogue à celle que l'on a utilisée pour les coordonnées globales (équation (1)).

$$\begin{Bmatrix} u_o \\ v_o \\ w_o \end{Bmatrix} = \sum_{L=1}^{M} N_L(\xi) \begin{Bmatrix} u_L \\ v_L \\ w_L \end{Bmatrix} \quad \text{et} \quad \begin{Bmatrix} \alpha \\ \beta \\ \gamma \end{Bmatrix} = \sum_{L=1}^{M} N_L(\xi) \begin{Bmatrix} \alpha_L \\ \beta_L \\ \gamma_L \end{Bmatrix}. \tag{15a, b}$$

Les efforts internes dans une section de l'élément sont définis dans la figure 7, où y* et z* sont les axes principaux. En partant des hypothèses courantes de la théorie des barres, ces efforts peuvent être exprimés en fonction des déformations par la relation matricielle suivante:

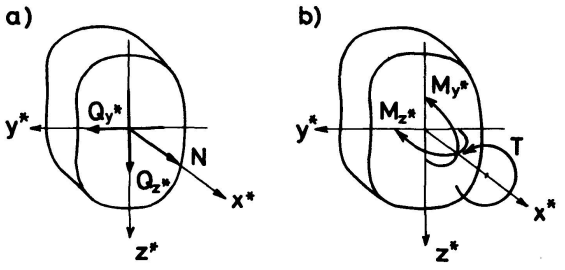


Fig. 7. Composantes de la résultante des efforts internes agissant sur la face positive de la section.

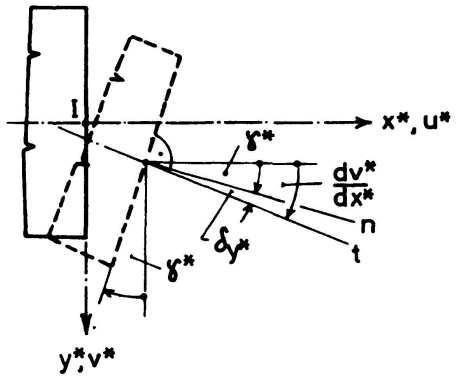


Fig. 8. Positions relatives d'une section et de l'axe d'un élément déformé, compte tenu de l'effet du cisaillement.

$$\begin{Bmatrix} N \\ Q_{y^*} \\ Q_{z^*} \\ T \\ M_{y^*} \\ M_{z^*} \end{Bmatrix} = \begin{bmatrix} EF & & & & & \\ & GF_{y^*} & & & 0 & \\ & & GF_{z^*} & & & \\ & & & GJ & & \\ & 0 & & & EI_{y^*} & \\ & & & & & EI_{z^*} \end{bmatrix} \left( \begin{Bmatrix} \frac{du_o^*}{dx^*} \\ \frac{dv_o^*}{dx^*} - \gamma^* \\ \frac{dw_o^*}{dx^*} + \beta^* \\ \frac{d\alpha^*}{dx^*} \\ \frac{d\beta^*}{dx^*} \\ \frac{d\gamma^*}{dx^*} \end{Bmatrix} - \begin{Bmatrix} {}^{o}\varepsilon_{x^*} \\ {}^{o}\delta_{y^*} \\ {}^{o}\delta_{z^*} \\ {}^{o}\vartheta_{x^*} \\ {}^{o}\varkappa_{y^*} \\ {}^{o}\varkappa_{z^*} \end{Bmatrix} \right) \tag{16a}$$

où $u_o^*$, $v_o^*$, $w_o^*$ et $\alpha^*$, $\beta^*$, $\gamma^*$ sont respectivement les déplacements et les rotations rapportés aux axes locaux de la section, et ${}^o\varepsilon_{x*}$, ${}^o\delta_{y*}$, ${}^o\delta_{z*}$, ${}^o\vartheta_{x*}$, ${}^o\varkappa_{y*}$, ${}^o\varkappa_{z*}$ sont les valeurs initiales des déformations associées aux efforts internes. Dans le cas d'une variation uniforme de température, par exemple, on aura:

$$ {}^o\varepsilon_{x*} = \alpha_T \Delta T, \quad {}^o\delta_{y*} = {}^o\delta_{z*} = {}^o\vartheta_{x*} = {}^o\varkappa_{y*} = {}^o\varkappa_{z*} = 0, $$

où $\alpha_T$ est le coefficient de dilatation thermique de la matière.

La relation (16a) appelle quelques commentaires. On remarquera que les déformations $\delta_{y*} = \dfrac{dv_o^*}{dx^*} - \gamma^*$ et $\delta_{z*} = \dfrac{dw_o^*}{dx^*} + \beta^*$ représentent les composantes de la déviation de la normale n à la section par rapport à la tangente t à l'axe (fig. 8). De plus, on notera que dans le cas d'une section rectangulaire, les surfaces réduites $F_{y*}$ et $F_{z*}$ multipliant ces déformations sont égales à $\frac{5}{6}F$.

Pour simplifier l'écriture, nous écrirons symboliquement la relation (16a) sous la forme

$$ \underline{\{M\} = [D](\{\varkappa\} - \{{}^o\varkappa\}),} \tag{16} $$

où $\{M\}$ désigne le vecteur des efforts internes, $[D]$ la matrice de transformation efforts internes-déformations, $\{\varkappa\}$ le vecteur des déformations totales et $\{{}^o\varkappa\}$ le vecteur des déformations initiales.

### 3. *Expression de la relation forces-déplacements de l'élément*

Le vecteur $\{\varkappa\}$ défini au paragraphe précédent peut être exprimé en fonction du vecteur $\{\Delta\}$ des déplacements nodaux. La matrice $[\Theta]$, qui définit la transformation orthogonale

$$ \{V\} = [\Theta]\{V^*\} \quad \text{et} \quad \{V^*\} = [\Theta]^T\{V\} $$

entre les coordonnées cartésiennes globales $\{V\}$ et locales $\{V^*\}$ d'un vecteur, aura pour expression

$$ [\Theta] = [\{i^*\}\ \{j^*\}\ \{k^*\}], \tag{17a} $$

où $\{i^*\}$, $\{j^*\}$ et $\{k^*\}$ sont les matrices-colonnes des coordonnées cartésiennes globales des vecteurs unités définis par les relations (6a) ou (7a); d'autre part,

$$ \frac{\partial}{\partial x^*}\{V^*\} = c[\Theta]^T \frac{\partial}{\partial \xi}\{V\} = c[\Theta]^T\{V\}', $$

où le coefficient c est égal à la valeur inverse de la longueur du vecteur-tangent $\vec{t}$

$$ c = \frac{1}{|\vec{t}|} = \frac{1}{\sqrt{\{N'\}^T[G_0]^T[G_0]\{N'\}}}. \tag{17b} $$

On aboutit à $\{\varkappa\} = \sum_{L=1}^{M} \left[\begin{array}{c|c} cN_L'[\Theta]^T & N_L[A][\Theta]^T \\ \hline \mathbf{0} & cN_L'[\Theta]^T \end{array}\right] \delta_L = \sum_{L=1}^{M} \mathbf{b}_L \cdot \delta_L$ (17)

avec $$[A]=\begin{bmatrix}0 & 0 & 0\\ 0 & 0 & -1\\ 0 & 1 & 0\end{bmatrix} \tag{17c}$$

Afin de rendre possible la condensation statique [équations (13)], les sous-vecteurs $\delta_L$ constituant le vecteur $\{\Delta\}$ seront considérés dans l'ordre suivant:

$$\{\Delta\}^T=[\delta_1^T\,\delta_M^T\,|\,\delta_2^T\,\text{—}\,\delta_{M-1}^T] \tag{18a}$$

En posant $$[B]\;=[\mathbf{b}_1\,\mathbf{b}_M\,|\,\mathbf{b}_2\,\text{—}\,\mathbf{b}_{M-1}] \tag{18b}$$

on obtient $$\{\varkappa\}=[B]\,\{\Delta\} \tag{18}$$

Pour calculer l'effet du poids propre du matériau, de poids spécifique $\gamma$, introduisons les vecteurs

$$\{\gamma\}=\begin{Bmatrix}\gamma_x\\ \gamma_y\\ \gamma_z\end{Bmatrix} \quad \text{et} \quad \{d_o\}=\begin{Bmatrix}u_o\\ v_o\\ w_o\end{Bmatrix}.$$

Les éléments du premier vecteur sont les composantes du poids spécifique $\gamma$ selon les axes globaux x, y et z. Le second vecteur peut encore s'écrire à partir de (15a), en fonction de $\{\Delta\}$:

$$\{d_o\}=[\mathbf{c}_1\,\mathbf{c}_M\,|\,\mathbf{c}_2\,\text{—}\,\mathbf{c}_{M-1}]\,\{\Delta\}=[C]\,\{\Delta\}, \tag{19}$$

avec $$\mathbf{c}_L=N_L\begin{bmatrix}1 & 0 & 0 & 0 & 0 & 0\\ 0 & 1 & 0 & 0 & 0 & 0\\ 0 & 0 & 1 & 0 & 0 & 0\end{bmatrix}.$$

En appliquant maintenant le théorème de stationnarité de l'énergie potentielle totale, $\delta\Pi=\delta V+\delta U=0$, on aboutit à:

$$\{\bar{S}\}=-\int_0^{\ell}[B]^T[D]\,\{{}^o\varkappa\}\,ds-\int_0^{\ell}F[C]^T\{\gamma\}\,ds,\quad [K]=\int_0^{\ell}[B]^T[D][B]\,ds.$$

Sachant que $ds=td\xi$, où $t=t(\xi)$ est la valeur absolue du vecteur tangent

$$t=|\vec{t}|=\sqrt{\{N'\}^T[G_0]^T[G_0]\{N'\}}\;, \tag{20a}$$

il est aisé de remplacer les intégrales suivant l'axe de l'élément par les intégrales selon la coordonnée curviligne $\xi$ entre les bornes $-1$ et $+1$, de sorte que l'on obtient finalement:

$$\boxed{\begin{gathered}\{\bar{S}\}=-\int_{-1}^{+1}t\;[B]^T[D]\,\{{}^o\varkappa\}\,d\xi-\int_{-1}^{+1}t\;F[C]^T\{\gamma\}\,d\xi,\\ [K]=\int_{-1}^{+1}t[B]^T[D][B]\,d\xi.\end{gathered}}$$

On calcule numériquement les intégrales en appliquant par exemple la quadrature de Gauss. Notons que les quantités F, $F_{y*}$, $F_{z*}$, J, $I_{y*}$ et $I_{z*}$ intervenant dans ces relations (matrice [D]) s'obtiennent soit à partir des dimensions b et h des sections rectangulaires (équations (6b), (7b)), soit par l'application de la relation (10) dans le cas d'une section quelconque.

### 4. *Calcul des efforts internes*

Une fois les déplacements nodaux $\{\Delta\}$ connus, les efforts internes des éléments peuvent être calculés au moyen des relations (16) et (17), d'où l'on tire:

$$\{M\} = -[D]\{^{o}\!\varkappa\} + [D]\sum_{L=1}^{M} \mathbf{b}_L \delta_L \,. \tag{21}$$

Quand la relation $\{S\} = \{\bar{S}\} + [K]\{\Delta\}$ ne sert que de point de départ pour développer les relations forces-déplacements telles que (13) ou (14), la résolution de l'assemblage des éléments ne fournit que les sous-vecteurs $\delta_1$, $\delta_M$ ou $\delta_A$, $\delta_B$. En partant de (13d) et en remarquant que $\{\delta\} = [T]\{\delta_{exc}\}$, où la matrice $[T]$ est définie par les relations (14a, e), on trouve:

$$\begin{Bmatrix} \delta_1 \\ \delta_M \end{Bmatrix} = \{\delta\} = [T]\{\delta_{exc}\},$$

$$\begin{Bmatrix} \delta_2 \\ | \\ \delta_{M-1} \end{Bmatrix} = -\mathbf{K}_{ii}^{-1}\,\bar{\mathbf{S}}_i - \mathbf{K}_{ii}^{-1}\mathbf{K}_{ei}^{T}\{\delta\} = -\mathbf{K}_{ii}^{-1}\,\bar{\mathbf{S}}_i - \mathbf{K}_{ii}^{-1}\mathbf{K}_{ei}^{T}[T]\{\delta_{exc}\}. \tag{21b}$$

Bien que les deux familles d'éléments présentées dans cette étude donnent généralement avec une très bonne précision les déplacements et les forces nodales des éléments pour tous les $M \geq 3$, l'expérience montre que les efforts internes obtenus avec les membres inférieurs de ces familles (éléments quadratiques $M = 3$ et éléments cubiques $M = 4$) ne sont pas suffisamment précis, à moins que les éléments soient relativement courts. Ceci est dû au fait que les fonctions de base de ces éléments ne sont pas suffisamment riches pour représenter convenablement certaines variations des efforts internes. Il est intéressant de remarquer que, dans ces cas-là, on obtient toutefois d'excellents résultats en partant des forces nodales équivalentes et en appliquant les conditions d'équivalence statique. Pour les efforts internes aux extrémités d'un élément, on obtient par exemple les formules suivantes:

$$\{M_1\} = -[\Theta_1]\mathbf{s}_1 = -[T_1]\,[\Theta_1]\mathbf{s}_A, \tag{22a}$$

$$\{M_M\} = [\Theta_M]\mathbf{s}_M = [T_M]\,[\Theta_M]\mathbf{s}_B, \tag{22b}$$

où les matrices $[\Theta_1]$ et $[\Theta_M]$ peuvent être calculées en appliquant la relation (17a).

## 3. Analyses numériques et applications

### 1. *Etude de la convergence*

Pour examiner l'efficacité des deux familles d'éléments proposées, nous avons étudié la poutre hélicoïdale représentée à la figure 9. Les calculs ont été tout d'abord effectués avec des éléments de la première famille (éléments de section rectangulaire). Les mêmes calculs ont été répétés avec des éléments de la deuxième famille (relations (10)), comme s'il s'agissait d'une barre de section quelconque.

Les différences entre les deux solutions étant rarement apparues avant le cinquième chiffre des résultats, nous présenterons uniquement l'analyse basée sur la première famille d'éléments.

L'étude de la convergence a été effectuée par comparaison des résultats obtenus au moyen d'éléments quadratiques (M = 3), cubiques (M = 4), quartiques (M = 5) et quintiques (M = 6) et pour un nombre N d'éléments variant entre 2 et 32. Le

*Tableau 1. Etude de la convergence. Poutre hélicoïdale (fig. 9).*
Effet du poids propre $\gamma = 2{,}5$ t/m³.

| Variables | M \ N | 2 | 4 | 8 | 12 | 16 | 32 | Unités |
|---|---|---|---|---|---|---|---|---|
| w ($\beta = 120^0$) | 3 | -0,0548 | -0,2328 | -0,3507 | -0,3634 | -0,3658 | -0,3669 | mm |
| | 4 | -0,2861 | -0,3644 | -0,3670 | -0,3670 | -0,3670 | -0,3670 | |
| | 5 | -0,3615 | -0,3670 | -0,3670 | -0,3670 | -0,3670 | | |
| | 6 | -0,3665 | -0,3670 | -0,3670 | | | | |
| $N_{max}$ ($\beta = 240^0$) | 3 | 2,060 | 2,158 | 2,147 | 2,152 | 2,153 | 2,156 | t |
| | 4 | 2,138 | 2,152 | 2,157 | 2,157 | 2,157 | 2,158 | |
| | 5 | 2,169 | 2,158 | 2,158 | 2,158 | 2,158 | | |
| | 6 | 2,160 | 2,158 | 2,158 | | | | |
| $Q_{z*max}$ ($\beta = 0^0$) | 3 | 1,688 | 1,627 | 1,628 | 1,621 | 1,617 | 1,613 | t |
| | 4 | 1,625 | 1,616 | 1,613 | 1,612 | 1,612 | 1,612 | |
| | 5 | 1,599 | 1,611 | 1,612 | 1,612 | 1,612 | | |
| | 6 | 1,610 | 1,612 | 1,612 | | | | |
| $T_{max}$ ($\beta = 240^0$) | 3 | 0,103 | 0,172 | 0,251 | 0,256 | 0,256 | 0,255 | tm |
| | 4 | 0,249 | 0,270 | 0,257 | 0,256 | 0,255 | 0,255 | |
| | 5 | 0,249 | 0,255 | 0,255 | 0,255 | 0,255 | | |
| | 6 | 0,251 | 0,255 | 0,255 | | | | |
| $M_{y*max}$ ($\beta = 120^0$) | 3 | 0,514 | 0,633 | 0,798 | 0,813 | 0,815 | 0,816 | tm |
| | 4 | 0,763 | 0,814 | 0,816 | 0,816 | 0,816 | 0,816 | |
| | 5 | 0,813 | 0,816 | 0,816 | 0,816 | 0,816 | | |
| | 6 | 0,816 | 0,816 | 0,816 | | | | |
| $M_{y*min}$ ($\beta = 0^0$) | 3 | -1,515 | -1,704 | -2,025 | -2,054 | -2,058 | -2,060 | tm |
| | 4 | -1,815 | -2,048 | -2,059 | -2,060 | -2,061 | -2,060 | |
| | 5 | -2,027 | -2,060 | -2,060 | -2,060 | -2,060 | | |
| | 6 | -2,060 | -2,060 | -2,060 | | | | |

*Tableau 2. Comparaison de l'élément courbe (quintique) avec élément droit.*
Poutre hélicoïdale (fig. 9); effet du poids propre $\gamma = 2{,}5$ t/m².

| Variables | Elément droit | | | | Elément courbe | | Unités |
|---|---|---|---|---|---|---|---|
| | N=4 | 8 | 16 | 32 | N=2 | 4 | |
| w ($\beta=120^0$) | -0,282 | -0,341 | -0,360 | -0,365 | -0,367 | -0,367 | mm |
| $N_{max}$ ($\beta=240^0$) | 2,17 | 2,18 | 2,17 | 2,17 | 2,16 | 2,16 | t |
| $Q_{z*max}$ ($\beta= 0^0$) | 1,50 | 1,57 | 1,69 | 1,60 | 1,61 | 1,61 | t |
| T ($\beta=240^0$) | -0,26 | -0,07 | 0,08 | 0,16 | 0,25 | 0,25 | tm |
| $M_{y*max}$ ($\beta=120^0$) | 0,58 | 0,75 | 0,80 | 0,81 | 0,82 | 0,82 | tm |
| $M_{y*min}$ ($\beta= 0^0$) | -2,13 | -2,18 | -2,15 | -2,11 | -2,06 | -2,06 | tm |

tableau 1 montre quelques résultats caractéristiques de cette étude. Il en ressort clairement que des éléments quartiques et quintiques conduisent à des résultats pratiquement exacts même avec un nombre très restreint d'éléments. Par contre, il faut un nombre beaucoup plus grand d'éléments quadratiques ou cubiques pour obtenir des résultats de la même qualité. L'expérience montre que les éléments quadratiques et cubiques sont aussi notablement moins économiques sur le plan de la préparation des données et du temps de calcul.

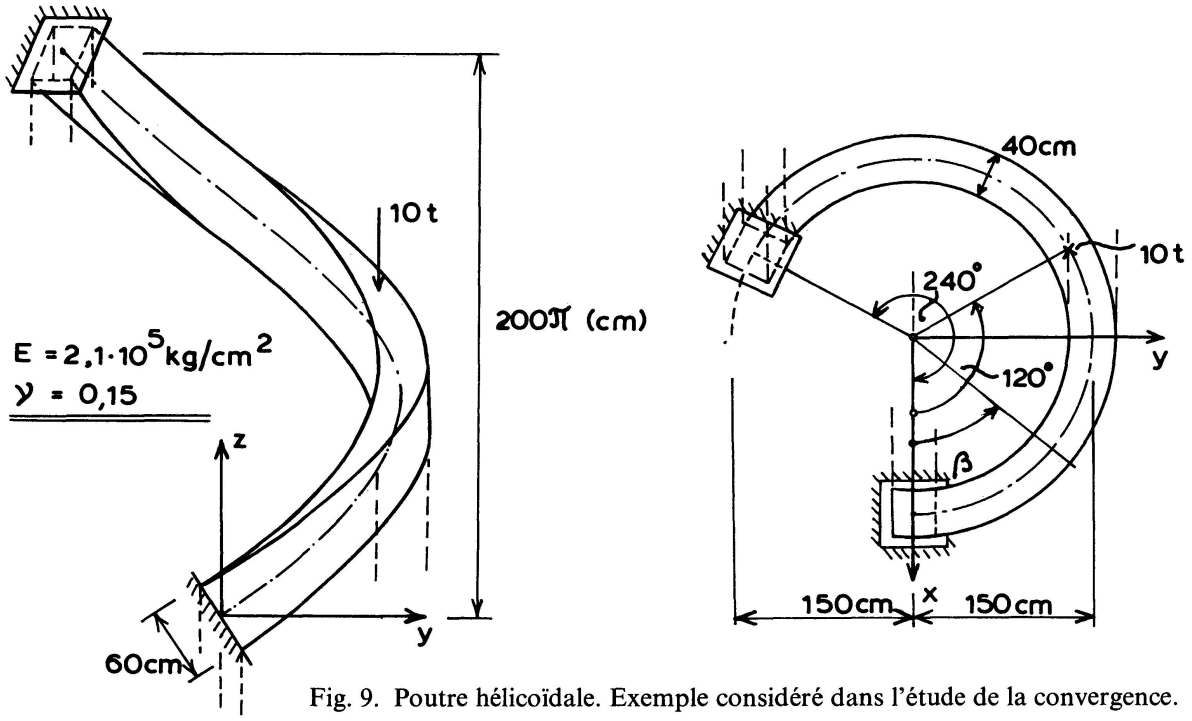


Fig. 9. Poutre hélicoïdale. Exemple considéré dans l'étude de la convergence.

En complément, le tableau 2 donne encore la comparaison entre la solution basée sur l'élément quintique et les résultats obtenus en remplaçant la poutre hélicoïdale par une succession de segments rectilignes. Il apparaît clairement que même avec 32 éléments rectilignes, on n'atteint pas la qualité des résultats obtenus avec deux éléments courbes seulement.

Notons que des résultats en tout point semblables à ceux des tableaux 1 et 2 (poids propre) ont également été obtenus pour une force isolée (fig. 9).

## 2. *Applications pratiques*

### *Calcul d'une coupole sphérique constituée de barres*

La coupole représentée sur la figure 10, qui rappelle par sa conception la halle de la Foire d'échantillons de Hanovre, est constituée par des tubes d'acier ($E = 2{,}1.10^6$ kg/cm$^2$, $\nu = 0{,}3$) de section circulaire ($F = 2F_{y*} = 2F_{z*} = 46$ cm$^2$, $J = 2I_{y*} = 2I_{z*} = 5020$ cm$^4$) liés rigidement entre eux à leurs intersections. Projetés verticalement, les axes des barres apparaissent comme des paraboles quadratiques régulièrement espacées sur le plan xy de l'ouvrage. Les figures 11 à 13 montrent quelques résultats obtenus pour une charge isolée P = 10 t au sommet de la coupole.

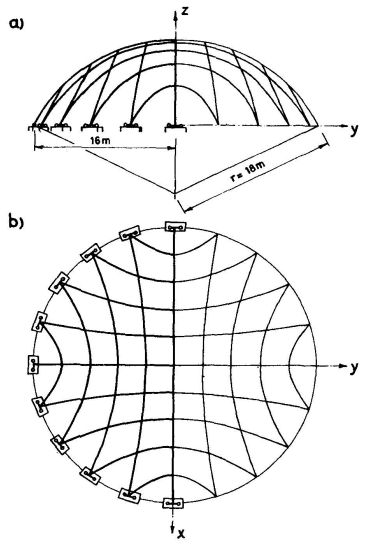


Fig. 10. Coupole sphérique constituée par un grillage de barres courbes de l'espace.

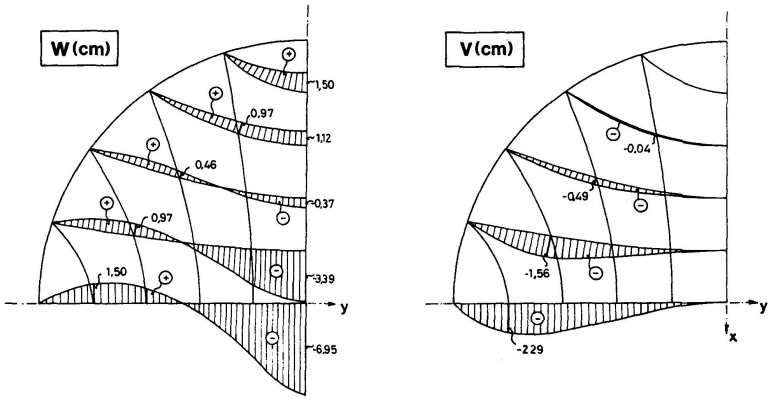


Fig. 11. Déplacements globaux v (selon y) et w (selon z) engendrés par une force verticale P = 10 t, appliquée au sommet de la coupole sphérique de la figure 10.

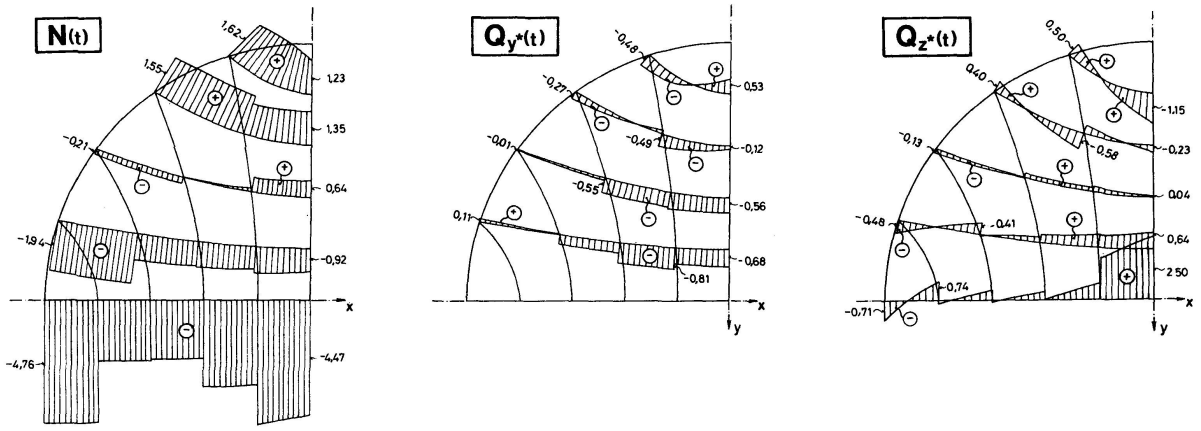


Fig. 12. Effort normal et efforts tranchants engendrés dans les barres de la coupole sphérique de la figure 10 par une force isolée P = 10 t, appliquée au sommet. L'axe principal y* des sections est horizontal ($\varphi = 0$).

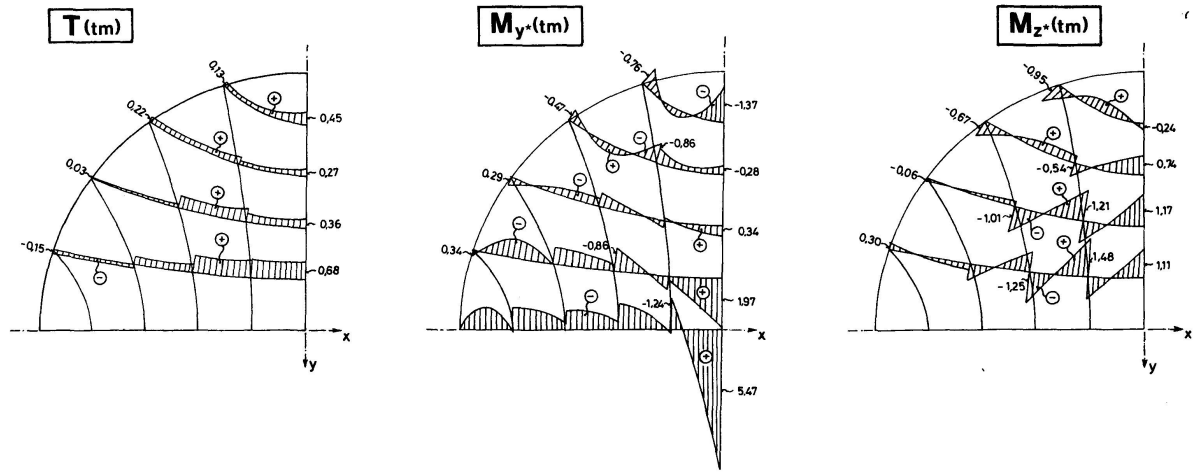


Fig. 13. Moment de torsion et moments fléchissants engendrés dans les barres de la coupole sphérique de la figure 10 par une force isolée P = 10 t, appliquée au sommet. L'axe principal y* des sections est horizontal ($\varphi = 0$).

*Calcul d'un pont courbe à trois travées continues*

Le pont courbe représenté sur la figure 14 est un ouvrage en acier ($E = 2{,}1.10^6$ kg/cm$^2$, $\nu = 0{,}3$) constitué par 5 poutres maîtresses ($F = 660$ cm$^2$, $F_{y*} = 250$ cm$^2$, $F_{z*} = 300$ cm$^2$, $J = 996923$ cm$^4$, $I_{y*} = 1512720$ cm$^4$, $I_{z*} = 414236$ cm$^4$) et 13 entretoises ($F = 300$ cm$^2$, $F_{y*} = 133{,}3$ cm$^2$, $F_{z*} = 116{,}7$ cm$^2$, $J = 174222$ cm$^4$, $I_{y*} = 253336$ cm$^4$, $I_{z*} = 77385$ cm$^4$). Les figures 15 et 16 montrent les diagrammes des moments fléchissants $M_{y*}$ et des moments de torsion T engendrés dans le pont par la force $P = 1$ t appliquée au milieu de la première poutre maîtresse.

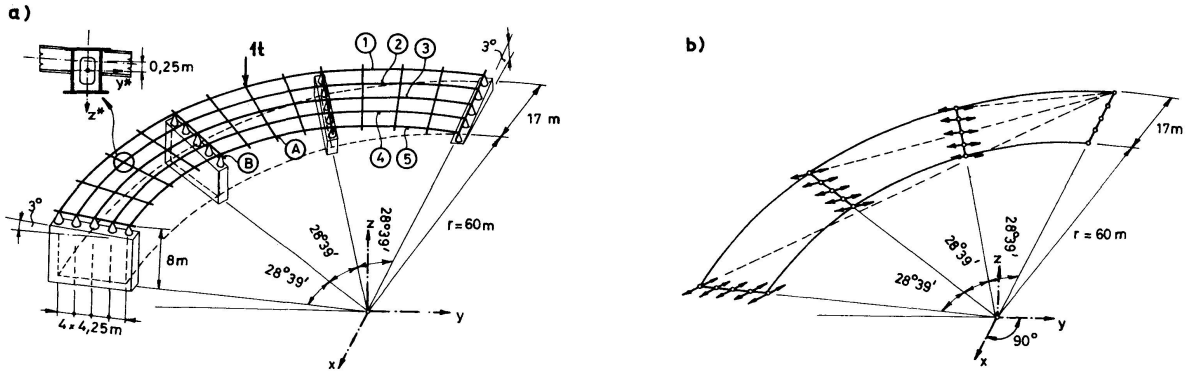


Fig. 14. Pont courbe à trois travées continues: *a*) Axonométrie du pont, *b*) Schéma de la mobilité directionnelle des appareils d'appuis.

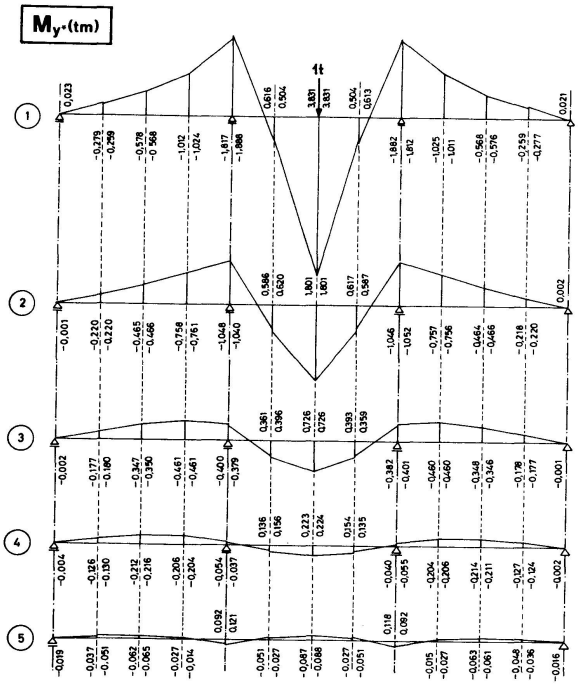


Fig. 15. Diagrammes des moments fléchissants dans les poutres maîtresses du pont courbe de la figure 14.

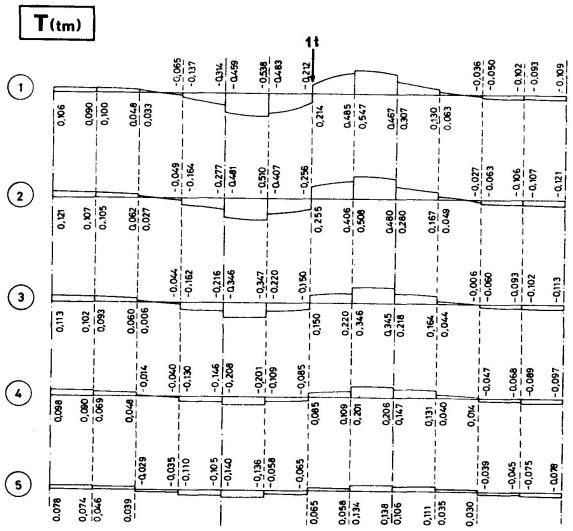


Fig. 16. Diagrammes des moments de torsion dans les poutres maîtresses du pont courbe de la figure 14.

*Calcul d'une rampe hélicoïdale en béton armé*

La figure 18 montre quelques résultats intéressants d'une étude de l'effet de l'excentricité des poutres aux intersections. La structure de la figure 17

($E = 210000$ kg/cm$^2$, $\nu = 0{,}15$) a été calculée en supposant à tour de rôle que les entretoises sont soit surélevées soit surbaissées de 20 cm par rapport à l'axe de la poutre hélicoïdale, ou encore qu'elles coupent l'axe de cette dernière. On remarquera que l'excentricité affecte ici essentiellement l'effort normal.

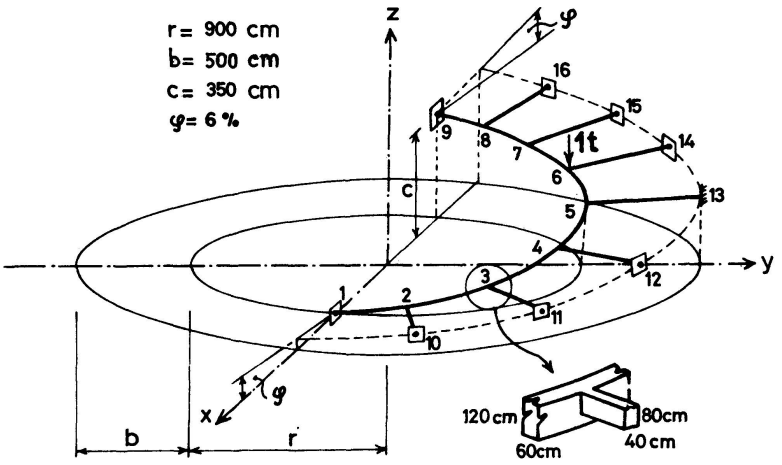


Fig. 17. Rampe hélicoïdale. La numérotation des nœuds correspond à la subdivision de la structure en éléments finis.

## 4. Aspects économiques des nouveaux éléments et leur importance pour la sécurité des structures

La comparaison donnée dans le tableau 2 montre clairement la supériorité des nouveaux éléments sur le calcul coutumier consistant à remplacer une barre courbe par une succession de segments droits. Le fait que l'assemblage de 32 éléments droits, conduisant à un système de 198 équations, ne suffit encore pas pour obtenir la même précision qu'avec 2 éléments «quintique» seulement (18 équations) est éloquent. Même si l'on admet que le temps de calcul ne croît qu'avec le carré du nombre d'équations, l'économie de temps de calcul et par conséquent également du coût de calcul est extraordinaire. Par ailleurs, la préparation des données pour un nombre très réduit d'éléments est beaucoup plus aisée et le risque d'erreurs diminue.

Dans certains cas, il pourrait devenir pratiquement impossible de subdiviser la barre courbe en un nombre suffisant de segments droits, à cause des limitations imposées par la mémoire centrale de l'ordinateur. (On remarquera par exemple que la succession de 32 segments droits remplaçant une structure aussi simple que celle étudiée dans le tableau 2 donne encore une erreur de 36% sur le moment de torsion.) L'utilisateur obligé de se contenter d'un nombre d'éléments insuffisant peut se trouver devant un dilemme: ou bien il accepte les résultats obtenus et ne pourra garantir une sécurité élevée de l'ouvrage, ou bien il sera obligé de dimensionner plus largement sa construction, de manière peu économique, pour tenir compte de l'imprécision des résultats.

Remarquons encore que dans le calcul des coques nervurées, les éléments proposés sont les seuls capables de satisfaire aux conditions de compatibilité avec les éléments superparamétriques de coque.

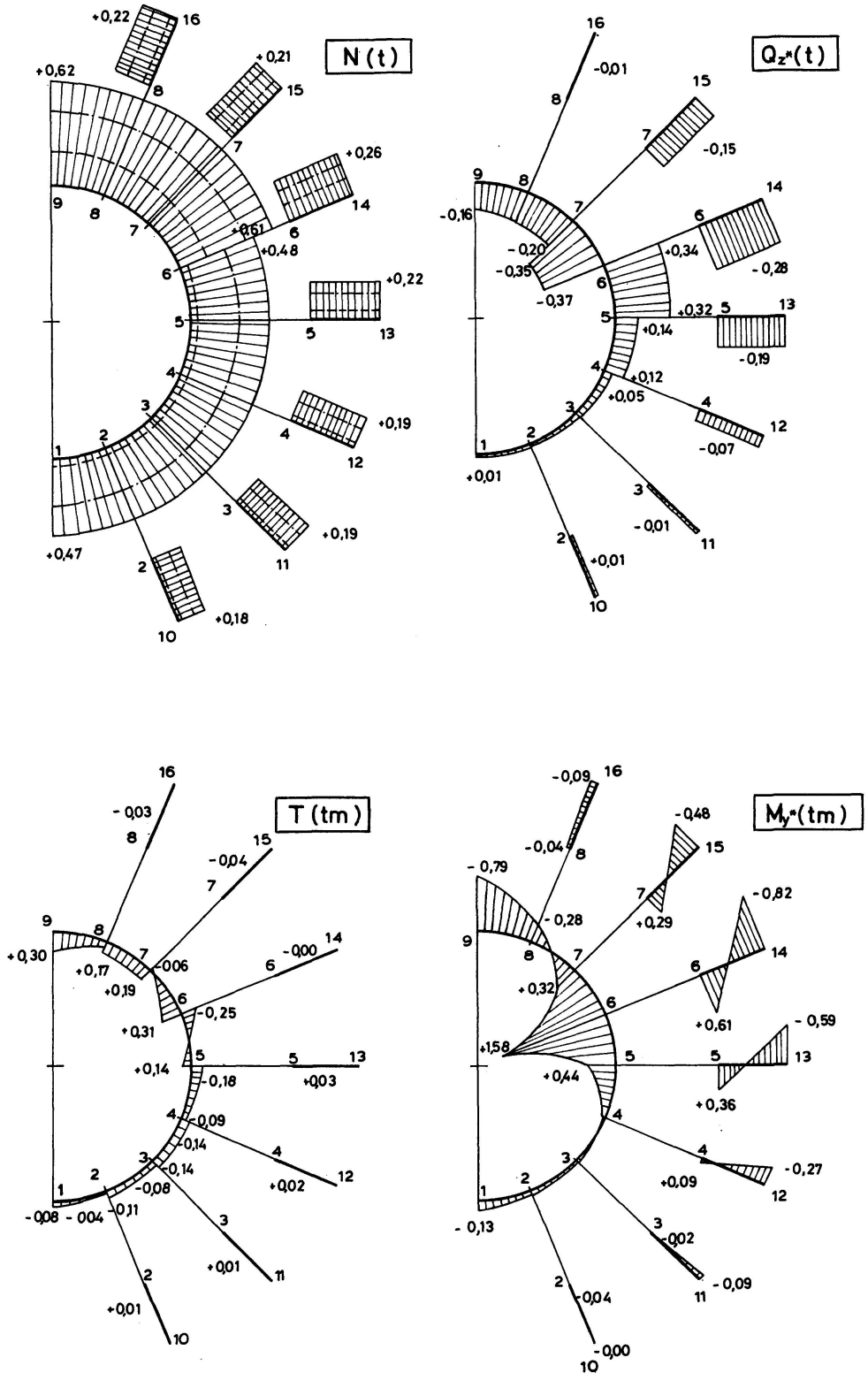


Fig. 18. Efforts internes engendrés dans la rampe hélicoïdale de la figure 17 par une force P = 1 t appliquée au nœud 6.

——— entretoises surélevées de 20 cm par rapport à l'axe de la poutre hélicoïdale.
– · – · – · – axes des entretoises coupant l'axe de la poutre hélicoïdale.
– – – – – – entretoises surbaissées de 20 cm par rapport à l'axe de la poutre hélicoïdale.

## Appendice

*Calcul des vecteurs* $\{B_L\}$

On commence par calculer, pour tous les L de l'élément (L = 1,2 ... M), les vecteurs-tangents

$$\vec{t} = \begin{Bmatrix} t_{xL} \\ t_{yL} \\ t_{zL} \end{Bmatrix} = \sum_{K=1}^{M} N'_K (\xi = \xi_L) \vec{r}_K = \sum_{K=1}^{M} N'_K (\xi = \xi_L) \begin{Bmatrix} x_K \\ y_K \\ z_K \end{Bmatrix} \tag{23}$$

Les coordonnées orthogonales des vecteurs $\{B_L\}$ seront alors obtenues par l'application des relations suivantes:

*a)* $$z_{L'} - z_L = \tfrac{1}{2} b_L \sin \varphi_L, \tag{24}$$

*b)* $$y_{L'} - y_L = \frac{-b \pm \sqrt{b^2 - 4ac}}{2a} \text{ avec } \pm\sqrt{\ } \text{ pour } t_x \lessgtr 0, \tag{25}$$

et où $a = t_{xL}^2 + t_{yL}^2$, $b = t_{yL} \cdot t_{zL} b_L \sin \varphi_L$, $c = \tfrac{1}{4} b_L^2 (t_{zL}^2 \sin^2 \varphi_L - t_{xL}^2 \cos^2 \varphi_L)$. (25a)

(On remarquera que dans (25) la racine carrée est nulle si $t_x = 0$.)

*c)* $$x_{L'} - x_L = -\frac{t_{yL}}{t_{xL}}(y_{L'} - y_L) - \frac{t_{zL}}{t_{xL}}(z_{L'} - z_L), \tag{26a}$$

ou encore, si $t_x = 0$,

$$x_{L'} - x_L = \pm\sqrt{\tfrac{b}{2}^2 - (y_{L'} - y_L)^2 - (z_{L'} - z_L)^2} \text{ avec } \pm\sqrt{\ } \text{ pour } t_y \gtrless 0. \tag{26b}$$

La formule (25) n'est pas applicable si $t_{xL} = t_{yL} = 0$, d'où la restriction suivante: *en aucun des points nodaux L, l'axe de l'élément ne doit être parallèle à l'axe global z.* Remarquons également qu'en donnant le «dévers» $\varphi_L$, on ne peut pas dépasser le complément à $\frac{\pi}{2}$ de l'angle de la tangente par rapport au plan xy (il est facile de s'en convaincre par une simple analyse géométrique). L'angle $\varphi_L$ doit alors satisfaire à la condition suivante:

$$|\varphi_L| \leq \frac{\pi}{2} - \text{arc tg} \frac{|t_{zL}|}{\sqrt{t_{xL}^2 + t_{yL}^2}} \,. \tag{27}$$

Notons encore que la relation (24) découle directement de la figure 2. Par ailleurs, les relations (25) à (26) s'obtiennent par la résolution du système de deux équations vectorielles:

$$\vec{t}_L (\vec{r}_{L'} - \vec{r}_L) = 0 \quad \text{et} \quad |\vec{r}_{L'} - \vec{r}_L| = \tfrac{1}{2} b_L,$$

dont la première exprime le fait que le nœud auxiliaire L' se trouve dans un plan normal à l'axe de l'élément et la seconde définit la longueur du vecteur LL'.

*Calcul des vecteurs* $\{C_L\}$

Les coordonnées du vecteur $\{C_L\}$ s'obtiennent au moyen du produit vectoriel $\vec{t}_L \times \vec{B}_L$, le vecteur ainsi défini étant ramené à la longueur $\frac{1}{2} h_L$. On trouve ainsi:

$$\{C_L\} = \frac{1}{2} \frac{h_L}{D_L} \begin{Bmatrix} D_{xL} \\ D_{yL} \\ D_{zL} \end{Bmatrix}$$

avec $$\begin{Bmatrix} D_{xL} \\ D_{yL} \\ D_{zL} \end{Bmatrix} = \begin{Bmatrix} t_{yL} B_{zL} - t_{zL} B_{yL} \\ t_{zL} B_{xL} - t_{xL} B_{zL} \\ t_{xL} B_{yL} - t_{yL} B_{xL} \end{Bmatrix} \quad \text{et} \quad D_L = \sqrt{D_{xL}^2 + D_{yL}^2 + D_{zL}^2}. \tag{28a}$$

## Remerciements

Cet article est issu d'un travail de recherche sur les systèmes spatiaux de poutres curvilignes croisées et les coques nervurées, financé par le Fonds national suisse de la recherche scientifique, auquel vont nos plus sincères remerciements.

Les auteurs remercient également MM. Raymond Schäffer et Fawaz Tarazi, ingénieurs EPF-L, de leur participation aux calculs numériques sur l'ordinateur de l'Ecole polytechnique fédérale de Lausanne.

## Références

1. Baron, F.: Matrix Analysis of Structures Curved in Space. Journal of the Structural Division, ASCE, Vol. 87, No. ST3, March 1961, pp. 17-38.
2. Shu-T'ien, Li: Metallic Dome-Structure Systems, Journal of the Structural Division, ASCE, Vol. 88, No. ST6, December 1962, pp. 201-226.
3. Eisemann, K., Who, L., Namyet, S.: Space Frame Analysis by Matrices and Computers, Journal of the Structural Division, ASCE, Vol. 88, No. ST6, December 1962, pp. 245-268.
4. Jirousek, J.: Kruhové rošty a prostorové rotační rámy (Circular Grillages and Circular Cylindrical Frames), Sborník Vysokého učení technického v Brně (Bulletin of the Technical University Brno, Czechoslovakia), 1963, No. 1-4, pp. 31-71.
5. Hutton, C.R.: Curvilinear Grid Frames, Engineering Journal, July 1964, Vol. 1, No. 3, AISC.
6. Michalos, J.: The Structural Analysis of Space Networks. Int. Conf. on Space Structures, University of Surrey, September 1966.
7. Fenton, D.L.: Matrix Computer Analysis of Curvilinear Grid Systems. Dissertation for the degree of Ph. D. in Civil Engineering, University of Missouri at Rolla, 1967.
8. Jirousek, J.: ELFIN-Programme de calcul des structures par la méthode des éléments finis, tome 1. Publication de la Chaire de Statique et de Résistance des Matériaux de l'EPF-L, N° 7, rédaction provisoire 1974.

## Résumé

L'étude analyse deux familles d'éléments spatiaux de barres courbes: l'une formée d'éléments superparamétriques de section rectangulaire variable, et l'autre d'éléments de section quelconque dont le centre de torsion se confond (au moins approximativement) avec le centre de gravité.

Les exemples pratiques se réfèrent principalement au calcul des ponts courbes et des coupoles constituées par des grillages de barres.

**Zusammenfassung**

Die vorliegende Studie legt zwei Familien gekrümmter räumlicher Balkenelemente vor. Bei der ersten handelt es sich um eine Familie supraparametrischer Elemente mit veränderlichem Rechteckquerschnitt. Die zweite umfasst Elemente beliebigen Querschnitts, deren Schubmittelpunkt (zumindest annähernd) mit dem Querschnittsschwerpunkt identisch ist.

Die Resultate dieser Arbeit finden insbesondere Anwendung bei der statischen Berechnung gekrümmter Brücken und räumlich gewölbter Trägerroste.

**Summary**

The study presents two families of space-curved rod elements: the first one is that of superparametric elements with variable rectangular cross section, the second one concerns the elements of arbitrary cross section provided that its shear centre identifies (at least approximately) with the centre of gravity.

The study is of special interest for the analysis of curved bridges and curvilinear grid system domes.

Leere Seite
Blank page
Page vide

# Reibungsmessungen an Gleitlagern

*Friction Tests on sliding bearings*

*Mesures du frottement d'appuis glissants*

R. FAVRE
Professor für Betontragwerke
Eidg. Technische Hochschule
Lausanne (Schweiz)

P. KROPF
Partner im Ingenieurbüro
Schalcher und Partner
Zürich (Schweiz)

## 1. Zweck der Versuche

Die rund 1500 m lange, sechsspurige Sihlhochstrasse wurde im Herbst 1974 dem Verkehr übergeben. Sie ist ein Bestandteil der mitten durch die Stadt Zürich geführten Expressstrasse, welche die bis an den Stadtrand gebauten Autobahnen miteinander verbinden wird. Sie bildet mit ihren Anschlussbauwerken eine Brückenfläche von 50000 $m^2$ und folgt bei Spannweiten von 42,4 m bis 57,8 m dem Flusslauf der Sihl[1].

Aus flussbaulichen Gründen (grosse Hochwasser und Eisschollenbildung) mussten die Abmessungen der Pfeiler gering gehalten werden. Andererseits wurden zur Verminderung des Unterhaltes möglichst wenige Dilatationsfugen gewählt. Es ergab sich damit ein mittlerer Dilatationsabschnitt von 821 m, dessen Festpunkt durch drei Pfeilerpaare mit festen Neotopflagern gebildet wird. Die Beanspruchung dieser Pfeiler wird nun hauptsächlich durch die Reibungskräfte erzeugt, die in den flussaufwärts bzw. -abwärts liegenden Gleitlagern entstehen. Wenn auch letzten Endes nur der Reibungsunterschied zwischen Oberwasser und Unterwasser massgebend ist, so ist doch klar ersichtlich, dass man sich zuerst für den Absolutwert der Reibung interessiert. Für den statischen Nachweis der Pfeiler mit beweglichen Lagern muss er ohnehin bekannt sein.

Wie im modernen Brückenbau immer öfter, wurden auch hier anstelle von Rollenlagern Gleitlager eingebaut, wobei die Gleitschicht aus Polytetrafluoräthylen (PTFE) besteht. Die von der Firma Proceq gelieferten Lager besitzen eine PTFE-Gleitschicht mit dem Handelsnamen «Teflon».

Der Zweck der nachfolgend beschriebenen Lagerversuche bestand darin, die angenommenen Rechenwerte der Reibungskoeffizienten $\mu$ zu überprüfen. Diese Rechenwerte stützen sich in der Schweiz auf den Angaben des Standardkataloges D 340 «Konstruktive Einzelheiten» des Eidg. Amtes für Strassen- und Flussbau.

[1] Siehe Schweizerische Bauzeitung Heft 21, 1974.

Sie wurden aus Laborversuchen extrapoliert, indem die unter günstigen Bedingungen ermittelten Versuchswerte mit Sicherheitszuschlägen behaftet wurden (siehe Kapitel 5). Damit wollte man dem Umstand Rechnung tragen, dass wichtige, ungünstige Faktoren im Labor schlecht oder nicht erfasst werden. Dazu gehören die Alterung, die Abnützung, das Entfetten und die Verschmutzung des Teflons. Des weiteren musste die grosse Streuung der Resultate und deren wesentliche Abhängigkeit

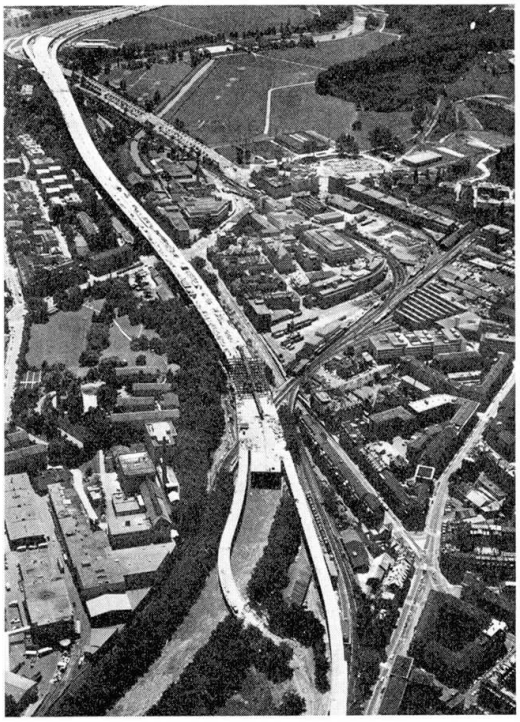

Fig. 1. Flugaufnahme der Sihlhochstrasse bei der Erstellung des letzten Brückenfeldes.

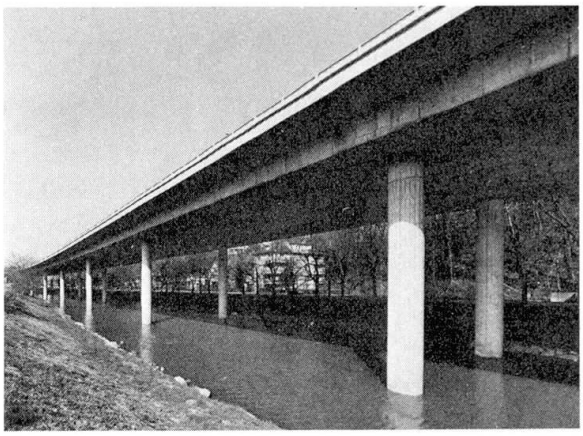

Fig. 2. Brückenansicht.

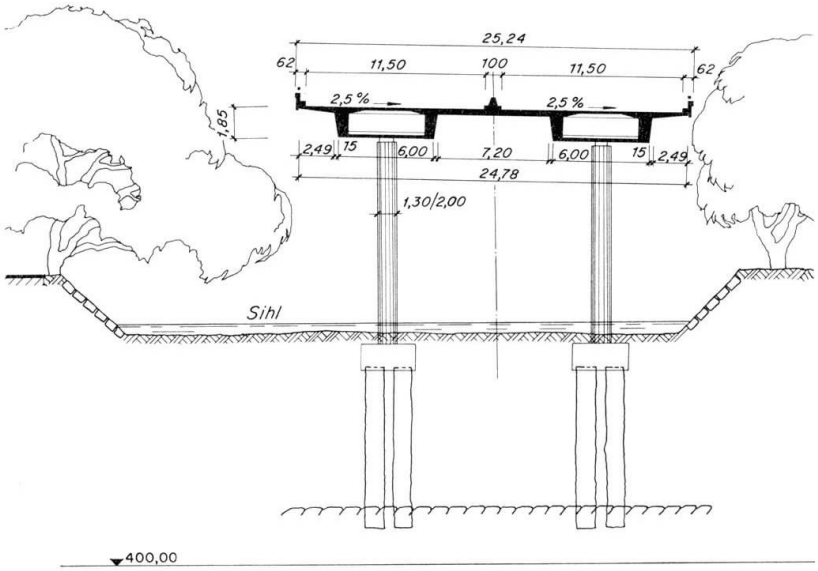


Fig. 3. Normalquerschnitt.

von spezifischer Pressung, Gleitgeschwindigkeit, Luftfeuchtigkeit und Kriecherscheinungen durch den Sicherheitswert abgedeckt werden. Ferner können auch Ausführungsungenauigkeiten und Kräfte auf Führungsleisten die globale Lagerreibung erhöhen.

Deshalb war es von ausserordentlich hohem Interesse, die Reibungswerte an zwei zufällig herausgegriffenen, seit drei Jahren eingebauten Lagern der Sihlhochstrassenbrücke *in situ* überprüfen zu können. Die Messungen wurden unter der Oberaufsicht des Projektverfassers (Schlacher und Partner, H. Eichenberger AG) durch die Eidg. Materialprüfungs- und Versuchsanstalt (EMPA) und die Lieferfirma (Proceq) ausgeführt. Grosser Dank gebührt dem Kantonalen Tiefbauamt Zürich für die Bereitschaft, diese allgemein interessierenden Versuche gefördert und finanziert zu haben.

## 2. Versuchsdurchführung

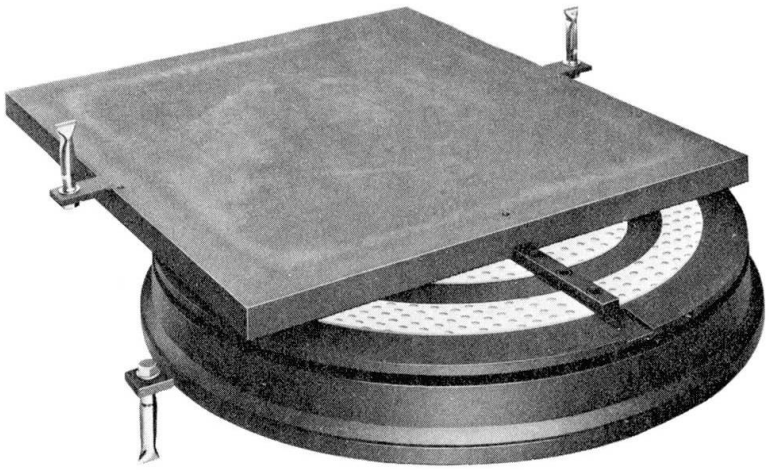

Fig. 4. Neotopfteflongleitlager Sihlhochstrasse Typ NGe 1250 t (Proceq).

Die Reibungsmessungen wurden im Herbst 1973 an zwei seit 3 Jahren eingebauten Neotopfteflongleitlagern am fertigen Bauwerk durchgeführt.

Im Zeitpunkt der Versuche war die Brücke noch nicht dem Verkehr übergeben, was eine erschütterungsfreie Durchführung der Versuche erlaubte.

Die ausgewählten Lager sind in Brückenlängsrichtung verschieblich; quer zur Brücke sind sie zur Übertragung des Seitenwindes auf den paarweise angeordneten elliptischen Pfeilern geführt.

Auf die Lagerführungen wirken horizontale Zwängungskräfte in der rechnerisch ermittelten Grössenordnung von 5 bis 8 t, hervorgerufen durch Schwinden, Vorspannung und Temperaturänderungen des Überbaus.

Die in den Versuchen ermittelten Reibungswerte schliessen diese Zwängungseinflüsse ein und sind deshalb mit im Labor ermittelten reinen Teflon-Reibungsmessungen nicht direkt vergleichbar.

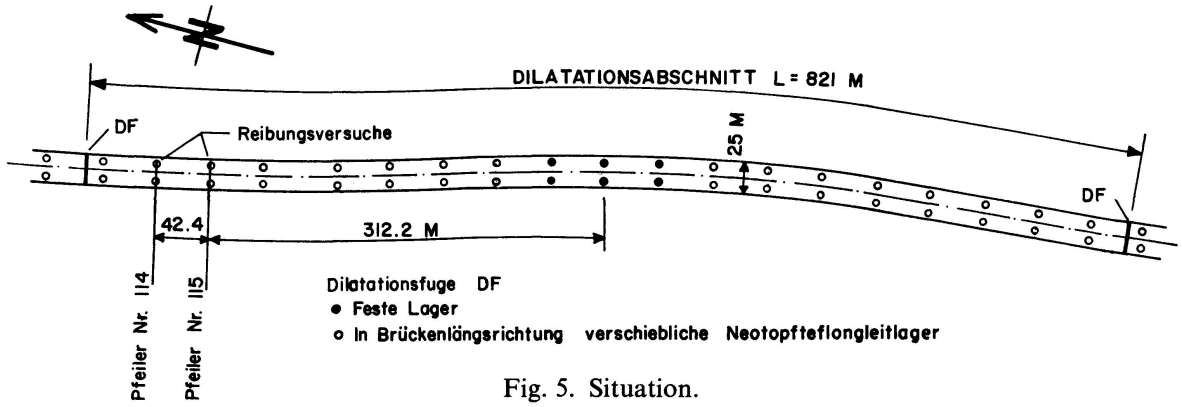


Fig. 5. Situation.

*Bekannte Daten bei Versuchsbeginn*

| | Lager 114 Ost | Lager 115 Ost |
|---|---|---|
| Brückenauflast | 810 t | 820 t |
| Mittlere Teflonpressung | 258 kg/cm² | 261 kg/cm² |
| Stützenabmessungen | Ellipse 2,0/1,3 ml | Ellipse 2,0/1,3 ml |
| Mittleres Stützenträgheitsmoment | 0,545 m⁴ | 0,545 m⁴ |
| Stützenträgheitsmoment auf Höhe der Dehnmessstreifen | 0,559 m⁴ | 0,559 m⁴ |
| Widerstandsmoment auf Höhe der Dehnmessstreifen | 0,559 m³ | 0,559 m³ |
| H: Abstand zwischen Pressenkraft und Fundament | 12,39 ml | 12,53 ml |
| $H_1$: Abstand zwischen Pressenkraft und Dehnmessstelle | 11,0 ml | 11,0 ml |
| Entfernung bis zum Festpunkt der Brücke | 354,6 ml | 312,2 ml |
| Aussentemperatur während der Versuche | Abnehmend 0° bis − 3° | Um 0° |
| Temperatur im Brückenkasten | Abnehmend + 1,5° bis − 1,5° | Nicht gemessen |

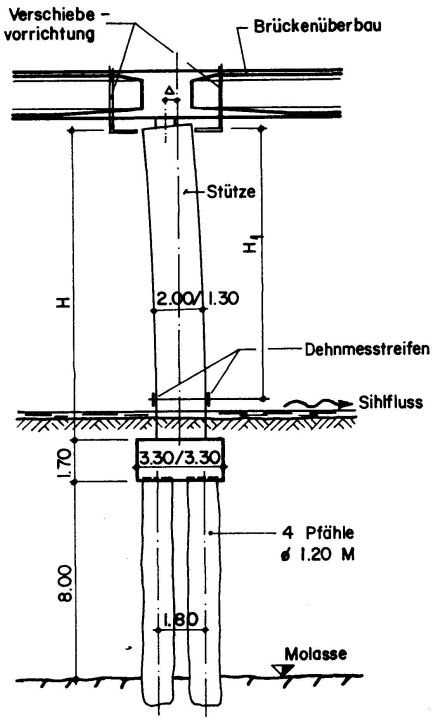


Fig. 6. Versuchsanordnung.

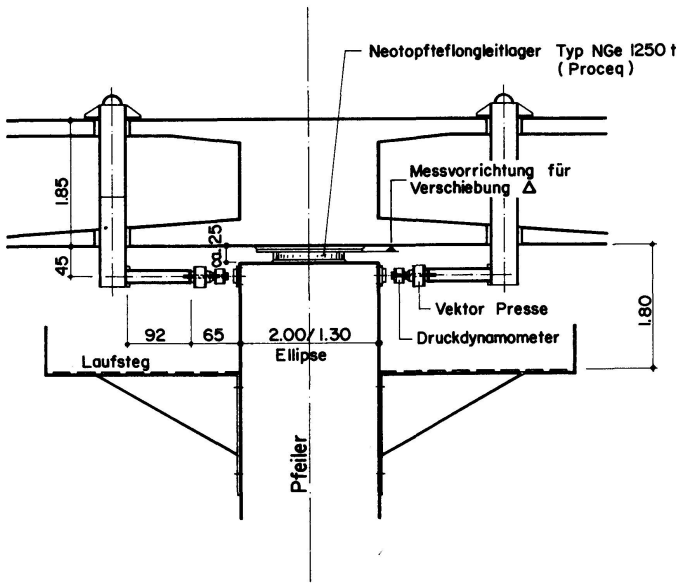


Fig. 7. Detail der Verschiebevorrichtung.

Bei den Versuchen wurden die Pfeiler der untersuchten Lager gegenüber dem Brückenüberbau mit hydraulisch gesteuerten Pressen hin- und hergeschoben. Durch einen gekoppelten Schreiber wurde die aufgebrachte Pressenkraft in Abhängigkeit der Pfeilerkopfauslenkung $\Delta$ direkt in einem Kraft-Weg-Diagramm aufgetragen. Mittels Dehnmessstreifen, die am Pfeilerfuss angeordnet waren, wurden die auftretenden Spannungen im Pfeilerquerschnitt laufend überwacht. Die gemessenen Dehnungen $\varepsilon$ wurden ebenfalls in Abhängigkeit der Pfeilerkopfauslenkung $\Delta$ direkt in einem $\varepsilon$-Weg-Diagramm aufgezeichnet.

Aus den aufgezeichneten Diagrammen konnte die Reibungskraft bestimmt und mittels der bekannten Brückenauflast auf den Reibungskoeffizienten $\mu$ geschlossen werden.

## 3. Ermittlung der Reibung aus den Versuchen

### *3.1. Reines Gleiten (linearer Bereich)*

#### *3.1.1. Beziehungen zwischen Reibung, Feder- und Pressenkraft*

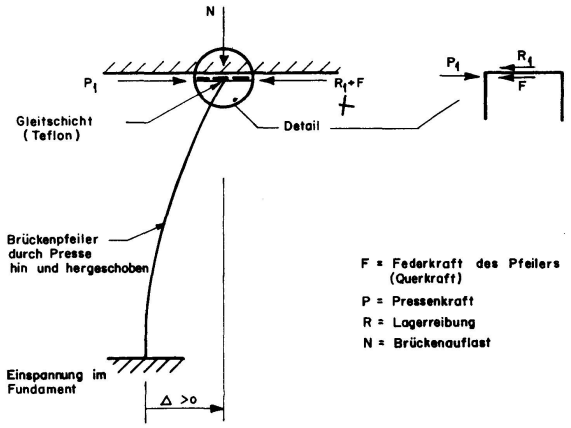


Fig. 8. Systemskizze mit angreifenden Kräften am Pfeilerkopf.

Da die Verformungen des Pfeilers sehr gering sind ($\Delta < 1$ cm), spielen sie bei der Gleichgewichtsbetrachtung am Pfeilerkopf eine vernachlässigbare Rolle (Problem erster Ordnung). Es gilt somit allgemein für einen nach rechts gedrückten Pfeiler:

$$P_1 - R_1 - F = 0 \tag{1}$$

Die als Federkraft F bezeichnete Querkraft wirkt konstant über die Pfeilerhöhe. Sie erzeugt ein linear zunehmendes Biegemoment im Pfeiler und ein Drehmoment im Fundament. Diese Momente bewirken die Pfeilerauslenkung $\Delta$. Da die Messdauer kurz (höchstens eine Stunde), der Beton schon alt (ca. vier Jahre) ist und nirgends Zugspannungen auftreten, darf Proportionalität zwischen Auslenkung und Federkraft vorausgesetzt werden.

Es gilt somit $$F = a_1 \cdot \Delta$$

Aus der Rechnung und den Versuchen zeigt sich, dass für das Fundament eine starre Einspannung angenommen werden darf.

Es folgt daraus $$F = \frac{3\,EJ}{H^3} \cdot \Delta \tag{2}$$

mit EJ = Biegesteifigkeit des homogenen Querschnittes Beton plus Armierung.

H = Pfeilerhöhe (bzw. Abstand Pressenkraft zum Fundament).

(2) in (1) eingesetzt ergibt:

$$R_1 = P_1 - \frac{3\,EJ}{H^3} \cdot \Delta \tag{3}$$

Diese Beziehung lässt leicht erkennen, dass die Reibungswerte R folgendermassen aus den Versuchsergebnissen ermittelt werden können:

a) unter Eliminierung von Δ.

Wird bei einem um $\Delta > 0$ ausgelenkten Pfeiler die Richtung der Pressenkraft geändert, so stellt sich folgendes Gleichgewicht ein:

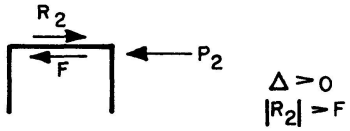


Fig. 9. Kräfte am Pfeilerkopf.

$$R_2 = P_2 + F = P_2 + \frac{3\,EJ}{H^3} \cdot \Delta \tag{3'}$$

Durch Addition der Gleichungen (3) und (3') wird Δ eliminiert:

$$R_1 + R_2 = P_1 + P_2 \tag{4}$$

Sofern die Reibungskräfte in beiden Bewegungsrichtungen gleich gross sind, gilt $R_1 = R_2 = R_0$ und

$$R_0 = \tfrac{1}{2}(P_1 + P_2) \tag{4'}$$

*b*) ohne Eliminierung von Δ.

Im linearen Bereich $P = f(\Delta)$ gilt, indem aus (3) für $P = 0$ und $\Delta = -\Delta_0$:

$$R_\Delta = \frac{3\,EJ}{H^3} \cdot \Delta_0 \tag{5}$$

dieser Sonderwert wieder in (3) eingesetzt wird:

$$P = R_\Delta + \frac{3\,EJ}{H^3} \cdot \Delta = \frac{3\,EJ}{H^3}(\Delta_0 + \Delta),$$

worin der Proportionalitätsfaktor $\frac{3\,EJ}{H^3} = \frac{P}{\Delta_0 + \Delta}$ die Neigung der Geraden $P = f(\Delta)$ bedeutet.

Die Reibung lässt sich also aus (5) ermitteln zu:

$$R_\Delta = P \frac{\Delta_0}{\Delta_0 + \Delta} \tag{5'}$$

wobei (4') ein Sonderfall von (5') darstellt, wenn $\Delta = \Delta_0$ und $P_1 = P$ und $P_2 = 0$ gesetzt werden.

Ist die Nullage des Pfeilers, d.h. der Koordinatenursprung der linearen Funktion $P = f(\Delta)$ bestimmt, so ist $\Delta = 0$ und $R_\Delta = P$. Die Biegesteifigkeit EJ, die genaue Pfeilerhöhe H bis zur Einspannstelle sowie eine eventuelle (elastische) Fundamentverdrehung brauchen für den linearen Bereich $P = f(\Delta)$ gar nicht bekannt zu sein. Wie unter 3.12 gezeigt werden wird, ist dies bei reinem Gleiten der Fall.

In Kapitel 3.2 dagegen wird auf die gemessenen Kriecherscheinungen eingegangen, für deren Auswertung die Federkraft F in Abhängigkeit der Auslenkung $\Delta$ bekannt sein muss.

Es gilt nach (2) und (3):

$$F = \frac{3\,EJ}{H^3} \cdot \Delta = P_1 - R_1 \text{ und, nachdem } R_1 \text{ in (5') zu } R_\Delta$$

bestimmt wurde, lässt sich die Federkonstante des Pfeilers leicht anschreiben zu

$$a_1 = \frac{3\,EJ}{H^3} = \frac{P_1 - R_\Delta}{\Delta} \tag{6}$$

Dabei kann noch überprüft werden, inwiefern die gemessenen Werte mit rechnerischen Werten E, J und H übereinstimmen. Ein weiterer Vergleich ergibt sich durch die Auswertung der gemessenen spezifischen Dehnungen $\varepsilon$ in Abhängigkeit der Auslenkung $\Delta$.

Es gilt nämlich folgende Beziehung:

$$\sigma = E \cdot \varepsilon = \frac{M \cdot b}{J} = \frac{F \cdot H_1 \cdot b}{J}$$

mit b = halbe Pfeilerstärke.

$H_1$ = Abstand Pressenkraft zu Dehnungsmessstelle und somit:

$$F = \frac{3\,EJ}{H^3} \cdot \Delta = \frac{EJ}{bH_1} \cdot \varepsilon \text{ oder } \frac{\Delta}{\varepsilon} = \frac{H^3}{3\,bH_1} \tag{7}$$

### *3.1.2. Versuchsauswertung*

Solange die Pfeiler mit konstanten Geschwindigkeiten hin- und hergeschoben wurden, konnten innerhalb eines Versuches erstaunlich konstante Reibungswerte anhand zweier parallelen Geraden im Kraft-Weg-Diagramm festgestellt werden. Dies bedeutet, dass hier die Reibung und die Federkonstante unabhängig von der Auslenkung $\Delta$, von der Pfeilernullage und von der Verschieberichtung wirklich

konstante Werte sind, die gemäss 3.1.1 ausgewertet werden können. Die Nullage der Pfeiler liegt in der Mitte zwischen den Schnittpunkten der Parallelen $P_1$ und $P_2$ mit der Abszisse.

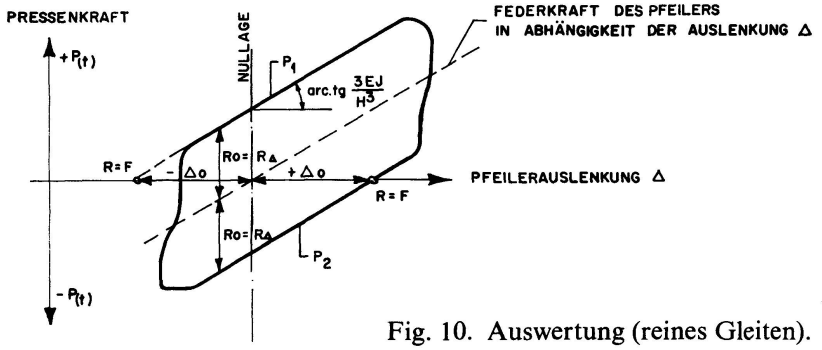


Fig. 10. Auswertung (reines Gleiten).

Für die Auswertung von $R_\Delta$ wurde für P der mittlere Abstand zwischen den aufgezeichneten, ca. parallelen Kraft-Weg-Linien herausgelesen. Für die Auswertung der Federkonstanten wurde die mittlere Neigung dieser Linien genommen. Der Vergleichswert $\frac{\Delta}{\varepsilon}$ schliesslich ergibt sich als reziproker Wert der Neigung des gemessenen $\varepsilon(\Delta)$ – Diagrammes.

*Numerische Auswertung*

| Lager Nr. | Versuch Nr. | In Nullage gemessene Gleitgeschwindigkeit V in mm/sec · $10^{-2}$ | Pressenkraft Aenderung pro Sekunde P/sec (t) | Gleitreibung $R_\Delta = P\frac{\Delta_o}{\Delta_o+\Delta}$ (t) | Gleitreibung $\mu$ % | Federkonstante $a_1 = \frac{3EJ}{H^3} = \frac{P_1 R_\Delta}{\Delta}$ (t/m) | Vergleichswert $\frac{\Delta}{\varepsilon} = \frac{H^3}{3bH_1}$ (m) |
|---|---|---|---|---|---|---|---|
| Lager 115 Ost, Auflast 820 t | 1 | 1,4 | 0,067 | 29 | 3,55 | -- | -- |
| | 2 | 29,0 | 1,33 | (25 - 40) | (3,05-4,90) | -- | -- |
| | 3 | 2,6 | 0,12 | 21,7 | 2,65 | $5{,}0\cdot10^3$ | 50,5 |
| | 5 | 4,3 | 0,2 | 15,6 | 1,90 | 4,8 " | 52,1 |
| | 6 | 21,8 | 1,0 | 15,3 | 1,87 | 4,81 " | 52,1 |
| | 7 | 21,8 | 1,0 | 14,7 | 1,79 | 4,70 " | 52,1 |
| | 8 | 65,3 | 3,0 | 13,3 | 1,62 | 4,65 " | 51,8 |
| | 10 | 21,8 | 1,0 | 11,3 | 1,38 | 4,60 " | 51,3 |
| | 11 | 0,65 | 0,03 | 8,3 | 1,01 | 4,50 " | 51,5 |
| | 12 | 4,3 | 0,2 | 8,8 | 1,07 | 4,65 " | 52,4 |
| | 13 | 5,4 | 0,25 | 9,2 | 1,12 | 4,65 " | 51,8 |
| | 15 | -- | -- | unbrauchbar | | -- | -- |
| | 16 | 21,6 | 1,0 | 11 | 1,34 | 4,50 " | 51,3 |
| | 17 | 21,6 | 1,0 | 11 | 1,34 | 4,50 " | 52,1 |
| | 18 | -- | -- | unbrauchbar | | -- | -- |
| | 19 | 1,8 | 0,08 | 8,7 | 1,06 | 4,5 " | 50,5 |
| | 20 | 10,8 | 0,5 | 9,3 | 1,13 | 4,4 " | 51,0 |
| | 21 | 0,7 | 0,03 | 7,7 | 0,99 | 4,4 " | 51,3 |
| | 22 | 2,4 | 0,11 | 8,3 | 1,01 | 4,6 " | 51,5 |
| | 23 | 7,2 | 0,33 | 8,0 | 0,98 | 4,6 " | 52,1 |
| | | | | Mittel | 1,31 | Mittel: $4{,}62\cdot10^3$ | Mittel: 51,65 |
| Lager 114 Ost, Auflast 810 t | 24 | -- | 0,083 | 26,0 | 3,21 | -- | -- |
| | 25 | -- | 4,0 | 30,0 | 3,70 | -- | -- |
| | 26 | -- | -- | unbrauchbar | -- | -- | -- |
| | 28 | 4,6 | 0,22 | 25,0 | 3,09 | $4{,}70\cdot10^3$ | 46,7 |
| | 29 | 2,9 | 0,13 | 18,0 | 2,22 | 4,85 " | 45,9 |
| | 30 | 1,3 | 0,06 | 14,5 | 1,79 | 4,70 " | 47,2 |
| | 31 | 21,0 | 1,0 | 20,6 | 2,54 | 4,70 " | 45,2 |
| | 32 | 21,0 | 1,0 | 17,5 | 2,16 | 4,70 " | 45,0 |
| | | | | Mittel | 2,67 | Mittel: $4{,}73\cdot10^3$ | Mittel: 46,0 |

Zum Vergleich seien noch rechnerische Werte angegeben, wobei die Höhe H das obere Einspannmoment berücksichtigt (Angriffsebene von R ca. 45 cm höher als jene von P).

$$\frac{3\,EJ}{H^3} = \frac{3 \cdot 4{,}5 \cdot 10^6 \cdot 0{,}545}{12{,}0^3} = 4{,}3 \cdot 10^3 \text{ t/m'}$$

$$\frac{H^3}{3\,b \cdot H_1} = \frac{12{,}0^3}{3 \cdot 1{,}0 \cdot 11{,}0} = 52 \text{ m'}$$

*Interpretation der Ergebnisse*

— Die Reibungskoeffizienten sind bei den ersten Versuchen am grössten und nehmen, bedingt durch die Hin- und Herbewegung der Pfeiler (Schmiereffekt), rasch ab.

— Die Rebungskoeffizienten sind in beiden Richtungen gleich gross.

— Der Reibungskoeffizient ist abhängig von der Gleitgeschwindigkeit, was besonders bei den ersten Versuchen zum Ausdruck kommt. Bei den nachfolgenden Versuchen kann dies infolge des eingetretenen Schmiereffektes nicht mehr eindeutig ausgesagt werden.

— Die Gleitgeschwindigkeiten betrugen bei den ersten Versuchen $1{,}4 \cdot 10^{-2}$ bis $29 \cdot 10^{-2}$ mm/sec.
Unter der ungünstigen Annahme, dass sich die mittlere Temperatur des Überbaus um 1 Grad pro Stunde ändern würde, ergeben sich Gleitgeschwindigkeiten von maximal $9 \cdot 10^{-4}$ mm/sec im Bereiche der Versuchslager. Diese Geschwindigkeiten sind somit 15 bis 300 mal kleiner als die Versuchsgeschwindigkeiten.

— Die ausgewerteten Gleitreibungen treffen für die Versuchs-Gleitgeschwindigkeiten zu, geben jedoch wegen des in den Versuchen festgestellten Kriechverhaltens des Teflons keinen Aufschluss über die in Wirklichkeit am Bauwerk auftretenden Lagerreibungen bei wesentlich geringeren Gleitgeschwindigkeiten.

### *3.2. Gleiten und Kriechen (nicht linearer Bereich)*

Nach dem Aufbringen und Halten einer bestimmten Pressenkraft stellte sich nicht sofort ein Gleichgewichtszustand zwischen Pressenkraft, Federkraft und Lagerreibung ein. Dies ist nicht etwa auf eine Fundament-Verdrehung zurückzuführen, was unter anderem durch das konstante Verhältnis $\frac{\Delta}{\varepsilon}$ nachgewiesen ist. Die Ursache liegt im Kriechverhalten des Teflons. Bei den ersten ungestörten Versuchen dauerte es jeweils mehrere Minuten, bis sich ein Gleichgewicht der Kräfte einstellte. Dasselbe Bild zeigte sich, wenn bei ausgelenkter Pfeilerlage die Pressen voll entlastet wurden.

In Wirklichkeit werden die Pfeiler durch Bewegungen des Brückenüberbaus nur soweit ausgelenkt, bis die Federkraft des Pfeilers die Lagerreibung erreicht hat. Alsdann stellt sich ein neuer Gleichgewichtszustand zwischen Feder- und Reibungskraft ein.

Entsprechend dem naturgetreuen Ablauf werden die Reibungswerte bei dieser Versuchsauswertung in jenen Punkten der Diagramme ermittelt, wo sich bei ausgelenkter Pfeilerlage ein Gleichgewicht der Kräfte einstellt.

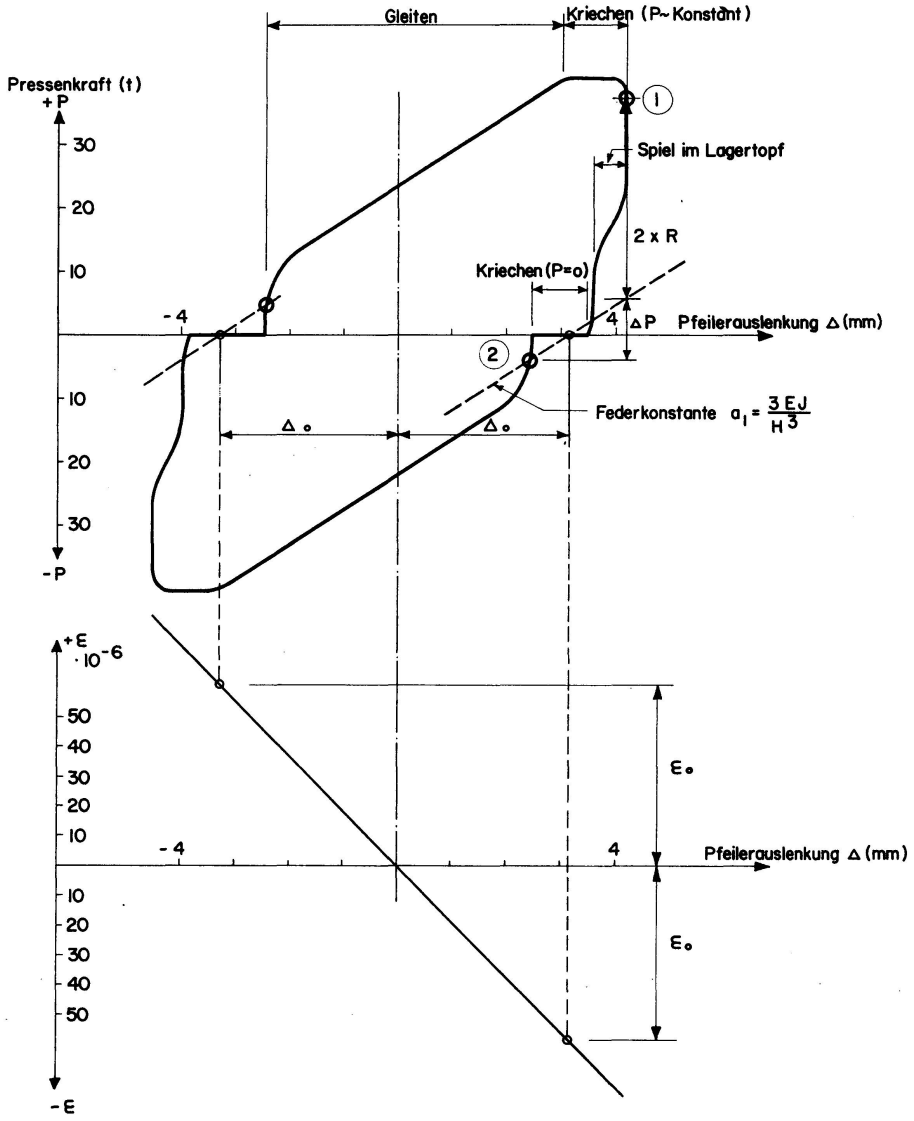


Fig. 11. Auswertung (Gleitung und Kriechen).

*Die Reibungswerte lassen sich auf 3 Arten bestimmen*

a) *Direkt aus dem Diagramm gemessen*

$\overset{P_1}{\rightarrow}\ \overset{+\ R_1}{\underset{F_1}{\leftarrows}}$ Gleichgewicht Pkt 1: $P_1 = F_1 + R_1$; $R_1 = P_1 - F_1$.

$\overset{R_2}{\rightarrow}\ \overset{P_2}{\underset{F_2}{\leftarrows}}$ Gleichgewicht Pkt 2: $R_2 = |P_2| + F_2 = |P_2| + F_1 - |\Delta P|$

unter der Annahme, dass $R_1 = R_2$ ist, gilt:

$$2 \cdot R = P_1 - F_1 + |P_2| + F_1 - |\Delta P|$$

$$R = \frac{P_1 + |P_2| - |\Delta P|}{2}$$

b) *In Abhängigkeit der Auslenkung* $\Delta_0$

für $P = 0$ folgt nach Gleichung (5)

$$F = R_\Delta = \frac{3 \cdot EJ}{H^3} \cdot \Delta = a_1 \cdot \Delta$$

Mittlere Federkonstante $a_1$ aus Versuchen:
für Stütze 115 Ost: $a_1 = 4{,}62 \cdot 10^3$ t/m'
für Stütze 114 Ost: $a_1 = 4{,}73 \cdot 10^3$ t/m'

c) *In Abhängigkeit der spezifischen Dehnungen* $\varepsilon_0$ *zur Auslenkung* $\Delta_0$

für $P = 0$ folgt:

$$F = R = \frac{E \cdot J}{b \cdot H_1} \cdot \varepsilon_0 = \frac{a_1}{\varepsilon} \cdot \varepsilon_0$$

aus Versuchen:

$$\frac{a_1}{\varepsilon} = \frac{\text{Mittlere Federkonstante}}{\text{Mittleres } \varepsilon}$$

für Stütze 115 Ost: $\frac{a_1}{\varepsilon} = 4{,}62 \cdot 10^3 \cdot 51{,}61 = 0{,}24 \cdot 10^6$ t

für Stütze 114 Ost: $\frac{a_1}{\varepsilon} = 4{,}73 \cdot 10^3 \cdot 46{,}0 = 0{,}22 \cdot 10^6$ t

*Versuchsauswertung*

| | Versuch Nr. | V mm/s·10$^{-2}$ | $\frac{\Delta P}{S}$ | Ergebnis aus gemessener Kraft R | $\mu$ % | Ergebnis aus gemessener Stützenauslenkung $\Delta$ ·10$^{-3}$m | $a_1$ ·10$^3$ $\frac{t}{m}$ | $R_\Delta$ | $\mu$ % | Ergebnis aus gemessenen Dehnungen $\varepsilon_0$ ·10$^{-6}$ | $\frac{a_1}{\varepsilon}$ ·10$^6$t | $R_\varepsilon$ | $\mu$ % | $\mu$ Mittel % |
|---|---|---|---|---|---|---|---|---|---|---|---|---|---|---|
| Lager 115 Ost Auflast 820 t | 1 | 1,4 | 0,067 t | 22,5 t | 2,8 | 3,6 | 4,62 | 16,6 t | 2,02 | 70 | 0,24 | 16,8 t | 2,05 | 2,29 |
| | 2 | 29 | 1,33 t | 18,5 t | 2,26 | 4,2 | " | 19,4 t | 2,37 | 83 | " | 19,9 t | 2,43 | 2,34 |
| | 3 | 2,6 | 0,12 t | 15 t | 1,83 | 3,3 | " | 15,2 t | 1,85 | 67 | " | 16,1 t | 1,96 | 1,88 |
| | 5 | 4,3 | 0,2 t | 14 t | 1,71 | 3,1 | " | 14,3 t | 1,74 | 50 | " | 12,0 t | 1,46 | 1,64 |
| Lager 114 Ost Auflast 810 t | 24 | - | 0,083 t | 21 t | 2,59 | kein Resultat, die Stütze ist unwesentlich aus der Nullage ausgelenkt | | | | kein Resultat, die Stütze ist nur unwesentlich aus der Nullage ausgelenkt | | | | |
| | 25 | - | 0,2 t | 22 t | 2,71 | 4,5 | 4,73 | 21,3 t | 2,63 | | | | | 2,67 |
| | 28 | | | | | | | | | | | | | |
| | 1. Umgang | 4,6 | 0,22 t | 20,3 t | 2,50 | 4,3 | " | 20,3 t | 2,51 | 95 | 0,22 | 20,9 t | 2,58 | 2,53 |
| | 2. Umgang | 4,6 | 0,22 t | 17 t | 2,10 | 3,7 | " | 17,5 t | 2,16 | 82 | " | 18 t | 2,22 | 2,16 |
| | 3. Umgang | 4,6 | 0,22 t | 15 t | 1,85 | 3,3 | " | 15,6 t | 1,93 | 74 | " | 16,3 t | 2,01 | 1,93 |
| | 29 | 2,9 | 0,13 t | 15 t | 1,85 | 3,25 | " | 15,4 t | 1,90 | 71 | " | 15,6 t | 1,93 | 1,89 |
| | 30 | 1,3 | 0,06 t | 12 t | 1,48 | 2,95 | " | 14,0 t | 1,73 | 64 | " | 14,1 t | 1,74 | 1,65 |
| | 31 | 21,0 | 1,0 t | 14,5 t | 1,79 | 3,2 | " | 15,1 t | 1,86 | 70 | " | 15,4 t | 1,90 | 1,85 |
| | 32 | 21,0 | 1,0 t | 14 t | 1,73 | 3,2 | " | 15,1 t | 1,86 | 71 | " | 15,6 t | 1,93 | 1,84 |

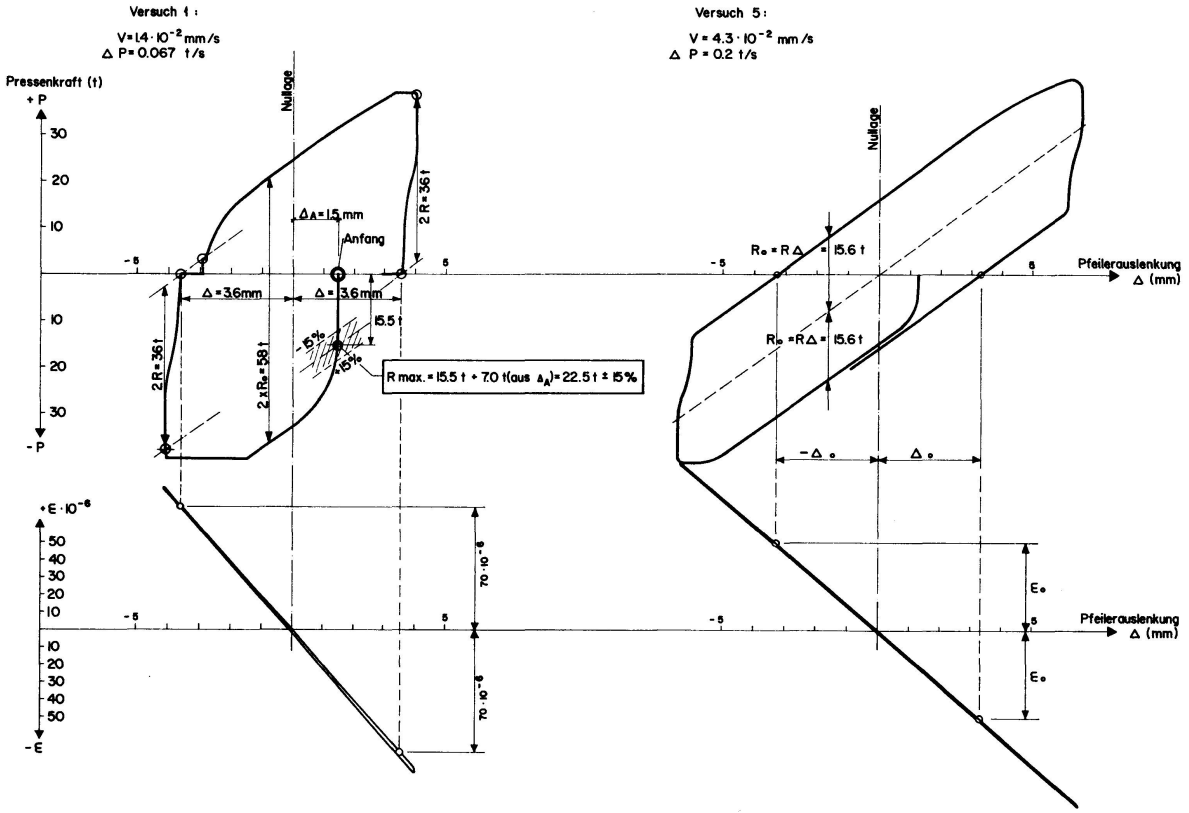


Fig. 12. Lager 115 Ost, Versuchsdiagramme 1 und 5.

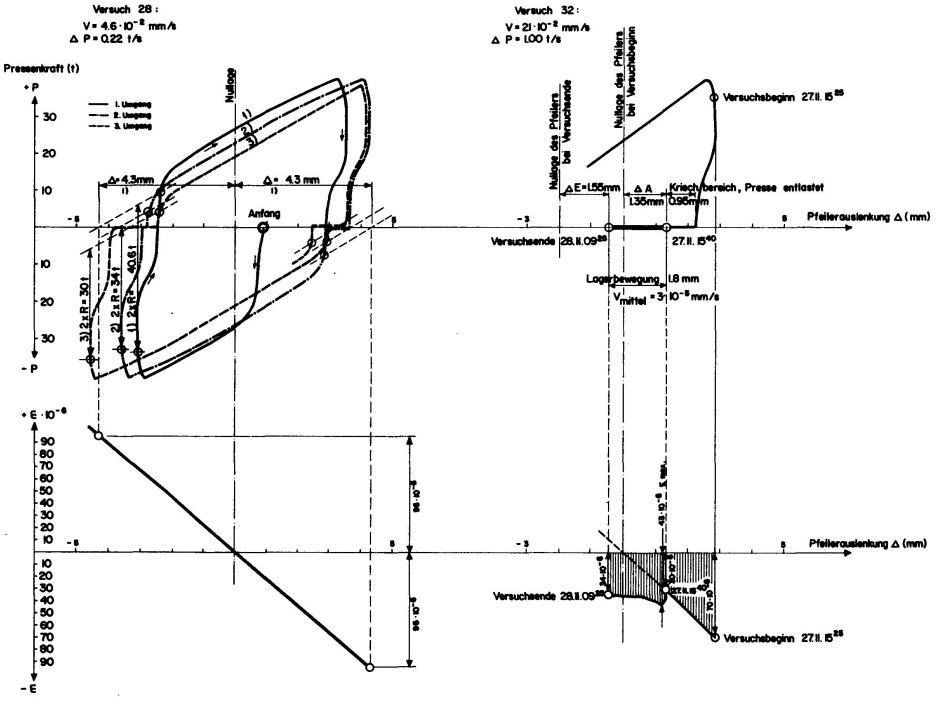


Fig. 13. Lager 114 Ost, Versuchsdiagramme 28 und 32.

*Beurteilung der Ergebnisse*

Der Übergang vom Lagerstillstand zur Lagerbewegung ist in den Diagrammen zum Teil schwierig erfassbar. (Schleifender Schnitt.) Die Ergebnisse sind deshalb mit einem Fehler behaftet, der bei beiden Lagern innerhalb von ± 15% liegen dürfte. (Siehe Auswertung Versuch 1.)

Die langsam durchgeführten Versuche (kleine Presskraftänderung pro Zeiteinheit) erlauben eine genauere Erfassung dieser Punkte als die schnell durchgeführten Versuche. Unter Berücksichtigung eines Zuschlages von 15% erhalten wir beim jeweiligen ersten Versuch folgende Werte:

| Lager | Versuch | | Reibung | |
|---|---|---|---|---|
| | Nr. | Geschwindigkeit | R | μ |
| Pfeiler 115 Ost . . . . . | 1 | $1{,}4 \cdot 10^{-2}$ mm/sec | 26 t | 3,2% |
| Pfeiler 114 Ost . . . . . | 24 | $0{,}7 \cdot 10^{-2}$ mm/sec | 24 t | 3,0% |

## 4. Ermittlung der Reibung infolge der natürlichen Brückendilatation

Beim Lager 114 Ost konnte dank günstiger Witterungsbedingungen beim letzten Versuch Nr. 32 eine Überprüfung der Lagerreibung über eine Zeitspanne von 17 Stunden vorgenommen werden.

Über diese Zeitspanne, welche durch eine ständige Abkühlung des Brückenkastens bei annähernd konstanter Aussentemperatur gekennzeichnet war, wurden einerseits die einseitigen Lagerbewegungen, anderseits die aufgetretenen Dehnungen am Pfeilerfuss laufend registriert.

| Versuch 32 | Reibung aus gemessenen ε – Werten | | | | Bemerkungen |
|---|---|---|---|---|---|
| | ε $\cdot 10^6$ | $\frac{a_1}{\varepsilon}$ $\cdot 10^6$ (t) | R (t) | μ % | |
| 27.11. $15^{25}$ | 70 | | | | – Versuchsbeginn: gemessenes ε bei maximaler Auslenkung mittels Pressen. |
| 27.11. $15^{40}$ | 30 | 0,22 | 6,6 | 0,82 | – Nach Einspielen des Pfeilers, Pressen entlastet. Wartezeit 15'. |
| | 43 | 0,22 | 9,4 | 1,16 | – Maximalwert während des Versuches. |
| 28.11. $09^{25}$ | 34 | 0,22 | 7,5 | 0,92 | – Wert bei Versuchsende. |

Bei diesem Versuch, wo die Lagerbewegung und die Pfeilerauslenkung entsprechend dem natürlichen Vorgang durch Eigenbewegungen des Überbaus bewirkt wurden, sind somit Reibungskoeffizienten zwischen 0,82% und 1,16% nachgewiesen.

Der untere Wert entspricht dem Gleitreibungskoeffizienten, der nach dem Einspielen des Pfeilers bei entlasteter Presse auch bei den übrigen Versuchen in dieser Grössenordnung festgestellt wurde, der obere Wert deutet auf einen Anfahrwert (Haftreibung) hin.

Die Bewegung des Lagers während des Versuches betrug total 1,8 mm, die mittlere Verschiebegeschwindigkeit $3 \cdot 10^{-5}$ mm/sec.

Ein Vergleich der Reibungswerte $\mu$ mit Hilfe der gemessenen Auslenkungen $\Delta$ zeigt eine gute Übereinstimmung.

| Zeit | Reibung aus Auslenkung | | | Bemerkungen |
|---|---|---|---|---|
| | $\Delta$ mm | R | $\mu$ % | |
| 27.11. $15^{40}$ | 1,35 | 6,4 t | 0,79 | – nach Einspielen des Pfeilers, Presse entlastet. |
| 28.11. $09^{25}$ | 1,55 | 7,4 t | 0,91 | – bei Versuchsende. |

## 5. Schlussfolgerungen für die Praxis

Der entwerfende Ingenieur, der PTFE-Gleitlager (z.B. aus Teflon) in einem Bauwerk einzubauen gedenkt, stützt sich für die Ermittlung der Reibung auf amtliche Richlinien oder Angaben des Lieferanten. In der Schweiz z.B. gelten die im Jahre 1973 durch das Eidg. Departement des Innern (Amt für Strassen- und Flussbau) herausgegebenen «Standardprojekte für Brücken», worin folgende Angaben stehen:

| PTFE-Pressung kg/cm$^2$ | 100 | 200 | 300 | 450 |
|---|---|---|---|---|
| Reibungsbeiwert $\mu$ . . . . . | 5% | 4% | 3% | 2,5% |

Mit diesen Angaben allein wird sich der entwerfende Ingenieur aber nicht begnügen, denn er wird wissen wollen, ob es sich dabei um Mittelwerte oder um mutmassliche oder absolute Grösstwerte handelt.

In der Tat stellen diese Werte mutmassliche Grösstwerte dar, die sich im Labor an Teflonmustern unter Berücksichtigung verschiedener Temperaturen, Gleitgeschwindigkeiten und Laufwege ergeben.

Man wird aber das unangenehme Gefühl nicht los, dass dabei wesentliche Aspekte unberücksichtigt bleiben. Dazu gehören, wie schon unter 1.) erwähnt, Alterung, Verschmutzung, Ausführungstoleranzen usw. Hinzu kommt die Frage nach dem Anfahrwert (Haftreibung).

Die hier an zwei seit drei Jahren in einem Brückenbauwerk eingebauten Lagern *in situ* durchgeführten Messungen konnten natürlich nicht über alle Fragen Auskunft geben. Die Messungen wurden bei niedriger Temperatur (ca. 0° Celsius) an normal verschmutzten, mit normalen Ausführungstoleranzen versehenen Lagern und mit normalen, durch die Führungsleiste erzeugten Zwängungen durchgeführt.

Um über die Alterung Auskunft zu erhalten, sollen die Versuche periodisch wiederholt werden.

Die gemessenen Werte stellen somit etwa Mittelwerte dar, die unter ungünstigeren Bedingungen grösser ausfallen würden.

Da die Teflon-Pressung in den untersuchten Lagern 258 bzw. 261 kg/cm$^2$ beträgt, ergibt sich durch Interpolation der oben angegebenen Reibungswerte $\mu$ ein Rechenwert von 3,4%. In den Versuchen wurden Gleitreibungswerte von 1,0 bis 3,7% festgestellt. Grössere Werte infolge Haftreibung beim Anfahren wurden nie festgestellt. Dagegen ergaben sich kleinere Werte bei sinkender Gleitgeschwindigkeit, besonders bei jener, die sich aus der natürlichen Brückendilatation ergab (siehe 4.). Hier wurden nur noch Reibungsbeiwerte von 0,8 bis 1,2% gemessen.

Als wesentlich neue Erkenntnis hat sich gezeigt, dass Teflon-Gleitlager kriechen, sofern man ihnen mit einer Schonzeit genügend Zeit lässt.

Diese Schonzeit, die einige Minuten bis Stunden dauert, ist aber bei den meisten Anwendungen immer vorhanden. Da die Bewegungen infolge Betonkriechen, Schwinden und Temperaturänderungen äusserst langsam vor sich gehen, ist für die Praxis nur jener Reibungswert von Interesse, der sich bei einer langandauernden, konstanten Horizontalkraft ergibt. Dieser Wert ist – wie gesagt – wesentlich kleiner als ein Gleitreibungswert wie er bis jetzt im Labor ermittelt wurde, geschweige von einem Haftreibungswert, der sich bei einer plötzlich auftretenden Horizontallast ergibt.

Zurzeit sind am «Centre d'Etude du Béton Armé et Précontraint» der Eidgenössischen Technischen Hochschule in Lausanne Versuche im Gange, die diese Vorgänge bestätigen.

Abschliessend kann folgendes festgehalten werden:

Obwohl weitere Untersuchungen an eingebauten Lagern unerlässlich sind, verhalten sich Teflon-Gleitlager dank Kriecherscheinungen günstiger als vermutet. Die oben angegebenen Reibungsbeiwerte $\mu$ in Abhängigkeit der Pressung können, sofern keine abnormale Verschmutzung vorliegt, als Rechenwerte für die statischen Nachweise bedenkenlos angewendet werden. Vollständigere Untersuchungen werden vielleicht zu noch kleineren Werten in den Rechenvorschriften führen.

## Zusammenfassung

An zwei seit drei Jahren eingebauten Teflon-Gleitlagern wurden eingehende Reibungsversuche in situ durchgeführt. Es hat sich dabei gezeigt, dass bei sehr langsamen Vorgängen, wie z.B. einer Brückendilatation, die Reibung dank dem Teflonkriechen wesentlich kleiner ausfällt als beim reinen Gleiten oder beim plötzlichen Anfahren.

Da für praktische Fälle immer mit einer genügenden Schonzeit gerechnet werden kann und die Kriecherscheinung stattfinden wird, verhalten sich solche Lager günstiger als vermutet. Damit konnten in der Praxis angewendete Rechenwerte der Reibung, die sich aus reinen Laborversuchen ergaben, bestätigt werden.

## Summary

This paper describes tests carried out "in situ" on two teflon sliding bearings, after three years of service. The study showed that friction is greatly reduced, compared to a pure sliding or a movement starting suddenly, by the creep-effect of

teflon, as long as the displacement is very slow, as it is by dilatation of bridges. Since, in practical cases, the bearings have always an adequate time to respond to an horizontal thrust with yelding by creep, the behaviour of such bearings will be better than expected. Thus, it has been possible to confirm the values of the friction factors assumed in practice, that were obtained by extrapoling laboratory tests results.

**Résumé**

L'article décrit les essais in situ effectués sur deux appuis glissants au teflon, qui étaient en service depuis trois années. L'étude de leur comportement a révélé que le frottement était grandement diminué — par suite de l'effet de fluage du teflon — lors de phénomènes très lents tels la dilatation d'un pont par rapport à un glissement pur ou un démarrage brusque. Etant donné que, dans la pratique, les appuis auront toujours le temps nécessaire de répondre à une sollicitation horizontale en cédant par fluage, ils se comportent plus favorablement que prévu. Il a été ainsi possible de confirmer les coefficients de frottement admis dans la pratique et résultant d'extrapolation d'essais en laboratoire.

# Ultimate Strength and Design of Reinforced Concrete Beams under Bending and Shear

*Résistance et dimensionnement des poutres en béton armé soumises à la flexion et à l'effort tranchant*

*Bruchwiderstand und Bemessung von Stahlbetonbalken unter Biegung und Schub*

JOSEF GROB
Dr. sc. techn.

BRUNO THÜRLIMANN
Professor Dr. sc. techn.

Institute of Structural Engineering, Swiss Federal Institute of Technology (ETH) Zurich (Switzerland)

## 1. Introduction

In the present paper the plastic resistance of underreinforced concrete beams under bending and shear is investigated using the theory of plasticity. A truss model with variable inclination of the concrete diagonals is applied. This model consists of the longitudinal reinforcing bars acting as stringers, the stirrups as vertical ties and the concrete diagonals as inclined struts forming a continuous compression field. The obtained solutions are special forms of the general yield criterion of underreinforced concrete walls with both the longitudinal and the stirrup reinforcement yielding. In this case a sufficient shear transfer within the cracks is assumed so that the concrete diagonals can reach their final inclination under ultimate loads. Due to the fact that the shear transfer within a crack decreases with increasing crack widths, additional considerations become necessary. Hence, limits of the inclination of the concrete diagonals are introduced.

Finally design equations for the dimensioning of reinforced and prestressed concrete beams under combined bending and shear are derived and compared with test results. The new Swiss Specifications based on these equations are discussed.

## 2. Shear Wall Element

The ultimate strength of many reinforced concrete structures, e.g. beams with solid, thin-walled open or closed cross sections, long cylindrical shells, depend on the carrying capacity of shear wall elements. For instance a beam with a thin-walled open cross section can be subdivided into a number of shear walls. To describe

their behavior a truss model is assumed with the longitudinal bars acting as stringers, the stirrups as vertical ties and the concrete diagonals as inclined compression struts.

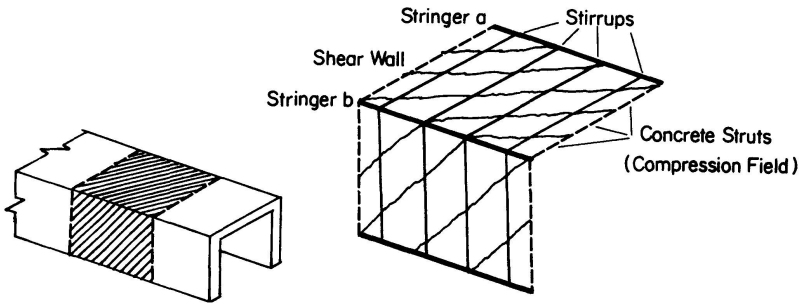


Fig. 1. Shear Walls of a Thin-Walled Reinforced Concrete Beam.

In order to simplify the mathematical treatment the longitudinal reinforcement is assumed to be concentrated into stringers located in the corners of the cross section.

### *2.1 Static Relations*

The static relations for a discret model with a 45°-inclination of the concrete diagonals were derived by Ritter and Mörsch about 70 years ago. In the case of torsion and bending, LAMPERT and THÜRLIMANN [8] introduced the more realistic truss model with variable inclination of the diagonals. This model has recently been applied to other cases like bending and shear or warping torsion.

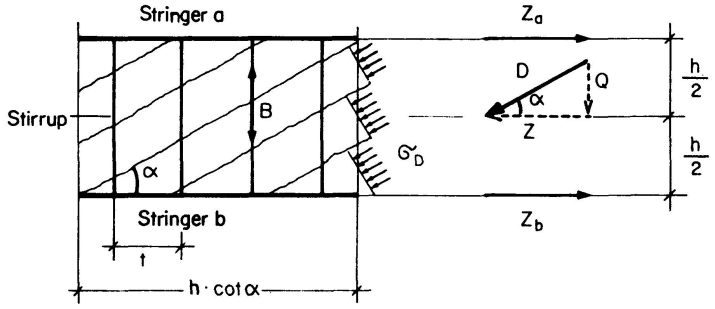


Fig. 2. Static Behavior of a Shear Wall Element.

The truss forces shown in Figure 2 are acting in the plane of the shear wall. The compression diagonals form a continuous compression field. The corresponding concrete stresses are assumed to be constant over the heigth of the shear wall element. Therefore these stresses furnish the resultant D acting at mid-heigth $\frac{h}{2}$. Its components Z and Q show that an applied shear force Q produces a normal force Z:

$$Z = Q \cdot \cot \alpha \tag{1}$$

Since the stirrups together with the stringers provide a continuous support for the diagonals, a constant distribution of stirrup forces is obtained in the shear

wall element. Because there are $\frac{h}{t} \cdot \cot \alpha$ stirrups per element the following relation exists between the shear force Q and the tensile force B of a stirrup:

$$Q = B \cdot \frac{h}{t} \cdot \cot \alpha \tag{2}$$

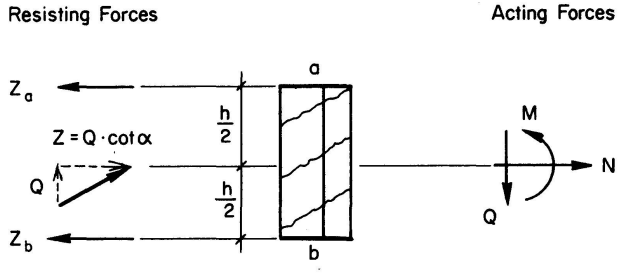


Fig. 3. Equilibrium in a Shear Wall.

If the shear wall element is subjected to a bending moment M, a normal force N and a shear force Q, the equilibrium conditions lead to the following stringer forces:

$$Z_a = -\frac{M}{h} + \frac{N}{2} + \frac{Q}{2} \cdot \cot \alpha \qquad Z_b = \frac{M}{h} + \frac{N}{2} + \frac{Q}{2} \cdot \cot \alpha \tag{3}$$

### *2.2 Plastic Resistance*

The plastic resistance of an underreinforced shear wall under bending and shear, Figure 3, is investigated. The amount of reinforcement is such that the resistance is determined by yielding of the reinforcements and not by crushing of the concrete. The carrying capacity is then calculated using the lower bound or static theorem of the theory of plasticity.

The yield force of the stringers a and b is $Z_f$ and that of one stirrup $B_f$, respectively.

The equilibrium conditions are obtained from Eqs. (2) and (3):

$$Q = B \cdot \frac{h}{t} \cdot \cot \alpha \qquad Z_a = -\frac{M}{h} + \frac{Q}{2} \cdot \cot \alpha \qquad Z_b = \frac{M}{h} + \frac{Q}{2} \cdot \cot \alpha$$

According to the lower bound theorem the highest values for $M_p$ and $Q_p$ (p = plastic) will lead to collapse provided equilibrium is fulfilled and the yield conditions are not violated. Here the maximum is reached if yielding of the stringer b and the stirrups occur. Thus the following equations are obtained:

$$Q_p = B_f \cdot \frac{h}{t} \cdot \cot \alpha \tag{4}$$

$$Z_f = \frac{M_p}{h} + \frac{Q_p}{2} \cdot \cot \alpha \tag{5}$$

Eq. (4) gives $\cot \alpha = \dfrac{Q_p}{B_f \cdot \frac{h}{t}}$

Substituting in Eq. (5) $Z_f = \dfrac{M_p}{h} + \dfrac{Q_p^2}{2 \cdot B_f \cdot \frac{h}{t}}$

It can be rewritten in the form of an interaction equation:

$$\frac{M_p}{M_{p0}} + \left(\frac{Q_p}{Q_{p0}}\right)^2 = 1 \tag{6}$$

with the reference values for the "Plastic Moment" $M_{p0}$ and the "Plastic Shear Force" $Q_{p0}$:

$$M_{p0} = Z_f \cdot h \qquad \text{for } Q_p = 0$$

$$Q_{p0} = \sqrt{2 Z_f \cdot B_f \cdot \frac{h}{t}} \qquad \text{for } M_p = 0$$

Eq. (6) is plotted in Figure 4. However, as will be discussed in Section 2.3, its validity is limited by the following values for the angle $\alpha$:

$$0.5 \leq |\tan \alpha| \leq 2.0 \tag{7}$$

Assuming the lower limit, $\tan \alpha = 0.5$, the highest shear capacity follows from Eq. (4):

$$Q_p = 2 B_f \cdot \frac{h}{t} \tag{8}$$

For the upper limit, $\tan \alpha = 2.0$, Eq. (5) gives

$$\frac{M_p}{M_{p0}} + \frac{1}{4} \cdot \frac{Q_p}{Z_f} = 1. \tag{9}$$

The derived Eqs. (6), (8) and (9) describe the bending-shear interaction diagram of Figure 4.

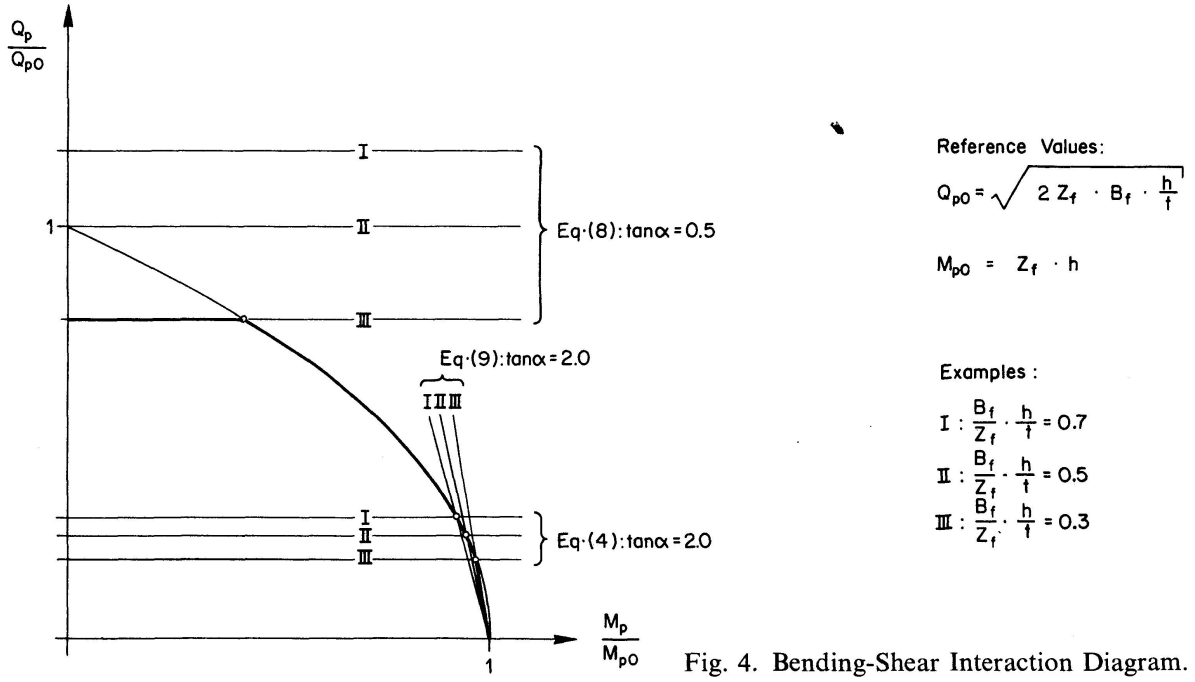


Fig. 4. Bending-Shear Interaction Diagram.

It can be seen from Figure 4 that the value $Q_{p0}$ will not be reached if the ratio of stirrup to longitudinal reinforcement is small, i.e. $\frac{B_f}{Z_f} \cdot \frac{h}{t} < 0.5$. The interaction is then limited by Eq. (8). Vice versa Eq. (9) bounds the interaction for high values of the bending moment, but the numerical influence of this limitation is negligible.

Using the upper bound or kinematic theorem of the theory of plasticity the equivalent kinematic solution has been derived in Ref. [5]. Since this solution agrees with the presented static solution, the following different mechanisms based on the interaction diagram can be distinguished.

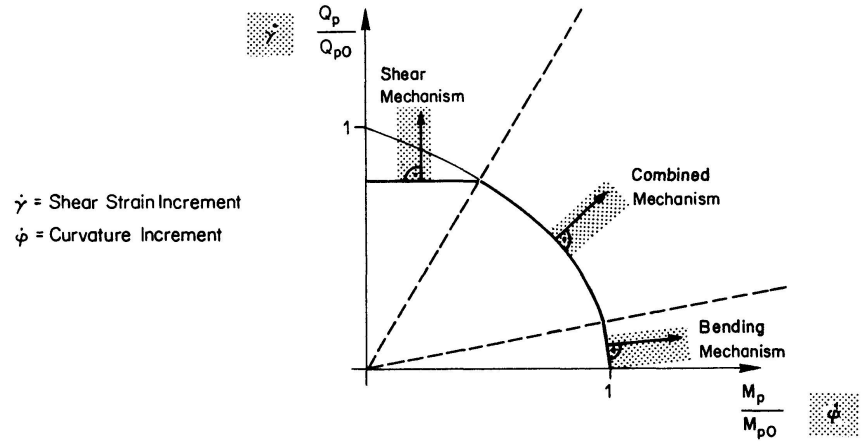


Fig. 5. Yield Surface and Mechanisms.

A combined mechanism occurs when both the longitudinal and stirrup reinforcement yield (Eq. (6)). A bending mechanism or a shear mechanism is obtained for yielding of the longitudinal ($\tan \alpha > 2.0$) or stirrup reinforcement ($\tan \alpha < 0.5$), respectively. Of course the bounds $\tan \alpha = 0.5$ or 2.0 should not be considered as fixed values. They indicate the transitions between the three different mechanisms.

### *2.3 Kinematic Considerations*

In this paper the kinematic relations are discussed only to the extent necessary to explain the limitations on the inclination of the concrete compression field. Further details are given in Ref. [5]. Since only underreinforced members are considered, the concrete is assumed to be rigid. Hence, all deformations are caused by elongations of the reinforcements.

Due to aggregate interlock the direction of the crack opening is first assumed to be normal to the crack direction. Hence, the following state of motion in a shear wall element is obtained for a constant displacement field, $\varepsilon_R$ being a convenient displacement parameter, i.e. the mean crack width divided by the mean crack distance.

The strains are directly obtained from the displacement diagram in Figure 6. The shearing strain $\gamma$ describing the distortion of the rectangular element is composed of the elongations in the longitudinal and transverse reinforcement:

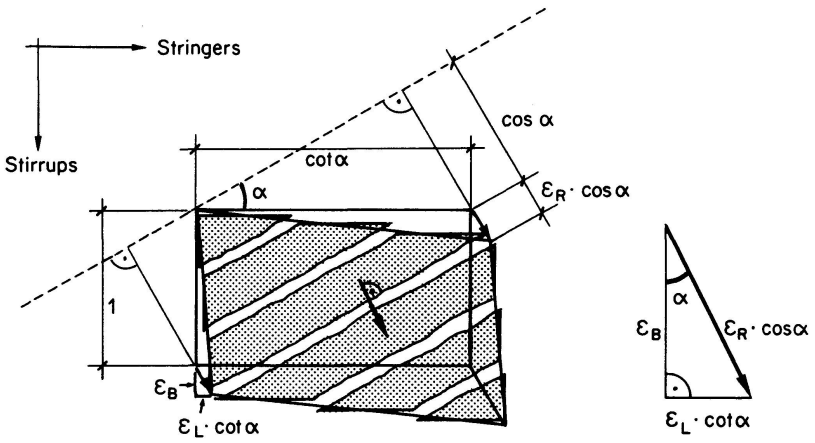


Fig. 6. Displacement Diagram for a Shear Wall Element.

$$\gamma = \varepsilon_L \cdot \cot\alpha + \varepsilon_B \cdot \tan\alpha \tag{10}$$

The elongations $\varepsilon_L$ and $\varepsilon_B$ are interconnected by

$$\varepsilon_B = \varepsilon_L \cdot \cot^2\alpha, \tag{11}$$

valid for an orthogonal crack opening. The displacement parameter $\varepsilon_R$ is related to the elongations of the reinforcement as follows

$$\text{With: } \varepsilon_R \cdot \sin^2\alpha = \varepsilon_L \qquad \varepsilon_R \cdot \cos^2\alpha = \varepsilon_B \qquad \rightarrow \varepsilon_R = \varepsilon_L + \varepsilon_B \tag{12}$$

However, the orthogonal crack opening as well as the inclination $\alpha$ of the compression field are subjected to certain limits. Responsible for these limits are the deformations, especially the crack widths necessary to reach ultimate resistance, i.e. yielding of both the longitudinal and stirrup reinforcement. To obtain an estimate of the ratios between the crack opening and the yield strains of the longitudinal and transverse reinforcement, respectively the relations (11) and (12) are taken. The parameter $\varepsilon_R$, significant for the crack widths, reaches the following values:

At yielding of longitudinal reinforcement: $\varepsilon_R = \varepsilon_f \cdot (1 + \cot^2\alpha)$
At yielding of stirrup reinforcement: $\varepsilon_R = \varepsilon_f \cdot (1 + \tan^2\alpha)$.

Thus the displacement parameter $\varepsilon_R$ and hence the crack widths at the onset of yielding is a function of the angle $\alpha$. Figure 7 shows that the parameter $\varepsilon_R$ is a minimum for $\alpha = 45°$ and increases to infinity for $\alpha = 0°$ or $\alpha = 90°$.

A redistribution of the internal forces from the cracking to ultimate load, due to changing of the angle $\alpha$, is only possible if a sufficient shear transfer by aggregate interlock in the previously formed cracks occurs. If the cracks start to open at an accelerated rate (see Fig. 7) the shear transfer deteriorates rapidly and no further redistribution becomes possible.

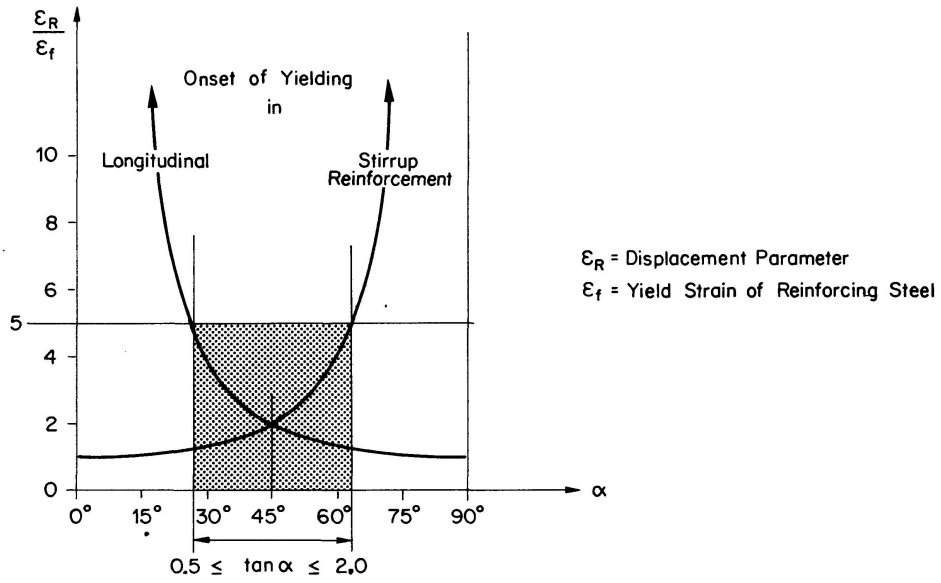


Fig. 7. Displacement Parameter $\varepsilon_R$ at Onset of Yielding.

From tests (6) the previously mentioned bounds have been chosen:

$$0.5 \leq \tan \alpha \leq 2.0$$

Eq. (11) expressing orthogonal crack opening is only applicable within these limits.

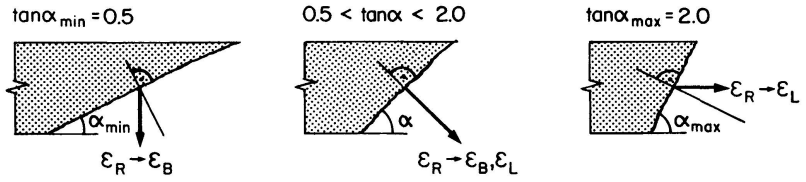


Fig. 8. Limit Inclinations of Concrete Diagonals.

In the range $0.5 < \tan \alpha < 2.0$ the strains of the longitudinal and transverse reinforcement are connected as shown in Figure 8. In this case the longitudinal *and* transverse reinforcement of a shear wall have to yield in order to form a collapse mechanism. Beyond the limits $\tan \alpha = 0.5$ or 2.0 yielding of the transverse *or* longitudinal reinforcement alone produces a mechanism.

The above results can also be obtained from a physical model using a saw-toothed crack as shown in Figure 9.

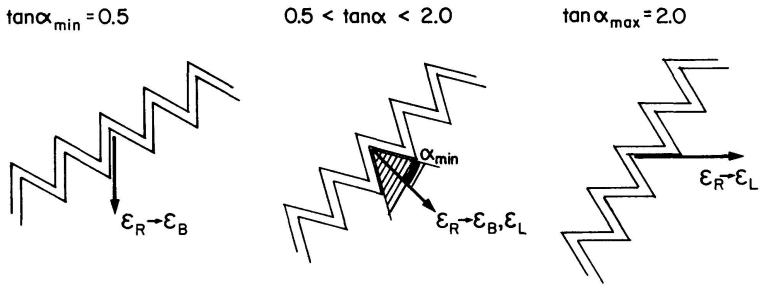


Fig. 9. Limit Inclinations of Concrete Diagonals.

In [2] BRAESTRUP defined his limit of the inclination $\alpha$ as a function of the concrete compression strength and the yield force of the reinforcement only. Based on test results (e.g. [3]) it can be stated that in the case where the reinforcement in one direction does not yield Braestrup's theory leads often to higher ultimate loads than observed.

### *2.4 Concrete Stresses*

So far only underreinforced shear walls have been considered where the reinforcement yields prior to failure of the concrete. Concrete failure can be caused by crushing of the bending compression zone or of the concrete compression diagonals. These kinds of failure should be avoided and therefore the concrete stresses must be checked.

The stresses in the bending compression zone can be determined by using the well-known bending theory. The case is treated in more details in [8] for combined torsion and bending.

The stresses $\sigma_D$ in the compression field are caused by the diagonal force D, Figure 10.

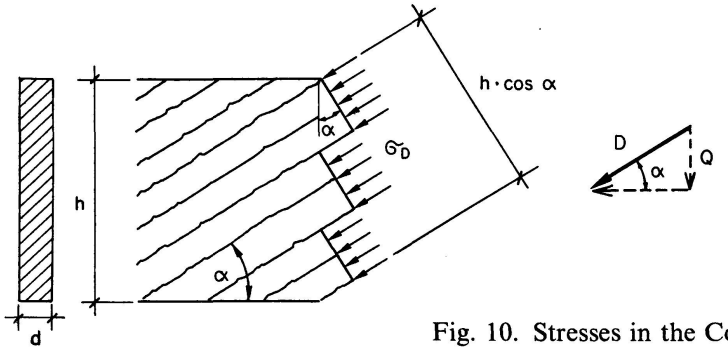


Fig. 10. Stresses in the Compression Diagonals.

$$\sigma_D = \frac{D}{d \cdot h \cdot \cos\alpha} = \frac{Q}{d \cdot h \cdot \sin\alpha \cdot \cos\alpha} \tag{13}$$

Introducing the nominal shear stress $\tau = \frac{Q}{d \cdot h'}$ (14)

the following expression is obtained: $\frac{\sigma_D}{\tau} = \frac{1}{\sin\alpha \cdot \cos\alpha}$ (15)

This term is plotted in Figure 11 as a function of the angle $\alpha$.

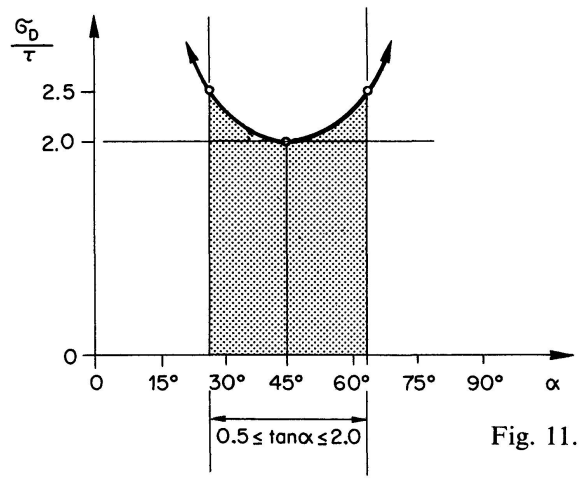


Fig. 11. Stress $\sigma_D$ as Function of Angle $\alpha$.

It is interesting to note that the compression stress $\sigma_D$ does not vary significantly within the given bounds of the angle $\alpha$. The maximum deviation from the minimum value at 45° is only 25%. Thus the average web stress $\sigma_D$ can be controlled by limiting the nominal shear stress $\tau$ independently of the inclination $\alpha$ of the compression diagonals.

## 3. Design of Reinforced Concrete Beams

To describe the behavior of shear wall elements a truss model was assumed in Section 2. The development of such a regular truss action in beams is disturbed by discontinuities caused by concentrated forces. Their influence is shown in Figure 12. A statically admissible stress field is found by introducing fan-shaped stress distributions which are in equilibrium with the concentrated forces [12].

The forces acting in the stirrups are the same in the fan as well as in the regular truss, whereas the stringer forces $Z_a$ and $Z_b$ are influenced by the fans. This effect is shown in Figure 12.

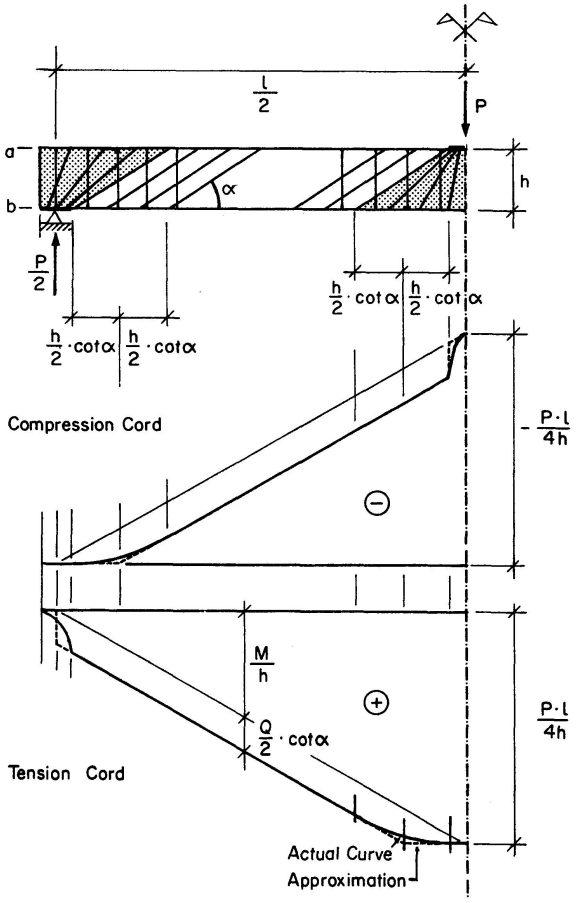


Fig. 12. Longitudinal Forces in Beam.

The actual curves for the stringer forces are sufficiently approximated by the dotted straight lines. Hence, the calculation of the reinforcement should be made at a distance $\frac{h}{2} \cdot \cot \alpha$ from the concentrated loads.

The following design provisions based on the described truss model have been introduced into the Swiss Specifications [11]. The longitudinal reinforcement $F_L(M)$ due to bending is calculated and the stresses in the bending compression zone are checked by using the simple bending theory:

$$F_L(M) \cdot \sigma_{fL} = \frac{M}{y} \tag{16}$$

with: y = distance between bending and compression resultant.

To simplify the procedure of calculating the shear reinforcement, the distance $h_o$ between the longitudinal reinforcing bars enclosed by the stirrups is used. Eq. (2) determines the cross sectional area of the stirrups due to shear:

$$F_B(Q) \cdot \sigma_{fB} = Q \cdot \frac{t}{h_o} \cdot \tan \alpha \tag{17}$$

The additional longitudinal reinforcement due to shear is obtained from Eq. (3).

$$F_L(Q) \cdot \sigma_{fL} = \frac{1}{2} \cdot Q \cdot \cot \alpha \tag{18}$$

The inclination $\alpha$ of the concrete diagonals is restrained within the bounds

$$\frac{3}{5} \leq |\tan \alpha| \leq \frac{5}{3} \tag{19}$$

For design closer limits are prescribed than given by Eq. (7). The evaluation of cracking of test beams ([3], [4] and [9]), showed an adequate behavior under service loads if the limiting values (Eq. (19)) are used. Figure 13 shows the observed maximum shear crack widths $r_{max}$ under service load taken as the theoretical ultimate load divided by a global safety factor of 1.8.

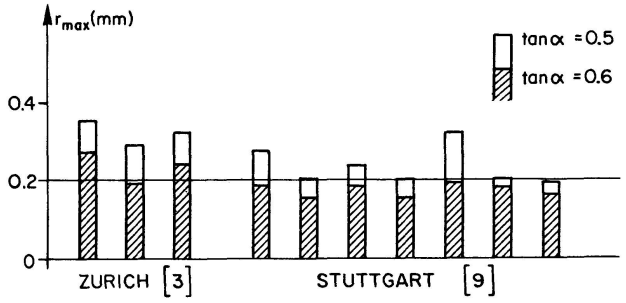


Fig. 13. Maximum Shear Crack Widths of Beams under Service Load.

Next the cost of the longitudinal and stirrup reinforcement as a function of the inclination of the concrete diagonals is investigated. The sum of the yield forces (Eqs. (16), (17) and (18)) of the longitudinal and stirrup reinforcement per unit beam length can be taken as a measure of the steel volume:

$$\overline{C} = \frac{M}{y} + Q \cdot \left( \frac{1}{2} \cdot \cot \alpha + \tan \alpha \right) \tag{20}$$

Introducing the ratio ρ between the costs of the stirrup and longitudinal reinforcement the following relative price index is obtained:

$$C = \frac{M}{y} + Q \cdot \left( \frac{1}{2} \cdot \cot \alpha + \rho \cdot \tan \alpha \right) \tag{21}$$

with: $\rho = \dfrac{\text{unit price of stirrup reinforcement}}{\text{unit price of longitudinal reinforcement}}$

The function c(α) determines the most favorable value for the angle α

$$c(\alpha) = \frac{1}{2} \cdot \cot \alpha + \rho \cdot \tan \alpha \tag{22}$$

This function is plotted in Figure 14 within the prescribed range of the inclination α of the diagonals.

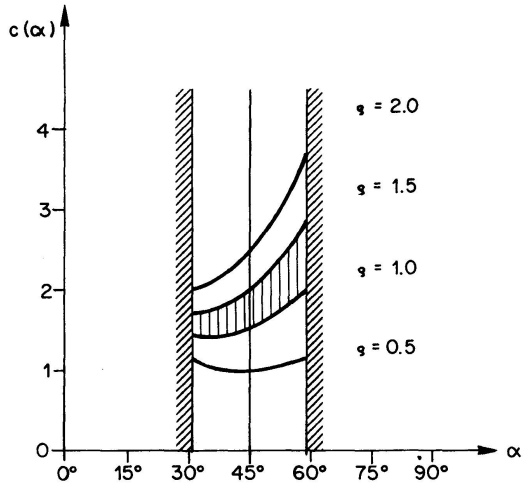


Fig. 14. Relative Cost Function of Reinforcement.

The practical value for ρ lies somewhere between $1.0 < \rho < 1.5$. Hence, the selection of an angle α approaching 30° gives the most economical solution.

The nominal shear stress τ is a measure of the concrete stress in the web:

$$\tau = \frac{Q}{d_o \cdot h_o} \tag{23}$$

with: $d_o$ = minimum web thickness;
$h_o$ = distance of the longitudinal reinforcing bars enclosed by the stirrups.

No shear cracks occur below the value $\tau_r$. Therefore the shear is carried by the concrete alone and no or only a nominal shear reinforcement is required.

$$\tau \leq \tau_r \tag{24}$$

The values of $\tau_r$ given in the current Swiss Code [10] and in the new Swiss Specifications [11] depend on the concrete strength $\beta_w$ (cube strength).

| | | | | |
|---|---|---|---|---|
| Cube Strength $\beta_w$ (kg/cm$^2$): | 200 | 300 | 400 | $\geq 500$ |
| Approx. Cylinder Strength $\beta_c$: | 150 | 225 | 300 | $\geq 375$ |
| Design Shear Stress $\tau_r$: | 8 | 10 | 12 | 14 |

(25)

On the other side the nominal shear stress $\tau$ should not exceed the maximum value $\tau_{max}$ which depends on the concrete strength and the maximum stirrup spacing t.

$$\tau \leq \tau_{max} \tag{26}$$

Normal Spacing: $\tau_{max} = 5\tau_r$ for $t \leq \frac{h_o}{2}$, but $t \leq 30$ cm

Close Spacing: $\tau_{max} = 6\tau_r$ for $t \leq \frac{h_o}{3}$, but $t \leq 20$ cm (27)

Between the uncracked state, $\tau \leq \tau_r$, and the fully developed truss action, about $\tau \geq 3\tau_r$, a transition takes place. Observations on test beams show that the initial shear strength of the uncracked beam is reduced progressively with the development of inclined cracks. The contribution of the concrete to the shear strength is certainly caused by its tensile strength. For design purposes the following approximation is used:

$$\begin{aligned} &\text{For } \tau_r < \tau < 3\tau_r: \quad Q_c = \tfrac{1}{2} \cdot (3\tau_r - \tau) \cdot d_o \cdot h_o \\ &\text{For } \tau \geq 3\tau_r: \quad Q_c = 0 \end{aligned} \tag{28}$$

This additional contribution is taken into account only for the design of the stirrup reinforcement by deducting $Q_c$ from the applied shear force Q. Thus the final design equations follow from Eqs. (17), (18) and (28):

Stirrup Reinforcement:

$$F_B(Q) \cdot \sigma_{fB} = (Q - Q_c) \cdot \frac{t}{h_o} \cdot \tan\alpha, \text{ but } \geq \tfrac{1}{2} \cdot \tau_r \cdot t \cdot d_o \text{ (min. stirrup reinforcement).} \tag{29}$$

Longitudinal reinforcement due so Shear:

$$F_L(Q) \cdot \sigma_{fL} = \tfrac{1}{2} \cdot Q \cdot \cot\alpha \tag{30}$$

These relations can be put in a non-dimensional form.

$$\text{For } \tau_r < \tau < 3\tau_r: \quad \frac{F_B(Q) \cdot \sigma_{fB}}{\tau_r \cdot t \cdot d_o} = \frac{3}{2} \cdot \left( \frac{\tau}{\tau_r} - 1 \right) \cdot \tan\alpha \geq \frac{1}{2}$$

$$\frac{F_L(Q) \cdot \sigma_{fL}}{\tau_r \cdot d_o \cdot h_o} = \frac{\tau}{\tau_r} \cdot \frac{\cot\alpha}{2}$$

$$\text{For } \tau \geq 3\tau_r: \quad \frac{F_B(Q) \cdot \sigma_{fB}}{\tau_r \cdot t \cdot d_o} = \frac{\tau}{\tau_r} \cdot \tan\alpha$$

$$\frac{F_L(Q) \cdot \sigma_{fL}}{\tau_r \cdot d_o \cdot h_o} = \frac{\tau}{\tau_r} \cdot \frac{\cot\alpha}{2}$$

In Figure 15 design diagrams based on the above expressions are given for the practical range of the inclination of the concrete diagonals, e.g. from about 30° to 45°. The current Code RL 17 of the Swiss Specifications SIA-162 lies between these two limits of tan $\alpha = 0.6$ and tan $\alpha = 1.0$. It is based on a 45°-truss model with a constant deduction $Q_c$ ([1], [10]). The new Code [11] uses the here described truss model with a variable inclination of the concrete diagonals. As shown in Figure 15 smaller inclinations lead to a reduction of the stirrup reinforcement but to an increase of the longitudinal reinforcement. Test results of beams which reached limit inclinations due to a weak stirrup reinforcement are also plotted in Figure 15. The observed ultimate loads exceeded the calculated theoretical strengths assuming tan $\alpha = 0.6$. Even with tan $\alpha = 0.5$, save values would be obtained. However as previously stated the higher value tan $\alpha = 0.6$ assures adequate cracking performance under working loads.

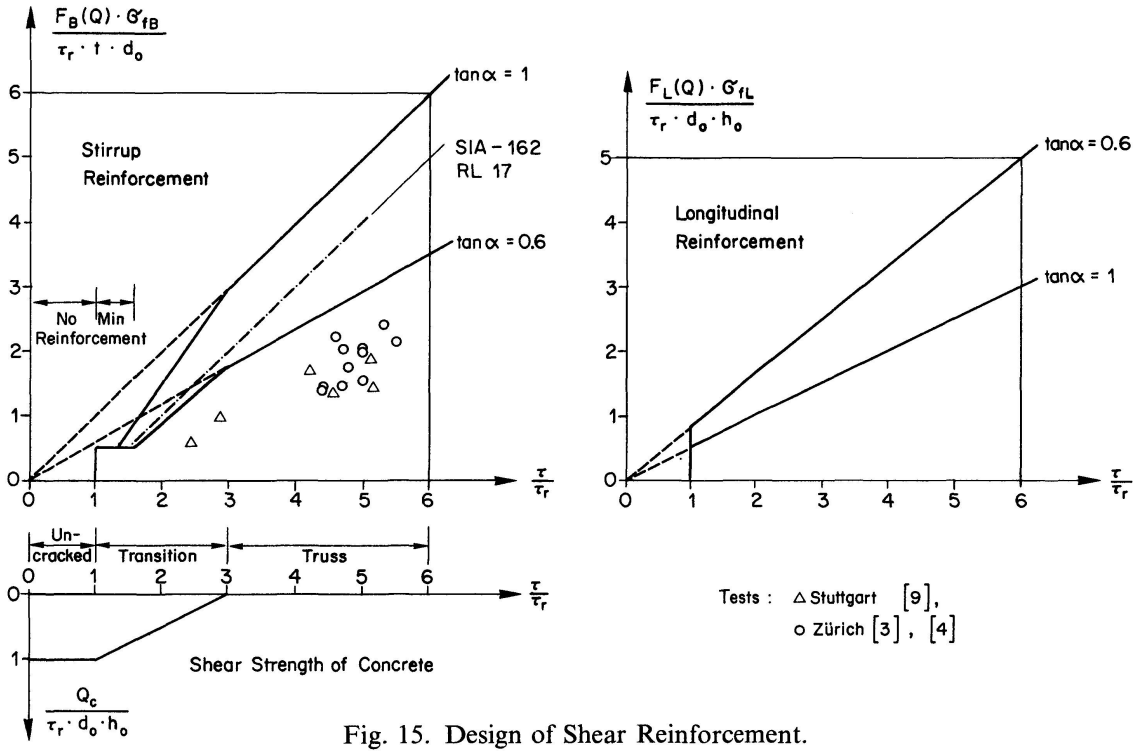


Fig. 15. Design of Shear Reinforcement.

So far the influences of a variable depth of the beam and of inclined prestressing tendons have not been considered. They can be taken into account by substituting the applied shear force Q by the effective web shear force $Q_{eff}$:

$$Q_{eff} = Q - \frac{M}{y} \cdot 2 \tan \frac{\delta}{2} - V \cdot \sin \beta \tag{31}$$

The sign convention for the forces and the angles are indicated in Figure 16.

Inclined tendons produce a vertical component corresponding with the deduction $V \cdot \sin \beta$ in Eq. (31). In order to simplify the design procedure the force V in the tendon is taken equal to the prestressing force of the tendon. Hence, no possible allowance for an increase of this force at ultimate load is made. Prestressing influences also the cracking behavior by retarding the onset of cracking in the

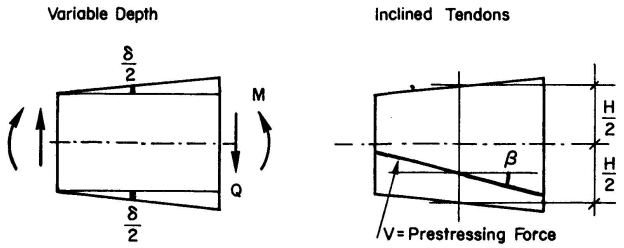


Fig. 16. Variable Depth and Inclined Tendons.

web. Thus, the contribution $Q_c$ to the shear strength decreases under higher nominal shear stresses in comparison with ordinary reinforced beams. Practical considerations show that this influence can be neglected without economical consequences except in cases where no bending cracks occur even at ultimate load (e.g. in support zones of precast pretensioned beams). If the maximum concrete tensile stresses due to bending do not exceed the value $2\tau_r$ the new Code [11] allows a higher deduction $Q_c$ than given in Eq. (28). This deduction can then be used in Eq. (29) for the design of the stirrup reinforcement.

$$\text{for } \kappa \cdot \tau_r < \tau < (2+\kappa)\cdot\tau_r\text{: } Q_c = \tfrac{\kappa}{2}\cdot[(2+\kappa)\cdot\tau_r - \tau]\cdot d_o \cdot h_o$$
$$\text{for } \tau \geq (2+\kappa)\cdot\tau_r\text{: } \qquad Q_c = 0 \tag{32}$$

$V$ = prestressing force;
$F_b$ = area of concrete.

$$\kappa = \sqrt{1 + \frac{V}{F_b \cdot \tau_r}}$$

## Acknowledgement

The study has been part of a research program at the Institute of Structural Engineering, Swiss Federal Institute of Technology, Zurich, financially supported by the Foundation for Scientific Research of the Society of Swiss Cement Manufacturers. The authors would like to express their sincere appreciation for this support.

## Notation

| | |
|---|---|
| $B$ | force in a stirrup. |
| $B_f$ | yield force of a stirrup. |
| $D$ | resultant force in the concrete compression diagonals. |
| $F_b$ | area of concrete. |
| $F_B(Q)$ | area of a stirrup due to shear. |
| $F_L(M)$ | area of the longitudinal reinforcement due to bending |
| $F_L(Q)$ | area of the longitudinal reinforcement due to shear. |
| $M$ | bending moment. |
| $M_p$ | plastic (ultimate) bending moment. |
| $M_{p0}$ | ultimate bending moment for pure bending. |
| $N$ | normal force. |
| $h$ | distance between top and bottom longitudinal stringer. |
| $h_o$ | distance between the longitudinal reinforcement enclosed by the stirrups. |
| $r_{max}$ | maximum shear crack width under service load. |
| $t$ | stirrup spacing. |
| $y$ | distance between compression and tension resultant in bending. |
| $\alpha$ | inclination of concrete diagonals. |
| $\beta$ | inclination of prestressing tendons. |
| $\beta_w$, $\beta_c$ | cube, cylinder strength of concrete. |
| $\gamma$ | shear strain. |
| $\delta$ | angle of cross sectional depth changing. |
| $\varepsilon$ | normal strain. |

$Q$ shear force.
$Q_c$ contribution of the concrete tensile strength to the shear capacity.
$Q_{eff}$ effective shear force in web.
$Q_p$ plastic (ultimate) shear force
$Q_{p0}$ ultimate shear force for pure shear.
$V$ prestressing force.
$Z$ longitudinal force due to shear.
$Z_a$, $Z_b$ force in top respectively bottom stringer.
$Z_f$ yield force of stringer.
$q(\alpha)$ parameter for relative reinforcement costs.
$d$ wall thickness.
$d_o$ minimum wall thickness.
$\varepsilon_B$ stirrup strain.
$\varepsilon_L$ stringer strain.
$\varepsilon_R$ displacement parameter of shear wall.
$\varepsilon_f$ yield strain of reinforcing steel.
$\kappa$ ratio, Eq. (32).
$\rho$ ratio between the costs of stirrup and longitudinal reinforcement.
$\sigma_D$ stress in concrete diagonals.
$\sigma_{fB}$ yield stress of stirrup reinforcement.
$\sigma_{fL}$ yield stress of longitudinal reinforcement.
$\tau$ nominal shear stress.
$\tau_r$ design shear stress, Eq. (25).
$\tau_{max}$ maximum shear stress, Eq. (27).

## References


1. BACHMANN, H., THÜRLIMANN B.: Schubbemessung von Balken und Platten aus Stahlbeton, Stahlbeton mit Spannzulagen und Spannbeton. (Sonderdruck aus Schweiz. Bauzeitung, 84. Jahrgang, Hefte 33 und 34.) Bericht Nr. 8 Institut für Baustatik und Konstruktion ETHZ, 1966, Vergriffen.
2. BRAESTRUP, W.M.: Plastic Analysis of Shear in Reinforced Concrete. Technical University of Denmark, Structural Research Laboratory, Magazine of Concrete Research, Vol. 26, No. 89, 1974.
3. CAFLISCH, R., THÜRLIMANN, B.: Schubversuche an teilweise vorgespannten Betonbalken, Versuchsberich Nr. 6504-2, Institut für Baustatik ETHZ, Birkhäuser Verlag Basel und Stuttgart, 1970.
4. CAFLISCH, R., KRAUSS, R., THÜRLIMANN, B.: Biege- und Schubversuche an teilweise vorgespannten Betonbalken. Serie C, Versuchsberich Nr. 6504-3, Institut für Baustatik ETHZ, Birkhäuser Verlag Basel und Stuttgart, 1971.
5. GROB, J.: Traglast von Stäben mit dünnwandigen offenen Querschnitten. Bericht Nr. 56, Institut für Baustatik und Konstruktion ETHZ, Birkhäuser Verlag Basel und Stuttgart, 1975.
6. LAMPERT P.: Bruchwiderstand von Stahlbetonbalken unter Torsion und Biegung, Bericht Nr. 26, Institut für Baustatik ETHZ, Birkhäuser Verlag Basel und Stuttgart, 1970.
7. LAMPERT, P.: Torsion und Biegung von Stahlbetonbalken. (Sonderdruck aus Schweiz. Bauzeitung, 88. Jahrgang, Heft 5.) Bericht Nr. 27, Institut für Baustatik ETHZ, Birkhäuser Verlag Basel und Stuttgart, 1970.
8. LAMPERT, P., THÜRLIMANN, B.: Ultimate Strength and Design of Reinforced Concrete Beams in Torsion and Bending. (Sonderdruck aus Band 31/I der IVBH-Abhandlungen der Internationalen Vereinigung für Brücken- und Hochbau, Zürich, 1972.) Bericht Nr. 42, Institut für Baustatik ETHZ, Birkhäuser Verlag Basel und Stuttgart, 1972.
9. LEONHARDT, F., WALTHER, R.: Schubversuche an einfeldrigen Stahlbetonbalken mit und ohne Schubbewehrung. Deutscher Ausschuss für Stahlbeton, Heft 151, Verlag Wilhelm Ernst und Sohn Berlin, 1962.
10. SIA-Norm 162, Norm für die Berechnung, Konstruktion und Ausführung von Bauwerken aus Beton, Stahlbeton und Spannbeton, Schweiz. Ingenieur- und Architekten-Verein, Zürich, 1968.
11. Richtlinie 34 zu SIA-Norm 162, Bruchwiderstand und Bemessung von Stahlbeton- und Spannbetontragwerken, Schweiz. Ingenieur- und Architekten-Verein, Zürich, 1976.
12. THÜRLIMANN, B., GROB, J., LÜCHINGER, P.: Torsion, Biegung und Schub in Stahlbetonträgern, Institut für Baustatik und Konstruktion ETHZ, 1975. Autographie zu Fortbildungskurs für Ingenieure aus der Praxis.


## Summary


A theoretical analysis of the strength of reinforced concrete beams subjected to combined bending and shear has been presented on the basis of a truss model with variable inclination of the concrete diagonals forming a continuous com-

pression field. The analysis of the carrying capacity is based on the theory of plasticity. In order to insure the formation of a mechanism by yielding of the reinforcing steel, both the concrete stresses in the bending compression zone and in the inclined compression field have to be limited. Based on the analysis presented in this paper new Swiss Specifications have been prepared and introduced for the design of reinforced and prestressed concrete beams under bending and shear.

## Résumé

La résistance à la rupture des poutres en béton armé soumises à la flexion et à l'effort tranchant a été analysée sur la base d'un modèle de treillis avec inclinaison variable des bielles. La déduction de la charge de rupture s'appuie sur la théorie de la plasticité. Pour avoir la certitude de la formation d'un mécanisme par écoulement des armatures, il est nécessaire de contrôler les contraintes dans le béton de la zone de compression et des bielles comprimées. La théorie exposée a servi de base à des recommandations suisses qui ont été développées et introduites pour le dimensionnement pratique des poutres en béton armé et précontraint soumises à la flexion et à l'effort tranchant.

## Zusammenfassung

Der Bruchwiderstand von Stahlbetonbalken unter Biegung und Schub wurde aufgrund eines Fachwerkmodelles mit variabler Neigung der Druckdiagonalen untersucht. Die Herleitung der Bruchlast erfolgt nach der Plastizitätstheorie. Um die Ausbildung eines Mechanismus durch Fliessen der Armierung zu gewährleisten, müssen die Betonspannungen sowohl in der Biegedruckzone als auch in den Druckdiagonalen kontrolliert werden. Aufgrund der beschriebenen Theorie wurden neue schweizerische Richtlinien ausgearbeitet und für die Bemessung von biege- und schubbeanspruchten Stahlbeton- und Spannbetonbalken eingeführt.

# Theory of Dynamic Analysis of Box Girder Bridges

*Théorie d'une analyse dynamique de ponts à poutres en caisson*

*Theorie einer dynamischen Berechnung von Kastenträgerbrücken*

KUANG HAN CHU, Ph.D.
Professor of Civil Engineering
Illinois Institute of Technology,
Chicago, Illinois, USA.

MARVIN JONES, Ph.D.
Project Engineer FMC Corp.,
Environmental Equipment Division,
Chicago, Illinois, USA.

## Introduction

In almost all the studies on bridge vibration subjected to moving loads (known to bridge engineers as impact loads), the bridge is idealized as a beam. A review of the literature and extensive list of references are omitted herein as it can be found in a recent (Oct. 1970) article [11]. While the aforementioned idealization is reasonable for computing bending moments and shears for the bridge as a whole, it is not possible to evaluate dynamic effects on stresses in various elements of the bridge. For instance, in the box girder bridges, such as those shown in Figure 1, dynamic effects on membrane forces, transverse moments and shears in plate elements cannot be evaluated by the beam method. Although the total bending moment due to dynamic effect is found, the distribution of longitudinal stresses in a cross section can be obtained approximately by the beam theory only when the load is symmetrical to the longitudinal centerline.

The purpose of this study is to make a more exact analysis of the dynamic effects on the deflections, stresses, and moments in all plate elements of box girder bridges. In order to reduce the problem to one consisting of finite number of degrees of freedom, the distributed masses of the plate elements were replaced by equivalent concentrated masses applying at the joints. (The edge where the plate elements joint together is referred to as a joint.) Since both inertia forces due to vertical and rotational displacements of the plate elements are considered, consistent masses [1] concentrated along the joints are used. Moreover, since taking each plate between two joints in a bridge cross section as an element would not provide enough accuracy of both frequency (eigenvalue) and mode shape (eigenvector), each plate element is further divided into several longitudinal plate strips and new joints are introduced along the edges joining the plate strips (see Fig. 2).

With the structure divided into many plate elements and each element involving a number of consistent masses, the matrix size become fairly large. In order to simplify the problem, only simply supported box girder bridges with end diaphragms but no intermediate diaphragms will be considered. Also instead of the elaborate

idealization of a truck the live load is simplified as consisting of four identical wheel loads represented by spring supported masses with the force in the spring distributed over a rectangular area (see Fig. 3). Unsprung masses and internal damping of the truck as well as structural damping of the bridge are neglected since their effects are relatively small [4, 11]. Although without the above simplifications, no great complication in formulation and programming results. The simplifications were introduced in order to save computer time and storage.

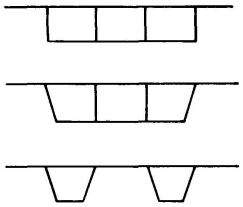

Fig. 1. Typical Box Girder Bridge Cross Section.

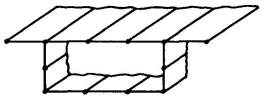

Fig. 2. Plate Element in a Box Girder Bridge.

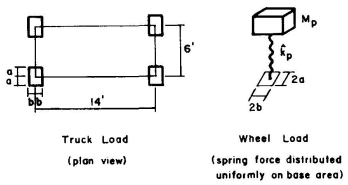


Fig. 3. Simplified Live Load.

The static relationships between displacements and internal forces are essentially those developed for folded plate analysis by GOLDBERG and LEVE [5] and others [2, 10]. Since these relationships and definition of symbols are virtually the same as given in reference [2] they will be omitted in the text. The main assumptions of the folded plate analysis are (a) plate elements are perfectly elastic, rectangular in shape and rigidly jointed along the longitudinal edges, (b) the transverse end of the plates are framed into diaphragms which are infinitely stiff in their own plane but perfectly flexible normal to their own plane and (c) no interaction exists between bending resisting forces (moments and shears) and membrane forces.

The approach of replacing the applied distributed forces by joint forces based on virtual work concept is believed to be novel. The expansion of distributed forces into a double Fourier series using normal mode functions is based on the work of IYENGAR and JAGADISH [7]. The matrix formulation of the equation of motion is based on a classical method [6].

A computer program was written in Fortran to be used in Univac 1108. Verification of the accuracy of the program were made by comparing the static and dynamic results obtained by the proposed method with those obtained by existing methods or with examples taken from published articles. Static and dynamic analysis were also performed for an example box girder bridge. However, since the inclusion of the above results will result in a paper too lengthy for publication, the results will be presented in a separate paper.

## Equations for the dynamic Analysis of Box Girder Bridges

### *Equation of Motion of the Structure*

With masses concentrated at the joints, the equation of motion of the structure neglecting damping may be written in the following form

$$[\Phi_{mn}]^t [\bar{M}_n] [\Phi_{mn}] \ddot{\Psi}_{mn} + [\Phi_{mn}]^t [\bar{K}_n] [\Phi_{mn}] \Psi_{mn} = [\Phi_{mn}]^t [Q_n] \quad (1)$$

$$\text{or } \ddot{\Psi}_{mn} + \omega_{mn}^2 \Psi_{mn} = [\bar{M}^*]^{-1} [\Phi_{mn}]^t [Q_n] \quad (2)$$

in which

$\Psi_{mn}$ = time function for m-th mode n-th Fourier component.
$\ddot{\Psi}_{mn}$ = double dots denotes second derivative of $\Psi_{mn}$ with respect to time (t).
$[\Phi_{mn}]$ = matrix (vector) of m-th mode for n-th Fourier component.
$[\Phi_{mn}]^t$ = superscript t denotes transpose of matrix $[\Phi_{mn}]$.
$\omega_{mn}$ = natural frequency of the m-th mode n-th Fourier component.
$[Q_n]$ = applied joint force matrix (vector) of n-th Fourier component to be defined later.
$[\bar{M}_n]$ = assembled consistent mass matrix of n-th Fourier component to be defined later.

$$[\bar{M}^*] = [\Phi_{mn}]^t [\bar{M}_n] [\Phi_{mn}] \tag{3}$$

$[\bar{M}^*]^{-1}$ = inverse of $[\bar{M}^*]$.
$[\bar{K}_n]$ = assembled stiffness matrix of n-th Fourier component $[\bar{K}_n]$ is an assembly of the stiffness matrices $[\bar{K}_n]_r$.

$$[\bar{K}_n]_r = [R]_r^t [K_n]_r [R]_r. \tag{4}$$

in which

$[K_n]$ = local stiffness matrix of n-th Fourier component.
$[R]$ = rotation matrix relating local and global displacements.
$[R]^t$ = transpose of $[R]$ and suscript r denotes r-th plate element.

### *Frequency Equation*

The m-th natural mode $\Phi_{mn}$ and frequency $\omega_{mn}$ of the n-th Fourier component are given respectively by the eigenvector and eigenvalue of the following equation

$$(\omega_{mn}^2 [\bar{M}_n] - [\bar{K}_n]) [\Phi_{mn}] = 0 \tag{5}$$

### *Applied Joint Forces*

If a moving force is applied along a joint line, Eq. (1) can be solved by representing the force as a Fourier series in the space variable. However, if a distributed force is applied on a portion of a plate element, it must be converted to forces applied on the edges of the element such that the edge forces will cause the same dynamic effect as the distributed force.

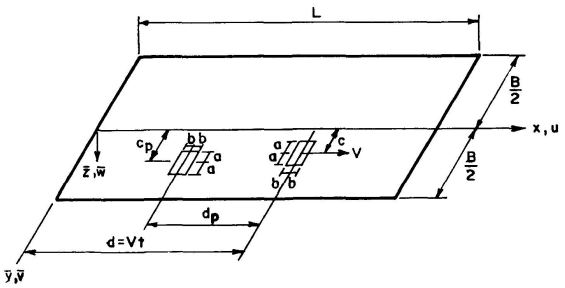


Fig. 4. Coordinates of the Wheel Loads.

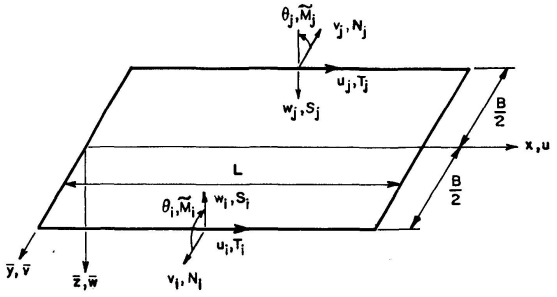


Fig. 5. Displacement Component in Local coordinate System.

As shown in Figure 4 the force $\bar{Q}$ is distributed on an area 2a × 2b, the center of which is at a distance c from the longitudinal centerline and a distance

$d = Vt$ from $x = 0$ in which V is the velocity and t is time. Let the force function $\hat{Q}(x, y, t)$ be expressed in the following form (6):

$$\hat{Q}(x, \bar{y}, t) = \sum_{m=1}^{\infty} \sum_{n=1}^{\infty} \Omega(t)\, \hat{\Phi}_{mn}(\bar{y}) \sin \frac{n\pi x}{L} \tag{6}$$

$$\hat{Q} = \frac{\overline{Q}}{4ab} \text{ for } d - b < x < d + b \text{ and } c - a < \bar{y} < c + a \tag{7a}$$

$$= 0 \text{ elsewhere} \tag{7b}$$

in which $\Omega$ is a time function defined below and $\hat{\Phi}(y)$ is a plate deflection function due to the mode displacement $\Phi_{mn}$ along the longitudinal edges. (Expression of the deflection function will be given later in the section on consistent mass matrix). $\hat{Q}$ is also taken as equal to $\dfrac{\overline{Q}}{4ab}$ when the load enters the bridge with $d > 0$ and $b > d > -b$.

Multiplying Eq. (6) by $\hat{\Phi}_{m'n'}(\bar{y}) \sin \dfrac{n'\pi x}{L}\, dx\, d\bar{y}$ and integrating, then using the orthogonality property of $\hat{\Phi}_{mn}$ and the sine function, one obtains

$$\begin{aligned} \Omega(t) &= \frac{\displaystyle\int_{c-a}^{c+a} \int_{d-b}^{d+b} \frac{\overline{Q}}{4ab} \hat{\Phi}_{mn}(\bar{y}) \sin \frac{n\pi x}{L}\, dx\, d\bar{y}}{\displaystyle\int_{-B/2}^{B/2} \int_{0}^{L} \hat{\Phi}^2_{mn}(\bar{y}) \sin^2 \frac{n\pi x}{L}\, dx\, d\bar{y}} \\ &= \frac{4}{n\pi}\left(\frac{\overline{Q}}{4ab}\right) \frac{\displaystyle\int_{c-a}^{c+a} \hat{\Phi}(\bar{y})\, d\bar{y}}{\displaystyle\int_{-B/2}^{B/2} \hat{\Phi}^2(\bar{y})\, d\bar{y}} \sin \frac{n\pi b}{L} \sin \frac{n\pi Vt}{L} \end{aligned} \tag{8}$$

The term $[\Phi_{mn}]^t [Q_n]$ in Eq. (1) may be considered as the virtual work of the force $Q_n$ due to virtual displacement $\Phi_{mn}$. In order that the edge forces will cause the same dynamic effect as the distributed force, the virtual work due to the edge forces must be equal to that due to the distributed force. Thus

$$\begin{aligned} [\Phi_{mn}]^t [Q_n] &= \int_{-B/2}^{B/2} \hat{\Phi}^t_{mn}(y)\, \Omega(t)\, \hat{\Phi}(y)\, d\bar{y} = \Omega(t) \int_{-B/2}^{B/2} \hat{\Phi}^2_{mn}(\bar{y})\, d\bar{y} \\ &= \frac{4}{n\pi} \frac{\overline{Q}}{4ab} \left( \int_{c-a}^{c+a} \hat{\Phi}_{mn}(\bar{y})\, d\bar{y} \right) \sin \frac{n\pi b}{L} \sin \frac{n\pi Vt}{L} \end{aligned} \tag{9}$$

If there are several forces $\overline{Q}_p$ applied at $y = c_p$ and $x = Vt - d_p$ (see Fig. 4) then

$$[\Phi_{mn}]^t [Q_n] = \sum_p \frac{Q_p}{n\pi ab} \left( \int_{c_p - a}^{c_p + a} \hat{\Phi}_{mn}(\bar{y})\, d\bar{y} \right) \sin \frac{n\pi b}{L} \sin \frac{n\pi (Vt - d_p)}{L} \tag{10}$$

*Equations of Motion of the Wheel Loads*

As stated previously, a wheel load is considered as consisting of a mass $\hat{M}_p$ supported by a spring with spring constant $= \hat{k}_p$. The deflection of the mass $\hat{M}_p$ from its equilibrium position is $\zeta^p$. For the mode component mn, the plate deflection at $\bar{y} = c_p$ and $x = Vt - d_p$ is given by $\Psi_{mn}(t)\,\hat{\Phi}_{mn}(c_p)\sin\dfrac{n(Vt - d_p)}{L}$. Then

$$\overline{Q}_p = \hat{M}_p g + \hat{k}_p\left[\zeta^p - \sum\sum_{mn} \Psi_{mn}(t)\,\hat{\Phi}_{mn}(c_p)\sin\frac{n\pi(Vt - d_p)}{L}\right] \tag{11a}$$

$$\overline{Q}_p = 0 \text{ when } Vt - d_p \leq 0 \text{ and } Vt - d_p \geq L \tag{11b}$$

$$\text{and } \hat{M}_p\ddot{\zeta}^p + \hat{k}_p\left[\zeta^p - \sum\sum_{mn} \Psi_{mn}(t)\,\hat{\Phi}_{mn}(c_p)\sin\frac{n\pi(Vt - d_p)}{L}\right] = 0 \tag{12}$$

in which g is the gravitational acceleration.

*Final Equations*

From Eqs. (2) and (10)

$$\ddot{\Psi}_{mn} + \omega_{mn}^2\,\Psi_{mn} = [\overline{M}^*]^{-1}\sum_p \frac{\overline{Q}_p}{n\pi ab}\left(\int_{c_p - a}^{c_p + a} \hat{\Phi}_{mn}(\bar{y})\,d\bar{y}\right)\sin\frac{n\pi b}{L}\sin\frac{n\pi(Vt - d_p)}{L} \tag{13}$$

in which $\overline{Q}_p$ is given by Eq. (11). If there are four wheel loads, the final equations consist of the above equation plus four equations of Eq. (12) with $p = 1, 2, 3, 4$.

*Consistent Mass Matrix*

The matrix $[\overline{M}]$ is an assembled mass matrix of $[\overline{M}]$ for all plate elements. For plate r

$$[\overline{M}]_r = [R]_r^t\,[M]_r\,[R]_r \tag{14}$$

in which $[M]_r$ is the consistent mass matrix. The element $M_{\alpha\beta}^{ij}$ of $[M]_r$ is given by (1)

$$M_{\alpha\beta}^{ij} = \int_{-B/2}^{-B/2} \rho\bar{t}\,\eta_{\bar{\alpha}i}\,\eta_{\bar{\beta}j}\,d\bar{y} \tag{15}$$

in which $\rho$ is the density, $\bar{t}$ is the thickness of the plate, $\eta_{\bar{\alpha}i}$ is a displacement function due to unit displacement of $\bar{\alpha} = (u, \bar{v}, \bar{w}, \text{or } \theta)$ at edge i with other displacements equal to zero, and $\eta_{\bar{\beta}j}$ is defined similar to $\eta_{\bar{\alpha}i}$. The mass $M_{\alpha\beta}^{ij}$ is corresponding to the stiffness $K_{\gamma\beta}^{ij}$ in which $\bar{\gamma} = (T, N, S \text{ or } M)$ is corresponding to $\bar{\alpha} = (u, v, w \text{ or } \theta)$ with T corresponding to u, etc. The mass distribution in the x direction is a Fourier cosine series for the u displacement and Fourier sine series for the displacement v, w and $\theta$.

The local displacement functions $\bar{w}_n$ $u_n$ and $\bar{v}_n$ and the elements for the consistent mass matrix $[M]_r$ with subscript r omitted are given in Reference 8.

## Method of Solution and Final Results

### *Method of Obtaining Eigenvalues and Eigenvectors*

The success of the mode superposition method depends on the accuracy of the eigenvalues and eigenvectors. In the present study, the eigenvalues and eigenvectors are obtained by means of a method given in Reference [12]. Briefly, the method is as follows, for an eigenvalue problem of the following standard form;

$$[\tilde{A}]\{\Phi\} = \tilde{\lambda}\{\Phi\} \tag{16}$$

The largest eigenvalue, $\tilde{\lambda}_1$ and its corresponding eigenvector, $\Phi_1$, are obtained by the usual method of iteration except that the pivot of the trial vector is taken in the same row as that of $[\tilde{A}]$ containing the largest absolute element. The eigenvector is normalized so that the sum of the squares of its components equal unity.

In the process of iterating for $\Phi_1$, a vector $\Phi_1^*$ is obtained at a few iterations before reaching the final $\Phi_1$. The vector $\Phi_1^*$ contains components of many modes $\phi_1$, $\phi_2$ ..., etc. Let $\phi_2' = [\tilde{A} - \tilde{\lambda}_1 I]\phi_1^*$ in which I is the identity matrix. Then in vector $\phi_2'$, the $\phi_1$ component is removed and the $\phi_2$ component will predominate. Using $\phi_2'$ as the starting trial vector, and using Eq. (16) for iteration, one obtains the eigenvalue $\tilde{\lambda}_2$ and its corresponding eigenvector $\phi_2$.

Let $\phi_2^*$ be the vector obtained at a few iterations before reaching the final $\phi_2$. The components of $\phi_1$ and $\phi_2$ in $\phi_2^*$ are removed by taking $\phi_3' = [\tilde{A} - \tilde{\lambda}_1 I]\phi_2^*$ and $\phi_3'' = [\tilde{A} - \tilde{\lambda}_2 I]\phi_3'$. The vector $\phi_3''$ is used as the starting trial vector in Eq. (16) for iteration to obtain $\tilde{\lambda}_3$ and $\phi_3$. After a number of iterations, a vector $\bar{\phi}_3$ is obtained which may contain errors due to components of $\phi_1$ and $\phi_2$. These components are removed by taking $\bar{\phi}_3' = [\tilde{A} - \tilde{\lambda}_1 I]\bar{\phi}_3$ and $\bar{\phi}_3'' = [\tilde{A} - \tilde{\lambda}_2 I]\bar{\phi}_3'$. The vector $\bar{\phi}_3''$ is again substituted back into Eq. (16) for iteration to obtain $\tilde{\lambda}_3$ and $\phi_3$.

Procedures similar to the one described above and used for obtaining other eigenvalues and eigenvectors. In order to save both time and storage, only single precision was used in the computation. As a result, a certain loss of accuracy becomes inevitable. Some indication of the accuracy of the results will be given in the numerical examples.

### *Reduction of Degrees of Freedom for Dynamic Analysis*

In order to save computer time and storage, the sizes of the matrices used in the dynamic analysis were reduced by limiting the degrees of freedom taken into consideration. Since the loading is in vertical direction and may be unsymmetrical to the bridge centerline, vibrations of the bridge are considered to cause inertia forces only in the directions of global vertical displacement ($\Delta_z$) and rotation about longitudinal axis ($\Delta_\theta$). Since there are no longitudinal and lateral oscillations, inertia forces in these global directions ($\ddot{\Delta}_x$, $\ddot{\Delta}_y$) will be assumed negligible. In Eqs. (1, 2 and 5), a reduced stiffness matrix as shown in references (6, 9) relating forces and displacements in the $\Delta_z$ and $\Delta_\theta$ directions will be used instead of $[\overline{K}_n]$ and a

mass matrix consisting only of the masses causing inertia forces in these directions will be used instead of $[\bar{M}_n]$. The reduced stiffness matrix $[\bar{K}]^*$ is obtained in the following manner. Let

$$\Delta_1 = \begin{bmatrix} \Delta_z \\ \Delta_\theta \end{bmatrix}, \quad \Delta_2 = \begin{bmatrix} \Delta_x \\ \Delta_y \end{bmatrix} \tag{17a, b}$$

$$\text{From} \quad \left[\begin{array}{c} \bar{F}_1 \\ \hline \bar{F}_2 \end{array}\right] = \left[\begin{array}{c|c} \bar{\bar{K}}_{11} & \bar{\bar{K}}_{12} \\ \hline \bar{\bar{K}}_{21} & \bar{\bar{K}}_{22} \end{array}\right] \left[\begin{array}{c} \Delta_1 \\ \hline \Delta_2 \end{array}\right] \tag{18}$$

with $\bar{F}_2 = 0$ it can be shown that $[\bar{\bar{K}}]^* = [\bar{\bar{K}}_{11}] - [\bar{\bar{K}}_{12}]\,[\bar{\bar{K}}_{22}]^{-1}\,[\bar{\bar{K}}_{21}]$ (19)

*Solution of the Dynamic Equations*

The dynamic equations 11, 12 and 13 were solved simultaneously for $\zeta^p_{mn}$ and $\Psi_{mn}$ by the 5th order ADAM'S method [3] using a Runge Kutta starting procedure.

*Displacements, Forces and Stresses*

Upon solution of the dynamic equations, the resulting displacements and forces must be obtained. The matrix (vector) of coefficients of the n-th Fourier component of edge displacements in global coordinates is given by

$$[\Delta_n] = \sum_m \Psi_{mn}\,[\Phi_{mn}] \tag{20}$$

The matrix $[\Delta_n]$ is the assembled matrix of $[\Delta_n]_r$

$$[\Delta_n]_r = [\Delta_{zi}\ \Delta_{yi}\ \Delta_{xi}\ \Delta_{\theta i}\ \Delta_{zj}\ \Delta_{yj}\ \Delta_{xj}\ \Delta_{\theta j}]^t_r \tag{21}$$

in which $\Delta_z$ $\Delta_y$ $\Delta_x$ and $\Delta_\theta$ are displacements in global z, y, x and $\theta$ (rotation about x) directions respectively and i and j denote longitudinal jointing edges of plate element r.

The matrix of coefficients of n-th Fourier components of local displacements $[\delta_n]_r$ is given by

$$[\delta_n]_r = [\theta_{ni}\ \theta_{nj}\ w_{ni}\ w_{nj}\ u_{ni}\ u_{nj}\ v_{ni}\ v_{nj}]^t = [R]_r\,[\Delta_n]_r \tag{22}$$

in which u, v, w, $\theta$ are displacements in the local x, y, z and $\theta$ (rotation about x) directions respectively (see Fig. 5 for positive directions of $\theta_{ni}$, $w_{nj}$, etc.) and $[R]$ is the rotation matrix defined previously.

The matrix of coefficients of n-th Fourier components of local edge forces acting on plate element r is given by

$$[F_n]_r = [\tilde{M}_{ni}\ \tilde{M}_{nj}\ S_{ni}\ S_{nj}\ T_{ni}\ T_{nj}\ N_{ni}\ N_{nj}]^t_r = [K_n]_r\,[\delta_n]_r = [K_n]_r\,[R]_r\,[\Delta_n]_r \tag{23}$$

in which $[K_n]$ = local stiffness matrix as defined previously, $\tilde{M}$ = transverse bending moment per unit length, S = transverse shear per unit length, T = membrane shearing stress resultant, N = membrane normal stress resultant and forces are acting along

edges i and j as indicated by subscripts. The positive directions of $[\tilde{M}_{ni}, \tilde{M}_{nj}, S_{ni}, S_{nj}, T_{ni}, T_{nj}, N_{ni}, N_{nj}]$ are corresponding to the positive directions of $[\theta_{ni}, \theta_{nj}, w_{ni}, w_{nj}, u_{ni}, u_{nj}, v_{ni}, v_{nj}]$ respectively.

The final edge displacements and forces for plate r are given by

$$[\delta]_r = \sum_{n=1}^{\infty} [\tilde{s}_n \tilde{s}_n \tilde{s}_n \tilde{s}_n \tilde{c}_n \tilde{c}_n \tilde{s}_n \tilde{s}_n] [\delta_n]_r \tag{24}$$

$$[F]_r = \sum_{n=1}^{\infty} [\tilde{s}_n \tilde{s}_n \tilde{s}_n \tilde{s}_n \tilde{c}_n \tilde{c}_n \tilde{s}_n \tilde{s}_n] [F_n]_r \tag{25}$$

$$\text{in which } \tilde{s}_n = \sin \frac{n\pi x}{L}, \ \tilde{c}_n = -\cos \frac{n\pi x}{L} \tag{26a, b}$$

The longitudinal stress at edge i in plate r is given by

$$(\sigma_{xi})_r = E \sum_{n=1}^{\infty} \frac{n\pi}{L} (u_{ni})_r \sin \frac{n\pi x}{L} + \frac{\nu}{t} \sum_{n=1}^{\infty} (N_{ni})_r \sin \frac{n\pi x}{L} \tag{27}$$

in which E = modulus of elasticity and $\nu$ = Poisson's ratio.

The interior moments in any plate strip are given by

$$\tilde{M}_{xI} = \sum_{n=1}^{\infty} D\left(\frac{n\pi}{L}\right)^2 (1-\nu) (\tilde{M}_{xI})_n \sin \frac{n\pi x}{L} \tag{28a}$$

$$\tilde{M}_{yI} = \sum_{n=1}^{\infty} D\left(\frac{n\pi}{L}\right)^2 (1-\nu) (\tilde{M}_{yI})_n \sin \frac{n\pi x}{L} \tag{28b}$$

The coefficients of $(\tilde{M}_{xI})_n$ and $(\tilde{M}_{yI})_n$ are given in Reference 8.

### *Static Solution and Impact Factor*

As indicated in Ref. [7], the static solution may be simply obtained by the following considerations: (a) In Eq. (11), consider only the term $\hat{M}_p g$ (omit the dynamic force in the spring). (b) In Eq. (1), consider only the effect of stiffness matrix (omit the term depending on time derivative of $\Psi$). Letting the solution of $\Psi$ thus obtained $= \overline{\Psi}$, Eq. (13) becomes

$$\omega_m^2 \overline{\Psi}_{mn}(t) = [\overline{M}^*]^{-1} \sum_p \frac{\hat{M}_p g}{n\pi ab} \left( \int_{c_p - a}^{c_p + a} \hat{\phi}_{mn}(\bar{y}) \, d\bar{y} \right) \sin \frac{n\pi b}{L} \sin \frac{n\pi (Vt - d_p)}{L} \tag{29a}$$

$$\hat{M}_p = 0 \text{ when } Vt - d_p \leq 0 \text{ and } Vt - d_p \geq L \tag{29b}$$

Since $\overline{\Psi}_{mn}(t)$ depends only on $Vt = d$, $\Psi_{mn}(t)$ is a function of d. Thus the static solution of $[\Delta_n]$ denoted by $[\bar{\Delta}_n]$ can be obtained by replacing $\Psi_{mn}$ with $\overline{\Psi}_{mn}$ in Eq. (27)

$$[\bar{\Delta}_n] = \sum_m \overline{\Psi}_{mn} [\Phi_{mn}] \tag{30}$$

with $[\bar{\Delta}_n]$ known, the responses (deflections, forces, moments, and stress) may be obtained by the same equations as given in the previous section.

The amplification factors $\Lambda_d$ and $\Lambda_s$ for dynamic responses $\Gamma_d$ and static response $\Gamma_s$ respectively are defined by

$$\Lambda_d = \frac{\Gamma_d}{\Gamma_{sm}} \qquad \Lambda_s = \frac{\Gamma_s}{\Gamma_{sm}} \tag{31a, b}$$

is which $\Gamma_{sm}$ is the maximum static response. The impact factor I, is defined as

$$I = \max |\Lambda_d| - 1 \tag{32}$$

It should be noted that in the evaluation of $\Lambda_d$, $\Lambda_s$ and I, the values of $\Gamma_d$, $\Gamma_s$ and $\Gamma_{sm}$ should be taken for the response at the point under consideration, for example, the deflection at a specific plate joint at midspan, the moment at center of top plate at midspan, etc.

## Conclusions

Theoretical formulation for the exact analysis of dynamic effects due to moving load on deflections, stresses and moments in all plate elements in simply supported box girder bridges is presented. Each plate element is further divided into several longitudinal plate strips and consistent masses are applied along the lines joining the strips. The truck is simplified into 4 identical wheel loads represented by spring supported masses with the force in the spring distributed over a rectangular area. Unsprung masses and internal damping of the truck as well as structural damping of the bridge are neglected. The spring force is expressed in the form of double Fourier series and the distributed force is replaced by forces along the joint lines based on the principle of virtual work. The general method is essentially based on mode superpositions and the method chosen for obtaining the frequencies and mode shapes are given. Governing matrix equations, displacement functions, consistent mass matrix and expressions for plate moments at interior points are presented.

Although numerical studies will be presented in a companion paper, two general observations may be made herein.

1. In order to obtain accurate results, many plate strips must be taken and many modes must be included. However, the higher the number of modes included, the smaller the time increment (which is proportional to the period of the highest mode) required in a dynamic analysis. As the computer tie is inversely proportional to the time increment, it becomes impractical to include large number of modes.
2. Since the proposed method is based on mode superposition, it is essential that not only the eigenvalues (frequencies) but also the eigenvectors (mode shapes) be determined efficiently and accurately. Many methods are available to determine accurate eigenvalues but such is not the case for eigenvectors. It is beyond the scope of this study to make an exhaustive evaluation of all available methods. However, it is hoped that more powerful methods will be developed in the near future.

As pointed out previously, practical application of the theory will be presented in a companion paper mainly for the reason of shortening the paper to reasonable length. By knowing more precisely the dynamic effects of moving loads on box

girder bridges, the theorectical formulation presented herein would undoubtedly make a meaningful contribution to the safety and economy on the design of such bridges.

## References


1. ARCHER, J.S.: Consistent Mass Matrix for Distributed Mass Systems, Journal of the Structural Division. ASCE, Vol. 89, No. ST4, Proc. Paper 3591, Aug., 1963, pp. 161-178.
2. CHU, K.H., and DUDNIK E.: Concrete Box Girder Bridges Analyzed as Folded Plates. First International Symposium Concrete Bridge Design. American Concrete Institute, Publication SP-23, 1969, pp. 221-246.
3. CRANDALL, S.H.: Engineering Analysis. McGraw-Hill Book Company, Inc., New York, N.Y., 1956.
4. EICHMANN, E.S.: Influence of Vehicle Suspensions on Highway Bridge Impact. Civil Engineering Studies, Structural Research Series No. 70, University of Illinois, Urbana, Ill., 1954.
5. GOLDBERG, J.E., and H.L. LEVE: Theory of Prismatic Folded Plate Structures. Inter. Assoc. of Bridge and Structural Engineering Publication, Vol. 17, 1957, pp. 59-86.
6. HURTY, W.C., and RUBINSTEIN M.F.: Dynamics of Structures. Prentice-Hall, Inc., Englewood Cliffs, New Jersey, 1964.
7. IYENGAR, K.T.S.R., and JAGADISH, K.S.: The Responses of Beam and Slab Bridges to Moving Forces. Inter. Assoc. of Bridge and Structural Engineering Publication. Vol. 28, 1968, p. 69.
8. JONES, M.A.: Dynamic Analysis of Box Girder Bridges. Thesis submitted to the Graduate School of Illinois Institute of Technology in Partial fulfillment of the degree of Doctor of Philosophy, May 1972.
9. RUBINSTEIN, M.F., and HURTY W.C.: Effect of Joint Rotation on Dynamics of Structures. Journal of the Engineering Mechanics Division, ASCE, Vol. 87, No. EM6, Proc. Paper 3028, Dec., 1961, pp. 135-157.
10. SCRODELIS, A.C., and DEFRIES-SKENE, A.: Direct Stiffness Solution for Folded Plates. Journal of the Structural Division, ASCE, Vol. 90, No. ST4, Proc. Paper 3994, Aug., 1964, pp. 15-47.
11. VELETSOS, A.S., and HUANG, T.: Analysis of Dynamic Response of Highway Bridges. Journal of the Engineering Mechanics Division, ASCE, Vol. 96, No. EM5, Proc. Paper 7591, Oct., 1970, pp. 593-620.
12. WILKINSON, J.H.: The Calculation of the Latent Roots and Vectors of Matrices on the Pilot Model of the A.C.E. Proceedings of the Cambridge Philosophical Society, Vol. 50, 1954, pp. 536-566.


## Summary

Theoretical formulation for elastic analysis of dynamic effects due to moving loads on deflections, stresses and moments in all plate elements in simply supported box girder bridges is presented. The truck is simplified into 4 identical wheel loads represented by spring supported masses with the force in the spring distributed over a rectangular area. Governing equations, displacement functions, consistent mass matrix and expressions for plate moments are given. Practical application of the theory will be given in another paper to demonstrate its contribution to the safety and economy of box girder bridge design.

## Résumé

L'article présente une théorie pour l'analyse élastique des effets dynamiques des charges mobiles sur les déflexions, tensions et moments dans tous les éléments de ponts à poutres en caisson sur appuis simples. Le véhicule est simplifié en

4 charges de roue qui sont représentées par des masses supportées par ressorts et dont la force du ressort est distribuée sur une surface rectangulaire. On établit les équations principales, les fonctions de déplacement, la matrice des masses et les moments des plaques. L'application pratique de la théorie sera présentée dans l'article suivant montrant aussi la contribution à la sécurité et à l'économie d'un pont à poutres en caisson.

## Zusammenfassung

Es wird eine theoretische Formulierung der elastischen Berechnung von Durchbiegungen, Spannungen und Momenten in allen Plattenelementen einfach gelagerten Kastenträgerbrücken unter dynamischen Einflüssen bewegter Lasten vorgelegt. Die Belastung wird durch 4 gleiche Radlasten mit elastisch aufgelagerter Masse dargestellt, wobei die Federkraft über eine rechteckige Fläche verteilt wird. Es werden bestimmende Gleichungen, Verschiebungsfunktionen, die folgerichtige Steifigkeitsmatrix und Ausdrücke für die Plattenmomente angegeben. Die praktische Anwendung der Theorie im Hinblick auf Sicherheit und Wirtschaftlichkeit der Kastenträgerbrücken wird im anderen Beitrag dargelegt.

Leere Seite
Blank page
Page vide

# Dynamic Analysis of a Box Girder Bridge

*Analyse dynamique d'un pont à poutres en caisson*

*Dynamische Berechnung einer Kastenträgerbrücke*

MARVIN JONES, Ph.D.
Project Engineer, FMC Corp.
Environment Equipment Division
Chicago, Illinois U.S.A.

KUANG HAN CHU, Ph.D.
Professor of Civil Engineering
Illinois Institute of Technology
Chicago, Illinois U.S.A.

The main purpose of this paper is to present numerical results obtained from a computer program based on a theoretical formulation for the analysis of dynamic effects due to moving loads on deflections, stresses and moments in all plate elements in a simply supported box girder bridge presented in a previous paper [7]. It mainly consists of two parts: (a) verification of the computer program and (b) analysis of an example bridge.

Verification of the computer program was necessary not only to check out the program but to find out the minimum number of plate strips, the minimum number of modes and the largest time increment to be taken for obtaining reasonable accurate results. It was done by comparing the results of the proposed method with those obtained by existing methods or with examples taken from published articles. For a check of natural frequencies and the static solution obtained, simply supported rectangular plates with various aspect ratios and subjected to a load at the center were examined. For a check of the dynamic solution, a slab bridge subjected to a moving load without spring and a beam bridge subjected to a wheel load consisting of both sprung and unsprung masses were checked with existing solutions. Results of static solution of a box girder bridge were compared with those obtained with existing methods. Since the proposed method is based on mode superposition, frequencies and mode shapes of various mode were obtained for the example bridge.

Dynamic analysis were performed for the same box girder bridge considered in the verification for the static solution. Five loading cases were investigated. The first four loading cases are: (a) single load moving along the bridge centerline, (b) single load moving along the curb, (c) two-axle truck moving along the bridge centerline and (d) two-axle truck moving along the curb. All wheel loads are spring borne, of the same magnitude and without initial deflection. The fifth loading case (e) is the same as loading case (c) except that the spring has an initial deflection. Typical history curves showing amplification factors for deflections, longitudinal stresses and plate moments are shown. Impact factors at various points for various loading cases are given in tables.

The amplification factors $\Lambda_d$ and $\Lambda_s$ for each dynamic response (deflection, stress or moment, etc.) $\Gamma_d$ and each static response $\Gamma_s$ at a specific point are defined respectively as

$$\Lambda_d = \frac{\Gamma_d}{\Gamma_{sm}}, \Lambda_s = \frac{\Gamma_s}{\Gamma_{sm}} \tag{1a, b}$$

in which $\Gamma_{sm}$ is the maximum static response at the point. The impact factor I is defined as

$$I = \max |\Lambda_d| - 1 \tag{2}$$

The motivation of making this study and relevant references were given in the previous paper [7]. The following items are also pointed out in that paper but they are repeated herein as they involve basic assumptions or definitions of relevant symbols.

1. The truck is simplified into one with two identical axle loads 14 ft. (4.26 m) apart [1]. Each axle consists of two identical wheel loads which are at 6 ft. (1.83 m) apart [1] and represented by spring supported masses with the force in the spring distributed over a rectangular area (see Fig. 1). Unsprung masses and internal damping of the wheel loads are neglected as their effects are relatively small (4, 8, 9).
2. The box girder bridge is simply supported with span length L and consists of a number of plate elements. As shown in Fig. 2, each plate element is further divided into several plate strips and consistant masses [3] are applied along the line joining the strips. The x axis is taken along the longitudinal direction of the bridge and has its origin at the left end of the bridge. The y direction is taken as perpendicular to x in the plane of any plate strip. Positive directions of longitudinal stress $\sigma_x$ and plate moments $M_x$ and $M_y$ (moment per unit width) in a plate element of thickness $\bar{t}$ are shown in Figure 3. Symbols for other force and moment resultants shown in Figure 3 are not given as they are not involved in this paper.

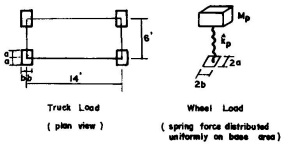


Fig. 1. Simplified Live Load.

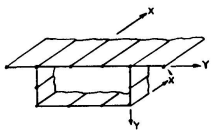

Fig. 2. Plate Element in a Box Girder Bridge.

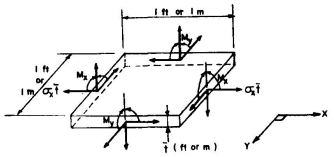

Fig. 3. Positive Directions for $\sigma_x$, $M_x$ and $M_y$ (Symbols are Omitted for Stress Resultants not Involved Herein).

3. The bridge is considered as having negligible structural damping [14] and it is supposed to satisfy the following main assumptions of folded plate analysis. (a) Plate elements are perfectly elastic, rectangular in shape and rigidly jointed along longitudinal edges. (b) The transverse end of the plates are framed into diaphragms which are flexible normal to their own plane but infinitely stiff in their own plane. (c) No interaction exists between bending resisting forces (moments and transverse shears) and membrane forces.

## Verification of the Computer Program

As stated in the introduction, the purpose of verifying the computer program is not only to check out the program but to find out the minimum number of plate strips, the minimum number of modes and the largest time increment to be taken for obtaining reasonable accurate results. Numerical results obtained for the various case considered are presented in the following.

### *Natural Frequencies and Static Solution of Centrally Loaded Rectangular Plates*

Natural frequencies and static solutions for centrally loaded simply supported rectangular plates were obtained. The concentrated load investigated is 25 k (111.2 kN) distributed on an area of 4.5′ × 4.5′ (1.38 m × 1.38 m). The plate thickness (t) is 8″ (20.32 cm); the modulus of elasticity (E) is 432 × $10^3$ ksf (3 × $10^6$ psi or 206 × $10^3$ kN/cm$^2$) and the Poisson's ratio (μ) is 0.3. The dimensions of the plates, numbers of plate elements used, the first 3 transverse mode frequencies, numbers of modes taken, moments and deflections under the load are given in Table 1, which shows the comparison of results of the proposed method with those of the series solution given by TIMOSHENKO's books [15, 16].

*Table 1. Comparison of Results of the Proposed Method (a) with those of the Series Solution (b) for Centrally Loaded Simply Supported Rectangular Plates*

| Plate Size (ft.) | L/B | No. of Elem. | Natural Frequencies $\frac{1}{\omega^2} \times 10^3$ | | $\frac{1}{\omega^2} \times 10^4$ | | $\frac{1}{\omega^2} \times 10^5$ | | No. of Modes Included | | $M_x$ (k ft/ft) | | $M_y$ (k ft/ft) | | Defl. (ft) | |
|---|---|---|---|---|---|---|---|---|---|---|---|---|---|---|---|---|
| | | | (a) | (b) | (a) | (b) | (a) | (b) | n | m | (a) | (b) | (a) | (b) | (a) | (b) |
| 31.5 x 22.5 | 1.5 | 5 | .3279 | .3281 | .3663 | .3678 | .8129 | .8273 | 9 | 7 | 3.789 | 5.218 | 5.292 | 6.014 | .0145 | .0152 |
| 45.0 x 22.5 | 2.0 | 5 | .4787 | .4788 | .4127 | .4142 | .8100 | .8745 | 9 | 7 | 3.746 | 5.075 | 5.711 | 6.300 | .0163 | .0169 |
| 45.0 x 22.5 | 2.0 | 8 | .4788 | .4788 | .4140 | .4142 | .8721 | .8745 | 9 | 7 | 4.069 | 5.075 | 6.048 | 6.300 | .0163 | .0169 |
| 45.0 x 22.5 | 2.0 | 8 | .4788 | .4788 | .4140 | .4142 | .8721 | .8745 | 15 | 8 | 3.942 | 5.075 | 5.953 | 6.300 | .0163 | .0169 |
| 75.0 x 22.5 | 3.3 | 5 | .6296 | .6298 | .4457 | .4473 | .8910 | .9055 | 9 | 7 | 3.464 | 5.053 | 5.544 | 6.429 | .0168 | .0174 |
| 90.0 x 22.5 | 4.0 | 5 | .6626 | .6628 | .4518 | .4534 | .8965 | .9110 | 9 | 7 | 3.268 | 5.052 | 5.383 | 6.431 | .0167 | .0174 |
| 90.0 x 22.5 | 4.0 | 8 | .6627 | .6628 | .4531 | .4534 | .9086 | .9110 | 9 | 7 | 3.640 | 5.052 | 5.919 | 6.431 | .0167 | .0174 |
| 90.0 x 22.5 | 4.0 | 8 | .6627 | .6628 | .4531 | .4534 | .9086 | .9110 | 15 | 8 | 3.968 | 5.052 | 6.090 | 6.431 | .0168 | .0174 |
| 135.0 x 22.5 | 6.0 | 5 | .7081 | .7083 | .4597 | .4612 | .9035 | .9180 | 9 | 7 | 2.644 | 5.052 | 4.790 | 6.431 | .0161 | .0174 |
| 281.2 x 22.5 | 12.5 | 5 | .7386 | .7387 | .4646 | .4661 | .9079 | .9224 | 9 | 7 | 1.413 | 5.052 | 3.384 | 6.431 | .0128 | .0174 |
| 281.2 x 22.5 | 12.5 | 8 | .7387 | .7387 | .4659 | .4661 | .9200 | .9224 | 9 | 7 | 1.509 | 5.052 | 3.623 | 6.431 | .0128 | .0174 |
| 281.2 x 22.5 | 12.5 | 8 | .7387 | .7387 | .4659 | .4661 | .9200 | .9224 | 15 | 8 | 2.358 | 5.052 | 4.725 | 6.431 | .0152 | .0174 |

1 ft = 0.3048 m  1 k-ft/ft = 4.448 kN-m/m

From Table 1, it can be seen that in general the accuracy of the frequencies are fairly good. For the number of modes considered, the deflections are also checked very well with the series solution except for long plates with L/B ≥ 6. The $M_x$ and $M_y$ values at points away from the concentrated load generally show fairly good agreement as will be shown in another example. However, the $M_x$ and $M_y$ values at center of application of the load depend on the length to width ratio (L/B) of the plate, number of plate elements ($n_s$) and number of modes (m and n) taken into consideration.

At the point under the concentrated load, for a plate with $L/B = 2$, $n_s = 5$, $n = 9$ and $m = 7$, the $M_y$ value is 90% of the series solution but $M_x$ value is only 74% of the series solution. For the same plate with $n_s = 8$, $n = 9$, and $m = 7$, the $M_y$ value is 96% and the $M_x$ value is 80% of the series solution. Thus improved accuracy is obtained with more plate elements. However, for the same plate with $n_s = 8$, $n = 15$ and $m = 8$, the $M_x$ and $M_y$ values are slightly worse than the case of $n_s = 8$, $n = 9$ and $m = 7$. This loss of accuracy with the inclusion of higher modes is undoubtedly due to the inaccuracies in the eigenvectors of the higher modes. The case of $L/b = 4$ is similar to the case of $L/B = 2$ except that $M_x$ and $M_y$ values show improvement as higher modes are included. Unfortunately, for a given number of $n_s$, n and m, as L/B increases, the accuracy of the $M_x$ and $M_y$ deteriorates. For a plate with $L/B = 12.5$, $n_s = 8$, $n = 9$ and $m = 7$ the value of $M_y$ is 56% of the series solution and that of $M_x$ is only 30% of the series solution. For the same plate with $n_s = 8$, $n = 15$ and $m = 8$, $M_y$ becomes 73% of the series solution and $M_x$ is 46.5% of the series solution.

It becomes evident that reliable moments at point of application of the concentrated load cannot be obtained for long narrow plates unless (a) large number of plate elements are used, (b) large number of higher modes are included, and (c) accurate frequencies and mode shapes can be obtained for higher modes. This becomes impractical particularly under dynamic conditions in that the time increment for numerical integration becomes so short (for convergence, the time increment must be about 1/10 of the period of the highest mode included) that the required computer time for a single loading case becomes unwieldy.

### *Verification of the Dynamic Solution of a Slab Bridge and a Beam Bridge*

A check of the dynamic solution is made for a slab bridge subjected to an unsprung moving load analyzed by IYENGAR and JAGADISH [11] and a beam bridge subjected to a sprung load attached to an unsprung load by EICHMANN [9]. Excellent agreements were obtained except for the moment $M_x$ at center of slab bridge in that the original paper was believed in error.

### *Static Solution and Vibration Modes of a Box Girder Bridge*

The static solution of a box girder bridge under a concentrated load is compared with that obtained by the well known elasticity method (6, 10, 13). Figure 4 shows the cross-section of the example bridge which is simply supported with 100 ft. (30.48 m) span. The mass density ($\rho$) is taken as .005 k-sec$^2$/ft$^4$; (161 pcf weight or 2570 kg/m$^3$) the modulus of elasticity (E) as $432 \times 10^3$ ksf ($3 \times 10^6$ psi or $206 \times 10^3$ kN/cm$^2$) and Poisson's ratio ($\mu$) as 0.2.

The concentrated load is 25 k (111 kN) applied on an area of $24'' \times 8''$ (61 cm $\times$ 20.3 cm) with 24" in the transverse and 8" in the longitudinal direction of the bridge. Two load cases are considered: (a) load applied at midspan of the centerline of the bridge (b) load applied at midspan with edge of the load touching inside of the right curb (see Fig. 9).

Plate elements used for analysis of the example bridge are as shown in Figure 5. The curb section is considered as a thick plate element which has the same centroidal

axis as the top slab. This will result in apparent discontinuity in the slab bending stress corresponding to $M_x$ at the junction of the curb and the top slab. This discontinuity can be removed if eccentricity of the curb section is taken into consideration.

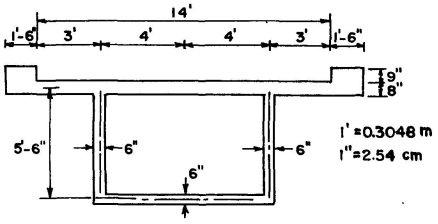


Fig. 4. The Example Bridge.

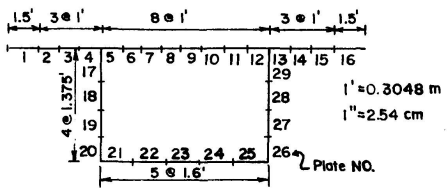


Fig. 5. Plate Elements Used for the Example Bridge.

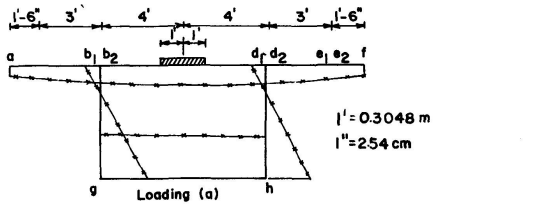


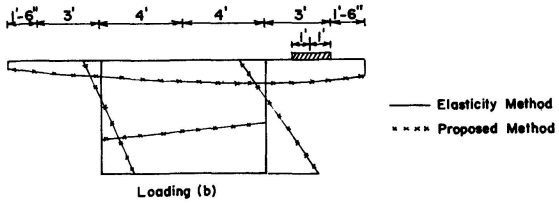


Fig. 6. Static Loading Cases and Longitudinal Stress Distribution.

The mode shapes of the first eight transverse modes (m = 1 to 8, n = 1) are as shown in Figure 7 and the frequencies and period of all the modes up to m = 8, n = 15 are given in Table 2. The computer running time for obtaining these frequencies and mode shapes is 20.0 min. on Univac 1108. It should be noted that the first mode frequency for the corresponding simply supported beam with cross-sectional area = 23.0 $ft^2$ (2.14 $m^2$) and moment of inertia = 124.0 $ft^4$ (1.07 $m^4$) is 21.3 as compare with 20.02 as shown in Table 2.

*Table 2. Circular Frequencies and Periods of the Various Modes of the Example Bridge*

| | | n = 1 | n = 2 | n = 3 | n = 4 | n = 5 | n = 6 | n = 7 | n = 8 | n = 9 | n = 10 | n = 11 | n = 12 | n = 13 | n = 14 | n = 15 |
|---|---|---|---|---|---|---|---|---|---|---|---|---|---|---|---|---|
| m = 1 | ω | 20.02 | 71.84 | 134.4 | 188.7 | 234.1 | 276.7 | 319.8 | 362.7 | 399.8 | 429.2 | 456.9 | 485.8 | 517.0 | 550.6 | 586.9 |
| | τ | .3138 | .0875 | .0467 | .0333 | .0268 | .0227 | .0196 | .0173 | .0157 | .0146 | .0138 | .0129 | .0122 | .0114 | .0107 |
| m = 2 | ω | 80.66 | 118.3 | 154.3 | 197.9 | 244.3 | 291.5 | 340.3 | 392.0 | 438.8 | 488.1 | 544.4 | 602.7 | 659.7 | 714.4 | 768.3 |
| | τ x 10 | .7790 | .5312 | .4071 | .3174 | .2572 | .2155 | .1846 | .1603 | .1432 | .1287 | .1154 | .1043 | .0952 | .0880 | .0818 |
| m = 3 | ω | 151.7 | 177.1 | 218.3 | 272.0 | 321.4 | 354.1 | 469.4 | 403.1 | 447.8 | 508.7 | 638.8 | 689.4 | 738.7 | 817.5 | 906.8 |
| | τ x 10 | .4142 | .3548 | .2878 | .2310 | .1955 | .1775 | .1338 | .1559 | .1403 | .1235 | .0984 | .0911 | .0851 | .0769 | .0693 |
| m = 4 | ω | 266.6 | 296.1 | 353.5 | 367.0 | 390.7 | 427.7 | 471.0 | 510.4 | 551.0 | 592.9 | 575.1 | 647.7 | 830.9 | 916.8 | 962.3 |
| | τ x 10 | .2357 | .2122 | .1777 | .1712 | .1608 | .1469 | .1335 | .1231 | .1140 | .1060 | .1092 | .0970 | .0756 | .0685 | .0653 |
| m = 5 | ω | 342.6 | 346.4 | 348.0 | 423.8 | 517.5 | 620.7 | 726.1 | 827.8 | 920.2 | 999.2 | 1064 | 1107 | 1165 | 1211 | 1255 |
| | τ x 10 | .1834 | .1814 | .1806 | .1483 | .1214 | .1012 | .0865 | .0759 | .0683 | .0628 | .0591 | .0568 | .0539 | .0519 | .0501 |
| m = 6 | ω | 625.4 | 641.3 | 673.0 | 724.1 | 796.2 | 887.2 | 992.5 | 1107 | 1175 | 1226 | 1287 | 1358 | 1421 | 1492 | 1560 |
| | τ x 10 | .1005 | .0980 | .0934 | .0868 | .0789 | .0708 | .0633 | .0567 | .0535 | .0513 | .0488 | .0463 | .0442 | .0421 | .0403 |
| m = 7 | ω | 963.6 | 1005 | 1026 | 1041 | 1058 | 1078 | 1103 | 1134 | 1227 | 1350 | 1474 | 1597 | 1714 | 1839 | 1955 |
| | τ x $10^2$ | .6520 | .6251 | .6126 | .6035 | .5940 | .5830 | .5698 | .5539 | .5119 | .4653 | .4262 | .3936 | .3664 | .3416 | .3214 |
| m = 8 | ω | 1216 | 1254 | 1295 | 1341 | 1391 | 1455 | 1509 | 1575 | 1648 | 1728 | 1816 | 1920 | 2027 | 2124 | 2391 |
| | τ x $10^2$ | .5166 | .5009 | .4851 | .4687 | .4515 | .4334 | .4164 | .3989 | .3813 | .3637 | .3461 | .3272 | .3098 | .2958 | .2628 |

$\tau = 2\pi/\omega$ sec.

A comparison of the results obtained by the elasticity method [6] with those by the proposed method is shown in Table 3 and in Figures 6 and 8. It can be seen that fairly good agreement of deflections, longitudinal stresses and plate moments is obtained at all points except those directly under the load. From the previous results of the centrally loaded simply supported plates, this lack of agreement for the response under the load is not unexpected.

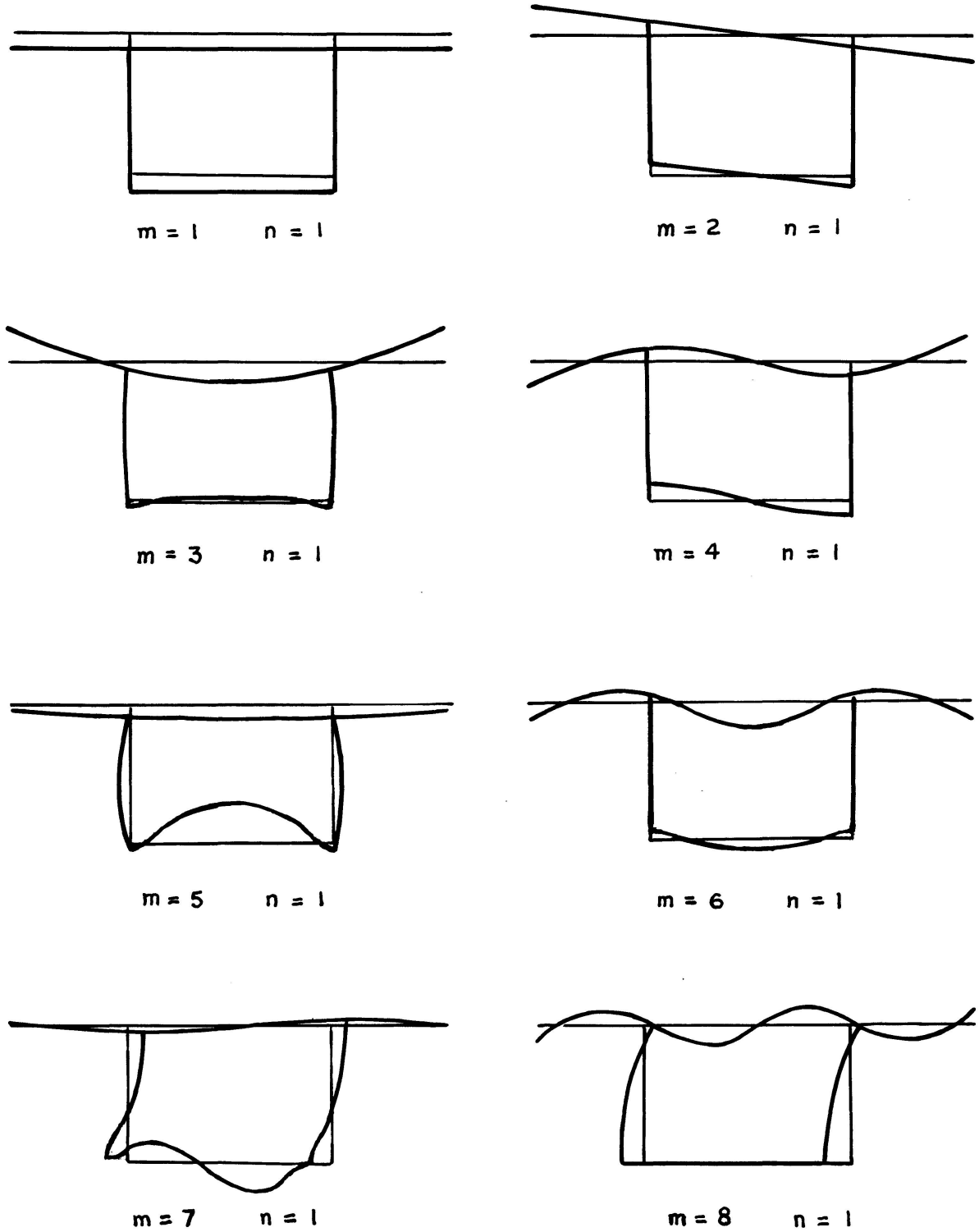


Fig. 7. Mode Shapes for the Example Bridge.

*Table 3. Comparison of Results of the Elasticity Method and the Proposed Method for Points on the Cross Section at Midspan of the Bridge*

Static Loading Case (a)

| Method | Deflection (ft) | | | Long. Stress (ksf) | | | $M_x$ (k-ft/ft) | | | | $M_y$ (k-ft/ft) | | | |
|---|---|---|---|---|---|---|---|---|---|---|---|---|---|---|
| | a,f | b,d | g,h | a,f | b,d | g,h | a,f | $b_1,d_2$ | $b_2,d_1$ | c | a,f | $b_1,d_2$ | $b_2,d_1$ | c |
| Elasticity | .0101 | .0109 | .0109 | -7.46 | -8.97 | 21.09 | .20 | -.01 | -.20 | 4.95 | 0 | -1.00 | -1.94 | 5.85 |
| Proposed | .0101 | .0109 | .0109 | -7.80 | -8.63 | 21.35 | .33 | -.02 | -.22 | 1.43 | 0 | -1.09 | -1.94 | 2.78 |

Static Loading Case (b)

| Method | Deflection (ft) | | | | | | Longitudinal Stress (ksf) | | | | | |
|---|---|---|---|---|---|---|---|---|---|---|---|---|
| | a | b | d | f | g | h | a | b | d | f | g | h |
| Elasticity | .0098 | .0101 | .0118 | .0144 | .0100 | .0117 | -6.95 | -7.21 | -10.34 | -8.24 | 16.00 | 25.33 |
| Proposed | .0098 | .0101 | .0118 | .0145 | .0100 | .0117 | -6.88 | -7.64 | -10.81 | -8.19 | 15.68 | 25.66 |

Static Loading Case (b)

| Method | $M_x$ (k-ft/ft) | | | | | | $M_y$ (k-ft/ft) | | | | | |
|---|---|---|---|---|---|---|---|---|---|---|---|---|
| | a | $b_1$ $b_2$ | c | $d_1$ $d_2$ | $e_1$ $e_2$ | f | a | $b_1$ $b_2$ | c | $d_1$ $d_2$ | $e_1$ $e_2$ | f |
| Elasticity | 1.13 | 0.12<br>0.06 | -.06 | -.05<br>-.40 | 0.95<br>6.91 | 7.05 | 0 | .09<br>-.19 | -.56 | -1.49<br>-3.20 | 1.33<br>1.33 | 0 |
| Proposed | 1.29 | 0.13<br>0.06 | -.08 | -.07<br>-.23 | 0.93<br>6.54 | 7.33 | 0 | .11<br>-.21 | -.69 | -0.82<br>-2.37 | 1.42<br>1.56 | 0 |

1 ft = 0.3048 m, 1 ksf = 0.4788 kN/cm$^2$, 1 k-ft/ft = 4.448 kN-m/m

## Dynamic Analysis of an Example Bridge

The example bridge considered is the same as shown in Figure 4 with the same span length and material properties as given previously. Five loading cases are considered. The first four cases are as shown in Figure 9: (a) single spring borne load along the bridge centerline, (b) single spring borne load along the inside of the right curb, (c) two axles (4 spring borne loads) 14 ft. (4.26 m) apart with their centerline coinciding with the bridge centerline, (d) two axles (4 spring borne loads) 14 ft. apart with exterior wheel touching the inside of the right curb. The fifth loading case (e) will be introduced later.

Each wheel load is taken as 16 k [71.2 kN see reference [1]] distributed over an area of 24″ (61 cm) transverse by 8″ (20.3 cm) longitudinal (83.3 psi tire pressure). The data represent a compromise of the data given in references [2] and [12]. The wheel load is considered a spring borne mass with a spring constant of 104 k/ft. (15.2 kN/cm) [see references [8] and [9]]. The speed (V) of the loads is taken as 100 ft/sec. (30.48 m/sec. or 68 miles per hr.). The springs are considered as starting at zero vertical displacement and zero velocity when the load is entering the bridge.

An examination of Table 2 shows that as expected, the frequency becomes higher and the period becomes shorter as m and n increase. In order to obtain convergence for dynamic analysis, it was found by trial that the time increment should be about 1/10 of the shortest period. At m = 8 and n = 15, the period is .0026 which would need excessive time for computer runs. By trial, it was found that

including the modes up to m = 6 and n = 9 would give static moments which agree fairly well with those obtained by the elasticity method at all points except those directly under the load. (The static plate moments for m = 5 may even differ in sign with the corresponding values from the elasticity method). That this being true can also be seen from the mode shapes shown in Figure 7 wherein third mode is included for the top plate only if m = 6. The time increment is .0005 sec. which is 1/10th of the period of the highest mode. The computer running time for a single load case is 192 sec. on Univac 1108. This computer time would be doubled if 4 loads are taken into consideration. Modes up to m = 6 and n = 15 have been included for loading case (a). The computer running time is 696 sec. with time increment of .00035 sec. (Time for evaluating the eigenvalues and vectors are not included in the computer running time).

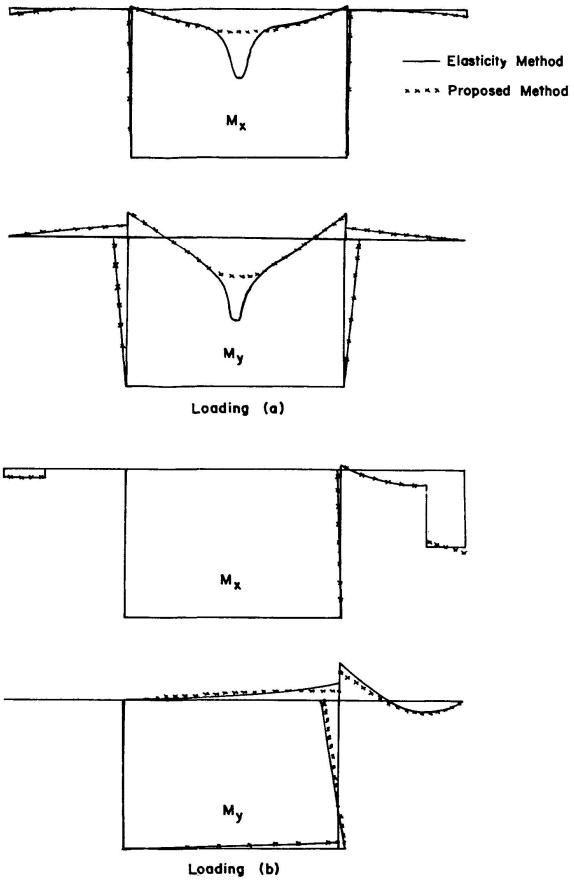


Fig. 8. Distribution of $M_x$ and $M_y$ by the Elasticity Method and the Proposed Method.

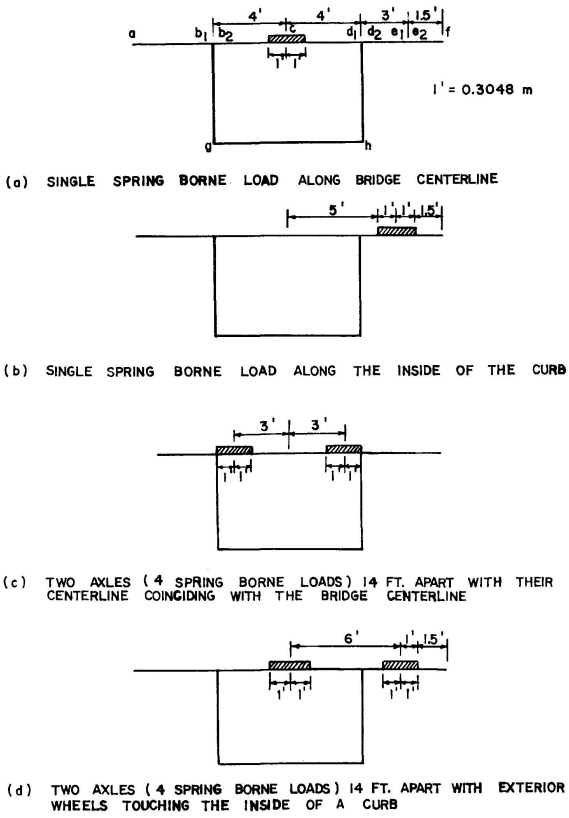


Fig. 9. Dynamic Loading Cases.

For the loading case (a), history curves for the static and dynamic amplification factors are shown in Figure 10 for the midspan deflection and longitudinal stress at point b or d shown in Figure 9a. Amplification factors for the respective midspan $M_x$ and $M_y$ at point $b_1$ or $d_2$ are shown in Figure 11. Impact factors at various points on the cross section at midspan shown in Figure 9a are given in Table 4. It can be seen that the maximum impact factor is about 19% for deflection, 16% for longitudinal stress, 4.8% for $M_x$ and 1.3% for $M_y$.

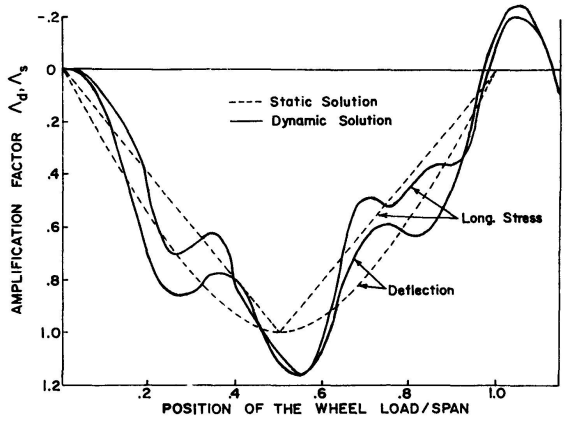


Fig. 10. History Curves for Midspan Deflection and Longitudinal Stress at Point b or d in fig. 9a, Loading Case (a).

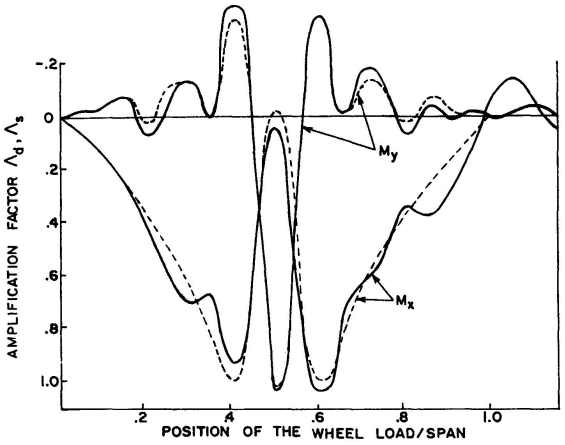


Fig. 11. History Curves for Midspan $M_x$ and $M_y$ at Point $b_1$ or $d_2$ in Fig. 9a, Loading Case (a).

Impact factors at various points on the midspan section shown in Figure 9a for the loadings (b), (c) and (d) are given in Tables 4 to 6. It can be seen that for loading case (b) the maximum impact factor is about 19% for both deflection and longitudinal stress. The former is the same as for loading case (a) but the latter is higher. Except for $M_x$ at point a the maximum impact factor for both $M_x$ and $M_y$ is slightly less than 4%. The former is somewhat lower than that for case (a) and the latter is somewhat higher. It may be worth noting that $M_x$ at the point which is on the opposite side of the load in an unsymmetrical loading case such as point a in loading cases (b) and (d) always have high impact factor. [19% for loading (b) 6.8% for loading (d)].

*Table 4. Impact Factor in Percentages for Loading Cases (a) and (c)*

| Loading & Modes | (a) m = 6, n = 15 | | | | (c) m = 6, n = 9 | | | |
|---|---|---|---|---|---|---|---|---|
| Point Fig. 9a | a,f | $b_1,d_2$ $b_2,d_1$ | c | g,h | a,f | $b_1,d_2$ $b_2,d_1$ | c | g,h |
| Defl. | 18.81 | 15.81 | 9.77 | 16.65 | 4.73 | 4.60 | 4.57 | 4.60 |
| Long. Stress | 10.84 | 15.80 | 8.46 | 15.43 | 4.43 | 4.36 | 4.43 | 4.31 |
| $M_x$ | -4.24** | 4.80<br>-3.87 | 1.84 | * | 4.20 | 3.63<br>3.52 | 1.83 | 1.77 |
| $M_y$ | 0 | 1.30<br>1.32 | 1.14 | * | 0 | 22.18<br>7.66 | 2.51 | * |

*Static value too small to give meaningful results.
**Negative sign indicates that the maximum dynamic moment is smaller than the maximum static moment.

*Table 5. Impact Factor in Percentages for Loading Case (b) (mode included m = 6, n = 9)*

| Point Fig. 9a | a | $b_1$ $b_2$ | c | $d_1$ $d_2$ | $e_1$ $e_2$ | f | g | h |
|---|---|---|---|---|---|---|---|---|
| Defl. | 19.30 | 17.91 | 17.00 | 15.31 | 13.25 | 12.59 | 17.89 | 15.05 |
| Long. Stress | 10.05 | 9.68 | 8.90 | 12.13 | 13.35 | 13.18 | 18.60 | 12.07 |
| $M_x$ | 19.16 | * | -5.88 | *<br>-1.99 | 2.51<br>2.73 | 2.58 | * | 3.93 |
| $M_y$ | 0 | *<br>1.70 | 2.56 | 3.76<br>1.03 | 1.85<br>1.78 | 0 | .34 | .48 |

*Static value too small to give meaningful results.

With few exceptions [$M_y$ at b for loading (c) and $M_x$ at a for loading (d)], the maximum impact factor for both $M_x$ and $M_y$ for loading cases (c) and (d) with 4-wheel loads is about 4 to 5% which is of the same order of magnitude as that for the single load cases (a) and (b). On the other hand, the maximum impact for both deflection and longitudinal stress for loading cases (c) and (d) is about 4.5 to 5% which is only ¼ to ⅓ of that for loading cases (a) and (b).

It might be of interest to compare the impact factor obtained with that given by the AASHO Specification [1] $I = \frac{50}{L + 125} = 22.2\%$ for L = 100 ft. (30.48 m). This

value appears to agree with the single load cases (a) and (b) then the 4-wheel load cases (c) and (d). Still it is quite a surprise that the impact factor for the 4-load case is only ¼ to ⅓ of that for the single load case. However, it is known (4) that initial deflection in the springs has quite an effect on the impact factor. For this reason a fifth loading case (e) is investigated.

The loading case (e) is the same as the loading case (c) except that the springs have an initial displacement of 0.1 ft. (3.05 cm) when the truck is entering the bridge. Modes up to $m = 6$ and $n = 15$ have been included. The time increment necessary for convergence is found to be .00035 sec. and the computer running time on Univac 1108 is 35 min. The impact factors in percentages at various points for loading case (e) as compared with those for loading case (c) is given in Table 7.

*Table 6. Impact Factor in Percentages for Loading Case (d) (modes included $m=6$, $n=9$)*

| Point Fig. 9a | a | $b_1$ $b_2$ | c | $d_1$ $d_2$ | $e_1$ $e_2$ | f | g | h |
|---|---|---|---|---|---|---|---|---|
| Defl. | 5.00 | 4.74 | 4.62 | 4.41 | 4.51 | 3.36 | 4.74 | 4.51 |
| Long. Stress | 4.46 | 4.63 | 4.67 | 4.37 | 4.51 | 4.45 | 4.85 | 4.38 |
| $M_x$ | 6.75 | 3.07<br>3.07 | 1.88 | 1.13<br>1.89 | 3.27<br>3.84 | 3.62 | * | 1.61 |
| $M_y$ | 0 | *<br>4.95 | 0.92 | 3.24<br>1.94 | 4.83<br>4.36 | 0 | 4.59 | -1.28 |

*Static value too small to give meaningful results.

*Table 7. Impact Factor in Percentages for Loading Case (e) as Compared with Those for Loading Case (c)*

| Loading & Modes | (e) m = 6, n = 15 | | | | (c) m = 6, n = 9 | | | |
|---|---|---|---|---|---|---|---|---|
| Point Fig. 9a | a,f | $b_1, d_2$<br>$b_2, d_1$ | c | g,h | a,f | $b_1, d_2$<br>$b_2, d_1$ | c | g,h |
| Defl. | 177.16 | 167.35 | 164.01 | 167.02 | 4.73 | 4.60 | 4.57 | 4.60 |
| Long. Stress | 152.35 | 117.13 | 121.50 | 141.86 | 4.43 | 4.36 | 4.43 | 4.31 |
| $M_x$ | 133.84 | 61.03<br>103.54 | 71.52 | 125.93 | 4.20 | 3.63<br>3.52 | 1.83 | 1.77 |
| $M_y$ | 0 | 159.02<br>83.05 | 37.26 | * | 0 | 22.18<br>7.66 | 2.51 | * |

*Static value too small to give meaningful results.

It can be seen from Table 7 that the impact factor is profoundly affected by the initial displacement in the springs. It may be as high as 177% for deflection, 152% for longitudinal stress and 159% for transverse moments. The corresponding values for springs without initial displacement (loading case (c)) are 4.73%, 4.43% and 22.18%, respectively.

An examination of the tables shows that the impact factors for deflections, longitudinal stresses and moments are generally not the same and different for different points. However, with few exceptions (such as $M_y$ at b for loading (c) and $M_x$ at a for loading (d)), it appears that the use of the maximum impact factor for deflection as the impact factor longitudinal stresses and plate moments will give results on the safe side.

A check of the impact percentage obtained for the spring initial displacement case with that obtained from curves given by BIGGS, et al. [4] may be of interest. In the present case, the total moving mass $\hat{M}_V = 4\hat{M}_p = 4 \times 16/32.2 = 1.98$ k-sec$^2$/ft. (29000 kg) and total mass of the bridge $= \hat{M}_B = 23.0 \times .005 \times 100 = 11.5$ k-sec$^2$/ft. (168000 kg). Then $2\hat{M}_V/\hat{M}_B = 0.344$ and frequency of the load $= \omega_p = \sqrt{4\hat{K}_p/4\hat{M}_p} = \sqrt{\dfrac{4 \times 104}{1.98}} = 14.5$ in which $\hat{K}_p$ is the spring constant of each wheel load. The frequency of the bridge for $m = 1$ and $n = 1$ is $\omega = 20.2$; see Table 2. Then $\omega/\omega_p = 1.38$ and $\beta = \zeta^p\omega_p^2/g = 0.1 \times 14.5^2/32.2 = 0.65$ in which $\zeta^p$ is the initial displacement in the springs. From the curves given in Figure 15 of reference [4], [Note $\hat{M}_V$, $\hat{M}_B$, $\zeta^p$, $\omega$, $\omega_p$ correspond respectfully to $M_v$, $2M_B$, $z_m$, $p_B$, $p_v$ in reference [4]], one obtains the ratio of dynamic to static deflection $\Delta_{yd}/\Delta_{ys} = (y_m/y_{st})_1 \times (CF)_\beta \times (CF)_M =$

$1.65 \times 1.37 \times 0.98 = 2.23$. This corresponds to an impact factor of 123% as compared with 177% obtained herein.

The method developed by BIGGS, et al. [4] is also used to check the results for spring borne loads without initial displacement. For loading case (c) with $\beta = 0$, $(CF)_\beta = 0.65$ (extrapolated from the curve) one obtains $\Delta_{yd}/\Delta_{ys} = 1.65 \times 0.65 \times 0.98 = 1.05$. The impact factor of 5% agrees very well with the value of 4.73% obtained herein. In the case of a single wheel load $2\hat{M}_v/\hat{M}_B = 0.344/4 = 0.086$, $(CF)_M = 1.07$, $\Delta_{yd}/\Delta_{ys} = 1.65 \times 0.65 \times 1.07 = 1.15$. The impact factor of 15% agrees fairly well with the value of 19% obtained for loading cases (a) and (b).

## Conclusions for Practicing Engineers

Based on the results of this study, the following conclusions may be reached.

1. With limited but sufficient number of modes, the proposed method gives correct results for defections, longitudinal stresses and plate moments at all points except for plate moments at points directly under the concentrated loads. Impact factors and amplification factors obtained from dynamic analysis of the example bridge are sufficiently accurate for the number of modes taken into consideration.

2. With moderate number of plate elements and modes, the larger the length to width ratio of a plate, the poorer will be the values of the plate moments at points directly under the concentrated loads. However, as pointed out in the previous paper [7] the higher the number of modes included, the smaller the time increment (which is proportional to the period of the highest mode) required in a dynamic analysis. Some special method must be developed for determining plate moments at point of application of a concentrated load.

3. As pointed out in one of the examples, inclusion of higher modes may even cause a loss of accuracy due to inaccuracies in the eigenvectors of the higher modes. As pointed out in the previous paper [7], the computer program is based on a method given in reference [17]. It is beyond the scope of this study to make an exhausive evaluation of all available methods. More powerful methods for determining accurate eigenvectors are urgently needed.

4. The impact factors for deflections, longitudinal stresses and plate moments are generally not the same and different for different points. However, with few exceptions, it appears that the use of maximum impact factor for deflection as the impact factor for longitudinal stresses and plate moments will give results on the safe side.

5. The impact factor for a bridge subjected to 4-wheel load may be less than that for the same bridge subjected to a single wheel load.

6. Initial deflection in the spring of the wheel load has profound effect on the impact factor.

7. For the example considered, an estimate of the maximum impact factor for deflection for wheel loads with or without initial displacement in the spring may be made by the method given by BIGGS, et al. [4].

8. As pointed out in the previous paper [7], the study made herein provides better knowledge of the dynamic effects of moving loads on box girder bridges. The information presented herein should be of value to the practicing engineers for providing safety and economy in their design of such bridges.

## References


1. American Association for State Highway Officials: Standard Specification for Highway Bridges, Washington, D.C., 1973.
2. American Institute of Steel Construction: Design Manual for Orthotropic Steel Plate Deck Bridges. AISC, New York, N.Y., 1963.
3. ARCHER, J.S.: Consistent Mass Matrix for Distributed Mass Systems, Journal of the Structural Division, ASCE, Vol. 89, No. ST4, Proc. Paper 3591, Aug., 1963, pp. 161-178.
4. BIGGS, J.M., SUER, H.S., and LOUW, J.M.: Vibration of Simple Span Highway Bridges. ASCE Transactions, 1959, Paper No. 2979, pp. 291-318.
5. BOEHNING, R.H.: Single and Tandem Axle Dynamic Effects on a Highway Bridge Model. Civil Engineering Studies, Structural Research Series No. 57, University of Illinois, Urbana, Ill., 1953.
6. CHU, K.H., and DUDNIK, E.: Concrete Box Girder Bridges Analyzed as Folded Plates, First International Symposium Concrete Bridge Design, American Concrete Institute, Publication SP-23, 1969, pp. 221-246.
7. CHU, K.H., and JONES, M.: Theory of Dynamic Analysis of Box Girder Bridges. Memoires of Int. Assoc. of Bridge & Struc. Eng., Vol. 36 II, 1976, p. 121.
8. FENVES, S.J., VELETSOS, A.S., and SIESS, C.P.: Dynamic Studies of the AASHO Road Test Bridges, The AASHO Road Test, Highway Research Board Special Report 73, pp. 83-96.
9. EICHMANN, E.S.: Influence of Vehicle Suspensions on Highway Bridge Impact. Civil Engineering Studies, Structural Research Series No. 70, University of Illinois, Urbana, Ill., 1954.
10. GOLDBERG, J.E., and LEVE, H.L.: Theory of Prismatic Folded Plate Structures. Inter. Assoc. of Bridge and Structural Engineering Publication, Vol. 17, 1957, pp. 59-86.
11. IYENGAR, K.T.S.R., and JAGADISH, K.S.: The Responses of Beam and Slab Bridges to Moving Forces. Inter. Assoc. of Bridge and Structural Engineering Publication, Vol. 28, 1968, p. 69.
12. KENT, M.F.: AASHO Road Test Vehicle Operating Cost Related to Gross Weight. Appendix B, Tire Data, The AASHO Road Test, Highway Research Board Special Report, p. 163.
13. SCRODELIS, A.C., and DEFRIES-SKENE, A.: Direct Stiffness Solution for Folded Plates. Journal of the Structural Division, ASCE, Vol. 90, No. ST4, Proc. Paper 3994, Aug., 1964, pp. 15-47.
14. VELETSOS, A.S., and HUANG, T.: Analysis of Dynamic Response of Highway Bridges. Journal of the Engineering Mechanics Division, ASCE, Vol. 96, No. EM5, Proc. Paper 7591, Oct., 1970, pp. 593-620.
15. TIMOSHENKO, S.P., and WORNOWSKY-KRIEGER, S.: Theory of Plates and Shells, McGraw-Hill Book Company, Inc., New York, N.Y., 1959.
16. TIMOSHENKO, S.P., and YOUNG, D.H.: Vibration Problems in Engineering, D. Van Nostrand Co., Inc., Princeton, N.J., 1955.
17. WILKINSON, J.H.: The Calculation of the Latent Roots and Vectors of Matrices on the Pilot Model of the A.S.E., Proceedings of the Cambridge Philosophical Society, Vol. 50, 1954, pp. 535-566.


## Summary

The main purpose of this paper is to present numerical results obtained from a computer program based on a theoretical formulation for the analysis of dynamic responses due to moving loads in all plate elements in simply supported box girder bridges presented in a previous paper. Verification of the computer program was made not only to check out the program but to find out the minimum number of plate strips, the minimum number of modes and the largest time increment to be taken for obtaining reasonable accurate results. Dynamic analysis were performed for an example bridge with five loading cases.

**Résumé**

Le but principal de l'article est de présenter les résultats numériques obtenus à l'aide d'un programme d'ordinateur basé sur une théorie pour l'analyse des effets dynamiques des charges mobiles dans tous les éléments de plaques de ponts à poutres en caisson tel qu'il est présenté dans l'article antérieur. La vérification du programme d'ordinateur a été opérée à titre de contrôle et pour déterminer le nombre minimum des lames, le nombre minimum des modes et l'augmentation maximum du temps afin d'arriver à des résultats d'une précision suffisante. L'analyse dynamique a été faite pour un pont théorique et pour cinq cas de charges.

**Zusammenfassung**

Die Nachprüfung des Computerprogrammes erfolgte nicht nur aus Kontrollgründen, sondern auch um die Mindestzahl von Plattenelementen und Formtypen sowie den grössten Zeitintervall zur Erzielung noch genügend genauer Resultate zu ermitteln. Als Beispiel wird die dynamische Berechnung an einer Brücke für fünf Belastungsfälle durchgeführt. Der Hauptzweck dieses Beitrages besteht darin, rechnerische Resultate eines Computerprogrammes vorzulegen. Dieses Programm stützt sich auf die im vorhergehenden Beitrag behandelte Theorie für die Berechnung von Kastenträgerbrücken unter dynamischen Lasten.

Leere Seite
Blank page
Page vide

# Failure Mechanisms for Reinforced Concrete Beams in Torsion and Bending

*Mécanismes de ruine pour des poutres en béton armé soumises à la torsion et à la flexion*

*Bruchmechanismen für Stahlbetonbalken unter Torsion und Biegung*

P. MÜLLER
Research Associate, Institute of Structural Engineering, Swiss Federal Institute of Technology (ETH), Zurich (Switzerland).

## Introduction

To describe the failure of reinforced concrete beams with thin-walled closed cross section in torsion and bending, LAMPERT [2, 3] used a space truss model based on the lower bound theorem of the Theory of Plasticity. The good correspondence between theory and test results stimulates to generalize the model. The application of the Theory of Plasticity to the general plane stress problem of reinforced concrete shear walls [5] has led to a better understanding of the collapse mechanisms of these beams. Indeed all collapse mechanisms, known so far, turn out to be incompatible with the state of stress assumed in the truss model.

The aim of this contribution is to develop new compatible mechanisms. The very simple basic mechanism has significance for engineering practice in allowing easy visualization of the failure modes assumed by the truss model. The truss model and the new mechanisms supply together, as lower and upper bound solutions, respectively, the exact interaction relation for thin-walled closed cross sections subjected to torsion and bending.

We confine ourselves to constant bending moment and torque, and, for simplicity, to rectangular cross sections. The present work is part of the study [5] which the reader is referred to for general cross sections and detailed information.

## Basic Theory

The present investigation is based on the classical Theory of Plasticity, e.g. [1], in particular on the concept of plastic potential and on the upper and lower bound theorems of limit analysis. The latter is based on the following idealizations and assumptions:

1. A rigid-perfectly plastic or elastic-perfectly plastic material is visualized (Fig. 1).

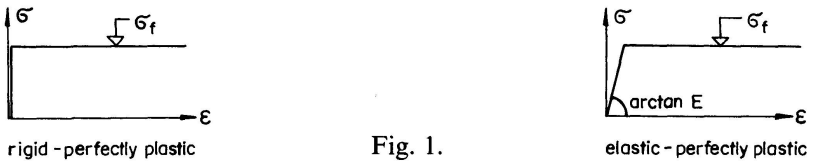


Fig. 1.

2. The elastic and plastic deformations are small in the sense of no significant changes in the geometry of the structure, so as to allow the formulation of equilibrium equations for the original configuration.

## Yield Criterion for Reinforced Concrete Shear Walls

The following assumptions are postulated:

1. The assumptions of the Theory of Plasticity in the sense of Section 2 are admissible.
2. The concrete is assumed to be in a state of plane compressive stress; in particular, the tensile strength of concrete is neglected.
3. The reinforcement is idealized as a state of plane stress in its direction.
4. The assumed redistribution of steel and concrete stresses stipulates for full aggregate interlock and dowel action in initial cracks. Local and bond failure are excluded.
5. The range of ratio of reinforcement is such that:
   a) no failure occurs at first crack formation;
   b) compressive strength of concrete is never reached.
6. The reinforcement is placed as a orthogonal net.

Assumption 1, in particular, the necessary ductility of failure, is sufficiently confirmed by [6, 7, 8]. 5b) and 6) are not postulated in [5]. But as the yield criterion merely serves to develop mechanisms compatible with the space truss model, we do not need more generality.

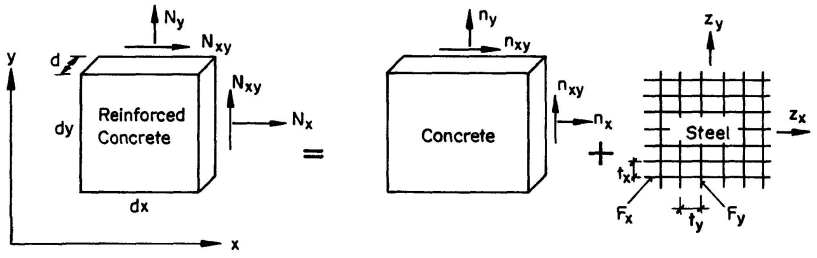


Fig. 2.

The membrane forces $N_x$, $N_y$, $N_{xy}$, acting on the differential element of Figure 2, are equivalent to the sum of the stress resultants $n_x$, $n_y$, $n_{xy}$ of the concrete and $z_x$, $z_y$ of the reinforcement. It is convenient to introduce the coordinate system (x, y) parallel to the orthogonal reinforcement.

$$\left.\begin{aligned} N_x &= n_x + z_x \\ N_y &= n_y + z_y \\ N_{xy} &= n_{xy} \end{aligned}\right\} \tag{1}$$

$$\text{where } z_x = \frac{\sigma_e F_x}{t_x},\ z_y = \frac{\sigma_e F_y}{t_y}. \tag{2}$$

The concrete stress not reaching compressive strength, the only yield condition is

$$n_I = \frac{n_x + n_y}{2} + \sqrt{\left(\frac{n_x - n_y}{2}\right)^2 + n_{xy}^2} \leq 0,$$

$$\text{or } n_{xy}^2 \leq n_x n_y, \quad n_x \leq 0, \quad n_y \leq 0, \tag{3}$$

whereas steel is governed by the yield criterion

$$\left.\begin{aligned} |z_x| \leq P_x &= \frac{\sigma_f F_x}{t_x}, \\ |z_y| \leq P_y &= \frac{\sigma_f F_y}{t_y}, \end{aligned}\right\} \tag{4}$$

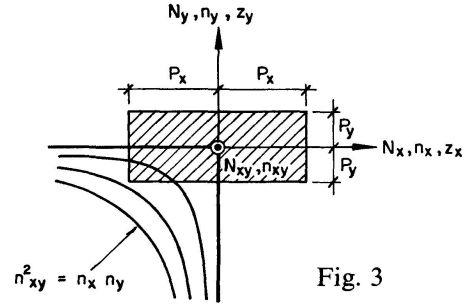


Fig. 3

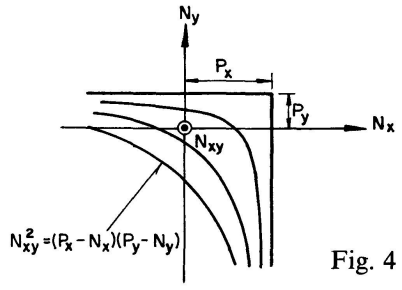


Fig. 4

In the three-dimensional space of stresses (Fig. 3) the yield surface of the concrete is an elliptic cone, while the yield locus of the reinforcement is represented by a rectangle in the plane ($N_x$, $N_y$). The sets of stress points with the properties (3) and (4) are convex sets. Hence, the convex set of stress points, satisfying the unknown yield criterion $\Phi(N_x, N_y, N_{xy}) \leq 0$, is defined by (1) as a linear combination of the convex sets defined by (3) and (4); i.e. $\Phi$ is found to be the envelope of all translationally shifted yield loci of concrete with centre within the shaded rectangle of Figure 3. Hence, $\Phi$ is represented by the concrete cone with tip at the point ($P_x$, $P_y$, 0) as illustrated in Figure 4, and the yield criterion may be written

$$\left.\begin{aligned} \Phi_1 &= N_{xy}{}^2 - (N_x - P_x)(N_y - P_y) \leq 0, \\ \Phi_2 &= N_x - P_x \leq 0, \Phi_3 = N_y - P_y \leq 0. \end{aligned}\right\} \tag{5}$$

Considering assumption 5b), the yield criterion (5) coincides with that reported by NIELSEN [10].

For stress points ($N_x$, $N_y$, $N_{xy}$) on the yield surface (5), the stress resultants in the components steel and concrete are

$$\left.\begin{aligned} &z_x = P_x,\ z_y = P_y, \\ &n_{xy}^2 = n_x n_y, \quad n_x \leq 0, \quad n_y \leq 0, \\ \text{or} \quad &n_{II} \leq n_I = 0, \end{aligned}\right\} \tag{6}$$

where $n_I$ and $n_{II}$ denote the major and minor principle concrete stress, respectively. Thus both components of reinforcement are yielding, while the concrete is in a uniaxial state of compressive stress. Evidently this coincides completely with the state of stress, the truss model is based on.

The longitudinal reinforcement and the stirrups of the shear wall shown in Figure 5 are interpreted as stringers and posts of a truss, whose struts idealize a uniform state of compressive stress in the concrete. The inclination of the struts is determined from the condition that both the longitudinal and the stirrup reinforcement are yielding. Assumption 5b is taken for granted.

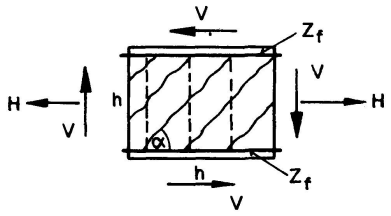


Fig. 5.

Whereas the truss model and the foregoing more general results harmonize with respect to the statical aspects, care is needed however in the translation of the kinematics of a truss to reinforced concrete shear walls.

## Yield Law and Kinematics

For states of stress at the yield limit (5), with non-zero $N_{xy}$, the following is true

$$\Phi_1 = 0, \Phi_2 < 0, \Phi_3 < 0, \tag{7}$$

and hence, according to the theory of plastic potential, the rates of plastic strain are related to the stresses as follows

$$\left.\begin{aligned} \dot{\varepsilon}_x &= \dot{\lambda}\frac{\partial \Phi_1}{\partial N_x} = -\dot{\lambda}(N_y - P_y) = -\dot{\lambda}n_y, \\ \dot{\varepsilon}_y &= \dot{\lambda}\frac{\partial \Phi_1}{\partial N_y} = -\dot{\lambda}(N_x - P_x) = -\dot{\lambda}n_x, \\ \dot{\gamma}_{xy} &= \dot{\lambda}\frac{\partial \Phi_1}{\partial N_{xy}} = \dot{\lambda}(2N_{xy}) = \dot{\lambda}2n_{xy}, \\ &\text{where } \dot{\lambda} \geq 0. \end{aligned}\right\} \tag{8}$$

Substituting the expressions (8) into (7) we find that

$$\left(\frac{\dot{\gamma}_{xy}}{2}\right)^2 = \dot{\varepsilon}_x \dot{\varepsilon}_y, \qquad \dot{\varepsilon}_x \geq 0, \dot{\varepsilon}_y \geq 0, \tag{9}$$

or, $\dot{\varepsilon}_I$ and $\dot{\varepsilon}_{II}$ denoting the major and minor principle strain-rate, respectively,

$$\dot{\varepsilon}_I \geq \dot{\varepsilon}_{II} = 0. \tag{10}$$

If $\Phi_1 = \Phi_2 = \Phi_3 = 0$, (10) is replaced by (11).

$$\dot{\varepsilon}_I \geq \dot{\varepsilon}_{II} \geq 0. \tag{11}$$

Thus the only velocity fields compatible with the considered stress fields are those with no compressive strains. (10) and (11) are merely the dual kinematical interpretation of assumption 5b preventing concrete crushing. Although this consequence of the upper limitation of reinforcement ratios seems somewhat trivial, it has been overlooked in all torsional collapse mechanisms proposed so far. Above all this is due to the fact that the yield criterion (5) and assumption 5b have only been used implicitly.

Calculating the direction of the minor principal strain-rate $\dot{\varepsilon}_{II} = 0$ in (10), there results

$$\tan 2\alpha = \frac{-\dot{\gamma}_{xy}}{\dot{\varepsilon}_y - \dot{\varepsilon}_x} = \frac{-2N_{xy}}{-(N_x - P_x) + (N_y - P_y)} = \frac{-2n_{xy}}{n_y - n_x} \tag{12}$$

Now the last expression in (12) equals the direction of concrete compressive trajectories. Thus the principal axis of plastic strain-rates and those of concrete stress-state coincide. Considering (9) in (12) we obtain

$$\tan 2\alpha = \frac{-\dot{\gamma}_{xy}}{\dot{\varepsilon}_y - \frac{\dot{\gamma}_{xy}^2}{4\dot{\varepsilon}_y}} = \frac{2\left(\frac{-\dot{\gamma}_{xy}}{2\dot{\varepsilon}_y}\right)}{1 - \left(\frac{-\dot{\gamma}_{xy}}{2\dot{\varepsilon}_y}\right)^2} = \frac{2\tan\alpha}{1 - (\tan\alpha)^2} \tag{13}$$

By means of $\tan\alpha$, (9) may also be expressed parametrically by two equations from (14) and (15)

$$\tan\alpha = \frac{-\dot{\gamma}_{xy}}{2\dot{\varepsilon}_y} = \frac{2\dot{\varepsilon}_x}{-\dot{\gamma}_{xy}} = \pm\sqrt{\frac{\dot{\varepsilon}_x}{\dot{\varepsilon}_y}}, \tag{14}$$

$$-\dot{\gamma}_{xy} = \frac{\dot{\varepsilon}_x}{\tan\alpha} + \dot{\varepsilon}_y \tan\alpha, \tag{15}$$

where $\dot{\varepsilon}_x \geq 0$, $\dot{\varepsilon}_y \geq 0$.

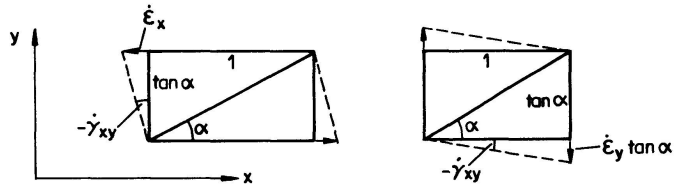


Fig. 6.

On the other hand, if we derive the kinematic relations using a truss with rigid strut, as shown in Figure 6 [2, 3], we only obtain equation (15). The kinematics of a truss does not correspond with the kinematics of shear walls governed by the flow rules (8). The truss only prevents compressive strains in the direction of the struts and therefore neglects the solid nature of the shear wall.

## Discontinuities in the Velocity Field

From the Theory of Plasticity we know that the velocity fields associated with collapse often are discontinuous. Therefore, we further have to derive the restrictions imposed to velocity jumps by (10). In doing so we have to visualize a

discontinuity line as the limiting case of a finite transition layer with rapidly but continuously (e.g. linearly) changing velocities as shown in Figure 7.

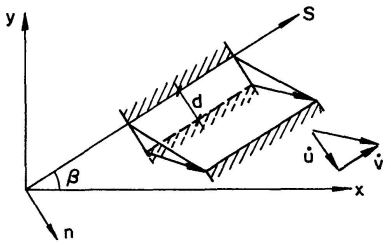


Fig. 7.

The depth of the transition layer tending toward zero, the plastic strain-rates are

$$\left.\begin{aligned} &\dot{\varepsilon}_n = \frac{\dot{u}}{d}, \quad \dot{\varepsilon}_t = 0, \quad \dot{\gamma}_{nt} = \frac{\dot{v}}{d}, \\ &\dot{\varepsilon}_I = \frac{1}{2}\left(\frac{\dot{u}}{d} + \sqrt{\left(\frac{\dot{u}}{d}\right)^2 + \left(\frac{\dot{v}}{d}\right)^2}\right), \; \dot{\varepsilon}_{II} = \frac{1}{2}\left(\frac{\dot{u}}{d} - \sqrt{\left(\frac{\dot{u}}{d}\right)^2 + \left(\frac{\dot{v}}{d}\right)^2}\right) \end{aligned}\right\} \tag{16}$$

Evidently (10) is only true, provided that

$$\dot{u} \geq 0, \; \dot{v} = 0. \tag{17}$$

Thus only the normal velocity component may jump, and discontinuity lines and concrete compressive trajectories coincide in direction, viz. $\alpha = \beta$. Now the physical crack pattern observed in tests tends towards the theoretical pattern of concrete compressive trajectories at collapse state [6-9]. We therefore may regard discontinuities governed by (17) as the cracks of the ideal rigid-plastic shear wall obeying (8), and we name them *collapse cracks*. (17) has been adopted in [4] in the following concise form: collapse cracks open normally to their direction. It must be emphasized that, for an elastic-perfectly plastic material, the statement only refers to the increments of crack widening at collapse state.

On the other hand, if there is also a jump in the tangential velocity component, viz. $\dot{v} \neq 0$, we obtain from (16) $\dot{\varepsilon}_I \geq 0$, $\dot{\varepsilon}_{II} \leq 0$. Hence, the concrete is crushing, and its contribution to the rate of energy dissipation must not be neglected. $\dot{\gamma}_{nt}$ being non-zero, the discontinuity lines and the concrete compressive trajectories coincide no more. Because the physical crack pattern, prior to failure, again tends toward concrete compressive trajectories, rather than toward the possible discontinuity lines, we avoid the term "crack" for the latter. According to the Theory of Plasticity for plane stress and strain such discontinuities are named *slip lines*. Thus "collapse crack" is reserved in its original meaning for discontinuities with no concrete crushing, whereas "slip lines" always imply concrete crushing. Together with a yield criterion including concrete crushing, such slip lines are studied in reference [5] in the context of shear in reinforced concrete and shear walls in general. In this connection, the reader is also referred to reference [11] recently published, where partially similar results have been derived independently.

The results of this Section may be summarized as follows: Only collapse cracks but not slip lines are compatible with the yield criterion (5).

## Reinforced Concrete Beams in Torsion and Bending

To prepare the derivation of a new mechanism, the space truss model [2, 3] and two mechanisms incompatible with the latter [2, 12] are recapitulated, as lower and upper bound approaches respectively to the ultimate strength of reinforced concrete beams in torsion and bending. From the theoretical point of view, it must be pointed out that the space truss model intrinsically applies to thin-walled closed cross sections. Hence, mechanisms compatible with the latter must be derived for the same statical system. The applicability of the same relations to solid cross sections is well confirmed by test results [6, 7, 8], but is not followed up theoretically in this study.

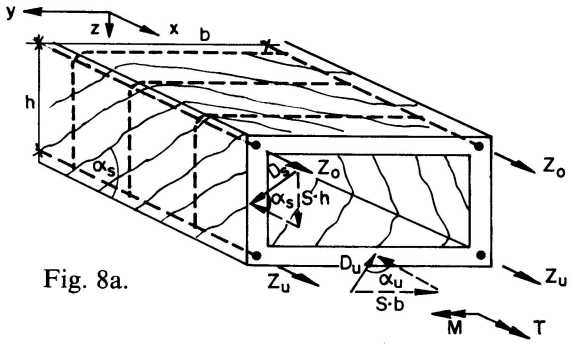


Fig. 8a.

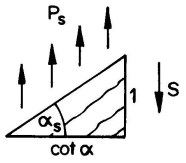


Fig. 8b.

Consider a beam with thin-walled closed rectangular cross section as shown in Figure 8a, for example. The longitudinal reinforcement is concentrated in four corner stringers of equal yield force $Z_f$. The yield forces of the stirrups, measured per unit length, equal $P_u$ in the top and bottom shear walls and $P_s$ in the side shear walls. The reinforcement ratio is within the range of no concrete crushing.

In the space truss model the concrete is assumed to be in a uniaxial state of compressive stress being uniform in each shear wall. Hence, the inclination of struts $\alpha$ and the shear flow S are uniform in each wall, the resultant of concrete stresses is acting in the centre of the wall, and the bending moment is sustained only by the top and bottom walls. The bending moment and the torque being constant, it is further assumed that the stringer forces are constant along the beam, or equivalently, that the shear flow S is constant around the sectional perimeter. For convex cross sections the reinforcement of all but one shear wall must reach the yield stress. Thus, for positive bending moment, only the reinforcement forces of the top wall are unknown. Conveniently the equilibrium equations of moments are then formulated relative to the x- and y-axis lying in the top wall

$$M = 2Z_f h - 2Sh \cot \alpha_s \tfrac{h}{2} - Sb \cot \alpha_u h, \tag{18}$$

$$T = 2Sh \tfrac{b}{2} + Sbh = 2S \cdot bh = 2SF_0. \tag{19}$$

From the free-body diagram Figure 8b we obtain

$$S = P_s \cot \alpha_s = P_u \cot \alpha_u. \tag{20}$$

In particular, (20) implies also that the strut inclinations of the side walls are the same, what we already have used in (18). Substituting from (19) and (20) into (18) we obtain the interaction relation

$$M = 2Z_f h - \frac{T^2}{4F_0}\left(\frac{h}{b}\frac{1}{P_s} + \frac{1}{P_u}\right) \tag{21}$$

The same relation may also be derived directly by means of the yield criterion (5), each shear wall being in a uniform state of membrane stress $N_x$, $N_y$, $N_{xy}$. To be a lower bound solution, the loads must be applied by rigid diaphragms. Additionally, proper anchorage of longitudinal reinforcement has to be ensured by an anchorage region, for which statically admissible stress fields must be found satisfying the end boundary conditions. However, within the beam theory these problems may be regarded as constructive problems. The transition from the space structure to the beam is effected by the transition from the yield criterion (5) to the yield criterion (21) in the generalized stresses acting on the differential beam element. Static boundary conditions are satisfied then in the generalized stresses. In this sense the truss model solution is a lower bound to the exact interaction relation. To have a complete solution, we still must find a mechanism related to the assumed state of stress by (8).

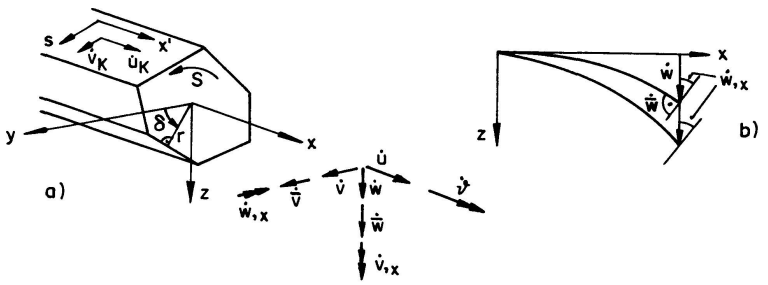


Fig. 9.

In [2] the usual assumption of beam theory is postulated: Cross sections normal to the beam axis remain plane. The velocities $\dot{u}_K$, $\dot{v}_K$ of shear wall K are related (Fig. 9) to the displacement parameter rates $\dot{u}$, $\dot{v}$, $\dot{w}$, $\dot{\bar{v}}$, $\dot{\bar{w}}$, $\dot{\vartheta}$ of the beam axis by

$$\left.\begin{aligned} \dot{u}_K &= \dot{u} - z\dot{w}_{,x} - y\,\dot{v}_{,x}, \\ \dot{v}_K &= -(\dot{v} + \dot{\bar{v}})\sin\delta + (\dot{w} + \dot{\bar{w}})\cos\delta + r\dot{\vartheta}, \end{aligned}\right\} \tag{22}$$

where v, w and $\bar{v}$, $\bar{w}$ result from pure bending and pure shearing, respectively, as shown in Figure 9b. $(\ )_{,x}$ and $(\ )_{,s}$ denote differentiation with respect to the x- and s-direction. The rates of strain are

$$\left.\begin{aligned} \dot{\varepsilon}_{LK} &= \dot{u}_{K,x} = \dot{u}_{,x} - z\dot{w}_{,xx} - y\dot{v}_{,xx}, \\ \dot{\gamma}_K &= \dot{u}_{K,s} + \dot{v}_{K,x} = -\dot{\bar{v}}_{,x}\sin\delta + \dot{\bar{w}}_{,x}\cos\delta + r\dot{\vartheta}_{,x}. \end{aligned}\right\} \tag{23}$$

Hence, the rate of longitudinal extension $\dot{\varepsilon}_{LK}$ varies linearly across the wall, whereas the shear strain-rate $\dot{\gamma}_K$ is constant (Fig. 10).

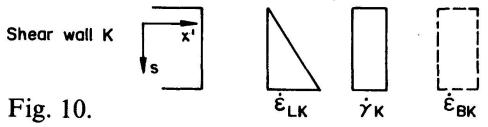


Fig. 10.

Considering (14): $\tan \alpha_K = \frac{2\dot{\varepsilon}_{LK}}{\dot{\gamma}_K}$,

the strut inclination varies linearly in each wall too. Hence, the mechanism is not compatible with the constant stress-state of the space truss model. Assuming in each wall a constant distribution of the stirrup strain-rate $\dot{\varepsilon}_{BK}$, and calculating $\dot{\varepsilon}_{BK}$ with (9) for the average rate of longitudinal extension $\dot{\varepsilon}_{LK}$ in the centre of the wall, we may derive (21). However, (9) is violated in general. If the contribution of concrete crushing to the rate of energy dissipation, in regions with $\dot{\gamma}_K^2 > 4\dot{\varepsilon}_{LK} \cdot \dot{\varepsilon}_{BK}$, would not be neglected, ultimate strength would be higher than (21).

An upper bound approach with discontinuous velocity fields is the well known "Skew Bending" mechanism [12].

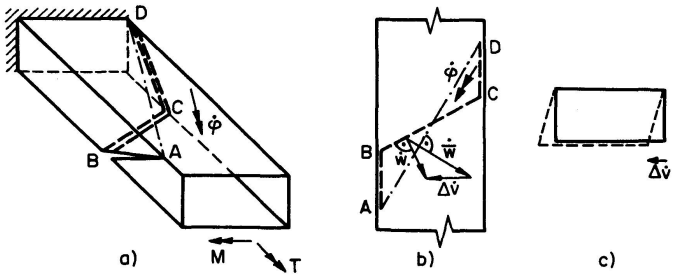


Fig. 11a, b, c.

Consider a rotation of the free end of the cantilever with thin-walled cross section shown in Figure 11a, about a skew axis AD. The position of the axis is fixed by the two ends of a crack ABCD running around the beam. The fact that the load factors derived from this mechanism are lower than predicted by (21), has erroneously been explained by nodal forces [13]. The true reason may be easily recognized from the top view Figure 11b. If the sectional shape is preserved as usually assumed, there must be a jump in the tangential velocity component along the discontinuity line BC in the bottom wall. Hence, the contribution of concrete crushing to the rate of energy dissipation must not be neglected, and higher load factors than predicted by (21) would be obtained, if concrete strength is assumed according to assumption 5b.

On the other hand, if only the normal velocity component is assumed to jump along ABCD, a sectional deformation $\Delta\dot{v}$ is forced upon the free end of the cantilever (Fig. 11b, c).

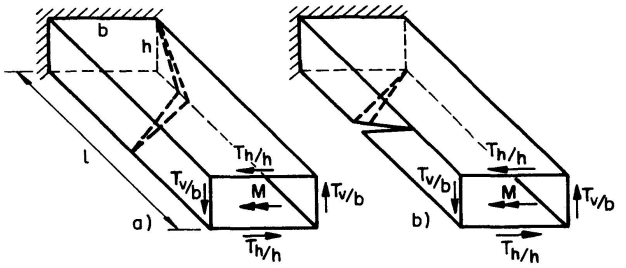


Fig. 12.

However, for a cantilever regarded as a folded structure, lower load factors may be obtained with mechanisms as suggested in Fig. 12. Because of the deformable cross section the results depend on the ratio of $T_v$ and $T_h$, i.e. of the torques applied

to the vertical and horizontal walls, respectively. For cantilevers of sufficient length, the load factors are always lower than predicted by (21). The latter is reached only for $T_v = T_h = T/2$, i.e. for the optimal load application corresponding to constant shear flow.

On the other hand, combining appropriately the two mechanisms shown in Figure 12a and Figure 12b, we may assume a non-deformable cross section without violating (17). This mechanism is treated in detail in the next Section. The resulting interaction relation coincides with (21), and the strut inclinations correspond to constant shear flow. Hence, the statical assumption of constant shear flow corresponds evidently to the kinematical assumption of a non-deformable cross section. This corresponds also to the assumption of a rigid diaphragm in (21), which prevents the mechanisms of Figure 12.

## Discontinuous Failure Mechanism

First a compatible mechanism with discontinuous velocity fields is derived. It allows not only easy visualization, but is also the basic element of all other continuous and discontinuous compatible mechanisms. As in the statical approach we only allow for membrane forces, and all resistance of the shear walls normal to their plane is neglected.

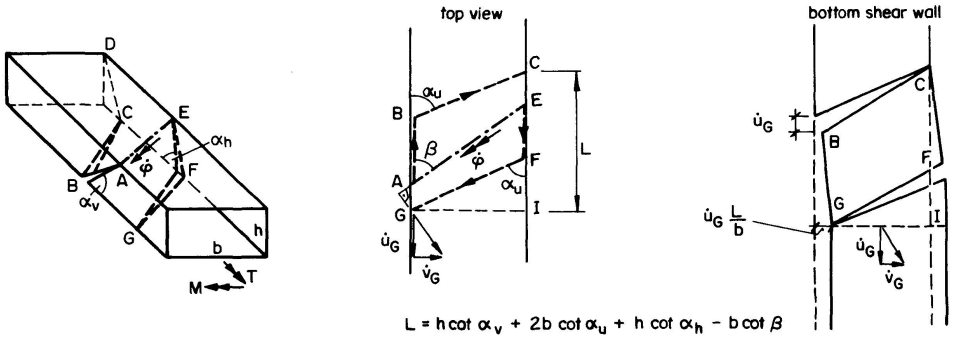


Fig. 13.

Consider again a rigid rotation of the front part of the beam shown in Figure 13 about a skew axis AE situated for instance in the top wall. However, contrary to Figure 11, the inclination $\beta$ of the axis of rotation is not determined from the position of the ends of *one* crack, but is an additional parameter to be determined from condition (17) and from the assumption that the sectional shape is preserved.

Consequently, *two* cracks have to be considered, starting from the points A and E of the axis of rotation. The hinge AE opens in the front wall the collapse crack AB, which, on his part, opens the crack BC in the bottom wall. At C the crack must be closed again, because there is no hinge in the top wall at D.

The same is true for the collapse crack EFG. The two cracks running around the beam separate in the bottom wall the portion BCFG being connected along the sides CF and BG with the fixed and the rotating part of the beam, respectively. Considering (17), the portion BCFG undergoes a rigid rotation in its plane.

Now, if the shape of cross section GI is preserved, the velocities of point G, in the plane of the bottom shear wall, are (top view)

$$\left.\begin{aligned} \dot{u}_G &= \dot{\varphi} h \sin \beta, \\ \dot{v}_G &= \dot{\varphi} h \cos \beta. \end{aligned}\right\} \tag{24}$$

On the other hand, considering the rigid body rotation of the portion BCFG in the bottom wall (Fig. 13 bottom shear wall), we obtain

$$\dot{v}_G = \dot{u}_G \tfrac{L}{b}, \tag{25}$$

where, according to Figure 13, L is a function of the inclination $\beta$ of the axis of rotation and of the free parameters of the mechanism, that is the inclinations $\alpha$ of the collapse cracks. Considering (24) in (25) and substituting for L we find

$$\cot \beta = \tfrac{L}{b} = \tfrac{1}{2} (\cot \alpha_v + \cot \alpha_h) \tfrac{h}{b} + \cot \alpha_u. \tag{26}$$

The mechanism satisfies condition (17) everywhere, and a deformation of the cross section is prevented for arbitrary crack inclinations by choosing the ratio of twist and flexural curvature cot $\beta$ according to (26). In particular, referring again to the example of Figure 8a, we may use the crack inclinations (20) obtained by the space truss model. Hence, the mechanism is compatible with the state of stress assumed in the lower bound approach, and the interaction relation (21) corresponds to the limit load of a beam with non-deformable cross section, within the scope of membrane theory.

To verify the statement, we equate the rate of external work

$$L_a = \dot{\varphi} \sin \beta \, M + \dot{\varphi} \cos \beta \, T \tag{27}$$

to the rate of energy dissipation

$$L_d = \dot{\varphi} \sin \beta \, \{h^2 \tfrac{1}{2} (\cot^2 \alpha_v + \cot^2 \alpha_h) P_s + hb \cot^2 \alpha_u P_u + 2Z_f h\}, \tag{28}$$

and considering (26) we obtain

$$\left.\begin{aligned} M = 2Z_f h &+ \tfrac{1}{2} (h^2 P_s \cot^2 \alpha_v - \tfrac{h}{b} T \cot \alpha_v) \\ &+ \tfrac{1}{2} (h^2 P_s \cot^2 \alpha_h - \tfrac{h}{b} T \cot \alpha_h) \\ &+ \tfrac{b}{h} (h^2 P_u \cot^2 \alpha_u - \tfrac{h}{b} T \cot \alpha_u). \end{aligned}\right\} \tag{29}$$

Minimizing M for fixed T with respect to the crack inclinations we find

$$2 \frac{\partial M}{\partial (\cot \alpha_v)} = 2h^2 P_s \cot \alpha_v - \tfrac{h}{b} T = 0,$$

and

$$\cot \alpha_v = \frac{T}{2bh} \frac{1}{P_s} = \frac{T}{2F_0} \frac{1}{P_s}.$$

Hence,

$$\cot \alpha_v = \cot \alpha_h = \frac{S}{P_s}, \quad \cot \alpha_u = \frac{S}{P_u}, \tag{30}$$

and by substitution into (29) relation (21) is obtained again:

$$M = 2Z_f h - \frac{T^2}{4F_0} \left( \frac{h}{b} \frac{1}{P_s} + \frac{1}{P_u} \right). \tag{21}$$

To get the whole range of interaction, we also have to consider the mechanisms with axis of rotation in the other shear walls. For pure torsion all the reinforcement is yielding in our example. Hence, each of these mechanisms is possible. In particular,

a mechanism with pure twist and extension, as shown in Figure 14, is also feasible. It may be regarded as a linear combination of the two mechanisms with axis of rotation in the top and bottom shear wall.

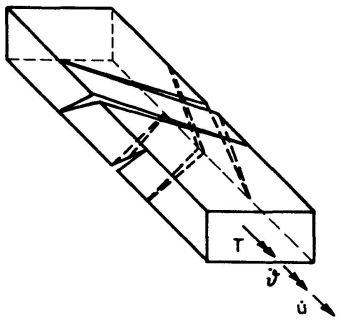


Fig. 14.

Finally, there should be pointed out that the length of the presented discontinuous mechanism, i.e. in our example

$$l_{Min} = h \cot \alpha_v + b \cot \alpha_u, \tag{31}$$

evidently is the minimum failure region required by a mechanism satisfying the conditions of no concrete crushing and no cross-sectional deformations. If the most critical part of the beam is shorter than the minimal failure length calculated with the corresponding reinforcement, (21) is to be regarded as a lower bound.

## Continuous Mechanisms and Beam Theory

Spreading the rotation $\dot{\varphi}$ in the top wall and the cracks over a finite length d we get a continuous mechanism as shown in Figure 15a. All relations still hold, if the reinforcement does not change over the additional length. Evidently it is not possible in general to describe these mechanisms by beam theory, which relates the displacements within a cross section to displacement parameters of the beam axis. Only in the case illustrated in Figure 15b this is partially possible.

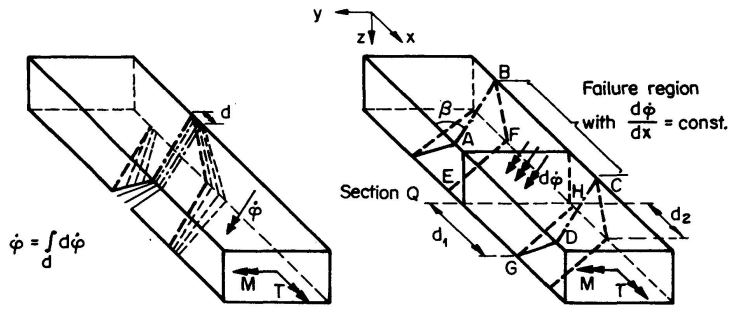


a) Fig. 15. b)

Consider a continuous mechanism with constant curvature-rate of the top wall within the zone ABCD, viz. $d\dot{\varphi}/dx = \text{const.}$, and hence, with a zone of uniform strain-rates EFGH in the bottom wall. If the failure region is long enough, as shown in Figure 15b, there exist sections Q lying completely within the region ABEF-CDGH. Obviously cross sections Q have plane strain-rate distributions, and all

their longitudinal fibers have the same curvature. Thus beam theory may be used for these sections. On the other hand, looking at the different distances $d_1$, $d_2$ between the section corners and the rigid parts of the beam, and considering that the rate of extension is the same for $d_1$ and $d_2$ and is zero in the top wall, we find that originally plane sections do not remain plane.

Hence, the beam assumptions (22) must be completed by warping terms. Referring again to Figure 9, the in-plane velocities of shear wall K are

$$\left.\begin{aligned} \dot{u}_K &= \dot{u} - z\,\dot{w}_{,x} - y\,\dot{v}_{,x} + \dot{U}(s), \\ \dot{v}_K &= -\dot{v}\sin\delta + \dot{w}\cos\delta + r\dot{\vartheta} + \dot{V}(s), \end{aligned}\right\} \tag{32}$$

where the terms $\dot{U}$, $\dot{V}$, $r\dot{\vartheta}$ account for warping, stirrup elongation and the assumption of a non-deformable cross section, respectively. The strain-rates $\dot{\varepsilon}_{LK}$, $\dot{\varepsilon}_{BK}$ of the longitudinal and stirrup reinforcement, respectively, and the shear strain-rates $\dot{\gamma}_K$ are

$$\left.\begin{aligned} \dot{\varepsilon}_{LK} &= \dot{u}_{K,x} &&= \dot{u}_{,x} - z\dot{w}_{,xx} - y\dot{v}_{,xx}, \\ \dot{\varepsilon}_{BK} &= v_{K,s} &&= \dot{V}_{,s} \\ \dot{\gamma}_K &= \dot{u}_{K,s} + v_{K,x} &&= \dot{U}_{,s} + r\dot{\vartheta}_{,x}. \end{aligned}\right\} \tag{33}$$

Contrary to equation (23) the shear strain-rate distribution across a wall depends now additionally on a warping term to be determined appropriately. Assuming a constant $\tan\alpha_K$ in each shear wall according to the state of stress in the truss model and considering (14) we find a linear variation of all strain-rate components:

$$\left.\begin{aligned} &\dot{\gamma}_K = 2\dot{\varepsilon}_{LK}\cdot\cot\alpha_K, \quad \dot{\varepsilon}_{BK} = \dot{\varepsilon}_{LK}\cot^2\alpha_K, \\ &\dot{\varepsilon}_{LK} \geq 0, \quad \dot{\varepsilon}_{BK} \geq 0. \end{aligned}\right\} \tag{34}$$

Integrating (33) and substituting from (34) we obtain

$$\left.\begin{aligned} \dot{U}(s) &= \int_s (2\dot{\varepsilon}_{LK}\cot\alpha_K - r\dot{\vartheta}_{,x})\,ds, \\ \dot{V}(s) &= \int_s \dot{\varepsilon}_{LK}\cot^2\alpha_K\,ds. \end{aligned}\right\} \tag{35}$$

Continuity of the $\dot{u}_K$ around the closed cross section is ensured, provided that

$$\oint_s \dot{U}_{,s}\,ds = 0 = \oint_s \dot{\gamma}_K\,ds - \dot{\vartheta}_{,x}\oint_s r\,ds,$$

$$\text{hence } \dot{\vartheta}_{,x} = \frac{1}{2F_0}\oint_s 2\dot{\varepsilon}_{LK}\cot\alpha_K\,ds. \tag{36}$$

$\tan\alpha_K$ being substituted from equation (20), the strain-rates are everywhere compatible with the state of stress assumed in the truss model. For zero strain-rates in the top wall of our example, equation (36), together with (33), evidently gives the same ratio of twist and curvature as equation (26).

However, it must be emphasized that the pure sectional or beam analysis, i.e. equations (32)-(36) alone, do not yet represent a kinematically admissible mechanism. Since the plastified sections are warping, kinematic boundary conditions are violated at cross sections separating rigid and plastified parts of the beam. In other words: Equations (35), (36), (33) imply that the parameters $\dot{u}_{,x}$, $\dot{\vartheta}_x$, $\dot{w}_{,xx}$, $\dot{v}_{,xx}$ are constant along the beam axis. This corresponds to the primary assumption that cross sections Q lay completely within the region ABEF-CDGH. To be kinematically admissible,

the beam mechanism must be completed at the ends with the more general mechanisms of Figure 15a and consequently corresponds to the mechanism shown in Figure 15b.

Assuming no change in the reinforcement within the failure region, and equating the rate of external work to the rate of energy dissipation for the mechanism of Figure 15b as well as for the differential beam element governed by (32)-(36), we obtain the interaction relation (21). Hence, although a pure sectional mechanism does not exist, the modified sectional approach is valid, standing for a mechanism of the type of Figure 15b. In particular, the essential results concerning arbitrary cross sections in [2] are preserved.

Finally, we realize that the presence of shear forces in general is inconsistent with the assumption of a plane strain-rate distribution over a cross section according to (32)-(36).

As shown in Figure 15b, this assumption implies that the longitudinal reinforcement is yielding over a long failure region. For step-wise constant longitudinal reinforcement, as usually used in engineering practice, such a mechanism is inconsistent with the presence of shear forces and varying bending moments. The introduction of additional pure shearing parameters for the beam axis $\bar{v}$, $\bar{w}$ (Fig. 9b) to allow for shear forces, as suggested in (22), does not change the state of affairs and, hence, only discontinuous mechanisms are promising.

## Application in Design and Conclusion

The space truss model represents a rational basis for the ultimate strength design of reinforced concrete beams in torsion and bending. Additional design rules are necessary to prevent premature concrete failure, local failure and excessive crack formation under working load. Corresponding design specifications have already been accepted in the Swiss Code SIA-162 RL 34 and in the Model Code of CEB (Comité Européen du Béton), and they are treated elsewhere at length [3, 4]. Taking advantage of the possible plastic redistributions of forces in the longitudinal and stirrup reinforcement, they allow a more economic design of the reinforcement. Moreover the design for shear, torsion and warping torsion can be put on a consistent basis.

The present paper is a contribution to the theoretical background of these developments. A rigorous kinematic or upper bound approach corresponding to the truss model has been missing so far. Allowing easy visualization of the failure model, the new design specifications are based on, the presented basic mechanism may also be helpful to design engineers. Moreover the paper shows that the term "truss model" has rather historical and phenomenological significance. From a theoretical point of view, the model is a strict application of the Theory of Perfectly Plastic Solids to thin-walled beams in torsion and bending governed by the yield condition (5).

## Acknowledgement

The study is based on results obtained in the course of a research project on the application of the theory of plasticity to the general plane stress problem of reinforced concrete shear walls under the direction of Professor B. Thürlimann.

## Notation

*Forces, Stresses*

| | |
|---|---|
| $D_s$, $D_u$ | resultant of concrete stresses in side resp. bottom shear wall. |
| $L_a$ | rate of external work. |
| $L_d$ | rate of energy dissipation. |
| M | moment. |
| $N_x$, $N_y$, $N_{xy}$ | membrane forces in shear wall, measured per unit length. |
| $n_x$, $n_y$, $n_{xy}$ | membrane forces in concrete, measured per unit length. |
| $P_x$, $P_y$ | yield force of x- resp. y-reinforcement, measured per unit length. |
| $P_s$, $P_u$ | yield force in side resp. bottom stirrups, measured per unit length. |
| S | shear flow. |
| T | torque. |
| $T_v$, $T_h$ | torque applied to vertical resp. horizontal shear wall. |
| $Z_o$, $Z_u$ | force in top resp. bottom longitudinal stringer. |
| $Z_f$ | yield force in longitudinal stringer. |
| $z_x$, $z_y$ | membrane forces in reinforcement, measured per unit length. |
| $\Phi$ | yield function, plastic potential. |
| $\sigma_e$ | steel stress. |
| $\sigma_f$ | yield stress in steel reinforcement. |

*Displacements, Rotations, Strains*

| | |
|---|---|
| u, v, w | displacements. |
| U, V | warping function resp. circumferential elongation. |
| $\varepsilon_x$, $\varepsilon_y$, $\gamma_{xy}$ | strains. |
| $\varepsilon_{LK}$, $\varepsilon_{BK}$ | strains in longitudinal resp. stirrup reinforcement of shear wall K. |
| $\gamma_K$ | shear strain in shear wall K |
| $\varphi$ | skew rotation. |
| $\lambda$ | proportionality factor. |
| $\vartheta$ | angle of twist. |

*Lengths, Areas, Angles*

| | |
|---|---|
| b | width of cross section. |
| d | layer depth, distance. |
| h | height of cross section. |
| $F_x$, $F_y$ | area of one reinforcement bar in x- resp. y-direction. |
| $F_0$ | area enclosed by reinforcement cage. |
| l, L | length. |
| r | distance to the shear wall plane from x-axis. |
| s | circumferential coordinate. |
| $t_x$, $t_y$ | spacing of x- resp. y-reinforcement. |
| x, y, z | coordinate system. |
| $\alpha$ | inclination of concrete compressive trajectories and collapse cracks; direction of minor principle strain. |
| $\beta$ | inclination of discontinuity line or axis of rotation. |
| $\delta$ | angle between y-axis and outward normal to the shear wall. |

*Subscripts*

| | |
|---|---|
| e | steel. |
| f | yield. |
| h | behind, horizontal. |
| n | normal. |
| o | top. |
| s | side. |
| t | tangential. |
| u | bottom. |
| v | front, vertical. |
| x, y, z | related to x-, y-, z-axis. |
| I, II | related to major resp. minor principle axis. |
| L | related to longitudinal reinforcement. |
| B | related to stirrup. |
| K | related to the shear wall K. |

## References


1. PRAGER, William: Probleme der Plastizitätstheorie. Birkhäuser Verlag Basel und Stuttgart, 1955.
2. LAMPERT, P.: Bruchwiderstand von Stahlbetonbalken unter Torsion und Biegung. Bericht Nr. 26, Jan. 1970, Institut für Baustatik, ETH Zürich (Dissertation Prom. Nr. 4445, 1970, ETH Zürich), Vergriffen.
3. LAMPERT, P., THÜRLIMANN, B.: Ultimate Strength and Design of Reinforced Concrete Beams in Torsion and Bending. Sonderdruck aus Band 31/I der Abhandlungen der Internat. Vereinigung für Brücken- und Hochbau, Zürich, 1971, Bericht Nr. 42, Institut für Baustatik ETHZ, Birkhäuser Verlag Basel und Stuttgart, Jan. 1972.

4. THÜRLIMANN, B., GROB, J., LÜCHINGER, P.: Torsion, Biegung und Schub in Stahlbetonträgern. Vorlesungen anlässlich des Fortbildungskurses für Bauingenieure, 9.-12. April 1975, Institut für Baustatik und Konstruktion, ETH Zürich, 1975.
5. MÜLLER, P.: Plastische Berechnung von Stahlbetonscheiben. Bericht in Vorbereitung, Institut für Baustatik und Konstruktion, ETH Zürich.
6. LAMPERT, P., THÜRLIMANN, B.: Torsionsversuche an Stahlbetonbalken. Bericht Nr. 6506-2, Juni 1968, Institut für Baustatik, ETH Zürich, Birkhäuser Verlag Basel und Stuttgart.
7. LAMPERT, P., THÜRLIMANN, B.: Torsions-Biege-Versuche an Stahlbetonbalken. Bericht Nr. 6506-3, Januar 1969, Institut für Baustatik, ETH Zürich, Birkhäuser Verlag Basel und Stuttgart.
8. LAMPERT, P., LÜCHINGER, P., THÜRLIMANN, B.: Torsionsversuche an Stahl- und Spannbetonbalken. Bericht Nr. 6506-4, Februar 1971, Institut für Baustatik, ETH Zürich, Vergriffen.
9. BAUMANN, Th.: Tragwirkung orthogonaler Bewehrungsnetze beliebiger Richtung in Flächentragwerken aus Stahlbeton. Heft 217, Deutscher Ausschuss für Stahlbeton, 1972.
10. NIELSEN, M.P.: Yield Conditions for Reinforced Concrete Shells in the Membrane State, Reprint from Non-Classical Shell Problems, Proc. IASS Symposium, Warswa, Sept. 2.-5., 1963.
11. BRAESTRUP, M.W.: Plastic Analysis of Shear in Reinforced Concrete. Magazine of Concrete Research, Vol. 26, No. 89, Dec. 1974.
12. GVOZDEV, A.A., LESSIG, N.N., RULLE, L.K.: Research on Reinforced Concrete Beams Under Combined Bending and Torsion in the Soviet Union. In Torsion of Structural Concrete, Journal American Concrete Institute, April 1968, p. 310; Publication SP-18.
13. ELFGREN, L., KARLSSON, I., and LOSBERG, A.: Nodal Forces in the Analysis of the Ultimate Torsional Moment for Rectangular Beams. Magazine of Concrete Research, Vol. 26, No. 86, March 1974, pp. 21-28.

## Summary

To predict the ultimate strength of reinforced concrete beams with thin-walled closed cross section in torsion and bending, the truss model has proved to be a powerful approach. However, all collapse mechanisms known so far turn out to be incompatible with the latter. In particular, it is shown, why mechanisms such as "Skew Bending" supply different load factors than the truss model. The yield criterion for reinforced concrete shear walls, implicitly used in the truss model, is derived. By means of the corresponding flow rules, new mechanisms are developed being compatible with the state of stress assumed in the truss model. The present study is based on the classical theory of plasticity and on the fundamental theorems of limit analysis.

## Résumé

Pour le calcul à la rupture des poutres-caisson à parois minces en béton armé soumises à la torsion et à la flexion, le modèle de treillis jouit d'un succès croissant. Cependant, tous les mécanismes de ruine connus à ce jour se montrent incompatibles avec ce modèle. En particulier, des mécanismes tels que le «Skew Bending» fournissent d'autres valeurs de la charge limite que le modèle de treillis. Le critère de plasticité pour les plaques en béton armé, usé implicitement dans le modèle de treillis, est introduit. A l'aide de la loi d'écoulement plastique correspondante, on développe des mécanismes nouveaux compatibles avec l'état de contrainte supposé dans le modèle de treillis. La présente étude est basée sur la théorie de la plasticité et sur les théorèmes fondamentaux de l'analyse limite.

**Zusammenfassung**

Zur Erfassung des Bruchwiderstandes von Stahlbetonbalken mit dünnwandigem geschlossenem Querschnitt unter Torsion und Biegung hat sich das Fachwerkmodell als sehr geeignet erwiesen. Dagegen zeigt sich, dass bis heute keine mit diesem Modell verträgliche Kollapsmechanismen bekannt sind. Insbesondere wird darauf eingegangen, warum Mechanismen wie «Skew Bending» zu anderen Traglastfaktoren führen als das Fachwerkmodell. Die dem Fachwerkmodell implizit zugrunde liegende Fliessbedingung für Stahlbetonscheiben wird hergeleitet. Unter Verwendung des zugehörigen Fliessgesetzes werden neue Mechanismen entwickelt, die mit dem im Fachwerkmodell angenommenen Spannungszustand verträglich sind. Grundlage der vorliegenden Arbeit sind die klassische Plastizitätstheorie und die Grenzwertsätze des Traglastverfahrens.

Leere Seite
Blank page
Page vide

# A Unified Design Method for Composite Columns

*Une méthode unifiée de calcul des colonnes mixtes acier-béton*

*Eine vereinheitlichte Methode für den Entwurf von Verbundstützen*

K.S. VIRDI
BSc, BTech, ME, DIC, PhD, CEng, MICE,
Research Fellow

P.J. DOWLING
BE, DIC, PhD, CEng, MICE, MIStructE,
Reader

Department of Civil Engineering,
Imperial College, London, SW7, 2BU.

## Introduction

A design method for rectangular composite columns was proposed by BASU and SOMMERVILLE [1] in 1969. The method was derived on the basis of results obtained from analytical studies on numerous composite columns in uniaxial bending. Later the method was extended [2] to include concrete filled circular steel tubular columns. Design studies [3, 4] which were subsequently carried out to explore the application of the method to practical cases concluded that, although it was more comprehensive than other available methods, there were also some shortcomings.

Two principal drawbacks were related to the design of axially loaded columns. In the first instance it was found that in the case of slender composite columns, design loads given by the new method for some encased sections were less than those allowed by existing codes for the corresponding uncased sections. Furthermore, no allowance was made for the augmentation in strength of concentrically loaded concrete filled circular steel tubular columns due to the triaxial containment of the concrete.

The aim of this paper is to present a design method, for axially loaded composite columns, which overcomes the objections to Basu and Sommerville's original proposals, and to establish the validity of the approach by comparison with available test results and analytically derived data of proven accuracy. The proposed method relates the design of axially loaded composite columns to the design of bare steel columns. A later paper will deal with the design of eccentrically loaded composite columns.

## Basu and Sommerville's Composite Column Curve

The strength of pin-ended axially loaded bare steel columns is related to the ratio of the length to the radius of gyration, L/r. In the case of columns made up of two or more materials with different material properties the radius of gyration

has no meaning. BASU and SOMMERVILLE [1], however, defined an equivalent radius of gyration for composite columns as

$$r_e = \sqrt{(\sigma_y^* I_s + \sigma_y^* E_c I_c / E_s)/P_s} \quad (1)$$

This radius of gyration was used to obtain the column slenderness ratio ($L/r_e$) for subsequent use in design. It was stated that by taking $E_c = 360\ \sigma_u$ and $\sigma_y^* = 16$ tonf/in$^2$ (247 N/in$^2$) it was possible to minimise the scatter in plotting a large number of analytical results as $P_a/P_s$ against $L/r_e$. In arriving at their basic buckling curve, or $K_1$ curve, they first found the lower bound of the narrow band of scattered points. The curve was subsequently lowered further, mainly in the intermediate slenderness range of $L/r_e = 50$-$150$, to ensure the safe design of certain eccentrically loaded rectangular hollow sections filled with concrete using other formulae they derived.

The excessively conservative nature of the $K_1$ curve so produced is illustrated by comparing available test ultimate loads [5, 6, 7, 8] with the corresponding design strength as shown in Figure 1. Nominal values of cross-sectional areas, and mean values of concrete strength, corrected for the minimum standard deviation as recommended by CEB [9] (see Appendix I), are used throughout. It may be seen that several columns, particularly those tested by Stevens, show markedly high strengths as compared with the $K_1$ curve. The mean value of the ratio of test ultimate loads to design strength is 1.928 with a standard deviation of 202 per cent. For a good design method, the two values should be 1.000 and 0 per cent, or as close to these values as possible.

A similar comparison is made with analytically computed results in Figure 2. The theoretical results [1] were obtained using a verified computer program [10]. The practical column cross-sections have concrete contribution parameter, $\alpha$, varying from 0.12 to 0.80. The stress-strain curve for concrete was assumed to be that given in the CEB recommendations [9], and a bi-linear curve was adopted for steel. An initial lack of straightness of L/1000 in the plane of bending is assumed throughout. It will be seen that the $K_1$ curve lies well below the lower envelope of all the analytical results, and that the margin of conservativeness increases with slenderness ratio. The mean value of the ratio of analytical ultimate loads to design strengths is 1.567 and the standard deviation is 59 per cent.

The comparison of the design strengths with both the experimental and theoretical ultimate loads shows clearly the conservative nature of the basic composite column buckling curve proposed by Basu and Sommerville, and confirms the findings of the design studies referred to earlier. The following sections show how the anomalies between the design of composite and bare steel columns are eliminated.

## New Bare Steel Column Curves

The design of bare metal sections has traditionally been based on relationships between the column critical stress and the column slenderness ratio. Typical of these relationships is the PERRY-ROBERTSON formula [11] which incorporates an

[1] Details of the analytical and experimental results plotted in this paper may be found in Reference 28.

imperfection factor to account for any initial lack of straightness, accidental eccentricity of loading, and residual stresses. The committee drafting the new European code for steel structures have given the problem the most exhaustive treatment to date. Following numerous tests and analytical studies, BEER and SCHULZ [12] recommended three basic buckling curves (Fig. 3) which are applicable to cross-sections of different shapes. A table, reproduced here as Table 1, is provided to enable designers to select the appropriate curve for a given column cross-section. Representative residual stress distributions in the cross-section and an initial lack of straightness of L/1000 are allowed for in the derivation of the curves. Two additional curves cater for certain extreme cases.

*Table 1.*

| SHAPE OF SECTION | CURVE |
|---|---|
| 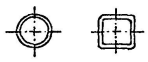 Rolled tubes<br>Welded tubes | a |
|  Welded box sections | b |
| 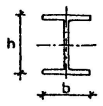 I and H rolled sections:<br>-Buckling parallel to the web<br>h/b > 1·2<br>h/b < 1·2<br>-Buckling parallel to flanges<br>h/b > 1·2<br>h/b < 1·2 | <br><br>a<br>b<br><br>b<br>c |
|  I and H welded sections:<br>-Buckling parallel to the web<br>a) Flame cut flanges<br>b) Rolled flanges<br>-Buckling parallel to flanges<br>a) Flame cut flanges<br>b) Rolled flanges | <br><br>b<br><br><br>b<br>c |
|  I and H sections with welded flange cover plates<br>-Buckling parallel to flanges<br>-Buckling parallel to web | <br>a<br>b |
|  Box sections, stress relieved by heat treatment | a |
|  I and H sections, stress releived by heat treatment<br>-Buckling parallel to the web<br>-Buckling parallel to flanges | <br>a<br>b |
|  T-sections or half I-sections | c |
|  Channels | c |

Parallel work carried out in connection with the new British code for steel buildings and steel bridges has resulted in four curves that approximate the European curves very closely. Both the British and European curves have small plateaux to take account of the strain hardening effects in stocky columns.

The European curves are presented as relationships between $\overline{N}$, the ratio of the column critical stress to its yield stress, and its slenderness factor $\overline{\lambda}$, the ratio

between the column slenderness ratio ($\lambda = L/r$) and a critical slenderness ratio $\lambda_e$. The critical slenderness ratio is defined as that for which the column Euler stress equals the yield stress of the material of the cross-section, and is given by

$$\lambda_e = \pi \sqrt{\frac{E_s}{\sigma_y}} \tag{2}$$

The use of the slenderness factor, $\bar{\lambda}$, rather than the slenderness ratio, $\lambda$, makes the curves independent of the material properties and thus the same curves can be used to design columns with different yield strengths.

## Application of Bare Steel Column Curves to Composite Column Design

### *Proposed Interpretation for Column Strength, $\bar{N}$*

In the context of the design of bare steel sections $\bar{N}$ is defined as the ratio of critical stress $\sigma_a$ to the yield stress $\sigma_y$, that is

$$\bar{N} = \frac{\sigma_a}{\sigma_y} \tag{3}$$

In the alternative interpretation now proposed, and which is applicable to bare metal sections as well as composite sections, $\bar{N}$ is defined as the ratio of the column critical load $P_a$ to its squash load $P_s$, thus

$$\bar{N} = \frac{P_a}{P_s} \tag{4}$$

For a composite column the squash load may be expressed as follows:

$$P_s = \Sigma\, A_s\, \sigma_y + A_c\, \sigma_u \tag{5}$$

The summation sign is intended to include not only the main steel core but also other steel areas such as longitudinal reinforcement. The column ultimate load under concentric loading may be expressed as

$$P_a = \Sigma\, A_s\, \sigma_a + A_c\, \sigma_b \tag{6}$$

where $\sigma_a$ and $\sigma_b$ are the average stresses in steel and concrete respectively, associated with the ultimate thrust $P_a$, and are not necessarily the stresses associated with the tangent modulus load.

It is easy to see that the new interpretation is an exact equivalent of the existing one when applied to bare metal sections. That is, for $A_c = 0$,

$$\bar{N} = \frac{P_a}{P_s} = \frac{A_s\, \sigma_a}{A_s\, \sigma_y} = \frac{\sigma_a}{\sigma_y}$$

Basu and Sommerville have also adopted a similar non-dimensionalisation for the failure loads of composite columns.

*Proposed Interpretation for Slenderness Factor* $\bar{\lambda}$

The existing expression for slenderness factor is

$$\bar{\lambda} = \frac{\lambda}{\lambda_e} \tag{7}$$

$$\text{where } \lambda = \frac{L}{r} \qquad r = \sqrt{I/A}$$

and $\lambda_e$ is as defined in Equation (2).

In the new interpretation applicable to bare metal sections as well as composite sections, the slenderness factor $\bar{\lambda}$ is defined as the ratio of the column length L to a unit critical length of the column $L_c$, which, in turn, is defined as the length of the column for which its Euler load equals its squash load. Thus

$$\bar{\lambda} = \frac{L}{L_c} \tag{8}$$

Also, by definition,

$$P_s = \pi^2 \frac{(\Sigma\, E_s I_s + E_c I_c)}{L_c^2} \tag{9}$$

$$\text{or } L_c = \pi \sqrt{\frac{(\Sigma\, E_s I_s + E_c I_c)}{P_s}} \tag{10}$$

For the bare metal section the proposed definition of the slenderness factor $\bar{\lambda}$ agrees exactly with the existing one, as

$$\bar{\lambda} = \frac{L}{L_c} = \frac{L}{\pi \sqrt{\dfrac{E_s I_s}{A_s \sigma_y}}} = \frac{L/\sqrt{I_s/A_s}}{\pi \sqrt{E_s/\sigma_y}} = \frac{L/r}{\lambda_e} = \frac{\lambda}{\lambda_e}$$

By adopting the proposed interpretation of slenderness factor $\bar{\lambda}$, it is no longer necessary to define an 'equivalent' radius of gyration. The column slenderness is now measured with respect to a single parameter which contains not only the geometric properties of the cross-section such as areas and moments of inertia, but also mechanical properties such as material strengths and moduli of elasticity. The merit of the new interpretation of slenderness factor thus lies in the generality of its application to bare metal sections as well as composite sections.

## Formulation of Design Method for Axially Loaded Composite Columns

*General*

The design procedure for composite columns should now be clear in outline. Having calculated the column slenderness factor $\bar{\lambda}$ using Equations (5), (10) and (8), the designer selects the appropriate basic buckling curve applicable to the corresponding bare metal section from Table 1. A value of $\bar{N}$ is then given directly by the particular curve of Figure 3, and the ultimate column load $P_a$ is calculated from Equations (5) and (4).

The method is applicable to composite columns of many types and all the cross-sectional shapes included in Table 1 can be adopted as the basic steel core. The particular problem of triaxial containment of concrete in concentrically loaded concrete filled circular hollow sections is discussed in a later section.

It is necessary, at this stage, to investigate which value of $E_c$ gives the best correlation with results before recommending an appropriate expression for the initial modulus. (See also Appendix I.)

### *Comparison with Analytical Results*

The 'exact' analytical results are now compared with design strengths obtained by the use of the corresponding European design curves. The mean value of the ratio of the analytical ultimate load to the design strengths for the three curves a, b, and c are 0.953 (standard deviation 3.88%), 0.966 (s.d. 10.0%) and 0.990 (s.d. 9.3%) respectively. The results are plotted in Figures 4-6 and a very good agreement between the theoretical values and the design curves may be observed. The correlation shown with the European curves is substantially better than that observed in the case of Basu and Sommerville's $K_1$ curve (cf. Fig. 2). The results shown are based on a value of $E_c$ equal to the CEB initial modulus $E_{co}$ as defined in Equation (21) which corresponds to the initial modulus of the stress-strain curve used in the theoretical calculations.

As an alternative to Equation (21) one may use the CP110 value given by Equation (23) to define $E_{co}$[1]. The CEB value of $E_{co}$ will be larger than the CP110 value for $\sigma_u > 4500$ N/cm$^2$ approximately. As all the theoretical results included in this study fall within this range, the use of the CP110 value will have the effect of reducing the slenderness factor for these cases, and consequently the results will appear to be on the unsafe side. The average values for the ratio of the theoretical ultimate load to the design ultimate load for the three curves a, b, and c are 0.881 (s.d. 8.67%), 0.832 (s.d. 19.36%), and 0.845 (s.d. 14.5%).

The design values can be made to appear safer by adopting a smaller value of $E_c$ than that previously assumed for design. Thus if $E_c$ is taken as 0.5 of the CEB value, representing the slope of the dashed line in Figure 12, it is found that the average values of the ratio of the theoretical ultimate load to the design ultimate loads for the three curves are 1.032 (s.d. 3.85%), 1.162 (s.d. 10.25%), and 1.257 (s.d. 11.05%). Most of the results now lie above the corresponding design curves.

*Key to symbols used in figures.*

Fig. 1, 7, 9. Tests on Rectangular Columns.

| TESTS REPORTED BY | REFERENCE | SYMBOL |
|---|---|---|
| STEVENS | [5] | ▲ |
| JONES AND RIZK | [6] | ◆ |
| BONDALE | [7] | X |
| JANSS(ENCASED) | [8] | ● |
| FURLONG | [20] | ✱ |
| NEOGI | [14] | ■ |
| KNOWLES AND PARK | [17] | ✱ |
| JANSS(SQUARE TUBES) | [21] | ⊡ |

Fig. 10, 11. Tests on Circular Filled Tubes.

| TESTS REPORTED BY | REFERENCE | SYMBOL |
|---|---|---|
| KLOEPPEL AND GODER | [13] | ▲ |
| KNOWLES AND PARK | [17] | ◆ |
| SALANI AND SIMS | [18] | X |
| GARDNER AND JACOBSON | [19] | ✱ |
| FURLONG | [20] | ✱ |
| NEOGI | [14] | ● |
| NEOGI,SEN | [15] | ■ |
| JANSS(OLD SERIES) | [21] | ⊡ |
| JANSS(NEW SERIES) | [21] | ⊠ |

[1] For the sake of simplicity, the value of $E_{co}$ given by Equation (21) will be referred to in this paper as the CEB value, and that given by Equation (23) as the CP110 value.

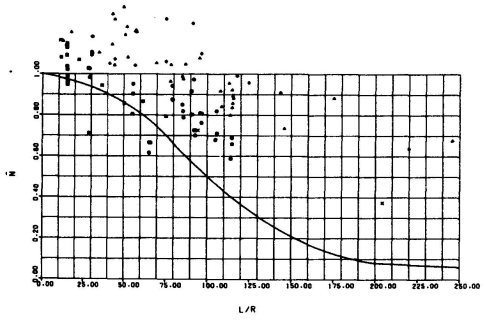

Fig. 1. Test Results for Rectangular Columns Compared with Basu and Sommerville's $K_1$ Curve.

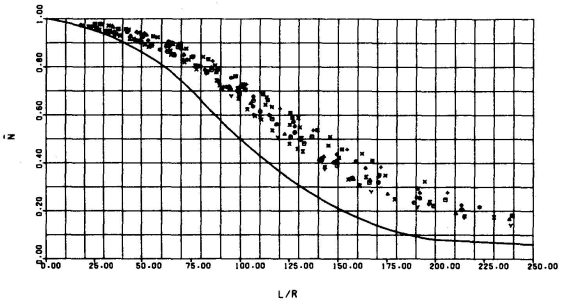

Fig. 2. Analytical Results for Rectangular Columns Compared with Basu and Sommerville's $K_1$ Curve.

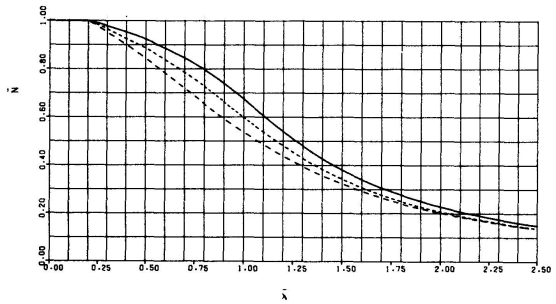

Fig. 3. European Curves a, b, and c — Top Downwards.

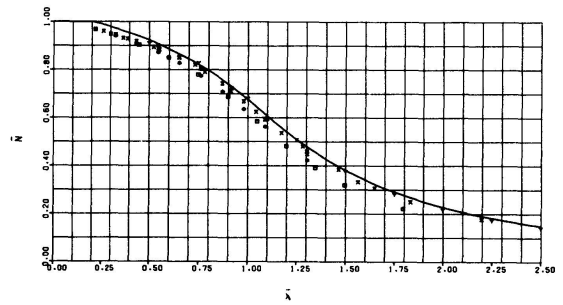

Fig. 4. Analytical Results for Rectangular Columns Compared with Curve a Using Equation (21).

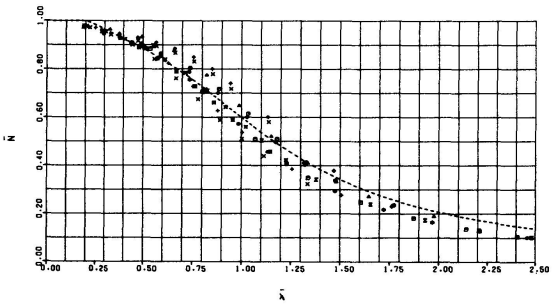

Fig. 5. Analytical Results for Rectangular Columns Compared with Curve b Using Equation (21).

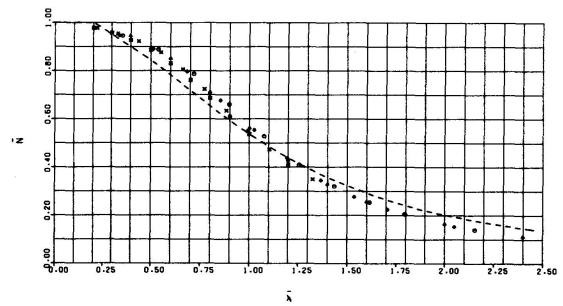

Fig. 6. Analytical Results for Rectangular Columns Compared with Curve c Using Equation (21).

It is evident that the reduction in the value of $E_c$ makes the results appear safer. However, it may be noted that the use of $E_c$ equal to the CEB value brings the theoretical results closest to the three design curves.

### *Comparison of Proposed Design Method with Test Results*

The available test results are now compared with the three European design curves. The results are computed for two values of $E_c$, namely, the CEB value and the CP110 value. Tables 2-4, corresponding to Figures 7-9, list the comparable values for the CEB value. The average value of the ratio of test loads to the design loads relevant to the three curves a, b, and c are 1.084 (s.d. 19.4%).

1.426 (s.d. 43.6%) and 1.230 (s.d. 28.9%) respectively. The corresponding values obtained when $E_c$ is taken as the CP110 value are respectively 1.069 (s.d. 20.7%), 1.225 (s.d. 17.2%), and 1.104 (s.d. 18.6%). It is noteworthy that in either case, the majority of test ultimate loads are safely predicted by the design curves since most of the test values appear above the design curves. In all the present comparisons with test loads, the value of $\gamma_m$ is taken as 1.0. If the value of $\gamma_m$ were taken in the range 1.3-1.6, as is required in real design situations, the few points lying below the design curves will shift closer to the design curves, and many more will lie above the line.

*Table 2. Comparison with european curve a.*

| NUMBER | COLUMN | L/C | P TEST | P S | (4)/(5) | - DESIGN N | (6)/(7) |
|---|---|---|---|---|---|---|---|
| (1) | (2) | (3) | (4) | (5) | (6) | (7) | (8) |
| 1 | RS120 | .807782 | 47.800 | 65.937 | .724934 | .792531 | .914707 |
| 2 | F1 | .303351 | 117800.000 | 99665.425 | 1.181955 | .977196 | 1.209537 |
| 3 | F2 | .303351 | 109800.000 | 99665.425 | 1.101686 | .977196 | 1.127395 |
| 4 | F3 | .305914 | 150000.000 | 137298.535 | 1.092510 | .976581 | 1.118709 |
| 5 | F4 | .305914 | 152000.000 | 137298.535 | 1.107077 | .976581 | 1.133625 |
| 6 | F5 | .282133 | 360000.000 | 365070.840 | .986110 | .982388 | 1.003789 |
| 7 | DF3 | .112362 | 549000.000 | 280003.946 | 1.960687 | 1.000000 | 1.960687 |
| 8 | DF4 | .110754 | 201600.000 | 172938.875 | 1.165730 | 1.000000 | 1.165730 |
| 9 | KP1 | .754644 | 80000.000 | 100745.378 | .794081 | .819078 | .969482 |
| 10 | KP2 | .620391 | 86600.000 | 100007.293 | .865937 | .877048 | .987332 |
| 11 | KP3 | .493728 | 95000.000 | 110813.849 | .857294 | .925195 | .926608 |
| 12 | KP4 | .358594 | 104000.000 | 110173.293 | .943967 | .963552 | .979675 |
| 13 | KP5 | .223195 | 113700.000 | 106297.506 | 1.069639 | .995561 | 1.074409 |
| 14 | KP6 | .111598 | 115000.000 | 106297.506 | 1.081869 | 1.000000 | 1.081869 |
| 15 | JS21 | .138685 | 445000.000 | 468678.755 | .949478 | 1.000000 | .949478 |
| 16 | JS22 | .138841 | 450000.000 | 433802.243 | 1.037339 | 1.000000 | 1.037339 |
| 17 | JS23 | .138007 | 475000.000 | 435182.014 | 1.091497 | 1.000000 | 1.091497 |
| 18 | JS24 | .138266 | 450000.000 | 471360.489 | .954683 | 1.000000 | .954683 |
| 19 | JS25 | .145186 | 598000.000 | 625617.413 | .955856 | 1.000000 | .955856 |
| 20 | JS26 | .146039 | 596000.000 | 616392.260 | .966917 | 1.000000 | .966917 |
| 21 | JS27 | .146160 | 595000.000 | 581678.061 | 1.022903 | 1.000000 | 1.022903 |
| 22 | JS28 | .146493 | 575000.000 | 581678.061 | .988519 | 1.000000 | .988519 |
| 23 | JS29 | .150132 | 825000.000 | 724112.272 | 1.139326 | 1.000000 | 1.139326 |
| 24 | JS30 | .151217 | 830000.000 | 722871.864 | 1.148198 | 1.000000 | 1.148198 |
| 25 | JS31 | .150491 | 815000.000 | 721167.194 | 1.130112 | 1.000000 | 1.130112 |
| 26 | JS32 | .149207 | 830000.000 | 730015.357 | 1.136962 | 1.000000 | 1.136962 |
| | | | | | | ARITHMETIC MEAN | 1.083667 |
| | | | | | | STANDARD DEVIATION | .194345 |

## Extension of Proposed Method to Concrete Filled Circular Steel Tubes

### *Background to Problem*

The behaviour of concrete filled circular hollow sections differs from other types of composite column in that under concentric loading such columns exhibit an enhanced strength, particularly for columns of short lengths. This is explained by the fact that the concrete core in such columns is contained triaxially thereby achieving far greater strength than the corresponding cube strength. The effects of triaxial containment tend to diminish as the column length increases, or as the end moments on the column increase. Different methods have been proposed [13, 14, 15, 16, 17] to account for the triaxial containment of concrete.

### *Formulation of Design Approach*

Based on the results from the tests carried out at Imperial College, Sen [15] derived an expression for the ultimate load of concentrically loaded concrete filled circular hollow sections of very short length:

$$P_H = A_s \frac{\sigma_y}{\bar{\phi}} + A_c\left(\sigma_u + \frac{2t\,\delta\,\phi\,\sigma_y}{d\,\bar{\phi}}\right) \tag{11}$$

where,

$\sigma_u$ = uniaxial concrete strength in member
$\sigma_y$ = yield strength of steel
$t$ = thickness of the tube
$d$ = diameter of the tube
$\delta$ = a constant (Sen's range of values = 4 to 10)
$\phi$ = another constant depending upon the Poisson's ratios of steel and concrete (Sen's range of values = 0.2 to 0.5)

$$\text{and } \bar{\phi} = \sqrt{1 + \phi + \phi^2} \tag{12}$$

Since the lengths of the test columns were around 5 times their diameter, it is reasonable to assume that Equation (11) gives the squash load of such columns including triaxial effects. It follows that the augmented strength of concrete under confinement from the surrounding steel shell is given by

$$\sigma_{cL} = \sigma_u + \frac{2t}{d}\frac{\delta\phi}{\bar{\phi}}\sigma_y \tag{13}$$

and the reduced strength of steel by $\sigma_{yL} = \dfrac{\sigma_y}{\bar{\phi}}$ (14)

*Table 3. Comparison with european curve b.*

| NUMBER | COLUMN | L/L C | P TEST | P S | (4)/(5) | DESIGN N | (6)/(7) |
|---|---|---|---|---|---|---|---|
| (1) | (2) | (3) | (4) | (5) | (6) | (7) | (8) |
| 1 | B1 | .689769 | 37.000 | 34.366 | 1.076654 | .790627 | 1.361772 |
| 2 | B2 | 1.076810 | 27.300 | 29.994 | .910172 | .551382 | 1.650710 |
| 3 | B3 | 1.285139 | 28.600 | 32.423 | .882093 | .436130 | 2.022544 |
| 4 | B4 | 1.631224 | 19.800 | 30.966 | .639416 | .297808 | 2.147074 |
| 5 | B5 | 1.778363 | 23.080 | 34.123 | .676379 | .255509 | 2.647181 |
| 6 | B6 | 2.144718 | 16.400 | 32.180 | .509633 | .182592 | 2.791096 |
| 7 | B7 | 2.255538 | 15.400 | 35.580 | .432827 | .166780 | 2.595197 |
| 8 | FA1 | .148610 | 478.000 | 397.098 | 1.203732 | 1.000000 | 1.203732 |
| 9 | FA2 | .292894 | 450.000 | 407.389 | 1.104595 | .967629 | 1.141548 |
| 10 | FA3 | .451128 | 421.000 | 389.381 | 1.081204 | .904949 | 1.194769 |
| 11 | FA4 | .587875 | 426.000 | 404.816 | 1.052329 | .844062 | 1.246743 |
| 12 | FA5 | .734844 | 424.000 | 404.816 | 1.047388 | .765339 | 1.368529 |
| 13 | S1G | .534047 | 240.000 | 199.200 | 1.204819 | .869838 | 1.385107 |
| 14 | S1E | .489563 | 281.000 | 232.391 | 1.209172 | .889379 | 1.359568 |
| 15 | S1S | .512859 | 258.000 | 212.684 | 1.213069 | .879413 | 1.379407 |
| 16 | S2G | .418803 | 290.000 | 235.689 | 1.230436 | .917579 | 1.340959 |
| 17 | S2E | .380600 | 380.000 | 286.294 | 1.327305 | .932860 | 1.422834 |
| 18 | S2S | .397107 | 310.000 | 260.175 | 1.191504 | .926186 | 1.286462 |
| 19 | S3G | .327777 | 364.000 | 287.190 | 1.267454 | .954189 | 1.328305 |
| 20 | S3E | .309542 | 380.000 | 331.778 | 1.145345 | .961374 | 1.191363 |
| 21 | S3S | .311101 | 423.000 | 327.084 | 1.293245 | .960771 | 1.346050 |
| 22 | FE1 | .819876 | 440.000 | 451.123 | .975343 | .714877 | 1.364350 |
| 23 | FE2 | .785619 | 471.000 | 476.850 | .987732 | .735628 | 1.342706 |
| 24 | RA1 | .656405 | 68.000 | 54.523 | 1.247177 | .808741 | 1.542122 |
| 25 | RA2 | .663310 | 58.000 | 52.773 | 1.099053 | .805046 | 1.365206 |
| 26 | RA3 | .386355 | 100.000 | 95.993 | 1.041742 | .930558 | 1.119481 |
| 27 | RA*1 | .847360 | 54.000 | 54.523 | .990405 | .697763 | 1.419400 |
| 28 | RA**1 | .518588 | 67.000 | 52.773 | 1.269596 | .876835 | 1.447930 |
| 29 | RA*2 | .856273 | 50.500 | 52.773 | .956934 | .692085 | 1.382683 |
| 30 | RA**2 | .518588 | 56.000 | 52.773 | 1.061155 | .876835 | 1.210210 |
| 31 | RA**3 | .302059 | 103.000 | 95.993 | 1.072995 | .964217 | 1.112814 |
| 32 | RW120 | 1.505184 | 23.600 | 63.151 | .373705 | .340682 | 1.096931 |
| 33 | J9.1 | .692323 | 233000.000 | 239511.563 | .972813 | .789222 | 1.232622 |
| 34 | J9.2 | .666517 | 258000.000 | 281913.760 | .915173 | .803346 | 1.139202 |
| 35 | J9.3 | .675550 | 210000.000 | 261666.793 | .802547 | .798447 | 1.005135 |
| 36 | J10.1 | .778122 | 235000.000 | 345770.894 | .679641 | .740108 | .918300 |
| 37 | J10.2 | .787282 | 276000.000 | 336893.824 | .819249 | .734631 | 1.115185 |
| 38 | J10.3 | .788142 | 241000.000 | 338833.498 | .711264 | .734115 | .968873 |
| | | | | | ARITHMETIC MEAN | | 1.426161 |
| | | | | | STANDARD DEVIATION | | .435730 |

If the modified strengths of concrete and steel as defined by Equations (13) and (14) are varied to take into account the fact that the effects of triaxial containment reduce with increasing column length, it is then possible to use these values to determine the column slenderness factor using Equations (10), (8) and (5). The design ultimate loads can then be obtained from the applicable curve a and Equations (5) and (4).

For ideally straight columns with elastic plastic behaviour, failure is governed by Euler buckling for $\bar{\lambda} > 1$ and by material yield for $\bar{\lambda} < 1$. It therefore appears reasonable to postulate that for columns having $\bar{\lambda} > 1$ the triaxial effects will be negligible. For columns in the range $0 < \bar{\lambda} \leq 1$, the triaxial effects will be maximum at $\bar{\lambda} = 0$ and zero at $\bar{\lambda} = 1$.

*Table 4. Comparison with european curve c*

| NUMBER | COLUMN | $L/\lambda_c$ | $P_{TEST}$ | $P_S$ | (4)/(5) | $\bar{N}$ DESIGN | (6)/(7) |
|---|---|---|---|---|---|---|---|
| (1) | (2) | (3) | (4) | (5) | (6) | (7) | (8) |
| 1 | A1 | .110357 | 160.000 | 137.726 | 1.161727 | 1.000000 | 1.161727 |
| 2 | A2 | .399866 | 140.000 | 134.188 | 1.043309 | .900071 | 1.159141 |
| 3 | A3 | .696097 | 144.000 | 137.726 | 1.045555 | .721159 | 1.449825 |
| 4 | A4 | .686022 | 135.000 | 140.084 | .963705 | .727546 | 1.324598 |
| 5 | A5 | 1.005506 | 131.000 | 137.136 | .955254 | .533882 | 1.789261 |
| 6 | A6 | 1.268328 | 105.000 | 142.796 | .735313 | .408319 | 1.800830 |
| 7 | RE1A | 1.012875 | 134.000 | 145.375 | .921756 | .530005 | 1.739146 |
| 8 | RE1B | 1.036667 | 125.000 | 141.837 | .881292 | .517633 | 1.702542 |
| 9 | RE2A | 1.024417 | 123.000 | 143.606 | .856510 | .524003 | 1.634553 |
| 10 | RE2B | .985105 | 120.000 | 150.091 | .799513 | .544694 | 1.467820 |
| 11 | RE3A | .963089 | 140.000 | 152.639 | .917197 | .556701 | 1.647558 |
| 12 | RE3B | .990755 | 124.000 | 147.359 | .841483 | .541700 | 1.553411 |
| 13 | RE4A | 1.016648 | 121.000 | 144.785 | .835721 | .528043 | 1.582676 |
| 14 | RE4B | 1.032501 | 127.000 | 142.427 | .891686 | .519799 | 1.715443 |
| 15 | AE6 | .364375 | 130.000 | 123.613 | 1.051621 | .918725 | 1.144653 |
| 16 | J1.1 | .747423 | 219000.000 | 287745.243 | .761090 | .688550 | 1.105352 |
| 17 | J1.2 | .756456 | 222000.000 | 275414.128 | .806059 | .682704 | 1.180686 |
| 18 | J1.3 | .752472 | 213000.000 | 263369.544 | .808750 | .685293 | 1.180151 |
| 19 | J2.1 | .624064 | 239000.000 | 272874.324 | .875861 | .767458 | 1.141249 |
| 20 | J2.2 | .636186 | 222000.000 | 253849.175 | .874535 | .759579 | 1.151342 |
| 21 | J2.3 | .618793 | 263000.000 | 279216.040 | .941923 | .770885 | 1.221873 |
| 22 | J3.1 | .431944 | 268000.000 | 281821.203 | .950958 | .882731 | 1.077290 |
| 23 | J3.2 | .428982 | 228000.000 | 283230.473 | .804998 | .884360 | .910261 |
| 24 | J3.3 | .438814 | 239000.000 | 264557.641 | .903395 | .878952 | 1.027809 |
| 25 | J4.1 | .227167 | 260000.000 | 264557.641 | .982773 | .986316 | .996407 |
| 26 | J4.2 | .231092 | 252000.000 | 245532.492 | 1.026341 | .984354 | 1.042654 |
| 27 | J4.3 | .219283 | 280000.000 | 272308.628 | 1.028245 | .990259 | 1.038360 |
| 28 | J5.1 | .680896 | 240000.000 | 304830.464 | .787323 | .730826 | 1.077305 |
| 29 | J5.2 | .669674 | 268000.000 | 315047.673 | .850665 | .737909 | 1.152805 |
| 30 | J5.3 | .676953 | 252000.000 | 307649.004 | .819115 | .733320 | 1.116996 |
| 31 | J6.1 | .911229 | 240000.000 | 364235.339 | .658915 | .586375 | 1.123709 |
| 32 | J6.2 | .896100 | 220000.000 | 374452.548 | .587524 | .595440 | .986706 |
| 33 | J6.3 | .906293 | 253000.000 | 367406.197 | .688611 | .589324 | 1.168475 |
| 34 | J7.1 | .733968 | 252000.000 | 360048.216 | .699906 | .697160 | 1.003939 |
| 35 | J7.2 | .724210 | 267000.000 | 368151.520 | .725245 | .703348 | 1.031133 |
| 36 | J7.3 | .732685 | 262000.000 | 360752.851 | .726259 | .697981 | 1.040513 |
| 37 | J8.1 | .520520 | 248000.000 | 373149.753 | .664613 | .831288 | .799498 |
| 38 | J8.2 | .506191 | 241000.000 | 391822.584 | .615074 | .839885 | .732331 |
| 39 | J8.3 | .507988 | 260000.000 | 390413.314 | .665961 | .838807 | .793938 |
| | | | | | | ARITHMETIC MEAN | 1.230102 |
| | | | | | | STANDARD DEVIATION | .288588 |

The above criterion would require the determination of $\bar{\lambda}$ twice during the design process; firstly, to determine whether the triaxial effects are to be considered at all, and secondly, having found the new concrete and steel strengths, to obtain the value of $\bar{N}$ from curve a. As the point where the triaxial effects cease to be worth considering can only be approximately defined, it is suggested that the criterion postulated above be replaced by an equivalent but simpler criterion. For most practical columns, the value of $\bar{\lambda} = 1$ corresponds to a length to diameter ratio (L/d) varying between 24 and 29. It is therefore proposed that the effects of triaxial containment be ignored for columns with $L/d > 25$. For columns in the rage $0 < L/d < 25$, the effects of triaxial containment may be considered by making $\delta$ and $\phi$ linear functions of L/d. Thus

$$\delta = 0.25\,(25 - L/d) \quad 0 \le \delta \le 6.25 \tag{15}$$

$$\text{and } \phi = 0.02\,(25 - L/d) \quad 0 \le \phi \le 0.5 \tag{16}$$

These expressions correspond to $\delta = 5.0$ and $\phi = 0.4$ for $L/d = 5$, the average values for Sen's tests.

*Table 5*

| L/D | $\delta$ | $\Phi$ | $\bar{\Phi}$ | $2\Phi\delta/\bar{\Phi}$ | $1/\bar{\Phi}$ |
|---|---|---|---|---|---|
| 1 | 6.000 | 0.480 | 1.3078 | 4.4043 | 0.7646 |
| 2 | 5.750 | 0.460 | 1.2929 | 4.0916 | 0.7735 |
| 3 | 5.500 | 0.440 | 1.2781 | 3.7868 | 0.7824 |
| 4 | 5.250 | 0.420 | 1.2635 | 3.4903 | 0.7915 |
| 5 | 5.000 | 0.400 | 1.2490 | 3.2026 | 0.8006 |
| 6 | 4.750 | 0.380 | 1.2347 | 2.9239 | 0.8099 |
| 7 | 4.500 | 0.360 | 1.2205 | 2.6547 | 0.8193 |
| 8 | 4.250 | 0.340 | 1.2065 | 2.3954 | 0.8289 |
| 9 | 4.000 | 0.320 | 1.1926 | 2.1465 | 0.8385 |
| 10 | 3.750 | 0.300 | 1.1790 | 1.9084 | 0.8482 |
| 11 | 3.500 | 0.280 | 1.1655 | 1.6817 | 0.8580 |
| 12 | 3.250 | 0.260 | 1.1522 | 1.4667 | 0.8679 |
| 13 | 3.000 | 0.240 | 1.1391 | 1.2641 | 0.8779 |
| 14 | 2.750 | 0.220 | 1.1262 | 1.0744 | 0.8879 |
| 15 | 2.500 | 0.200 | 1.1136 | 0.8980 | 0.8980 |
| 16 | 2.250 | 0.180 | 1.1011 | 0.7356 | 0.9082 |
| 17 | 2.000 | 0.160 | 1.0889 | 0.5878 | 0.9184 |
| 18 | 1.750 | 0.140 | 1.0768 | 0.4550 | 0.9286 |
| 19 | 1.500 | 0.120 | 1.0651 | 0.3380 | 0.9389 |
| 20 | 1.250 | 0.100 | 1.0536 | 0.2373 | 0.9492 |
| 21 | 1.000 | 0.080 | 1.0423 | 0.1535 | 0.9594 |
| 22 | 0.750 | 0.060 | 1.0313 | 0.0873 | 0.9696 |
| 23 | 0.500 | 0.040 | 1.0206 | 0.0392 | 0.9798 |
| 24 | 0.250 | 0.020 | 1.0101 | 0.0099 | 0.9900 |
| 25 | 0.000 | 0.000 | 1.0000 | 0.0000 | 1.0000 |

*Table 6. Comparison with european curve a*

| NUMBER | COLUMN | L/t C | P TEST | P S | (4)/(5) | DESIGN N | (6)/(7) |
|---|---|---|---|---|---|---|---|
| (1) | (2) | (3) | (4) | (5) | (6) | (7) | (8) |
| 1 | KG7 | .580450 | 212900.000 | 222713.070 | .955939 | .892129 | 1.071525 |
| 2 | KG8 | .579317 | 210800.000 | 224202.624 | .940221 | .892560 | 1.053398 |
| 3 | KG9 | .578139 | 203500.000 | 219989.411 | .926863 | .893007 | 1.037912 |
| 4 | KG10 | .372079 | 228800.000 | 250590.256 | .913081 | .950180 | .950947 |
| 5 | KG11 | .370916 | 226600.000 | 250067.658 | .906155 | .950471 | .943448 |
| 6 | KG12 | .370916 | 232400.000 | 250067.658 | .929348 | .950471 | .967597 |
| 7 | KG13 | .795878 | 199300.000 | 218146.834 | .913615 | .798561 | 1.144064 |
| 8 | KG14 | .780111 | 203800.000 | 212294.593 | .960458 | .801444 | 1.198408 |
| 9 | KG15 | .795972 | 206100.000 | 216377.895 | .952500 | .798514 | 1.192341 |
| 10 | KG41 | .388148 | 147500.000 | 129847.864 | 1.135945 | .955081 | 1.188126 |
| 11 | KG42 | .415024 | 154300.000 | 149093.340 | 1.034922 | .949043 | 1.090430 |
| 12 | KG43 | .391412 | 147500.000 | 126282.757 | 1.168017 | .955233 | 1.222753 |
| 13 | KG44 | .599577 | 127400.000 | 117540.905 | 1.083678 | .884957 | 1.224781 |
| 14 | KG45 | .640127 | 136200.000 | 135079.923 | 1.008292 | .869248 | 1.159959 |
| 15 | KG46 | .604761 | 129400.000 | 114108.289 | 1.134011 | .882991 | 1.284283 |
| 16 | KG47 | .805429 | 120600.000 | 107313.877 | 1.123805 | .793731 | 1.415853 |
| 17 | KG48 | .858065 | 127200.000 | 122294.915 | 1.040109 | .764557 | 1.360407 |
| 18 | KG49 | .812471 | 109600.000 | 104549.868 | 1.048304 | .790065 | 1.326857 |
| 19 | KG53 | .409506 | 230000.000 | 370960.800 | .620012 | .950528 | .652281 |
| 20 | KG54 | .415834 | 412400.000 | 385114.498 | 1.070850 | .948825 | 1.128607 |
| 21 | KG55 | .413031 | 514600.000 | 417488.512 | 1.232609 | .946558 | 1.298073 |
| 22 | KG56 | .412329 | 503300.000 | 415585.341 | 1.199232 | .949771 | 1.262653 |
| 23 | KG69 | .465462 | 553400.000 | 587351.351 | .942180 | .935351 | 1.005214 |
| 24 | KG70 | .460385 | 544300.000 | 586729.676 | .927684 | .935885 | .991238 |
| 25 | KG71 | .417362 | 630300.000 | 545077.976 | 1.156348 | .948412 | 1.219246 |
| 26 | KG72 | .465257 | 659200.000 | 655573.288 | .990424 | .934618 | 1.059824 |
| 27 | KG73 | .810274 | 112000.000 | 109629.413 | 1.021624 | .791252 | 1.291148 |
| 28 | KG74 | .813087 | 103300.000 | 101976.832 | 1.012975 | .789733 | 1.282680 |
| 29 | KG75 | .829224 | 106300.000 | 109501.212 | .970765 | .781019 | 1.242348 |
| 30 | KG76 | .804498 | 92810.000 | 105809.466 | .877143 | .794206 | 1.104427 |
| 31 | KG83 | .357813 | 156300.000 | 160385.396 | .970889 | .951797 | 1.007359 |
| 32 | KG84 | .372151 | 167800.000 | 176641.064 | .949949 | .960162 | .989363 |
| 33 | KG85 | .353810 | 188100.000 | 175261.875 | 1.073251 | .962248 | 1.115359 |
| 34 | KG86 | .372343 | 194900.000 | 190325.454 | 1.024035 | .960114 | 1.066577 |
| 35 | KG89 | .383917 | 224400.000 | 245305.204 | .914779 | .957182 | .955700 |
| 36 | KG90 | .383039 | 228900.000 | 238291.520 | .960168 | .957410 | 1.002881 |
| 37 | KG91 | .377278 | 247100.000 | 238057.954 | 1.037983 | .956891 | 1.082494 |
| 38 | KG92 | .373329 | 242500.000 | 235850.322 | 1.028151 | .959868 | 1.071138 |
| 39 | KG95 | .711555 | 144000.000 | 132837.905 | 1.084028 | .839700 | 1.290971 |
| 40 | KG96 | .738176 | 141500.000 | 144206.807 | .981230 | .827275 | 1.186098 |
| 41 | KG97 | .725524 | 156300.000 | 142820.850 | 1.094378 | .833304 | 1.313301 |
| 42 | KG98 | .740292 | 169300.000 | 152383.728 | 1.114292 | .826254 | 1.348607 |
| 43 | KG101 | .757764 | 176800.000 | 199213.530 | .887490 | .817518 | 1.085591 |
| 44 | KG102 | .756146 | 183400.000 | 193639.106 | .947123 | .818327 | 1.157399 |
| 45 | KG103 | .747697 | 196400.000 | 197167.253 | .996109 | .822552 | 1.210398 |
| 46 | KG104 | .739349 | 194500.000 | 188323.165 | 1.032799 | .826712 | 1.249285 |
| 47 | KP1 | .825493 | 138200.000 | 173185.560 | .797988 | .783039 | 1.019091 |
| 48 | KP2 | .694170 | 160000.000 | 180255.520 | .887629 | .847148 | 1.047784 |
| 49 | KP3 | .563574 | 160800.000 | 191907.044 | .837905 | .898605 | .932461 |
| 50 | KP4 | .427058 | 206500.000 | 210905.416 | .979112 | .945724 | 1.035304 |
| 51 | KP5 | .279443 | 223000.000 | 230248.698 | .968518 | .993039 | .985228 |
| 52 | KP6 | .889572 | 50500.000 | 77955.666 | .647713 | .745757 | .868531 |
| 53 | KP7 | .744149 | 66200.000 | 75993.333 | .871129 | .824325 | 1.056773 |
| 54 | KP8 | .598503 | 80000.000 | 83776.351 | .954823 | .885352 | 1.078581 |
| 55 | KP9 | .450040 | 90000.000 | 89554.560 | 1.004974 | .939188 | 1.070046 |
| 56 | KP10 | .292417 | 110000.000 | 96789.916 | 1.136482 | .979895 | 1.159799 |
| 57 | KP11 | .161401 | 119200.000 | 103786.548 | 1.148511 | 1.000000 | 1.148511 |
| 58 | S530F | .966078 | 27100.000 | 39263.990 | .689848 | .697288 | .989330 |
| 59 | S542F | .859712 | 72000.000 | 73509.768 | .978131 | .861218 | 1.135753 |
| 60 | S549F | 1.945567 | 3540.000 | 10393.952 | .340583 | .239720 | 1.420754 |
| 61 | S550F | 1.945567 | 3480.000 | 10393.952 | .335772 | .239720 | 1.400687 |
| 62 | S551F | 1.369063 | 25400.000 | 40627.903 | .625186 | .442787 | 1.411933 |
| 63 | S552F | 1.369063 | 24000.000 | 40627.903 | .590727 | .442787 | 1.334110 |
| 64 | S571F | .701792 | 51800.000 | 53809.175 | .962520 | .843929 | 1.140891 |
| 65 | GJ1 | .744067 | 184000.000 | 189549.623 | .970722 | .824367 | 1.177537 |
| 66 | GJ2 | .747001 | 180000.000 | 186713.954 | .964041 | .822900 | 1.171518 |
| 67 | GJ5 | .431038 | 260000.000 | 258229.036 | .969321 | .944609 | 1.026160 |
| 68 | GJ6 | .432851 | 245500.000 | 259855.369 | .945869 | .944102 | 1.001872 |
| 69 | GJ7 | .434832 | 213500.000 | 252695.967 | .844889 | .943547 | .895439 |
| 70 | GJ11 | .495284 | 211000.000 | 240064.187 | .878932 | .924651 | .950555 |
| 71 | GJ12 | .494884 | 198000.000 | 240319.798 | .823902 | .924756 | .890940 |
| 72 | GJ18 | .806685 | 55000.000 | 52829.518 | 1.041085 | .793091 | 1.312693 |
| 73 | GJ20 | .355343 | 92500.000 | 78645.052 | 1.176171 | .964364 | 1.219633 |
| 74 | GJ21 | .358741 | 74250.000 | 66762.779 | 1.112147 | .963515 | 1.154260 |
| 75 | F1 | .378681 | 160000.000 | 192722.387 | .830210 | .959530 | .865128 |
| 76 | F2 | .378681 | 170000.000 | 192722.387 | .882098 | .958530 | .920261 |
| 77 | F3 | .301254 | 141000.000 | 166994.717 | .844338 | .977699 | .863597 |
| 78 | F4 | .301254 | 140000.000 | 166994.717 | .838350 | .977699 | .857472 |
| 79 | F5 | .301254 | 148000.000 | 166994.717 | .886256 | .977699 | .906471 |
| 80 | F6 | .260158 | 153400.000 | 153316.919 | 1.000542 | .987664 | 1.013039 |
| 81 | F7 | .258769 | 162200.000 | 169462.959 | .957141 | .987983 | .968783 |
| 82 | F8 | .258769 | 164800.000 | 169462.959 | .972484 | .987983 | .984312 |
| 83 | A1 | .245091 | 2576000.000 | 2092912.088 | 1.230821 | .991080 | 1.241899 |
| 84 | A4 | .245975 | 2408000.000 | 2005576.737 | 1.200652 | .990885 | 1.211695 |
| 85 | A5 | .221352 | 790700.000 | 878545.086 | .899987 | .995930 | .902562 |
| 86 | A6 | .258337 | 1671000.000 | 1448733.953 | 1.153421 | .985782 | 1.170056 |
| 87 | B1 | .243038 | 289000.000 | 234957.479 | 1.230010 | .991532 | 1.240515 |
| 88 | B1X | .238208 | 289000.000 | 225711.179 | 1.280397 | .992558 | 1.289997 |
| 89 | B2 | .252674 | 293500.000 | 290578.187 | 1.010055 | .989385 | 1.020992 |
| 90 | B2X | .245438 | 293500.000 | 274284.463 | 1.070057 | .990593 | 1.079783 |
| 91 | DF1 | .127975 | 663000.000 | 439169.233 | 1.523545 | 1.000000 | 1.523545 |
| 92 | DF1X | .128671 | 663000.000 | 439808.447 | 1.507132 | 1.000000 | 1.507132 |
| 93 | DF2 | .129574 | 410000.000 | 306475.277 | 1.337791 | 1.000000 | 1.337791 |
| 94 | DF2X | .131027 | 410000.000 | 313391.228 | 1.308269 | 1.000000 | 1.308269 |
| 95 | SC1 | .211474 | 451000.000 | 360220.322 | 1.252012 | .997820 | 1.254747 |
| 96 | SC2 | .210590 | 502000.000 | 405449.081 | 1.238133 | .997888 | 1.240630 |
| 97 | SC3 | .210809 | 475000.000 | 404765.416 | 1.173519 | .997846 | 1.175934 |
| 98 | SC4 | .211974 | 392000.000 | 326135.663 | 1.201954 | .997744 | 1.204672 |
| 99 | M11 | .202765 | 201.000 | 158.813 | 1.265643 | .999475 | 1.266308 |
| 100 | M12 | .202034 | 224.000 | 181.430 | 1.234638 | .999614 | 1.235115 |
| 101 | M13 | .203067 | 175.000 | 146.347 | 1.195789 | .999417 | 1.195486 |
| 102 | M14 | .202013 | 212.000 | 179.901 | 1.178426 | .999617 | 1.178877 |
| 103 | M15 | .204011 | 261.000 | 208.442 | 1.252146 | .999238 | 1.253101 |
| 104 | M16 | .202197 | 253.000 | 212.685 | 1.189552 | .999583 | 1.190048 |
| 105 | M17 | .204301 | 280.000 | 232.111 | 1.206317 | .999183 | 1.207304 |
| 106 | M18 | .204918 | 241.000 | 203.305 | 1.185411 | .999066 | 1.186520 |
| 107 | M19 | .204783 | 268.000 | 232.206 | 1.154149 | .999091 | 1.155198 |
| 108 | M20 | .207858 | 294.000 | 250.769 | 1.172396 | .998507 | 1.174149 |
| 109 | M21 | .212798 | 340.000 | 288.151 | 1.179938 | .997568 | 1.182814 |
| 110 | M22 | .208399 | 349.000 | 290.886 | 1.199784 | .998404 | 1.201702 |
| 111 | M23 | .208121 | 340.000 | 271.400 | 1.252762 | .998457 | 1.254698 |
| 112 | M24 | .208177 | 351.000 | 299.270 | 1.206270 | .998446 | 1.208147 |
| 113 | 1J | .760419 | 175000.000 | 213899.049 | .818143 | .816194 | 1.002387 |
| 114 | 2J | .589775 | 210500.000 | 240526.967 | .875162 | .888585 | .984893 |
| 115 | 3J | .413698 | 246000.000 | 249101.508 | .987549 | .949402 | 1.040181 |
| 116 | 4J | .190069 | 281000.000 | 292278.789 | .961411 | 1.000000 | .961411 |
| 117 | 5J | .189455 | 280000.000 | 289316.941 | .967797 | 1.000000 | .967797 |
| 118 | 6J | .188506 | 286000.000 | 281570.516 | 1.015731 | 1.000000 | 1.015731 |
| 119 | 8.1J | 1.684819 | 20500.000 | 47295.721 | .433549 | .311058 | 1.400541 |
| 120 | 8.2J | 1.681357 | 15800.000 | 46745.772 | .337998 | .312166 | 1.082753 |
| 121 | 8.3J | 1.677149 | 14300.000 | 46380.808 | .308317 | .313541 | .983340 |
| 122 | 9.1J | 1.110580 | 28500.000 | 48451.917 | .588212 | .598905 | .982144 |
| 123 | 9.2J | 1.110687 | 28700.000 | 47917.645 | .598944 | .598833 | 1.000186 |
| 124 | 9.3J | 1.107625 | 29700.000 | 48932.565 | .606214 | .600915 | 1.008819 |
| 125 | 10.1J | .751509 | 37000.000 | 46118.339 | .802284 | .820645 | .977626 |
| 126 | 10.2J | .753119 | 41500.000 | 45291.656 | .895490 | .819841 | 1.093493 |
| 127 | 10.3J | .753575 | 41500.000 | 46288.126 | .896558 | .819613 | 1.093881 |
| 128 | 11.1J | .587748 | 45500.000 | 51132.737 | .889930 | .889356 | .996148 |
| 129 | 11.2J | .588314 | 45000.000 | 50736.387 | .886937 | .889141 | .997522 |
| 130 | 11.3J | .590120 | 50500.000 | 50312.324 | 1.003730 | .888456 | 1.129747 |
| 131 | 12.1J | .418591 | 53500.000 | 55826.457 | .958327 | .948080 | 1.010808 |
| 132 | 12.2J | .417377 | 51700.000 | 54344.755 | .951334 | .948408 | 1.003085 |
| 133 | 12.3J | .418617 | 54400.000 | 55399.701 | .981955 | .948073 | 1.035737 |
| 134 | 13.1J | .225721 | 65000.000 | 63295.301 | 1.027582 | .995056 | 1.032889 |
| 135 | 13.2J | .225087 | 64000.000 | 63771.804 | 1.003578 | .995183 | 1.008436 |
| 136 | 13.3J | .225574 | 68000.000 | 63492.335 | 1.070995 | .995085 | 1.076285 |
| 137 | 1 JN | .174330 | 770000.000 | 738471.368 | 1.042694 | 1.000000 | 1.042694 |
| 138 | 2 JN | .176815 | 770000.000 | 774382.797 | .994340 | 1.000000 | .994340 |
| 139 | 3 JN | .132142 | 785000.000 | 752420.777 | 1.043289 | 1.000000 | 1.043289 |
| 140 | 4 JN | .133638 | 760000.000 | 765806.598 | .992418 | 1.000000 | .992418 |
| 141 | 5 JN | .137822 | 1000000.000 | 1172815.144 | .852849 | 1.000000 | .852849 |
| 142 | 6 JN | .138561 | 1000000.000 | 1125043.015 | .888955 | 1.000000 | .888955 |
| 143 | 7 JN | .182463 | 720000.000 | 675658.268 | 1.065612 | 1.000000 | 1.065612 |
| 144 | 8 JN | .187955 | 695000.000 | 681021.995 | 1.020525 | 1.000000 | 1.020525 |
| 145 | 9 JN | .187179 | 733000.000 | 658079.181 | 1.113849 | 1.000000 | 1.113949 |
| 146 | 10 JN | .304289 | 835000.000 | 850185.171 | .982138 | .976971 | 1.005289 |
| 147 | 11 JN | .303506 | 830000.000 | 850566.300 | .975820 | .977159 | .998531 |
| 148 | 12 JN | .306246 | 855000.000 | 849236.824 | 1.006786 | .976551 | 1.031014 |
| 149 | 13 JN | .306246 | 820000.000 | 849236.824 | .965573 | .976501 | .988809 |
| 150 | 14 JN | .315802 | 850000.000 | 844605.163 | 1.006387 | .974149 | 1.033093 |
| 151 | 15 JN | .315191 | 840000.000 | 844416.828 | .994769 | .974052 | 1.021269 |

ARITHMETIC MEAN 1.103291
STANDARD DEVIATION .145673

Thus for columns with $L/d < 25$ the designer may use Equations (12)-(16) to calculate the modified values of concrete and steel strength to be used in determining the slenderness factor $\bar{\lambda}$. Once the slenderness factor is known the strength of the column can be taken from column curve a, and Equations (5) and (4). For convenience, the values of $1/\bar{\phi}$ and $2\delta\phi/\bar{\phi}$ have been listed in Table 5 for different values of L/d. It may be added that for L/d values ranging between 20 and 25, the collapse loads calculated with or without triaxial effects would not be much different. Hence, to minimise effort, the upper limit of L/d for which triaxial effects are calculated may be restricted to 20.

### *Comparison of Proposed Method with Test Loads*

The validity of the proposed design methods for concrete filled circular tubular columns under concentric loading is now verified against all known test results [13-21]. It must be noted that the material strengths used in the following comparison are not corrected for the recommended standard deviation errors as this correction is of little significance in terms of the enhanced concrete strength. The factors $k_1 = 0.67$ for cubes and $k_2 = 0.85$ for cylinders are applied as appropriate and the value of $\gamma_m$ is again assumed to be unity.

Table 6 lists the comparative test ultimate loads against the design loads obtained from European curve a and the results are also shown in Figure 10. The value of $E_c$ used is obtained from Equation (21) (CEB value) using the uniaxial strength of concrete. The average value of the ratio of the test ultimate load to the corresponding design strength for 151 columns is 1.109 with a standard deviation of 14.7 per cent. Similar comparison based on $E_c$ as given by Equation (23) (CP110 value) gives the average value of the ratio of test ultimate load to the relevant factored design load as 1.097 (s.d. 14.1%). It is clear that both values of $E_c$ yield good correlation with tests.

To illustrate the effect of ignoring the triaxial effects, Figure 11 shows the comparative values with $E_c$ equal to the CEB value. The average value of the ratio of test ultimate load to the corresponding design strength is 1.297 (s.d. 21.9%). With the CP110 value this ratio becomes 1.285 (s.d. 22.3%).

The proposed design method has thus been shown to give good correlation with a very large number of available test results on concrete filled circular tubes loaded concentrically.

## Recommended Design Procedure for Concentrically Loaded Composite Columns

### *Summary of Design Procedure*

The following design procedure covers axially loaded concrete encased steel sections and concrete filled rectangular and circular steel tubes.

1. For sections other than concrete filled circular steel tubes proceed to step 6.
2. Calculate column L/d ratio.
3. If $L/d > 20$ proceed to step 6.
4. Obtain values of $1/\bar{\phi}$ and $2\delta\Phi/\bar{\phi}$, from Table 5.
5. Calculate modified strength of concrete and steel using Equations (13) and (14).

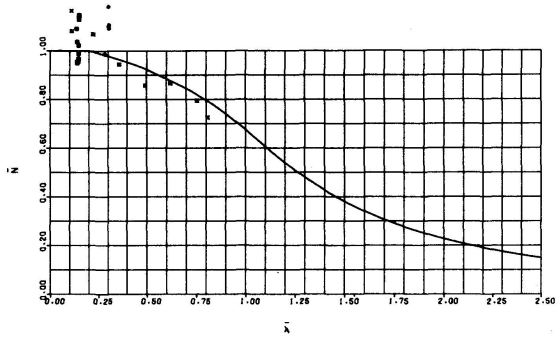

Fig. 7. Test Results for Rectangular Columns Compared with Curve a Using Equation (21).

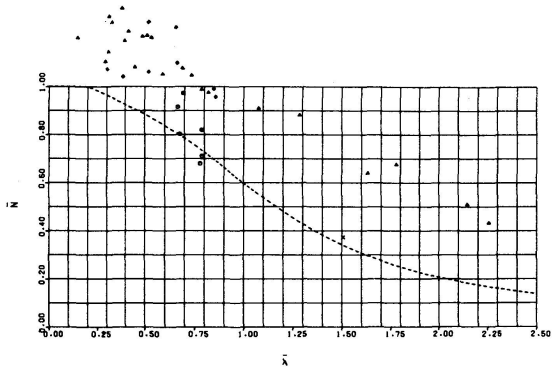

Fig. 8. Test Results for Rectangular Columns Compared with Curve b Using Equation (21).

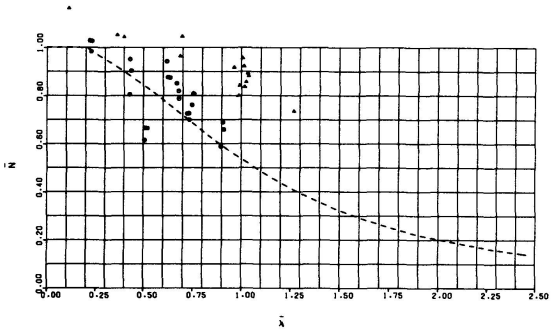

Fig. 9. Test Results for Rectangular Columns Compared with Curve c Using Equation (21).

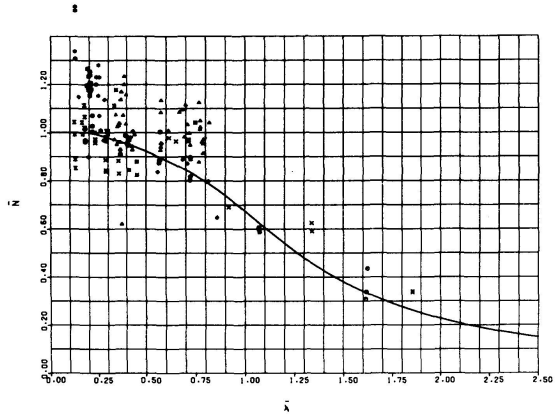

Fig. 10. Test Results for Circular Filled Tubes Compared with Curve a Using Equation (21) and Including Triaxial Effects.

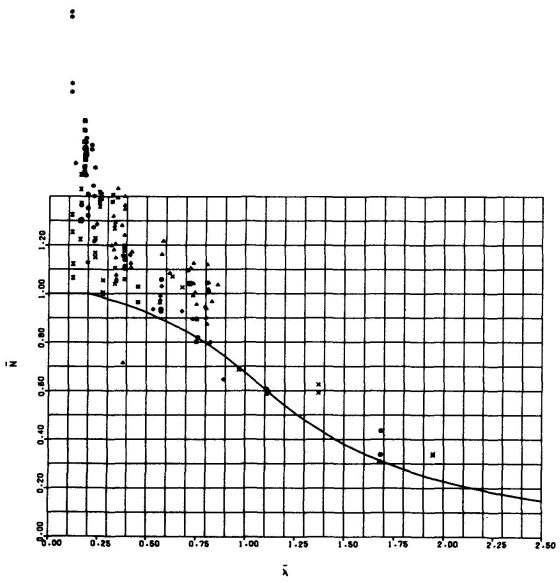

Fig. 11. Test Results for Circular Filled Tubes Compared with Curve a Using Equation (21) and Ignoring Triaxial Effects.

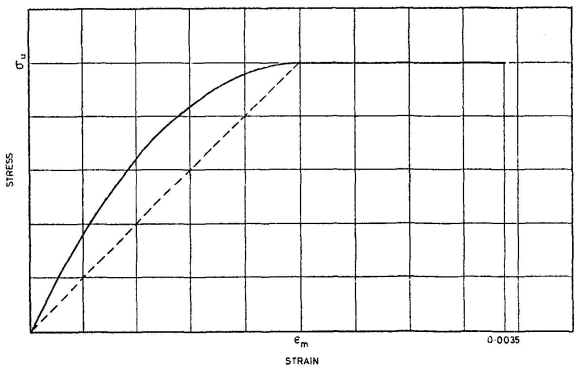


Fig. 12. Stress-strain Relationship for Concrete.

6. Calculate the column slenderness factor $\bar{\lambda}$ using Equations (10), (5) and (8) (using the modified material strengths where applicable).
7. Select appropriate European Curve from Table 1 for the bare steel section, and obtain $\bar{N}$ from Figure 3. As an alternative to Figure 3, the values of $\bar{N}$ may be calculated from Tables given in Ref. 27.
8. Calculate $P_a$, the ultimate load from Equations (5) and (4) (using modified material strengths where applicable).

To calculate $\bar{\lambda}$, the value of $E_c$ should be that derived from Equation (21), i.e. the CEB value, and should be based on the uniaxial strength of concrete.

*Table 7*

| | Length in | Theoretical* tonf | Present Design Method tonf | Basu and Sommerville tonf | Present Design Steel Core Only tonf |
|---|---|---|---|---|---|
| UCE | 100 | 586.508 | 594.707 | 561.214 | 154.118 |
| Minor Axis | 300 | 498.225 | 465.499 | 373.619 | 53.879 |
| Curve 'c' | 500 | 321.574 | 319.083 | 153.551 | 22.296 |
| RHA | 100 | 232.281 | 238.802 | 219.644 | 154.191 |
| Major Axis | 300 | 191.266 | 194.853 | 165.078 | 129.256 |
| Curve 'a' | 500 | 110.895 | 115.719 | 75.136 | 82.35 |
| IBA | 100 | 165.141 | 158.910 | 137.994 | 36.391 |
| Minor Axis | 300 | 46.359 | 55.968 | 14.250 | - |
| Curve 'b' | 500 | - | (Outside Slenderness Range) | - | - |

*Excluding root areas.

*Table 8*

| Diameter 6.625 in Thickness 0.176 in $\sigma_u$ = 2400 lbf/in$^2$ $\sigma_y$ = 16 tonf/in$^2$ | | | | | |
|---|---|---|---|---|---|
| Length | L/d | Analytical Ultimate Load | Basu and Sommerville's Ultimate Load | Present Design | |
| | | | | without containment | with containment |
| in | | tonf | tonf | tonf | tonf |
| 72 | 10.8 | 83.9 | 82.5 | 86.4 | 99.4 |
| 144 | 21.6 | 72.2 | 63.6 | 73.6 | 73.6 |
| 216 | 32.4 | 50.0 | 37.0 | 52.3 | 52.3 |
| Diameter 12.75 in Thickness 0.250 in $\sigma_u$ = 7200 lbf/in$^2$ $\sigma_y$ = 23 tonf/in$^2$ | | | | | |
| 72 | | 685.4 | 667.5 | 695.0 | 855.5 |
| 144 | | 657.1 | 604.6 | 654.7 | 720.8 |
| 216 | | 592.0 | 499.8 | 594.0 | 606.8 |
| 288 | | 479.4 | 353.0 | 509.7 | 509.7 |

## *Examples of Application of the Design Method*

The design method has been used to calculate the ultimate load capacities of a concrete encased joist section, a concrete encased H universal column, and a concrete filled rectangular hollow section over a range of column lengths. The results are presented in Table 7 and are compared with the theoretically exact ultimate loads, those predicted using the method of Basu and Sommerville, and the

ultimate design loads for bare steel columns alone. It will be noted that the design loads given by the new method correspond more closely with the 'exact' ultimate loads than do the values given by Basu and Sommerville's design method. It will also be seen that the latter method predicts a lower carrying capacity for the concrete filled rectangular section than is predicted for the bare steel tube. No such anomaly can arise with the new approach.

In Table 8 the design load capacities of a range of practical concrete filled tubes of varying lengths are presented. These are compared with the exactly calculated capacities ignoring triaxial containment and those obtained using the design method of Basu and Sommerville. The enhanced load-carrying capacities of short concentrically loaded columns due to triaxial effects as predicted by the new method can be seen by comparing the tabulated values.

## Practical and Economic Consequences

The design of composite columns under axial loading has been made just as simple as the design of bare steel axially loaded columns. By suitably redefining the column slenderness factor, the newly developed European curves for the design of bare steel columns can be used as the basic design curves for composite columns. Thus full advantage can be taken of the contribution of concrete towards the strength of composite columns. In the case of axially loaded circular tubes filled with concrete, further economies can be made by allowing for the enhanced strength of concrete due to triaxial containment in the design method.

## Conclusions

A new method of design for composite columns under concentric loading has been presented. The method unifies the design of concrete filled circular tubular sections under concentric loading with that of other types of concentrically loaded composite columns, such as encased sections and rectangular filled tubes, by calculating an augmented strength of concrete and a corresponding reduced strength of steel. The effects of triaxial containment are made to vary with the column length to diameter ratio up to a value of 25, beyond which no such effects are considered.

The design method introduces a new concept of column slenderness. The column slenderness factor is defined as the ratio of column length to a unit critical length. This unit critical length is the length for which the column Euler load equals its squash load. This definition leads to the same expression as that used in the currently proposed European design curves for bare steel columns and enables these curves to be used as the basic design curves for composite columns. It is not therefore necessary to define a fictitious radius of gyration for such sections.

The method has been compared with a large number of known experimental results on encased sections as well as rectangular and circular filled tubes. The agreement is shown to be excellent. Good correlation has also been obtained with a large number of theoretically exact results for several encased sections and filled

rectangular tubes for the range of practical slenderness factors. The proposed method overcomes many of the disadvantages of a method proposed earlier by Basu and Sommerville and can be confidently recommended for use in design specifications.

## Appendix

### *Factors Affecting the Value of Slenderness Factor* $\bar{\lambda}$

The mechanical properties of steel are, in general, well defined both with respect to $\sigma_y$ and $E_s$. Problems arise, however, in the determination of the appropriate values of $\sigma_u$ and $E_c$ for use in the expression for slenderness factor.

### *Design Strength of Concrete* $\sigma_u$

In both the CEB recommendations [9] and the British code of practice [22] the design strength of concrete, i.e. the maximum design stress attainable by concrete in a reinforced concrete column is specified as

$$\sigma_u = \frac{k_1 \sigma_{cu}}{\gamma_m} = \frac{k_2 \sigma_{cyl}}{\gamma_m} \tag{17}$$

The recommended value of $k_1$ is 0.67 [22]. The factor $k_2$ which is used when the concrete strength is obtained from cylinder tests rather than cube tests has a recommended value of 0.85 [9]. This corresponds to the observation that the ratio of concrete cylinder strength to concrete cube strength is approximately 0.80.

The value of the characteristic concrete strength as obtained from tests is frequently taken as the mean value of the strengths of the specimen tested. However, both the CEB recommendations [9] and the Handbook on CP110 [23] stipulate that the characteristic strength of concrete should be taken in accordance with the formula

$$\sigma_k = \sigma_m - 1.64\,S \tag{18}$$

where S is the standard deviation of test results. The CEB recommendations further stipulate that when the probabilistic distribution of test data is not known a minimum value of 300 N/cm$^2$ should be taken for *in situ* concrete and 200 N/cm$^2$ for factory cast concrete. In most practical cases, as also in laboratory tests, only a few cube or cylinder tests are carried out. Thus when comparing ultimate load calculations with test results, in the absence of sufficient experimental data, a minimum value of 200 N/cm$^2$ for cylinder tests, or 250 N/cm$^2$ for cube tests, or their equivalent related to factory cast concrete, should be used as the value of S in Equation (18) to obtain the characteristic strength of concrete.

The coefficient $\gamma_m$ is the material safety factor. The design value of $\gamma_m$ associated with the ultimate limit state of design recommended by CP110 is 1.5 while the CEB recommendations specify values in the range 1.3-1.6 depending upon the care and control exercised in the production of concrete. When correlating test results with ultimate load calculations, it is customary to take $\gamma_m = 1.0$, assuming that the laboratory conditions permit the production of concrete of a uniform quality.

*Modulus of Elasticity of Concrete, $E_c$*

A number of equations have been proposed to represent the concrete stress-strain relationship [24, 25, 26]. The curves recommended by CEB and CP110 have similar shapes (Fig. 12) characterised by a parabolic section up to the peak concrete stress, followed by a horizontal plateau, even though the observed stress-strain relationships do not exhibit any discernible flat plateau. Both curves have the same limiting value of strain corresponding to the crushing of concrete, namely 0.0035, but the exact shapes of the parabolas in the two curves are defined by slightly different criteria. The general equation of the parabola may be written as

$$\frac{\sigma}{\sigma_u} = \frac{\varepsilon}{\varepsilon_m}\left(2 - \frac{\varepsilon}{\varepsilon_m}\right) \tag{19}$$

The value of the initial modulus is thus given by $E_{co} = 2\,\dfrac{\sigma_u}{\varepsilon_m}$ (20)

In the CEB recommendations, the value of $\varepsilon_m$ is fixed at 0.0020. This results in the following value, independent of units, for the initial modulus of concrete:

$$E_{co} = 1000\ \sigma_u \tag{21}$$

In CP110, on the otherhand, the value of the initial modulus of concrete is specified as

$$E_{co} = 55000\sqrt{\frac{\sigma_{cu}}{\gamma_m}} \tag{22}$$

where both $E_{co}$ and $\sigma_{cu}$ are expressed in N/cm$^2$. By substituting $k_1 = 0.67$ in Equation (17), Equation (22) may be rewritten as follows

$$E_{co} = 67193\sqrt{\sigma_u} \tag{23}$$

This value of $E_{co}$ is close to the value of

$$E_{co} = 66000\sqrt{\sigma_u} \tag{24}$$

specified in the CEB recommendations for the initial modulus of concrete for cases where the stresses under working conditions do not exceed 40 per cent of the compressive strength. Thus it appears that while the CEB recommendations differentiate between the elastic moduli of concrete at origin relating to the ultimate limit state calculations and to the instantaneous loading calculations, CP110 recommends the use of a single initial modulus of elasticity.

The value of $\varepsilon_m$ as deduced from CP110 may be expressed as follows

$$\varepsilon_m = \frac{2}{67193}\sqrt{\sigma_u} \tag{25}$$

which implies that $\varepsilon_m$ depends upon $\sigma_u$, unlike the CEB recommendations in which $\varepsilon_m$ is fixed at 0.0020.

## Notation

| | |
|---|---|
| $A$ | area of cross-section |
| $A_c$ | area of concrete |
| $A_s$ | area of steel |
| $d$ | nominal diameter of tube |
| $E_c$ | modulus of elasticity of concrete |
| $E_{co}$ | modulus of elasticity of concrete at origin |
| $E_s$ | modulus of elasticity of steel |
| $I$ | second moment of area |
| $I_c$ | second moment of area for the concrete section |
| $I_s$ | second moment of area for the steel section |
| $K_1$ | Basu and Sommerville's coefficient for basic column strength under axial load ($=P_a/P_s$) |
| $k_1$ | coefficient relating the bending strength of concrete in a member to its characteristic cube strength |
| $\delta$ | coefficient used in estimating triaxial concrete strength |
| $\varepsilon$ | strain |
| $\varepsilon_m$ | strain in concrete corresponding to peak stress |
| $\lambda$ | slenderness ratio |
| $\bar{\lambda}$ | slenderness factor |
| $\lambda_c$ | unit critical slenderness ratio ($= Lc/r$) |
| $\sigma$ | stress |
| $\sigma_a$ | average stress in steel |
| $\sigma_b$ | average stress in concrete |
| $\sigma_{cL}$ | augmented concrete strength under triaxial containment |
| $L$ | column length |
| $L_c$ | unit critical length, for which the Euler load equals the squash load for a given column cross-section |
| $\bar{N}$ | column strength non-dimensionalised with respect to its squash load ($= P_a/P_s$) |
| $P_a$ | column strength for axial load |
| $P_s$ | column squash load |
| $r$ | radius of gyration |
| $r_e$ | equivalent radius of gyration for composite columns |
| $S$ | standard deviation of test results on concrete strength |
| $t$ | tube thickness |
| $\alpha$ | concrete contribution parameter [1] |
| $\gamma_m$ | partial safety factor for material strength |
| $\sigma_{cu}$ | characteristic cube strength |
| $\sigma_{cyl}$ | characteristic cylinder strength |
| $\sigma_k$ | characteristic concrete strength |
| $\sigma_m$ | mean value of concrete strength from tests |
| $\sigma_u$ | design strength of concrete |
| $\sigma_y$ | yield strength of steel |
| $\sigma_y^*$ | reference yield strength of steel [1] |
| $\sigma_{yL}$ | reduced longitudinal strength of steel under hoop tension |
| $\phi$ | coefficient used in estimating reduced steel strength and enhanced concrete strength |
| $\bar{\phi}$ | $\sqrt{1+\phi+\phi^2}$ |

## References


1. Basu, A.K., and Sommerville, W.: Derivation of Formulae for the Design of Rectangular Composite Columns. Proc. Instn Civ. Engrs, 1969, Supplementary volume, Paper 7206S.
2. Basu, A.K., and Ghosh, S.K.: Circular Composite Columns (filled tubes) — Derivation of Design Formulae. CIRIA Tech. Note 58, 1975.
3. Freeman Fox and partners: B/116 Design Studies Report on Composite Columns. May 1972, Revised January 1973.
4. Johnson, R.P., and Anderson, D.: Design Studies for Composite Columns. TP83 and 84 Sub-Committee B/20/5, British Standards Institution, January 1974 (Not for publication).
5. Stevens, R.F.: The Strength of Encased Stanchions. National Building Studies Research Paper 38, H.M.S.O.
6. Jones, R. and Rizk, A.A.: An Investigation on the Behaviour of Encased Steel Columns Under Load. The Structural Engineer, 1963, 41, Jan.
7. Bondale, D.S.: The Effect of Concrete Encasement on Eccentrically Loaded Steel Columns, Ph.D. Thesis, University of London, 1962.
8. Anslijn, R., and Janss, J.: Le calcul des charges ultimes des colonnes métalliques enrobées de béton. Report MT89, CRIF, Brussels, 1974, April.
9. CEB-FIP: International Recommendations for the Design and Construction of Concrete Structures. Principles and Recommendations, June 1970.
10. Virdi, K.S.: Inelastic Column Behaviour — its Application to Composite Columns in Biaxial Bending and Stiffened Plates in Compression. Ph.D. Thesis, University of London, 1973.
11. Pippard, A.J.S., and Baker, J.F.: The Analysis of Engineering Structures, 4th ed., London, Arnold, 1968.

12. BEER, H., and SCHULZ, G.: The Theoretical Bases of the New Column Curves of the European Convention of Construction Steelwork (in French). Construction Métallique, N° 3, Septembre 1970.
13. KLÖPPEL, von K., and GODER, W.: Traglastversuche mit ausbetonierten Stahlrohren und Aufstellung einer Bemessungformel, Der Stahlbau, Berlin, 1957, 26, January and February.
14. NEOGI, P.K.: Concrete Filled Tubular Columns. Ph.D. Thesis, University of London, 1969.
15. SEN, H.K.: Triaxial Effects in Concrete Filled Tubular Steel Columns. Ph.D. Thesis, University of London, 1969.
16. GUIAUX, P., and JANSS, J.: Buckling Behaviour of Columns Made with Steel Tubes and Filled with Concrete (in French). Report MT65, CRIF, Brussels, 1970, Nov.
17. KNOWLES, R.B., and PARK, R.: Strength of Concrete Filled Steel Tubular Columns. J. of the Struct. Div. Proc. Am. Soc. Civ. Engrs, 1969, 95, December, 2565-2587.
18. SALANI, H.J., and SIMS, J.R.: Behaviour of Mortar Filled Steel Tubes in Compression. Proc. Am. Conc. Inst. 1964, 61, October, 1271-1283.
19. GARDNER, N.J., and JACOBSON, E.R.: Structural Behaviour of Concrete Filled Steel Tubes. Proc. Am. Conc. Inst., 1967, 64, July, 404-413. Also (Discussion), 1968, 65, January, 66-69.
20. FURLONG, R.W.: Strength of Steel Encased Concrete Beam Columns. J. of the Struct. Div. Proc. Am. Soc. Civ. Engrs, 1967, 93, October, 113-124.
21. JANSS, J.: Charges ultimes des profils creux remplis de béton chargés axialement. Report MT101, CRIF, Brussels, 1974, Nov.
22. CP110: The Structural Use of Concrete. British Standards Institution, 1972.
23. Handbook on the Unified Code for Structural Concrete (CP110: 1972): Cement and Concrete Association, 1972.
24. DESAYI, P., and KRISHNAN, S.: Equation for the Stress-strain Curve for Concrete. Proc. Am. Conc. Inst., 1964, 61, March.
25. HOGNESTAD, E.: A Study of Combined Bending and Axial Load in Reinforced Concrete Members. Univ. of Illinois, Bulletin No. 399, 1951, November.
26. BARNARD, P.R., and JOHNSON, R.P.: Ultimate Strength of Composite Beams. Proc. Instn Civ. Engrs, 1965, 32, October, 161, 179.
27. ECCS Commission 8: Stability. Recommendations, 1974.
28. VIRDI, K.S., and DOWLING, P.J.: A Unified Design Method for Composite Columns. CESLIC Report CC8, Engineering Structures Laboratories Civil Engineering Department, Imperial College, London, 1975, July.

## Summary

A new method for the design of composite columns under concentric loading is presented. The method adopts the recently developed European curves for the design of axially loaded bare metal sections as the basic design curves for composite columns. The column slenderness factor has been redefined as the ratio of column length to a unit critical length, which is defined as the length for which the column squash load equals its Euler load. The design load shows excellent agreement with over 200 analytically exact results and with over 100 experimental results.

The method has been extended to include the design of concrete filled circular tubes taking due account of triaxial containment of the concrete. Comparison with over 150 experimental results on concrete filled circular tubes shows that the unified method gives very good correlation with the experimentally obtained ultimate load.

## Résumé

Les auteurs présentent une nouvelle méthode pour le calcul des colonnes mixtes soumises à des efforts centrés. Les courbes de base adoptées sont les courbes de flambement de la Convention Européenne. L'élancement intrinsèque a été défini

comme rapport de la longueur de la colonne à celle pour laquelle la charge de ruine de la colonne est égale à la charge de flambage d'Euler. La méthode montre une excellente concordance avec plus de 200 résultats analytiques et plus de 100 résultats expérimentaux.

Le procédé a été étendu à l'étude des tubes remplis de béton, en tenant particulièrement compte des sollicitations triaxiales du béton. Là aussi la comparaison avec plus de 150 résultats expérimentaux montre une très bonne concordance.

## Zusammenfassung

Die Autoren behandeln eine neue Methode für den Entwurf von zentrisch beanspuchten Verbundstützen. Als grundlegende Entwurfskurven werden dabei die Knickkurven der europäischen Stalbaukonvention angenommen. Der bezogene Schlankheitsgrad wurde neu definiert als Verhältnis der Stützenlänge zur derjenigen Länge, für welche die Quetschlast der Stütze ihre Eulersche Knicklast erreicht. Die Übereinstimmung des Verfahrens mit über 200 theoretischen genauen Resultaten und über 100 Versuchsergebnissen ist ausgezeichnet.

Die Methode wurde auf betongefüllte Rohrstützen unter besonderer Berücksichtigung der dreiachsigen Betonbenaspruchung erweitert. Auch hier zeigt ein Vergleich mit über 150 entsprechenden Versuchsergebnissen eine sehr gute Übereinstimmung.

# Das Computerprogramm FLASH

*The Computer Program FLASH*

*Le programme FLASH*

U. WALDER
Wissenschaftlicher Mitarbeiter am Institut
für Baustatik und Konstruktion der ETH Zürich

E. ANDERHEGGEN
Privatdozent an der ETH Zürich

D. GREEN
Lecturer an der Universität Glasgow
ehem. Gast am Institut für Baustatik und Konstruktion, ETH Zürich, Schweiz

## Einleitung

In diesem Artikel wird das in den letzten drei Jahren am Institut für Baustatik und Konstruktion der ETH Zürich entwickelte Computerprogramm FLASH (Finite ELement Analysis of SHells) für die numerische Berechnung linear-elastischer Flächentragwerke nach der Methode der finiten Elemente vorgestellt.

Wozu ein weiteres Statikprogramm?

Es ist heute unbestritten, dass der an Computeranwendungen interessierte Bauingenieur in der Praxis imstande sein sollte, kommerziell angebotene Finite-Element-Programme selbständig zu benützen. Dazu ist notwendig:

— Dass an der Hochschule die erforderlichen theoretischen Grundkenntnisse vermittelt werden (eine neue Vorlesung über Computerstatik ist z.B. zu diesem Zweck an der ETHZ vor kurzem eingeführt worden).

— Dass den Bauingenieurstudenten die Möglichkeit geboten wird, direkte Erfahrungen bei der Verwendung vorhandener Statikprogramme zu sammeln. Sie sollen mit dem Computer etwas «spielen» können, was ihnen später in der Praxis kaum mehr möglich sein wird. (Das Programm FLASH wird heute zur Durchführung von Übungen der erwähnten Vorlesung «Computerstatik» sowie auch für Semester- und Diplomarbeiten eingesetzt.)

— Dass die für die Praxis bestimmten Programme sehr leicht anzuwenden sind, wobei sie aber gleichzeitig ein breites Anwendungsspektrum haben sollen. (FLASH kann beliebige Scheiben, Platten, Schalen, Faltwerke sowie auch Rahmen berechnen. Seine Programmbeschreibung umfasst jedoch lediglich vierzig Seiten.)

— Dass möglichst geringe Rechenkosten verursacht werden. Dem Programmbenützer muss jedoch ein Maximum an Ein- und Ausgabekomfort angeboten werden. (Zur Lösung des Gleichungssystems verwendet FLASH einen sehr

effizienten Algorithmus (die «frontal solution»), wodurch sich im Vergleich zu anderen Programmen sehr schnelle Ausführungszeiten ergeben. Bezüglich Benützerkomfort ist in erster Linie seine formatfreie problemorientierte «Eingabesprache» zu erwähnen, deren syntaktische Struktur sich mit einem kurzen und übersichtlichen Eingabeschema in allen Details beschreiben lässt.)

Damit sollen die mit der Entwicklung des Programmes FLASH verfolgten Ziele ersichtlich sein. Gestützt auf langjährige Erfahrungen auf dem Gebiete der Statikprogramme hat man versucht ein Instrument zu schaffen, das sich sowohl für den Baustatik-Unterricht als auch für die Praxis optimal eignet. Zu erwähnen sind zudem die zahlreichen für den Theoretiker interessanten Neuerungen, die im Programm eingebaut wurden, und die seinen Anwendungsbereich in mancher Hinsicht gegenüber demjenigen anderer Programme erweitern.

Dieser Artikel richtet sich in erster Linie an den Praktiker, der schon einige Erfahrung in der Anwendung finiter Elemente besitzt. Mathematische Herleitungen sowie auch die genaue Begründung der im Programm gewählten Lösungen werden deshalb hier nicht angegeben und sollen Gegenstand einer späteren Veröffentlichung sein.

Einzig die Herleitung der elastisch gestützten hybriden Plattenelemente, welche erstmals in einem Computerprogramm verwendet werden, und die eine der wesentlichsten theoretischen Neuerungen in FLASH darstellen, wird im Anhang angegeben.

## Anwendungsmöglichkeiten von FLASH

FLASH berechnet nach der Theorie 1. Ordnung elastische, homogene:

— Schalen, versteift oder unversteift;
— Faltwerke;
— Platten und Rippenplatten;
— Scheiben;
— Stabtragwerke.

unter statischen Beanspruchungen.

Die folgenden Punkte sollen noch eingehender auf die vielfältigen Anwendungsbereiche hinweisen:

— Fundamentplatten auf elastischer Unterlage, elastisch gebettete Schalen sowie elastisch senkbare oder unsenkbare Stützen können dank neuentwickelten Elementen erfasst werden.
— Die Berücksichtigung des Querkrafteinflusses bei Platten- und Schalenelementen erlaubt die Berechnung relativ dicker Flächentragwerke (z.B. Bogenstaumauern).
— Elementweise konstante, linear-elastische isotrope oder orthotrope Materialeigenschaften können behandelt werden.
— Die Möglichkeit, Stabelemente exzentrisch anzuschliessen, erlaubt die Berechnung von Rippenplatten als ebenes Problem.
— Alle wünschbaren Auflager- und Randbedingungen sind erfassbar.
— Flächen- und Knotenlasten sowie Auflagerverschiebungen sind in beliebigen Richtungen möglich. Auch Temperaturlasten können behandelt werden.

— Als Resultate erhält man in den Knotenpunkten und z.T. in den Elementschwerpunkten,
  · Deformationen,
  · Reaktionen,
  · Auflagerdrücke elastisch gestützter Elemente,
  · Momente aus Plattenwirkung,
  · Spannungen aus Scheiben- und Membranwirkung,
  · Hauptspannungen und Hauptmomente,
  · Armierungsmomente.
— Im weiteren ist es möglich, Schnitte am Gesamttragwerk zu definieren, in welchen integrale Schnittkräfte berechnet werden. Dies stellt vor allem für die Bemessung eine wesentliche Hilfe dar.

## Problemeingabe und Programmtechnik

Erfolg oder Misserfolg eines für praktisch tätige Ingenieure entwickelten Computerprogrammes hängen zum grossen Teil davon ab, ob es eine ihm schnell vertraute und seiner gewohnten Terminologie entsprechende Dateneingabe besitzt. Die Eingabe der Daten erfolgt bei FLASH mit Hilfe einer vorgeschriebenen Folge formatfreier, aus Worten und Problemdaten bestehender Befehle, die klar abgegrenzt nacheinander die Geometrie, Materialeigenschaften, Auflagerbedingungen, usw. definieren [1]. Hat der Ingenieur einmal ein oder zwei Probleme mittels FLASH gelöst, kann er auf die eingehende Beschreibung verzichten und sich an ein nur dreiseitiges, streng logisch aufgebautes Schema der Befehlsfolge halten. Obwohl dieses äusserst einfach und kurz ist, beinhaltet es doch einen grossen Eingabekomfort, wie z.B. das automatische Generieren von Knoten- und Elementmaschen, die Kreisgenerierung, etc.

Ebenso wesentlich wie die leichte Eingabe der Daten ist deren bequeme Kontrolle. FLASH kann ohne etwas zu rechnen die Eingabefehle auf syntaktische und logische Fehler kontrollieren. Hunderte von Fehlermeldungen helfen dabei Korrekturen rasch anzubringen. Neben einem «Echoprint» der Daten kann auch eine axonometrische Zeichnung der Elementmasche auf Film oder Papier verlangt werden.

Eine weitere Forderung, welche an ein erfolgreiches Programm gestellt wird, stellt die Einsparung von Rechenzeit dar. Tatsächlich benötigt FLASH gegenüber herkömmlichen Programmen erheblich kürzere Rechenzeiten. Die folgenden Hinweise sollen einen Eindruck der gewählten Programmtechnik im Hinblick auf die Kostenersparnis geben:

— Die Steifigkeits-, Spannungs- und Lastmatrizen von Elementen gleicher Form und gleichen Materials werden nur einmal berechnet.
— Wie erwähnt, erfolgt die Lösung des Gleichungssystems nach der «frontalsolution»-Methode, d.h. das Zusammenstellen der globalen Steifigkeitsmatrix geschieht gleichzeitig mit dem Lösen der Gleichungen.
— Die Datenspeicherung erfolgt voll dynamisch, d.h. kleine Probleme belegen weniger Foldlänge im Computer und werden deshalb mit höherer Priorität und niedrigeren Einheitskosten behandelt.

— Die Problemgrösse wurde auf ca. 5000 Freiheitsgrade (= Anzahl zu lösender Gleichungen) beschränkt, um den sogenannten «overhead», d.h. die Programmteile, die nur Daten verwalten, auf ein Minimum zu reduzieren.

Die im weiteren angegebenen Beispiele sollen nicht nur die Genauigkeit der Berechnungen selbst, sondern anhand der Eingabeanweisungen und Rechenzeiten auch die Handlichkeit und Effizienz des Programmes FLASH aufzeigen.

## Scheibenprobleme

Zur Lösung von Scheibenproblemen verwendet FLASH beliebig geformte dreieckige und viereckige hybride Elemente. Diese stellen eine Weiterentwicklung des ursprünglich von T.H. Pian [2] vorgeschlagenen Modelles dar. Dabei werden bekanntlich die Steifigkeitseigenschaften einzelner Elemente, d.h. deren lokale Steifigkeitsmatrizen und Lastvektoren aufgrund des Minimumprinzips der komplementären Energie mit Hilfe elementinterner Spannungsansätze sowie kinematischer Randverschiebungsansätze bestimmt. Die Elementzusammensetzung erfolgt dann, wie bei den rein kinematischen Modellen, nach dem gewöhnlichen Matrix-Deformationsverfahren.

Als wesentliche Merkmale der FLASH Scheiben- und Schalenelemente sind die in den Knoten zusätzlich eingeführten Rotationsfreiheitsgrade $R_z$, welche einer Drehung um eine senkrecht zur Scheibenebene stehenden Achse entsprechen sowie die numerischen Integrationsprozeduren zur Berechnung der Flächen- und Randintegrale zu erwähnen.

Abgesehen vom Befehl mit den Anweisungen FREI und NICHTFREI, welcher die Auflagerbedingungen definiert, dürfte die Befehlsfolge in Bild 1 auch dem Computerlaien verständlich sein. (Die Randbedingungen der Scheibe werden durch Festhalten oder Freilassen der Verschiebungen u und v sowie der Rotation $R_z$ in den Auflagerknoten oder Symmetrieschnitten bestimmt.) Die Eingabebefehle sind hier in ihrer ausführlichsten Form angegeben worden. Anstelle ganzer Wörter darf auch nur der Anfangsbuchstabe stehen, einige könnten gar ganz weggelassen werden.

Die Resultate zeigen neben dem guten Übereinstimmen mit der theoretischen Lösung eine weitere positive Eigenschaft hybrider Elemente. Singularitäten erscheinen deutlich, ohne jedoch die Resultate in den umliegenden Knoten zu beeinträchtigen. Dies trifft nicht nur für die Scheibenelemente, sondern vor allem auch für die Plattenelemente zu.

Die Scheibenelemente lassen sich auch ohne Schwierigkeiten zusammen mit Stabelementen verwenden (z.B. ebene Rahmen mit Wandaussteifungen).

## Plattenprobleme

Zur Berechnung von Platten werden ebenfalls hybride dreieckige und viereckige Elemente verwendet [2]. Eine Neuentwicklung stellen die hybriden elastisch gestützten Elemente dar. Ihre theoretische Herleitung ist im Anhang angegeben. Sie erlauben eine wirklichkeitsgetreuere Berechnung von Flächenlagerungen als

*Beispiel 1:* Ringspannungen.

Problem:

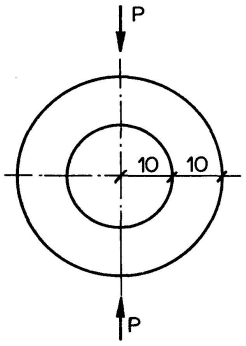


E = 30'000
$\nu$ = 0.
t = 1.
P = 62.83185

Elementmasche:

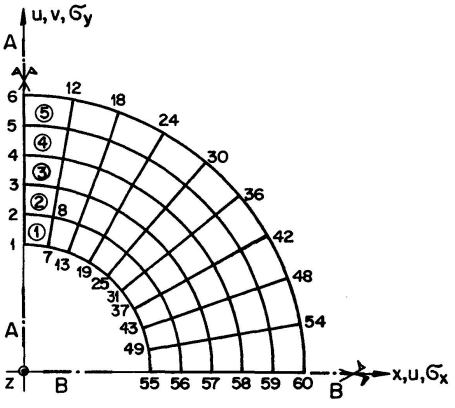


Resultate:

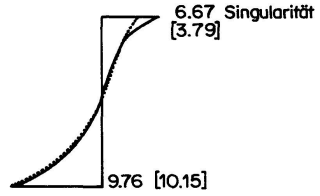


$\sigma_x$: Schnitt A-A




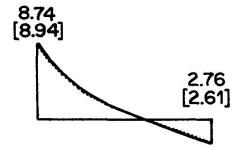


$\sigma_y$: Schnitt B-B

Eingabeanweisungen:

```
BEGINN
BEISPIEL 1: RINGSPANNUNGEN
INPLANE 60 45 45
KNOTEN 1 0. 10. PLUS 0. 2.    2 BIS 6
KNOTEN 55 10.  PLUS   2.     56 BIS 60
CIRCLE  1 55 ZENTRUM 0. PLUS 8   7 BIS 49 SCHRITT 6
CIRCLE  2 56 ZENTRUM 0. PLUS 8   8 BIS 50 SCHRITT 6
CIRCLE  3 57 ZENTRUM 0. PLUS 8   9 BIS 51 SCHRITT 6
CIRCLE  4 58 ZENTRUM 0. PLUS 8  10 BIS 52 SCHRITT 6
CIRCLE  5 59 ZENTRUM 0. PLUS 8  11 BIS 53 SCHRITT 6
CIRCLE  6 60 ZENTRUM 0. PLUS 8  12 BIS 54 SCHRITT 6
*
ISOTROP 30000. 0. 1. TYP  1 BIS 45
*
MASCHE 5 9 ELEMENT 1 KNOTEN 7 8 2 1
*
TYP  1 45 ELEMENT 1 BIS 45
*
NICHTFREI FREI NICHTFREI KNOTEN 1 BIS 6
FREI NICHTFREI NICHTFREI KNOTEN 55 BIS 60
*
PLOT 1. BLICKPUNKT 0. 0. 1.
*
LASTFALL RADIALE EINZELLASTEN
KNOTENPUNKT 0. -15.708 KNOTEN 6
*
LASTFALL 1
DEFORMATIONEN $ REAKTIONEN $ SPANNUNGEN KNOTENWEISE
*
```

Rechenzeiten : (auf CDC-6500, CP-Zeit)

| | | |
|---|---|---|
| Steifigkeits-, Spannungs- und Lastmatrizen | : | .21 sek / Element |
| Lösen des Gleichungssystems (180 Unbekannte) | : | 2.38 sek |
| Totale Ausführungszeit | : | 20.33 sek |
| Totale Rechenkosten am Rechenzentrum der ETHZ | : | ~ 14.50 SFr. |

Bild 1.

mit den üblichen hybriden Plattenelementen, welche lediglich in den Knotenpunkten gestützt werden können. So lassen sich zum Beispiel die über Punktstützungen auftretenden Momentensingularitäten durch die Approximation der Stützenköpfe mit elastisch gestützten Elementen elegant vermeiden (siehe Beispiel 2). Dem gewählten Modell liegt die Annahme eines gleichmässig verteilten Reaktionsdruckes auf das Element zugrunde (Bettungszifferverfahren bei Fundamentplatten). Die Elemente bleiben frei drehbar, d.h. die Stützen weisen keine Einspannung in der Platte auf. Der Fall der nicht senkbaren Stütze kann ebenfalls behandelt werden.

Die folgenden Beispiele sollen auf die praktischen Anwendungsmöglichkeiten der elastisch gestützten Elemente hinweisen.

*Beispiel 2:* Flachdecke mit Mittelstütze.

Problem + Elementmasche :

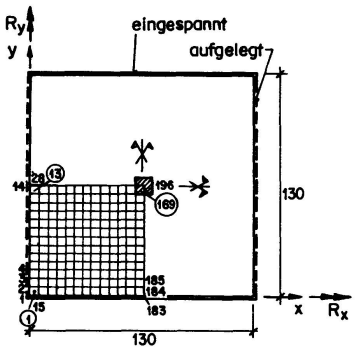


E = 11.52
$\nu$ = .2
t = 1.

Belastung:
g = 1.

Eingabeanweisungen :

```
BEGINN
DOPPELSYMMETRISCHE PLATTE MIT MITTELSTUETZE
PLATTE 196 169 2
MATRIX 14 14 KNOTEN 1 1 14 0. PLUS 0. 5. UND 5.
*
ISOTROP 11.52 .2 1. TYP 1
ISOTROP 11.52 .2 1. FEDERKONSTANTE 100.93 TYP 2
*
MASCHE 13 13 ELEMENT 1 KNOTEN 15 16 2 1 TYP 1
*
TYP 2 ELEMENT 169
*
NICHTFREI NICHTFREI NICHTFREI KNOTEN 1 BIS 183 SCHRITT 14
NICHTFREI NICHTFREI FREI KNOTEN 1 BIS 14
F N F 28 B 182 S 14
F F N 184 B 195
F N N 196
*
NO - PLOT
*
LASTFALL FLAECHENLAST
GLEICHMAESSIG -1. ELEMENTE 1 BIS 169
*
LASTFALL 1
DEFORMATIONEN $ REAKTIONEN $ AUFLAGERDRUCK $ MOMENTE KNOTENWEISE
*
```

Resultate :

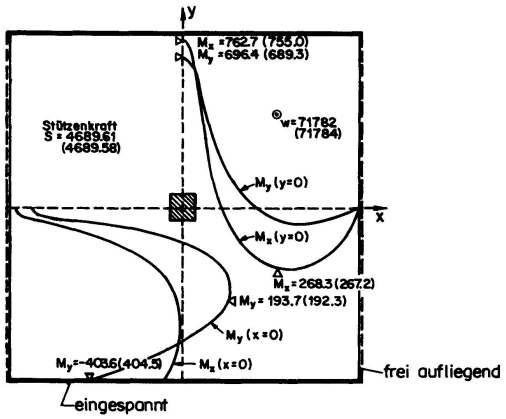


Rechenzeiten : (auf CDC - 6500 ; CP - Zeit)

| | | |
|---|---|---|
| Steifigkeits-, Spannungs- und Lastmatrizen | : | 1.86 sek |
| Lösen des Gleichungssystems (588 Unbekannte) | : | 17.98 sek |
| Totale Ausführungszeit | : | 29.35 sek |
| Totale Rechenkosten am Rechenzentrum der ETHZ | : | ~25.— SFr. |

Bild. 2.

Die Resultate in Klammern wurden mit dem PLATE-FOURIER-Programm [4] gerechnet.

Die drei Knotenfreiheitsgrade der Platte sind die senkrechte Verschiebung w und die beiden Verdrehungen $R_x$ und $R_y$. Die Auflager- und Symmetriebedingungen werden wie bei den Scheiben durch Festhalten der entsprechenden Freiheitsgrade beschrieben. Dieses Festhalten braucht übrigens nicht starr zu sein; auch in den Knoten besteht die Möglichkeit einer gefederten Lagerung.

Das zweite Plattenbeispiel zeigt einen Genauigkeitsvergleich mit der bekannten Lösung der elastisch gestützten Kreisplatte unter einer Einzellast [5]. Die Voraussetzung eines gleichmässig verteilten Reaktionsdruckes unter der Kreisplatte erlaubt, unter Ausnützung der Kreissymmetrie, die Berechnung mit einem einzigen Element durchzuführen.

*Beispiel 3:* Fundamentplatte unter einer Einzellast.

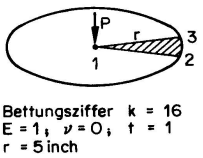


Bettungsziffer k = 16
E = 1; ν = 0; t = 1
r = 5 inch

| FLASH | Theorie [5] | |
|---|---|---|
| $43 \cdot 10^{-3}$ | $43 \cdot 10^{-3}$ | $\omega_{max}$ (r = 0) |
| $39.1 \cdot 10^{-3}$ | $39.1 \cdot 10^{-3}$ | $\omega_{min}$ (r = 5) |

Bild 3.

Die Berechnung von Rippenplatten kann mit FLASH auf verschiedene Arten durchgeführt werden. Will man zum Beispiel eine Kassettendecke als reines Plattenproblem behandeln, können die Rippen durch exzentrisch angeschlossene Stäbe approximiert werden. Der Vorteil einer solchen Berechnungsart besteht in der geringeren Anzahl zu lösender Gleichungen (drei Freiheitsgrade pro Knoten) gegenüber einer Schalenberechnung (sechs Freiheitsgrade pro Knoten). Als Nachteil muss in Kauf genommen werden, dass sich die Platte wie auch die Rippen in Plattenebene nicht verformen können. Die Schalenberechnung berücksichtigt diese Verformung. Die Rippen können dabei ebenfalls mit exzentrisch angeschlossenen Stäben oder aber mit Flächenelementen berücksichtigt werden.

## Schalenprobleme

Die in FLASH verwendeten Schalenelemente sind eben und setzen sich aus je einem der vorher erwähnten Scheiben- und Plattenelemente zusammen. Die Knotenfreiheitsgrade sind die drei Verschiebungen und Verdrehungen, weshalb sich die Elemente auch beliebig in räumliche Rahmensysteme integrieren lassen. FLASH wurde mit Erfolg bereits für eine grosse Anzahl praktischer Flächentragwerksberechnungen eingesetzt (Kastenträgerbrücken, Unterführungen, Staumauern, Schalendächer, Maschinenteile, etc.). Da für solche Probleme aber keine analytischen Lösungen vorliegen, wird hier als Berechnungsbeispiel der Vergleich mit der Lösung einer Schalenaufgabe aus [6] angegeben.

Die Dateneingabe für Schalenprobleme folgt dem gleichen Schema wie für Platten und Scheiben. Nützt man alle Möglichkeiten der Knoten- und Elementmaschengenerierung aus, benötigt man zur Beschreibung des Problems des halb gefüllten Rohres nur ungefähr 40 Befehle. Am gleichen Beispiel zeigt sich auch besonders deutlich der Vorteil, die Elementsteifigkeitsmatrizen für Elemente gleicher Form und gleicher Materialeigenschaften nur einmal berechnen zu müssen. Würde man die Steifigkeitsmatrizen für jedes der 192 Elemente einzeln bestimmen, bedeutete dies eine Erhöhung der Rechenkosten um ca. 300%.

Die Möglichkeit, als Resultate nicht nur die Schnittkräfte in den Knoten und Elementschwerpunkten, sondern auch in ausgewählten Schnitten am Gesamttragwerk zu verlangen, erweist sich speziell bei der Bemessung von Schalentrag-

*Beispiel 4:* Halb gefülltes Rohr.

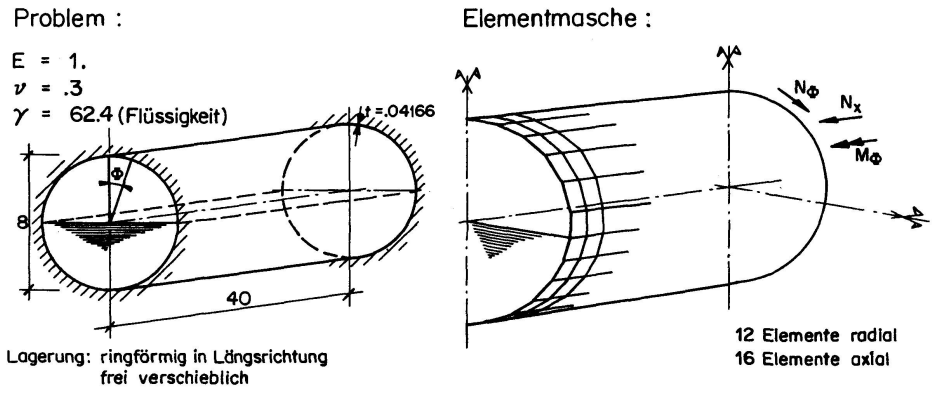


Resultate :

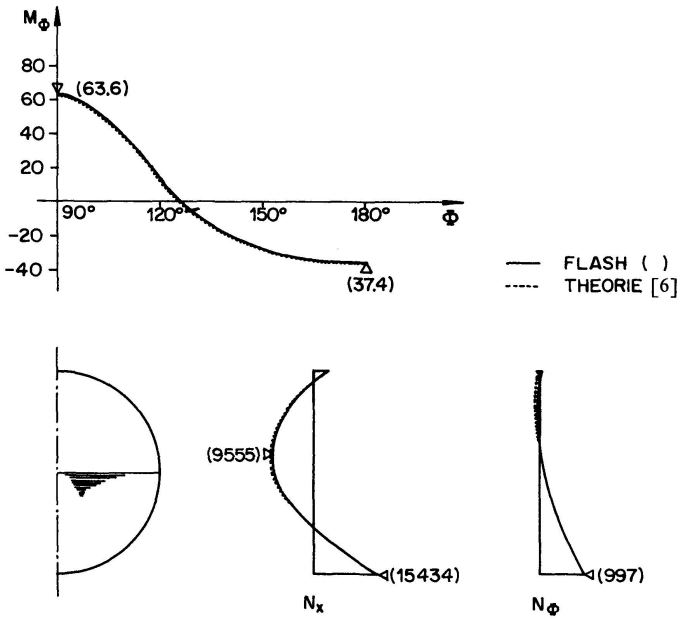


Rechenzeiten : (auf CDC-6500 ; CP - Zeit)

| | | |
|---|---|---|
| Steifigkeits-, Spannungs- und Lastmatrizen | : | 2.2 sek |
| Lösen des Gleichungssystems (1326 Unbekannte) | : | 96.4 sek |
| Totale Ausführungszeit | : | 121.8 sek |
| Totale Rechenkosten am Rechenzentrum der ETHZ | : | ~95.– SFr. |

Bild 4.

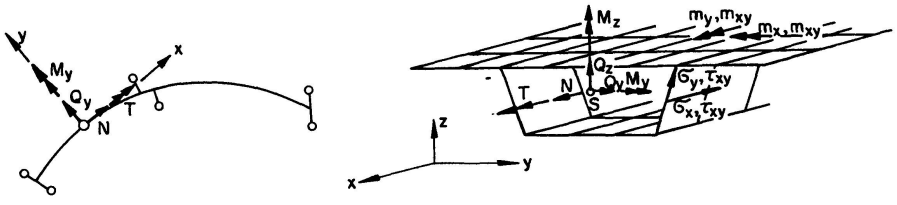


Bild. 5. FLASH liefert neben den lokalen Beanspruchungen auch globale, integrale Schnittkräfte.

werken als sehr praktisch. Die Elementschnittkräfte sind ja stets eine Summe der Beanspruchungen aus Biegung, Torsion, Normal- und Querkräften, und eine Trennung der verschiedenen Anteile ist besonders bei komplizierteren Lagerungsbedingungen nicht möglich. Die integralen Schnittkräfte geben diese Anteile und ersparen die grosse Arbeit um von den lokalen Beanspruchungen zu den für die Bemessung massgebenden Gesamtschnittkräften zu kommen (siehe Bild 5).

## Stabtragwerke

Das Programm FLASH wurde nicht zu einem eigentlichen Stabtragwerksprogramm ausgebaut. Die Stabelemente stellen vor allem eine Ergänzung zu den Flächenelementen dar. Die grosse rechnerische Effizienz des Programmes kann jedoch bei sehr grossen Systemen gleichwohl eine Berechnung mit FLASH rechtfertigen. Als praktisches Beispiel sei die Berechnung von Stahlrahmen eines 64-stöckigen Hochhauses mit jeweils mehr als 1500 Stäben erwähnt. Die Rechenzeit für einen Rahmen lag unter drei Minuten auf der CDC-6500 Anlage des Rechenzentrums der ETH Zürich, was einem Kostenaufwand von ca. SFr. 200.— entsprach.

## Anhang

### *Elastisch gestützte hybride finite Elemente*

Eine Lösung für das Problem elastisch gebetteter Elemente wurde erstmals für ein Deformationsmodell in [8] angegeben.

Um den Rahmen eines Anhanges nicht zu sprengen, werden hier nur die neuen Terme der elastischen Stützung in die Variationsgleichung für das hybride Spannungsmodell eingeführt. Die Voraussetzungen und allgemeine Herleitung findet man in [7, S. 87 ff], worin auch die hier verwendete Nomenklatur erläutert wird.

Das hybride Spannungsmodell basiert auf folgender Variationsgleichung ([7, S. 91]):

$$\delta\bar{I}(\sigma, v) = \sum_{e} \int_{V_e} [\delta\sigma(D^{-1} \cdot \sigma - \Delta v) + \delta v(\nabla\sigma + g)] \cdot dV + \int_{D} \ldots + \int_{R} \ldots$$

Mit der Einführung des Stützendruckes s ergibt sich folgende erweiterte Gleichgewichtsgleichung und folgende zusätzliche kinematische Bedingung:

$$\nabla\sigma + g - s = 0: \text{ Gleichgewichtsgleichung}$$
$$v - \tfrac{1}{f} \cdot s = 0 \quad : \text{ kinematische Bedingung}$$

wobei: f = Federkonstante, d.h. Druck pro Einheitsverschiebung v = 1
v = Plattendurchbiegung.

Die Variationsgleichung lautet dann wie folgt:

$$\delta\bar{I}(\sigma, v, s) = \sum_{e} \int_{V_e} [\delta\sigma(D^{-1} \cdot \sigma - \Delta v) + \delta v(\nabla\sigma + g - s) - \delta s(v - \tfrac{1}{f} \cdot s)] \cdot dV +$$
$$\int_{D} \ldots + \int_{R} \ldots$$

Die Integration mit: $\delta v \cdot s + v \cdot \delta s = \delta(v \cdot s)$

und den weiteren in [7, Anhang E] gegebenen Formeln ergibt ($F_e$ = Elementfläche):

$$\bar{I}(\sigma, v, s) = \sum_e \left(\tfrac{1}{2} \int_{V_e} \sigma \cdot D^{-1} \cdot \sigma \cdot dV + \tfrac{1}{2} \int_{F_e} \tfrac{1}{f} \cdot s^2 \cdot dF + \int_{V_e} v(\nabla\sigma + g - s) \cdot dV - \int_D \ldots - \int_R \ldots\right.$$

Die Lösung ergibt sich aus $\delta\bar{I} = 0$, d.h. aus der Bedingung, dass $\bar{I}(\sigma, v, s)$ stationär sein muss (Spezialform des Helliger-Reissner-Prinzips). Die finite Elementformulierung schreibt sich folgendermassen:

$$\bar{I}(\sigma, v, s) = \sum_e \bar{I}_e(\sigma, v, s) = \sum_e \left(\tfrac{1}{2} \int_{V_e} \sigma \cdot D^{-1} \cdot \sigma \cdot dV + \tfrac{1}{2} \int_{F_e} \tfrac{1}{f} \cdot s^2 \cdot dF + \int_{V_e} v(\nabla\sigma + g - s) \cdot dV\right) - \int_R \ldots$$

*Hybride elastisch gestützte Plattenelemente*

Es werden nur die von der allgemeinen Herleitung [7, S. 100 ff] abweichenden Ansätze für die Spannungen $\sigma$ angegeben. Die Darstellung erfolgt in der gebräuchlicheren Matrixschreibweise.

lokale Spannungsansätze: $\{\sigma\} = [\psi]\{\beta\} + \{\Psi_0\}$, dh:

$$\{\sigma\} = \begin{Bmatrix} m_x \\ m_y \\ m_{xy} \\ q_x \\ q_y \end{Bmatrix} = [\{\psi_1\} \text{ —— } \{\psi_n\} \mid \{\psi_{n+1}\}] \begin{Bmatrix} \beta_1 \\ | \\ \beta_n \\ \hline \beta_{n+1} \end{Bmatrix} + \{\psi_0\}$$

$[\psi]$ wird dabei so gewählt (in FLASH: Polynom 2. Grades mit n = 17), dass

$$\begin{aligned} \{\nabla\psi_0\} &= -g \\ \{\nabla\psi_1\} \ldots \{\nabla\psi_n\} &= 0 \\ \{\nabla\psi_{n+1}\} &= 1 \\ \beta_{n+1} &= s \end{aligned}$$

womit die Gleichgewichtsbeziehung der Platte:

$$m_{x,xx} + 2m_{xy,xy} + m_{y,yy} + g - s \equiv \nabla\sigma + g - s = 0$$

erfüllt ist. Die Formänderungsenergie des Elementes lässt sich dann folgendermassen schreiben:

$$\bar{I}_e(\sigma, v_R, s) = \tfrac{1}{2} \underset{1\times(n+1)}{\{\beta\}^T} \underset{(n+1)\times(n+1)}{\left[[F] + [F_s]\right]} \underset{(n+1)\times 1}{\{\beta\}} + \underset{1\times(n+1)}{\{\beta\}^T} \underset{(n+1)\times 1}{\{F_o\}} - \bar{W}_e(\sigma, v_R)$$

wobei:

$$[F] = \int_{F_e} [\psi]^T [D]^{-1} [\psi] \cdot dF: \quad \text{Flexibilitätsmatrix}$$

$$\{F_o\} = \int_{F_e} [\psi]^T [D]^{-1} \{\psi_0\} \cdot dF$$

$$[F_s] = \begin{bmatrix} 0 & & \\ & \frac{F_e}{f} & \end{bmatrix} \text{ Nullmatrix mit } F_{s\,(n+1),(n+1)} = \frac{F_e}{f}$$

$$\left( \text{folglich: mit } \beta_{n+1} = s: \tfrac{1}{2} \{\beta\}^T [F_s] \{\beta\} = \tfrac{1}{2} \int_{F_e} \frac{s^2}{f} \cdot dF \right)$$

Die Wahl der Ansätze für die Randverschiebungen $v_R$ ([7, S. 100 ff]), wie auch die weitere Berechnung der lokalen Steifigkeits-, Spannungs- und Lastmatrizen entspricht dem bekannten Vorgehen ([2], [7, S. 101 ff]). Den Stützendruck s erhält man aus der Bestimmung der Spannungsparameter $\{\beta\}$ ($s = \beta_{n+1}$). Auch diese Berechnung folgt dem bekannten Algorithmus ([7, S. 102 ff]). Es bleibt zu erwähnen, dass der eben dargestellte Algorithmus im Gegensatz zu dem in [8] gegebenen, auch für Dreieckselemente anwendbar ist.

## Literaturverzeichnis


1. WALDER, U.: Programmbeschreibung zum Statikprogramm FLASH. Institut für Baustatik und Konstruktion, ETH Zürich, 1975.
2. PIAN, T.H.H.: Element Stiffness Matrices for Boundary Compatibility and for Prescribed Boundary Stresses. Proc. of the Conference on Matrix Methods in Structural Mechanics, Dayton/Ohio, Oct. 1965, AFFDL-TR-66-80 (Nov. 1966).
3. PESTEL, E.C., LECKIE, F.A.: Matrix Methods in Elasto-Mechanics. McGraw-Hill Co., 1963.
4. PFAFFINGER, D., THÜRLIMANN, B.: Tabellen für unterzugslose Decken. Verlags-AG der akademischen technischen Vereine Zürich, 1967.
5. TIMOSHENKO, S.P., WOINOWSKY-KRIEGER, S.: Theory of Plates and Shells. Internat. Student Edition, 2. Auflage, McGraw-Hill Co.
6. FLÜGGE, W.: Stresses in Shells, 4. Auflage, Springer-Verlag, 1967.
7. ANDERHEGGEN, E.: Grundlagen der Computerstatik. Autographie. Institut für Baustatik und Konstruktion ETHZ, 1975.
8. ANDERHEGGEN, E.: Programme zur Methode der finiten Elemente. Institut für Baustatik ETHZ, Bericht Nr. 23, 1969, Birkhäuser Verlag Basel und Stuttgart.


## Zusammenfassung


Das Computerprogramm FLASH berechnet nach der Methode der finiten Elemente linear elastische Scheiben, Platten, Faltwerke, Schalen und Stabtragwerke unter statischen Beanspruchungen. Es zeichnet sich durch eine sehr einfache Benützung und hohe rechnerische Effizienz aus. Anhand einiger Beispiele werden seine vielfältigen Anwendungsmöglichkeiten erläutert. Das Programm verwendet hybride Finite-Element-Modelle. Auf die zum ersten Mal eingeführten «elastisch gestützten» Elemente wird im Anhang näher eingegangen.


## Summary


The computer program FLASH analyzes by the finite element method linear elastic shells, folded-plates, plates in bending and stretching as well as frames under statical loads. The main characteristics of the program are its simple applica-

tion and its great numerical efficiency. The program FLASH uses a hybrid finite element model. In the appendix the derivation of "elastic-supported elements» which have been used for the first time is given in some detail.

**Résumé**

Avec le programme d'ordinateur FLASH on calcule les plaques, les voiles et les cadres élastiques par la méthode des éléments finis. Le programme offre une facilité d'emploi remarquable et une grande efficacité numérique. Ses applications pratiques sont démontrées par quelques exemples. FLASH utilise un modèle d'éléments finis hybrides. Dans l'appendice on décrit en détail les «éléments appuyés élastiquement» qui ont été utilisés ici pour la première fois.